THÈSE

En vue de l'obtention du

DOCTORAT DE L'UNIVERSITÉ DE TOULOUSE

Délivré par *Institut National Polytechnique de Toulouse*

Spécialité : *Dynamique des fluides*

Présentée et soutenue par Dirk WUNSCH

le 16 décembre 2009

Theoretical and numerical study of collision and coalescence - Statistical modeling approaches in gas-droplet turbulent flows

---

JURY

Julien REVEILLON	Président
Marc MASSOT	Rapporteur
Martin SOMMERFELD	Rapporteur
Pierre RUYER	Examinateur
Amsini SADIKI	Examinateur
Philippe VILLEDIEU	Examinateur
Olivier SIMONIN	Directeur de thèse
Pascal FEDE	Co-Directeur de thèse

École doctorale: Mécanique, Energétique, Génie Civil, Procédés (MEGeP)
Unité de recherche: Institut de Mécanique des Fluides de Toulouse (IMFT)
Directeurs de thèse: Olivier SIMONIN, Pascal FEDE

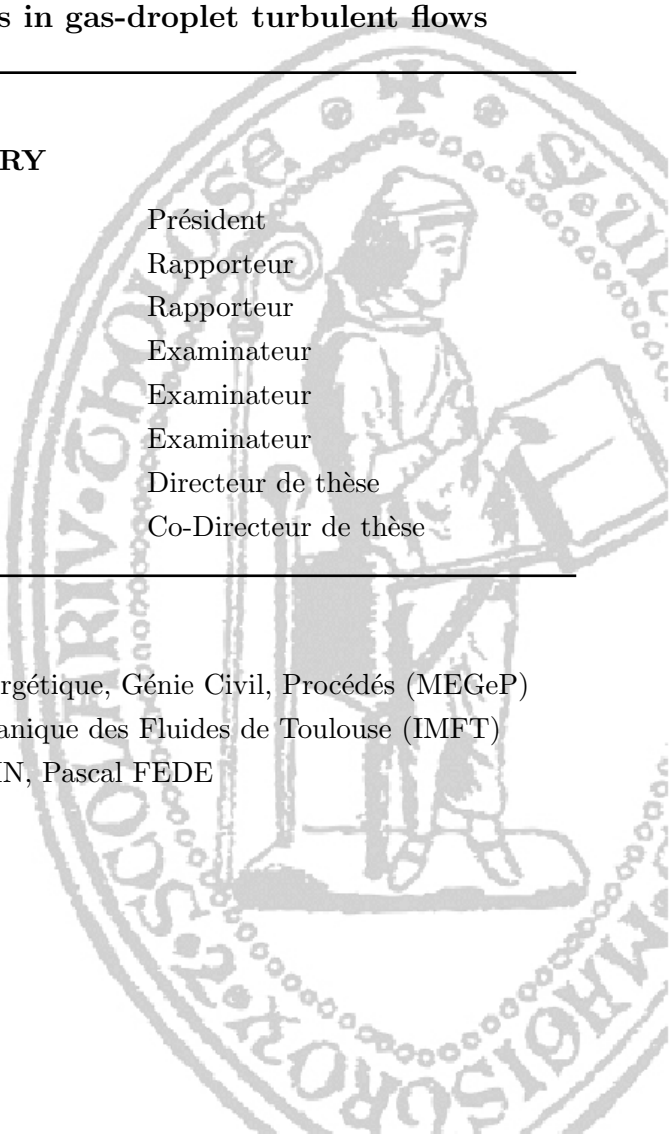

Résumé

Les écoulements multiphasiques sont au centre de nombreux enjeux scientifiques et industriels. Si on se limite au problèmes liés à la coalescence (c'est à dire la réunion de deux gouttes après collision), une grande variété de problèmes techniques sont concernés. On peut mentionner d'abord la combustion. Une combustion efficace et propre est essentielle pour notre bien-être économique et écologique. Si on prend l'exemple de l'injection du carburant liquide dans des moteurs à combustion interne, le spray du carburant subit une série de transformations, de la désintégration d'une nappe liquide jusqu'au la coalescence des gouttes plus en aval. La tailles des gouttes a une influence importante sur le processus de combustion. Lorsque le diamètre des gouttes augmente, le temps d'évaporation de celles-ci augmente. Dans les moteurs à combustion interne, une distribution homogène de petites gouttes est recherchée, afin d'obtenir un allumage le plus tard possible et d'éviter la expansion du gaz par la combustion au cours de la compression mécanique du piston. D'autres exemples de la coalescence existent dans le domaines de la météorologie, de conversion d'énergie nucléaire ou des vols spatiaux, où de l'aluminium liquide est injecté dans les réacteurs à combustible solide afin qu'augmenter la poussé (Hylkema [59]).

Ce travail se concentre sur l'interaction entre la turbulence d'un fluide et la coalescence des gouttes ainsi que sur différentes approches de modélisation statistique de cet interaction. Il y a deux enjeux principaux: l'interaction entre la phase continue et la phase dispersée et l'interaction entre les éléments de la phase dispersée. La phase dispersée peut être classé en fonction de sa fraction volumique ou massique.

Les écoulements dilués, c'est à dire avec une charge volumique $\alpha_p < 10^{-4}$, sont principalement gouvernés par le transport des particules en interaction avec le fluide. L'effet des collisions entre les particules peut être negligé.

Pour des charges volumiques $\alpha_p > 10^{-4}$ l'effet des collisions doit être pris en compte, car il influence la distribution des gouttes d'une manière importante. Il n'existe pas de théorie unifiée, qui décrit les caractéristiques de l'interaction des particules/gouttes, avec un écoulement turbulent. Seuls dans les deux cas limite une théorie existe; pour le cas de

l'inertie zéro (Saffman & Turner [110]) et pour une inertie très élevée (Abrahamson [1]). Dans le premier régime, les particules/gouttes suivent parfaitement l'écoulement turbulent. A l'invers elles ne répondent presque pas à l'écoulement pour les inerties très élevées. Le régime entre ces deux cas limites est l'objet de recherche de plusieurs groupes de travail ([48], [72], [119], [127], [133], [142], [145]).

Si la charge massique depasse $\phi_p > 10^{-2}$, l'influence de la phase dispersée sur la phase continue doit être prise en compte. Ce couplage inverse est l'objet de plusieurs études [35], [125], mais est negligée dans ce travail.

La question est: comment peut-on simuler les écoulement multiphasique en générale? A l'échelle microscopique ($\approx 10^{-3}m$) la simulation directe numérique de l'écoulement diphasique est possible. Les approches utilisé sont les méthodes VOF [5], [64] ou Level Set [55], [128]. Cette description microscopique est très détaillée et n'est pas adaptée pour mesurer les statistiques nécessaires à la validation des approches statistiques que l'on cherche à développer. A l'échelle "mésoscopique" ($\approx 10^{-1}m$), la mesure de ces statistiques devient accessible. Afin d'introduire le niveau le plus faible de modélisation possible, le champ fluide est résolu par la simulation numérique directe DNS. La phase dispersée est traitée par la simulation discrète des particules DPS ([34], [41], [73], [124], [140]). La trajectoire de chaque particule est suivie d'une manière déterministe et les collisions entre particules/gouttes sont traitées une par une. La coalescence mène à un système polydispersé en taille.

Dans la première partie de ce travail, un algorithme de détection et de traitement de collision pour la prise en compte d'une phase polydispersée est développé. Le couplage entre la DNS et la DPS permet ensuite d'effectuer des "expériences numériques", prenant en compte l'interaction entre la phase fluide turbulente et la phase de gouttes polydispersées subissant la coalescence. Ce type de simulation, appelé DNS/DPS par la suite, permet d'introduire un minimum de modélisation. Les simulations effectuées avec cette approche, servent à la compréhension de l'interaction entre un champ turbulent et une phase de gouttes polydispersées, ainsi que de base de référence pour la validation et le support de développement des approches de modélisation statistique utilisées dans des configurations industrielles. En particulier, les résultats des simulations sont comparés avec les prédictions d'une approche Lagrangienne de type Monte-Carlo et de l'approche Eulerienne 'Direct Quadrature Method of Moments' (DQMOM). Dans ces approches, différentes fermetures des termes de coalescence sont validées. Les unes sont basées sur l'hypothèse de chaos-moléculaire, les autres permettent de prendre en compte les possibles corrélations entre les vitesses des gouttes avant leur collision. Il est montré que cette dernière fermeture prédit beaucoup mieux le taux de coalescence par comparaison avec les résultats des simulations déterministes. Comme mentionné précédement, la modélisation des collisions

interparticulaires en présence d'un champ fluide turbulent, comprend deux domaines très intéressants mais difficiles de la mécanique des fluides: l'interaction entre le fluide et la phase dispersée d'un côté et l'interaction entre les éléments de la phase dispersée de l'autre. C'est la coalescence des gouttes, qui est traité dans le chapitre 2. Les interactions entre les gouttes peuvent s'écrire principalement en fonction de deux paramètres: le paramètre d'impact, une grandeur géometrique de la collision et le nombre de Weber qui compare l'inertie des gouttes à la tension superficielle de la goutte. Plusieurs études [4, 37, 38, 103] ont établi des diagrammes de résultats de collision entre gouttes en fonction de ces deux paramètres. Le cas simplifié utilisé dans ce travail, comporte trois régimes: la coalescence permanente, la séparation par réflexion et la séparation par étirement. Les courbes délimitant ces trois régimes sont présentées.

Le chapitre 3 présente brièvement la méthode de simulation numérique directe du gaz et la simulation déterministe de la phase dispersée, en introduisant les forces agissants sur les particules/gouttes. Ensuite, un apercu des algorithmes de détection de collision est donné, puis l'algorithme développé dans ce travail pour une phase polydispersée est introduit. Cet algorithme est ensuite validé dans la configuration d'un écoulement granulaire sec (sans fluide), ce qui permet de valider les collisions seules sans l'influence "perturbatrice" du fluide par comparaison avec les prédictions de la théorie cinétique des gaz. Les algorithmes de détection en générale, ainsi que l'algorithme développé ici, recherchent les partenaires de collisions dans le voisinage de la particule de référence. Les collisions sont repérées par chevauchement de particules: ce qui introduit un critère sur le pas de temps et limite dans le cas d'un nuage de particules monodispersées l'avancement moyen d'une particule à environ 10% de son diamètre. L'introduction d'un deuxième critère de détection dans l'algorithme développé ici permet d'augmenter le pas de temps d'un facteur 10. Ce critère de pas de temps compare le produit scalaire entre la vitesse relative et le vecteur reliant les centres de deux particules en cours de collision pendant deux pas de temps consécutive. En utilisant la définition donnée dans ce chapitre pour ces deux grandeurs, un produit scalaire négatif indique que les deux particules sont en train de s'approcher, alors qu'une valeur positive indique que les deux particules s'éloignent. Le changement du signe entre deux pas de temps consécutifs montre par conséquent que les particules ont inversé leur position relative. Ils sont des candidats pour une collision non-détectée par le critère de chevauchement. L'algorithme est ensuite re-validé après son introduction dans le code de calcul du gaz et sa vectorisation sur différentes plateformes.

Le chapitre 4 présente la modélisation statistique d'un brouillard de gouttes dans un écoulement turbulent. Après la dérivation d'une équation de transport de PDF de type Boltzmann, les fermetures pour les termes apparaissant dans cette équation sont données.

La fermeture des termes collisionnels est donnée, en utilisant deux fermetures différentes. La première est basée sur l'hypothèse de chaos-moléculaire, basée sur la théorie cinétique des gaz raréfiés, qui ne prend pas en compte les corrélations de vitesse des gouttes induites par le champs turbulent. La deuxième fermeture permet de prendre en compte ces corrélations [73]. La forme de la distribution jointe des vitesse de gouttes et du fluide, permet d'écrire les termes collisionnels. Deux approches sont présentées: une approche Lagrangienne de type Monte-Carlo et l'approche Eulerienne 'Direct Quadrature Method of Moments' (DQMOM). Les termes sources collisionnels utilisé dans l'approche DQMOM [11] sont explicités.

Le chapitre 5 présente les résultats d'une étude DNS/DPS de l'interaction de la turbulence avec la coalescence des gouttes. D'abord l'initialisation et la validation des écoulements fluide turbulents sont présentés. Le premier objectif de l'initialisation des écoulements fluides est d'avoir une bonne résolution de la turbulence, en particulier des échelles dissipatives car elles jouent un rôle important sur des gouttes peu inertielles. Le second objectif est de doubler le nombre de Reynolds, afin de pouvoir évaluer l'influence de la turbulence sur les effets de la coalescence. Les nombres de Reynolds obtenus sont: $Re_\lambda = \{18.1, 32.9, 60.5\}$. Ensuite cinq classes de gouttes initialement monodisperse en taille sont choisies, de manière à conserver les nombres de Stokes à travers les calculs gaz-gouttes, ce qui permet d'évaluer l'influence de la turbulence sur la coalescence. Les calculs gaz-gouttes sont initialisés dans un régime de collision de gouttes, mais pas de coalescence, jusqu'à l'obtention d'un équilibre local avec le fluide. A partir de cet équilibre local, la coalescence est déclenchée. Il est montré que l'écoulement turbulent a une forte influence sur le taux de coalescence en fonction de l'inertie des gouttes. Le taux de coalescence le plus fort est obtenu pour des gouttes dont le nombre de Stokes (basé sur l'échelle intégral) est proche de 1. Ce sont ces classes de gouttes qui présentent la plus forte vitesse relative en moment de la collision. Deux effets jouent sur le taux de coalescence: le premier, est une corrélation de vitesse des gouttes par le fluide, qui a tendance à diminuer le taux de coalescence. Le deuxième effet est l'accumulation des gouttes dans des zones préférentielles, i.e. des zones à basse vorticité. Il s'agit d'un effet qui tend à augmenter le taux de coalescence. L'étude de la variation de l'intensité de la turbulence montre que pour le plus faible Stokes étudié ($St = 0.1$) que le taux de coalescence augmente avec une augmentation de la turbulence. A l'inverse pour un Stokes intermédiaire, une augmentation de l'intensité de la turbulence a pour conséquence une diminution du taux de coalescence. Ce phénomène peut être expliqué de la manière suivante: pour un Stokes fixé et un niveau de corrélation similaire, une augmentation de l'intensité de la turbulence a tendance à diminuer l'accumulation préférentielle [42]. Enfin, des simulations sont effectuées en utilisant une distribution de taille de type log-normale et

leurs résultats sont discutés.

Le dernier chapitre 6 compare les résultats des simulations DNS/DPS avec les prédictions des approches statistiques du chapitre 4 appliquees aux cas de calcul présentés en chapitre 5. Les prédictions Lagrangienne de type Monte-Carlo ne montrent un bon accord avec les résultats des simulations DNS/DPS que si les corrélations des vitesses de gouttes sont prises en compte. Bien que l'effet d'accumulation préférentielle n'est pas incluse dans cette modélisation, l'accord avec les résultats DNS/DPS est bon. De même, les prédictions de type DQMOM ne prédisent un bon accord avec les résultats DNS/DPS que si la corrélation des vitesse des gouttes est prise en compte.

Acknowledgements

The here presented work had been performed in the group Écoulements et Combustion at the Institut Mécanique des Fluides de Toulouse in the frame of the ECCOMET project (Efficient and Clean Combustion Experts Training). I acknowledge the financial support: This research project has been supported by a Marie Curie Early Stage Research Training Fellowship of the European Community's Sixth Framework Programme under contract number 'MEST-CT-2005-020426'.

I am deeply indebted to Prof. Olivier Simonin for his confidence and for giving me the opportunity to do this work, which provided me the unique opportunity to enter the world of multiphase flow modeling in an excellent scientific environment. I would like to thank Dr. Pascal Fede for accompanying me during my thesis, for his guidance and help with all the smaller and bigger problems one might necessarily encounter in such a work.

I am grateful to Prof. Marc Massot and Prof. Martin Sommerfeld for accepting to review my manuscript and I am honored by the time they invested in the careful lecture of my manuscript and their opinion on my work.

I would like to thank Prof. Julien Reveillon for having accepted to participate and chair my defense jury. Equally, I would like to thank Dr. Pierre Ruyer, Prof. Amsini Sadiki and Dr. Philippe Villedieu for their participation in my defense jury and their interest in my work.

Many thanks to Dr. Arthur Konan N'Dri for the many discussions during my thesis, in particular at the beginning, as well as to Dr. Roel Belt, with whom I appreciated to work on the DQMOM approach as well as for his opinion (sometimes categorical) on many issues.

I gratefully acknowledge the support of the IMFT services, with which I was in contact during my thesis: COSINUS (Annaig Pedrono and Hervé Neau) for their immediate help with the code and software I used, 'Service Informatique' for the persistent help with my two constant companions 'blow' and 'king' and Muriel Sabater at the Reprographie. I would like to thank Florence Colombies for managing the administrative issues and equally

Michèle Campassens at CERFACS, who had been accompanying me for the last three years with commitment and care.

I would like to address many thanks to all of you at IMFT, but especially in the group EEC, either Ph.D. students, Post-Docs or permanent staff for the warm, pleasant and amicable atmosphere throughout the year, the inevitable 'pots' (although some seem to forget about important occasions like: halftime of first year of thesis, beginning of second year, halftime of second year or first time the code compiled... just to give some ideas) as well as for those many discussions about all imaginable and unimaginable subjects.

Finally, I would like to thank my family for their support and especially Jeanne; the last year had been tough for the two of us, but it gives us the confidence to tackle all future challenges.

Contents

Nomenclature

Latin symbols

Symbol	Signification	Dimension
$a_\alpha^{(i)}$	Source terms in DQMOM	$-$
a_i^F	Random force in turbulence forcing	$kg\ m/s^2$
$b_\alpha^{(i)}$	Source terms in DQMOM	$-$
$\mathbf{b}$	Complex vector in turbulence forcing	$-$
$b_{b,ij}$	Normalized anisotropy tensor	$-$
C_A	Added mass coefficient	$-$
C_D	Drag coefficient	$-$
$c_{p,i}$	Droplet velocity in phase space	m/s
$c_{f,i}$	Fluid velocity in phase space	m/s
$c_{f@p,i}$	Undisturbed fluid velocity at droplet position in phase space	m/s
d_p	Droplet diameter	m
d_{32}	Sauter mean diameter	m
e_c	Elasticity coefficient	$-$
$\mathbf{F}_A$	Added mass force	$kg\ m/s^2$
$\mathbf{F}_B$	Basset force	$kg\ m/s^2$
$\mathbf{F}_D$	Drag force	$kg\ m/s^2$
$\mathbf{F}^d$	Force on droplet disturbed by its presence	$kg\ m/s^2$
$\mathbf{F}^{ud}$	Force on droplet undisturbed by its presence	$kg\ m/s^2$
f_c	Mean droplet collision frequency	$1/m^3/s$
$f(r)$	Longitudinal auto-correlation function	$-$
f_{pq}^κ	Theoretical collision frequency	$1/m^3/s$
f_f	Fluid velocity PDF	$-$
f_{fp}	Joint fluid-particle velocity PDF	$-$

Latin symbols

Symbol	Signification	Dimension
f_p	Droplet velocity PDF	–
$\mathcal{F}_p$	Instantaneous particle velocity PDF	–
$G_{fp,ij}$	Correlation tensor in Langevin equation	–
$\mathbf{g}$	Gravitational acceleration	m/s^2
$g(r)$	Transversal auto-correlation function	–
g_0	Radial distribution function	–
g	Droplet mass PDF in DQMOM	–
h_{fp}	Joint fluid-particle velocity PDF in DQMOM	–
$\mathbf{k}$	Normalized droplet center connecting vector	–
$\mathbf{J}$	Collision impulsive vector	kgm/s
L_b	Size of computational domain	m
L_f	Longitudinal fluid integral length scale	–
L_g	Transversal fluid integral length scale	–
m_p	Droplet mass	kg
m_{pq}	Droplet reduced mass	kg
N_c	Number of collisions	1
$N_{\mathcal{H}_{fp}}$	Number of realizations fluid-particle	1
N_{num}	Number of numerical particles	1
N_p	Number of particles	1
N_θ	Collision angle distribution function	–
$N_{w_{pq}}$	Collision relative velocity distribution function	–
N_{We}	Weber number distribution function	–
N_X	Impact parameter distribution function	–
n_p	Droplet number density	$1/m^3$
$\mathbf{x}_{p,0}$	Droplet initial position of linear trajectory	m
q_p^2	Droplet kinetic energy	m^2/s^2
q_m^2	Kinetic energy of particle mixture	m^2/s^2
q_f^2	Fluid kinetic energy	m^2/s^2
q_{fp}	Fluid-particle covariance	m^2/s^2
$\mathbf{R}_{ij}$	Two-point velocity correlation tensor	m^2/s^2
$\widehat{R}_{p,ij}$	Two-point velocity correlation tensor with trace 0	m^2/s^2
S_p	Droplet surface	m^2

Latin symbols

Symbol	Signification	Dimension
t_c	Deterministic collision time of droplet pair	s
T_e	Eddy turn over time	s
T_E	Eulerian time scale of fluid turbulence	s
T_F	Characteristic forcing time	s
T_p	Droplet agitation	m^2/s^2
T_m	Droplet agitation of mixture	m^2/s^2
$u^{'}$	Characteristic turbulent fluid velocity	m/s
u_η	Kolmogorov velocity scale	m/s
$u_{f,i}$	Fluid velocity	m/s
$u_{f@p,i}$	Undisturbed fluid velocity at the droplet position	m/s
$u'_{f,i}$	Fluid velocity fluctuation	m/s
$u'_{f@p,i}$	Undisturbed fluid velocity fluctuation at droplet position	m/s
$U_{f,i}$	Mean fluid velocity	m/s
$U_{f@p,i}$	Mean undisturbed fluid velocity at droplet position	m/s
$V_{d,i}$	Drift velocity	m/s
V_p	Droplet volume	m^3
$V_{p,i}$	Mean droplet velocity	m/s
$v_{p,i}$	Droplet velocity	m/s
$v'_{p,i}$	Droplet velocity fluctuation	m/s
$w_{pq,i}$	Droplet relative velocity	m/s
$V_{r,i}$	Mean droplet relative velocity	m/s
$W_{r,i}$	Mean droplet relative velocity at collision	m/s
x	Impact parameter	m
$x_{p,i}$	Droplet position vector	m

Greek symbols

Symbol	Signification	Dimension
α_p	Droplet volume fraction	$-$
δl	Mean droplet propagation during time step	m
δW	Stochastic Wiener process	$-$
Δ	Droplet diameter ratio	$-$
Δt	Time step	s
ϵ	Dissipation rate of turbulent kinetic energy	m^2/s^3
$\boldsymbol{\zeta}_p$	Quantity in physical space in PDF modeling	$-$
ζ_p	Droplet temperature in phase space	K
η_K	Kolmogorov length scale	m
θ	Collision angle	rad
Θ_p	Droplet temperature in physical space	K
κ	Wave number	$1/m$
λ_f	Longitudinal Taylor length scale	$-$
λ_g	Transversal Taylor length scale	$-$
μ_p	Droplet mass in phase space	kg
$\mu_{p,\alpha}$	Droplet mass in DQMOM for class α	kg
μ_p	Droplet dynamic viscosity	$kg/(ms)$
ν_f	Kinematic viscosity of the fluid	m^2/s
$\boldsymbol{\xi}_p$	Quantity in phase space in PDF modeling	$-$
ξ_{fp}	Fluid-particle velocity correlation coefficient	$-$
ρ_f	Fluid density	kg/m^3
ρ_p	Dispersed phase density	kg/m^3
σ	Surface tension	kg/s^2
σ_F	Forcing amplitude	$-$
σ_{pq}	Collision diameter	m
τ_η	Kolmogorov time scale	s
τ_c	Mean droplet collision time	s
τ_p	Particle response time	s
τ_f^t	Fluid Lagrangian time scale	s
τ_{fp}^t	Fluid Lagrangian time scale along droplet path	s
τ_{fp}^F	Mean particle relaxation time	s

Greek symbols

Symbol	Signification	Dimension
ϕ_p	Particle mass fraction	–
ω_α	Weight of abscissa α in DQMOM	–

Dimensionless numbers

Symbol	Signification
Re_L	Turbulent Reynolds number based on the integral length scale
Re_λ	Turbulent Reynolds number based on Taylor micro scale
Re_p	Dispersed phase Reynolds number
St	Droplet Stokes number based on integral Lagrangian time scale
St_K	Droplet Stokes number based on Kolmogorov time scale
We	Weber number
We_{crit}	Critical Weber number
X	Dimensionless impact parameter
X_{crit}	Critical dimensionless impact parameter

Abbreviations

Abbreviation	Signification
DNS	Direct Numerical Simulation
DPS	Discrete Particle Simulation
$DQMOM$	Direct Quadrature Method of Moments
$DSMC$	Direct Simulation Monte-Carlo
ED	Event Driven
HIT	Homogeneous Isotropic Turbulence
LES	Large Eddy Simulation

Abbreviations

Abbreviation	Signification
PDF	Probability Density Function
$QMOM$	Quadrature Method of Moments
SFM	Shape Function Method
TD	Time Driven

Chapter 1

Introduction

Multiphase flows take the center stage of many of mankind's today and tomorrow challenges as well as of a variety of everyday life phenomena. If we restrict ourselves to problems directly linked with coalescence (i.e. the effect of merging of two droplets after collision), which is one of these multiphase-flow phenomena, we treat a wide range of technical fields. The foremost to mention is combustion. An efficient and clean combustion of any kind of fuel (solid, liquid or gaseous) is crucial to our ecological and economic common destiny. If we think, for example, of liquid-fuel injection in internal combustion engines, the fuel spray undergoes a series of droplet formation processes, from liquid-sheet disintegration and atomization to coalescence further down stream [10], [74], [84] and for a review on experimental investigation on primary atomization of liquid streams [33]. The droplet size has an important influence on the combustion process. The larger the droplets, the longer they need to evaporate. Thus, in terms of internal combustion engines, the smallest possible and most homogeneously distributed droplets are desirable in order to start the combustion at the latest possible moment during the compression stroke and avoid expanding the gas more than necessary against the mechanical compression. Other examples would be furnaces, boilers or even space flight, where liquid aluminum is injected into solid rocket boosters, which are a chemical propulsion system used in order to enhance thrust of carriers at take off (Hylkema [59]). Nuclear energy conversion is another domain with a current research interest in droplet coalescence, where spray-injected atomized water droplets are used in the case of an accident in order to diminish the pressure and temperature in the interior of the reactor building (Rabe [104]).

Besides combustion, coalescence plays an important role in many chemical processes, in the oil and gas production or in medical sprays designed to treat pulmonary diseases, where the droplet size is of significant importance. And last, to mention a daily concern:

weather forecasts. Meteorological models, which should predict whether it rains or not, depend on a correct estimation of droplet size distributions in the cloud. As droplets are moving inside clouds and might collide and coalesce, the droplet size distribution is subject to modifications. If said in a simplified manner, once the gravitational force on the rain droplet exceeds the lift force, due to its increase in volume, it starts to rain [77], [86], [136].

Multiphase-flow phenomena other than coalescence, which concern the dispersed phase in a wide range of industrial applications, are for example particle-wall interaction, deposition of particles at the wall, liquid-sheet disintegration or particle break-up.

This work focuses on the interaction of fluid turbulence and droplet coalescence and its modeling. It consists of two main challenges. First, the interaction between a continuous and a dispersed phase, and second, the interaction within the dispersed phase. In order to research the first challenge, the dispersed phase is usually classified in function of its volume α_p and/or mass fraction ϕ_p.

Highly diluted flows, with a particle volume fraction $\alpha_p < 10^{-4}$ are basically governed by transport of particles, which are in interaction with the fluid phase. Inter-particle collisions may be omitted.

With an increasing particle volume fraction $\alpha_p > 10^{-4}$, collisions need to be taken into account as they start to influence the particle distribution significantly. In gas-solid flows particle-particle collisions lead to the exchange of momentum or of heat, as well they might agglomerate or break-up. In gas-liquid flows droplet-droplet collisions might result in permanent coalescence or break-up of droplets. This might alter significantly the particle or droplet size distribution. This work is mainly concerned with this regime, where particle-particle interactions take place. No unifying theory exists, which describes the characteristics of inertial particle/droplet collisions in turbulent flows, except for the limiting cases of small and high particle inertia. In the case of small particle inertia, where the particles behave like fluid elements, collisions are driven by a shear flow and caused due to the physical extension of the particles. This regime is often referenced as the regime of Saffman and Turner (see Saffman & Turner [110]). In the second limiting case with high particle inertia the particles hardly respond to the continuous phase and therefore its influence on the particles is negligible (see Abrahamson [1]). This regime approaches the conditions of the kinetic theory of rarefied gases. The regime in between these two limiting cases is subject of ongoing research in order to assess and clarify the physics of fluid-particle interaction. (see for example [48], [72], [119], [127], [133], [142], [145])

If the particle mass fraction increases ($\phi_p > 10^{-2}$), the influence of the dispersed phase on the continuous phase needs to be taken into account. The characteristics of the fluid turbulence can be significantly modified by the interaction with the dispersed phase. This

back coupling is subject to many studies (see for example [35], [125]), but is not considered within this work.

After appointing the physical interaction phenomena that are taken into account (fluid-particle and particle-particle interaction), the question arises how to simulate two-phase flows in general, and which of these methods are best suitable to investigate the underlying physics as well as to model the influence of fluid turbulence and droplet coalescence. There are two main goals of this work. First, to perform numerical simulations which can be considered as exact, in order to serve as reference for comparison with model predictions and to study the physical mechanisms of fluid-coalescence interaction. Chapters 3 and 5 are concerned with this type of simulation. These simulations are a kind of 'numerical experiment'. Second, to validate and support the development of statistical modeling approaches in comparison with the performed 'numerical experiments'. This subject is treated in chapters 4 and 6. These modeling approaches can be used in industrial-size simulations.

On a microscopic length scale ($\sim 10^{-3}m$) full direct numerical simulations of two-phase flows are possible. Such simulation are for example volume of fluids (VOF) [5], [64] or level-set methods [55], [128]. These simulations comprise only a few droplets, but all the physics are resolved on all scales: flow around and inside the droplets, deformation of the droplets, heat, mass and momentum transfer. This means to solve both the Navier-Stokes equations and the continuum mechanic equations. With this approach, however, it is not possible to measure the necessary dispersed-phase statistics that are needed for development of the above mentioned modeling approaches.

On a mesoscopic length scale ($\sim 10^{-1}m$) the measurement of these statistics becomes feasible. The simulation of the two-phase flow is divided into two parts, one for the fluid phase and one for the dispersed phase. In order to introduce the least modeling possible, the fluid phase can be handled by means of Direct Numerical Simulation (DNS). All the scales of fluid turbulence are resolved. Alternatively, if one is interested in a more developed fluid turbulence, Large Eddy Simulations (LES) may be conducted instead of DNS. In LES only the large scales of fluid turbulence are resolved and the smaller scales are modeled. This introduces a higher degree of modeling compared with DNS and does not allow to investigate the influence of the small scales of turbulence on the dispersed phase. In this work Direct Numerical Simulations will be conducted making use of an existing DNS solver (see chapter 3). The dispersed phase will be treated by means of so-called Discrete Particle Simulations (DPS) ([34], [41], [73], [124], [140]). Every single particle path is followed individually and as the particles or droplets may interact (collide or coalesce) each single collision is detected and handled. As it is easily understandable, coalescence leads to a poly-dispersion in particle size even with an initially monodisperse distribution. The DPS code

as well as the collision detection algorithm must handle correctly a wide range of different particle diameters. An adequate collision detection algorithm is developed, validated and implemented within this work. (see chapters 3) With the introduction of Discrete Particle Simulations for the dispersed phase, two more degrees of modeling are needed. First, the particle-particle collisions need to be modeled, once they are detected. Second, the fluid-particle transfer needs to be modeled. As mentioned above, the influence of the dispersed phase on the fluid is omitted. Thus, there remains to model the influence of the fluid flow on the particle. This part is already implemented in the used DNS solver, but needs to be adapted to the new polydisperse configuration. The 'numerical experiments' performed here consist, therefore, of Direct Numerical Simulations of the fluid coupled with Discrete Particle Simulations for the dispersed phase accounting for particle-particle interactions or droplet coalescence. This kind of simulations will be referred to as DNS/DPS and represent the least degree of modeling possible within this work.

On a macroscopic length scale ($\sim 10m$) industrial-flow configurations become accessible. This corresponds to the second type of simulations that are conducted here. In order to describe the dispersed phase several authors apply an approach based on the kinetic theory of rarefied gases to the dispersed phase due to the analogy between the motion of molecules in a gas and the random motion of particles in turbulent two-phase flows (see for example [91], [107], [144]). Therefore, a dispersed-phase probability density function (PDF) is introduced and a transport equation on this PDF is derived. This leads to a closure problem in the term describing the particle-particle collisions. A collision depends not only on the properties of one particle, but simultaneously on the properties of the two particles that are involved in the collision. This is why a particle-pair distribution function appears in the corresponding collision terms. The standard approach is to model the collision, in analogy to the regime of rarefied gases, as molecular chaos. This means that the particle velocities are entirely uncorrelated before collision, and allows to write the particle-pair distribution function as a product of two one-particle distribution functions. While this is definitely correct in a rarefied gas and maybe in two-phase flows with very inertial particles, it is not correct for small or even intermediate particle inertia. The question arises, how to account for the interaction of the fluid and dispersed phase within this PDF modeling approach and how to account for the correlation of the particle velocities. Simonin [117] introduces the joint-fluid-particle PDF, which accounts not only for the particle properties, but also for the fluid velocity at the particle position. A transport equation can be written on the joint-fluid-particle PDF. Lavieville [73] shows that the closure problem in the pair joint-fluid-particle PDF, which appears writing a transport equation of the joint-fluid-particle PDF, can be written in such a way that the correlation of the particle velocities by the fluid

turbulence are accounted for, based on the joint-fluid-particle PDF approach. Laviéville [73] shows a significant improvement using this closure in comparison with predictions applying the molecular-chaos assumption turbulent gas-solid flows.

Once the PDF transport equation is written and all terms are closed, it needs to be solved. There are two basically different possibilities to solve this equation. First, it is possible to apply a Lagrangian stochastic method for the resolution of the PDF transport equation, the so-called Direct Simulation Monte-Carlo (DSMC) ([12], [15], [60], [123]). Particle collisions or droplet coalescence are handled using a random number method. The second possibility is an Eulerian approach, in which moments of the particle PDF are calculated and transport equations on those moments are solved (multi-fluid methods [54], [70], [71], quadrature based methods, [81], [88] or quadrature based methods, where the source terms and not the moments are transported [11], [82]). For the simulation of the fluid turbulence coupled with the PDF approach, DNS/LES or RANS can be used. If RANS is used, the instantaneous turbulent fluid properties are generated using a random process for the determination of interphase transfers. Concepts that provide these instantaneous properties are for example the eddy-life time model [51] or the Langevin equation [118].

Within this work, Direct Simulation Monte-Carlo (DSMC) [59] and Direct Quadrature Method of Moments (DQMOM) [11] are applied and their predictions are compared with results of inertial droplet coalescence gained from DNS/DPS. First, using collision models based on the molecular chaos assumption and second, accounting for the correlation of droplet velocities by the fluid turbulence. Both approaches, DSMC and DQMOM, have been applied to investigate droplet coalescence [45], [60], [71], [114], [130]. For a formal description of these approaches the reader may refer to chapter 4 and for a comparison of their predictions with DNS/DPS to chapter 6.

Chapter 2

On coalescence

2.1 The physics of coalescence

As mentioned in chapter 1, this work focuses on the interaction of a turbulent flow field with particle-particle collisions and droplet coalescence. This comprises two of the most interesting and difficult fields within fluid dynamics: fluid-particle interaction on the one hand and droplet collision dynamics on the other hand. This chapter is concerned with the latter: the phenomenology of liquid-droplet collision outcomes.

2.1.1 Critical parameters

While trying to understand droplet collisions two main questions need to be answered. Which are the critical parameters defining the collision outcome? Which are these outcomes and their characteristics? The second question will be assessed in 2.1.2, the first directly here in 2.1.1. Several studies, mainly experimental but also numerical ones, focused on these two questions [4, 37, 38, 103].

If the geometry of two colliding droplets is considered as seen in fig. 2.1 and the influence of the surrounding fluid is neglected, the binary droplet collision can be described in terms of the droplet density ρ_p, viscosity μ_p, surface tension σ, diameters of the droplets d_p and d_q, where $d_p > d_q$, as well as their velocities $\mathbf{v}_p$ and $\mathbf{v}_q$ with a particle relative velocity $\mathbf{w}_{pq} = \mathbf{v}_q - \mathbf{v}_p$. A dimensional analysis leads to a set of four dimensionless numbers.

The particle **Reynolds number**

$$Re_p = \frac{\rho_p d_p \left|\mathbf{w}_{pq}\right|}{\mu_p} \tag{2.1}$$

which expresses the ratio of inertial to viscous forces. Following Ashgriz & Poo [4] the

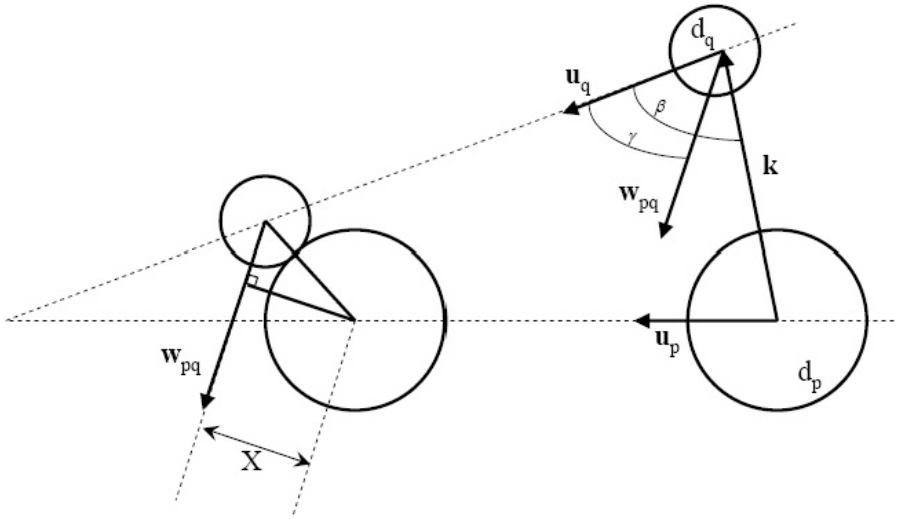

Figure 2.1: Sketch of the collision of two droplets with velocities $\mathbf{v}_p$ and $\mathbf{v}_q$ and diameters d_p and d_q colliding with a relative velocity $\mathbf{w}_{pq}$ under an impact parameter X.

particle Reynolds number seems to play an insignificant role in the collision outcome. The main influencing parameters are usually the following three.

The **Weber number**

$$We = \frac{\rho_p d_q \left|\mathbf{w}_{pq}\right|^2}{\sigma} \tag{2.2}$$

which can be thought as the ratio of the droplet inertia to its surface tension.

The droplet **diameter ratio**

$$\Delta = \frac{d_q}{d_p} \tag{2.3}$$

which varies between 0 and 1.

The **impact parameter**

$$X = \frac{2x}{d_p + d_q} \tag{2.4}$$

where X is the dimensionless impact parameter. x is defined as the distance from the center of one droplet to the relative velocity vector placed in the center of the other droplet (see fig. 2.1). An impact parameter of 0 describes a head-on collision, such that there is no eccentricity of the two droplet paths. The closer the values of X to 1, the more grazing the collision becomes. Reaching a value of 1 the two droplets touch, but do not collide anymore.

With these parameters usually five different regimes of collision outcome are distin-

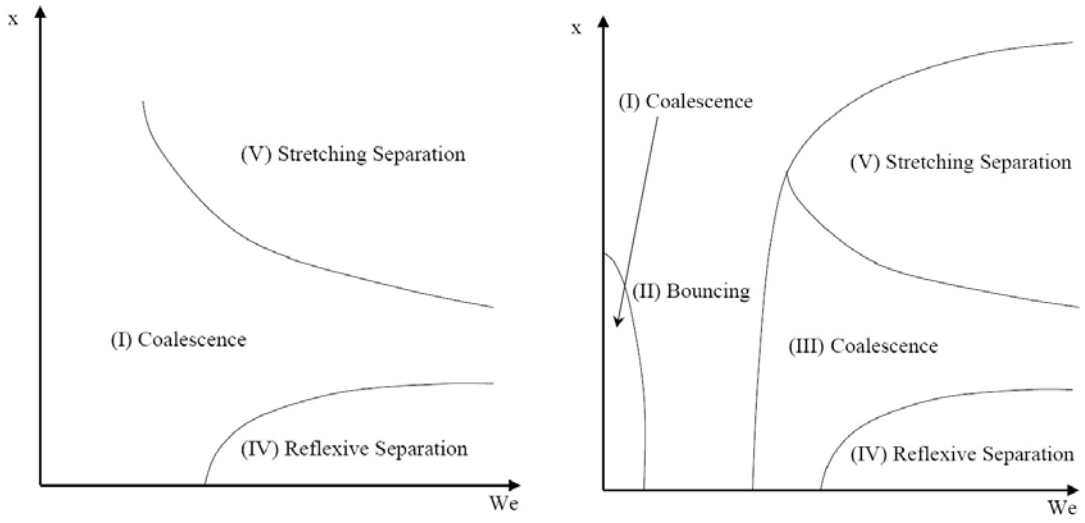

Figure 2.2: (Left) Sketch of the regimes of collision outcome for water droplets. (Right) Sketch of the regimes of collision outcome for hydrocarbon droplets

guished. The different regimes are detailed in 2.1.2, the corresponding frontier models are given in 2.1.3.

2.1.2 Regimes of collision outcome

Most authors reporting on experimental studies of droplet-droplet interaction distinguish five different regimes of collision outcome for hydrocarbon droplets and three different regimes for water droplets. An extensive literature review of these studies and the experimental devices used is given by Estrade [38]. Qian & Law [103] give the commonly used schematic overview for water in fig. 2.2 (left) and hydrocarbons as shown in fig. 2.2 (right).

Regimes (I) coalescence and (II) bouncing are not found for water, which is due to the different rheological properties of water and hydrocarbons. Where water droplets always initially coalesce and maybe separate later, hydrocarbons do not necessarily exhibit this initial coalescence under certain conditions. These conditions are given within the bouncing regime (II). The phenomenology of the five distinct regimes will be given based on the experimental results from Qian & Law [103].

(I) Coalescence: Figure 2.3 (left) shows a typical coalescence regime. The particles are approaching each other, exhibiting very small deformation when in contact. This is the case until 1.15ms. From 1.21ms on the particles start to connect and move away from each other. Qian & Law [103] emphasize that the bulk of the droplets is moving away

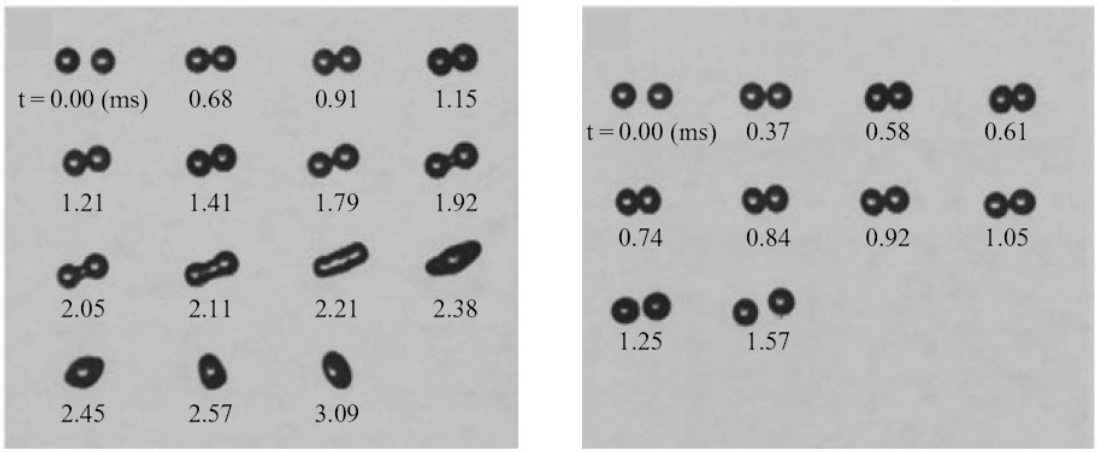

Figure 2.3: (Left) Coalescence regime (I). (Right) Bouncing regime (II). Taken from Qian & Law [103].

from each other shortly before, but certainly after coalescence has occurred. This leads in the following to the formation of a stretched liquid cylinder as it can be seen at about 2.11ms. In a final stage of this collision regime (I) surface tensions pulls the liquid back into a spherical shape, with almost no oscillations as mentioned by Qian & Law [103].

(II) Bouncing: Figure 2.3 (right) shows the collision outcome with an increasing relative velocity. The droplets bounce off without coalescence. The droplet deformation in fig. 2.3 (right) is small as its Weber number is just slightly higher than the transition Weber number from regime (I) to (II). However, with an increasing Weber number the droplet deformation will reach an extent of up to the particle size. Again, while the droplets are moving apart an outward motion of the liquid inside the droplet is noticed. These phenomena can be explained following Qian & Law [103] by the fact that the gas in the gap between the two droplets needs to be squeezed out until the inter-droplet gap reaches the dimensions of molecular interaction. Therefore, as the droplets approach each other, pressure is built up in the gap, leading to a conversion of droplet kinetic energy into surface tension energy. If the gap reaches the size of molecular interaction coalescence can take place, otherwise if the gap remains larger, the droplets are bouncing off. The decision whether coalescence or bouncing occurs should therefore also depends to a certain extent on the properties of the gas surrounding the droplets.

(III) Coalescence: Figure 2.4 (left) shows another coalescence regime, which is close to the transition between regimes (II) and (III). Following Qian & Law [103] the collisional inertia in this case is just high enough to overcome the resistance force of the gas film

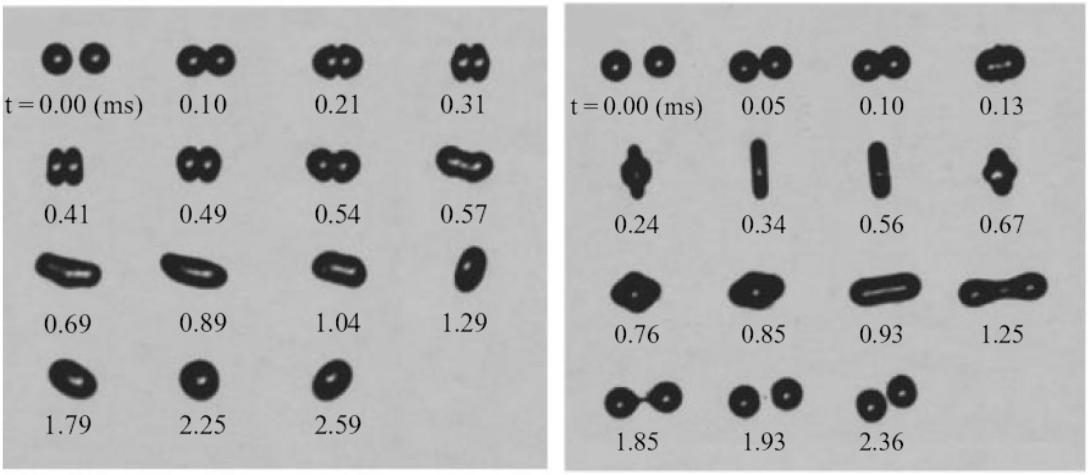

Figure 2.4: (Left) Coalescence regime (III). (Right) Reflexive separation regime (IV). Taken from Qian & Law [103].

between the two droplets by creation of a loss in viscous force due to the droplet deformation. Thus, coalescence is possible. Comparing fig. 2.3 (left) and fig. 2.4 (left) shows that the collision sequences are very similar, however in the latter case the droplet mass oscillates, which is not the case in collision regime (I). The point of actual coalescence might be indicated in fig. 2.4 (left). At at time of 0.49ms the connection of the two droplets has a pointy form, while at 0.54ms it exhibits a round shape. The connection of the two droplet surfaces should rapidly smooth out the pointy form. The period in which this smoothing occurs can be interpreted as the state of coalescence. If the Weber number increases in this regime an important amount of axial inertia remains after coalescence in the liquid mass, which leads to an outward motion. The higher the initial impact inertia the higher the subsequent outward motion. If the inertial energy does not exceed a certain limit the surface tension is able to pull the liquid back into a spherical shape. Reaching this limit in inertial energy, which can be expressed in terms of Weber number, the transition to the reflexive separation regime is approached, which will be detailed in the following.

(IV) Reflexive separation: Figure 2.4 (right) shows this regime of reflexive separation, which follows out of an increase in droplet inertial energy in regime (III). In fig. 2.4 (right) it is seen that the droplet mass has now sufficient inertia to overcome the surface tension forces which lead in regime (III) to permanent coalescence in the case of an elevated Weber number. The coalesced mass separates again and forms two new particles. The formation of a tiny satellite droplet is also observed. For higher Weber numbers this satellite droplet will be larger in size.

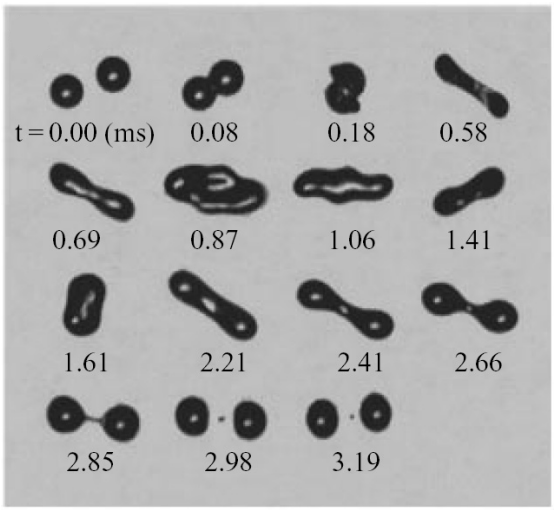

Figure 2.5: Stretching separation regime (V). Taken from Qian & Law [103].

(V) Stretching separation: The stretching separation regime seen in fig. 2.5 is a bit more difficult to define. As can be seen from fig. 2.5 and as is indicated in the schematic in fig. 2.2, the impact parameter starts to play a significant role for this regime. Stretching separation occurs for off-center collisions. Therefore, the particle kinetic energy has a distinct normal component in the direction of collision as well as a tangential component. As explained by Qian & Law [103] the normal component is considered mainly for overcoming the gaseous film between the droplets, while the tangential component leads to a rotational motion of the coalesced mass. A typical stretching separation regime is given in fig. 2.5. The droplets connect in an off-center collision, temporarily coalesce and start to rotate, due to the tangential component of the droplets. A cylinder is formed as a consequence of the normal component of droplet inertia. The merged mass keeps rotating. This rotation leads to centrifugal forces, which stretch the merged mass and eventually lead to separation of two droplets. This break-up is also described by Brazier-Smith *et al.* [19], who state that a break-up is possible if the centrifugal forces exceed the surface tension energy needed to keep one droplet.

As it can be seen in fig. 2.2, the impact parameter has to be the higher, the smaller the Weber number is at the limit between the coalescence regime (III) and the stretching separation regime (V) to obtain stretching separation. This shows the importance of the normal component of the impact inertial force. For an intermediate Weber number the inertial energy of the droplets in the direction of the collision does not suffice to overcome the surface tension forces maintaining one single merged mass at a given impact parameter,

and thus permanent coalescence persists. Another reason for the normal component of the impact inertial force not to be sufficient in order to cause a separation into two droplets is given at the limit between the bouncing regime (II) and the stretching separation regime (V). If the collision is all-too grazing the more and more inertial energy is found in the tangential component, turning coalescence impossible.

In fig. 2.5 the formation of a satellite droplet is observed. Increasing Weber number and impact parameter lead to the formation of larger ligaments after separation, which could lead to one or more satellite droplets. For a more detailed description of satellite-droplet formation the reader may refer to [38] or [103].

2.1.3 Boundary models for regimes of collision outcome

With the description of the phenomenology of possible collision outcomes a new question arises, which has been answered by several authors. How can the boundaries between the different collision regimes be described based on the phenomenology of droplet-droplet collisions? Here, only boundaries for the transition (III)/(V) and (III)/(IV) will be detailed as only these two will be used in the collision models applied in this work. A more exhaustive description is given in [38].

Boundary models for transition from regime (III) coalescence to regime (V) stretching separation

Four different models will be presented, which are based on the work of Park [97], Arkhipov *et al.* [3], Brazier-Smith [19] and Ashgriz & Poo [4]. The predictions of these models are presented in comparison with experimental results from Ashgriz & Poo [4] for permanent coalescence and stretching separation in fig. 2.6. As seen in fig. 2.6 only the models of Brazier-Smith [19] and Ashgriz & Poo [4] lead to a correct description of the boundary between the coalescence (III) and stretching separation (V) regimes. This effect is even more pronounced for a particle diameter ratio of $\Delta = 0.5$ as shown in [4].

The four different models will be detailed in the following. Given that separation in regime (V) occurs when the surface tension force is less than the centrifugal forces of the bulk liquid of the coalesced mass, Park [97] derives a relation for the impact parameter X, the particle diameter ratio Δ and the Weber number We

$$X = \sqrt{\frac{\pi}{12}}\sqrt{\frac{\Delta^2-\Delta+1}{\Delta^2 We}}\left(\frac{\left(1+\Delta^2\right)\left(\Delta^2-\Delta+1\right)}{5\Delta^3}+\frac{1+\Delta}{2}\right)$$

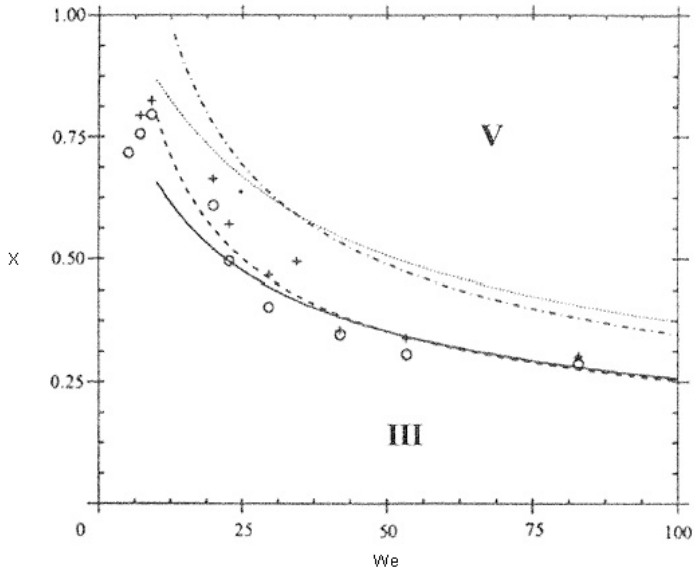

Figure 2.6: Boundary models for coalescence (III) - stretching separation (V) transition for $\Delta = 1$. From Ashgriz & Poo [4]. Legend: - - - Brazier-Smith [19], — Ashgriz & Poo [4], ... Park [97], -.-.- Arkhipov *et al.* [3], + Stretching Separation, o Coalescence

$$\times \left(4 - \left(X\left(1+\Delta\right) - \frac{1-\Delta}{X} \right)^2 \right)^{\frac{1}{4}} \quad . \tag{2.5}$$

For water droplets by verification of the stability of the temporarily coalesced mass, Arkhipov *et al.* [3] find the following dependence of the impact parameter X on particle diameter ratio Δ and Weber number We

$$X = \frac{1}{\Delta^3}\sqrt{\frac{6\left(1+\Delta^3\right)}{We}} \quad . \tag{2.6}$$

Brazier-Smith [19] studies droplet collisions based on a global energy balance for the derivation of the boundary function. The impact parameter X is expressed again as a function of the particle diameter ratio Δ and the Weber number We

$$X = \sqrt{\frac{24}{5We}}\frac{\left(1+\Delta^3\right)^{\frac{11}{16}}}{\left(1+\Delta\right)\Delta^{\frac{5}{2}}}\sqrt{1+\Delta^2-\left(1+\Delta^3\right)^{\frac{2}{3}}} \quad . \tag{2.7}$$

Ashgriz & Poo [4] obtain a relation for the boundary between the coalescence (III) and

stretching separation (V) regimes based on the balance of kinetic energy and surface energy in the region of separation. There the kinetic energy is supposed to be larger than the surface energy at the moment of separation. The region of separation is taken as the overlapping volume of the two interacting droplets. The width of this region is given by Ashgriz & Poo [4] as the sum of the droplet radii minus the impact parameter $h = 0.5(d_p + d_q)(1 - X)$. The reader may be reminded that the following convention is valid for the droplet diameters $d_p > d_q$. The interacting volumes $V_{p,int}$ and $V_{q,int}$ are found to verify:

$$\begin{aligned} V_{p,int} &= \phi_p V_p \\ V_{q,int} &= \phi_q V_q \end{aligned} \tag{2.8}$$

where ϕ_p and ϕ_q are defined as follows:

$$\phi_p = \begin{cases} 1 - \frac{1}{4}(2-\tau)^2(1+\tau) & \text{for } h > 0.5d_p \\ \frac{\tau^2}{4}(3-\tau) & \text{for } h < 0.5d_p \end{cases} \tag{2.9}$$

$$\phi_q = \begin{cases} 1 - \frac{1}{4\Delta^3}(2\Delta-\tau)^2(\Delta+\tau) & \text{for } h > 0.5d_q \\ \frac{\tau^2}{4\Delta^3}(3\Delta-\tau) & \text{for } h < 0.5d_q \end{cases} \tag{2.10}$$

with $\tau = (1-X)(1-\Delta)$. Eventually, with the balance of kinetic energy and surface energy in the region of separation, the following relation for the Weber number We, particle diameter ratio Δ and impact parameter X is obtained

$$We = \frac{4\left(1+\Delta^3\right)^2\sqrt{3(1+\Delta)(1-X)(\Delta^3\phi_q+\phi_p)}}{\Delta^2\left((1+\Delta^3)-(1-X^2)(\phi_q+\Delta^3\phi_p)\right)} \quad . \tag{2.11}$$

Boundary models for transition from regime (III) coalescence to regime (IV) reflexive separation

Ashgriz & Poo [4], Jiang *et al.* [63] and Qian & Law [103] propose models for the transition from the coalescence regime (III) to the reflexive separation (IV) regime.

Jiang *et al.* [63] write a set of two boundary equations not only for the transition from regime (III) to (IV) but also for the transitions (I)/(II) and (II)/(III). However, their work is based on experiments of equal-size droplets and thus the droplet diameter ratio is not taken into account.

Qian & Law [103] propose a boundary transition model for transition (III)/(IV). They write a critical Weber number as a function of the dimensionless Ohnesorg number, which expresses the ratio of the viscous to surface energies, a term that accounts for the extra surface tension energy due to the deformed droplet surface as well as a geometry parameter

that is independent of the fluid properties. This last parameter however depends on geometric quantities of the deformed droplet after the collision leading to reflexive separation. Thus, it is not applicable for the purpose of this work, as those deformations are always unknown.

Finally, Ashgriz & Poo [4] give a relation that depends on the Weber number We, the particle diameter ratio Δ and the impact parameter X. They postulate that reflexive separation will occur when *the effective reflexive kinetic energy is more than 75% of its nominal surface energy* [4]. The relation writes as follows

$$\frac{We}{\Delta\left(1+\Delta^3\right)^2}\left(\Delta^6\eta_1+\eta_2\right)+3\left(4\left(1+\Delta^2\right)-7\left(1+\Delta^3\right)^{\frac{2}{3}}\right)=0 \quad , \tag{2.12}$$

where η_1 and η_2 are

$$\begin{aligned}\eta_1 &= 2\left(1-\xi\right)^2\sqrt{\left(1-\xi^2\right)}-1\\ \eta_2 &= 2\left(\Delta-\xi\right)^2\sqrt{\left(\Delta^2-\xi^2\right)}-\Delta^3\end{aligned} \tag{2.13}$$

with

$$\xi=\frac{1}{2}X\left(1+\Delta\right) \quad . \tag{2.14}$$

2.2 Remarks on microscopic collision outcome modeling

Only a brief discussion of the microscopic modeling of collision outcomes will be addressed here. A complete description of deterministic simulations of two-phase flows is given in chapter 3. After describing the different collision outcomes and providing the transition equations for the boundaries between the different collision regimes, the question of implementation into the determinsitc simulation approach arises. As already mentioned in section 2.1.3 only the regimes of permanent coalescence, stretching separation and reflexive separation are considered within this work. Therefore, only the the transition equations between these three regimes are given above.

In a first step, within this work on coalescence, only permanent coalescence is taken into account. Each time that two droplets collide they coalesce. This corresponds to the case of low Weber numbers of water droplets as seen in fig.2.2. Numerically, the liquid used for the droplets does not correspond to water only, as it is shown in chapter 5. Due to the parameterization, which focuses on constant non-dimensionless numbers, which describe turbulent two-phase flows, the liquid density is varied to achieve this goal. As a consequence the liquids, that would correspond to the used densities, vary from Water over Mercury to

Californium. The latter is well known as a strong neutron emitter and highly radioactive.

In a second step, the three different collision outcomes (permanent coalescence, stretching separation, reflexive separation) will be modeled. The exact modeling for these terms in the deterministic collision treatment is introduced in chapter 3. However, the reader may already note the modeling assumptions for the reflexive and stretching separation regime under the impression of the collision phenomenology. The reflexive separation regime is treated as a hard-sphere collision. If the stretching separation regime applies, the collision does not lead to an alternation of the particle paths. Stretching separation introduces a rotational movement of the droplets, as seen in section 2.1.2. As rotation is not accounted for within the deterministic simulations used here, it will not be modeled. The normal components of the droplets after a stretching separation collision are only slightly altered by the collision. Not to alter the particle paths seems therefore justifiable, although it represents a strong simplification. Satellite droplets are neither considered within the modeling, due to numerical constraints.

Chapter 3

Deterministic description of gas-particle flows with collisions/coalescence

A deterministic description of turbulent two-phase flows on a length scale (mesoscopic length scale $\sim 10^{-1}m$) that allows to measure statistical quantities of the two-phase flow, while introducing the least modeling possible, requires several elements. These elements comprise Direct Numerical Simulation (DNS) of the turbulent flow field, Discrete Particle Simulation (DPS) of the dispersed phase, a one-way coupling between the two phases, which accounts for the interphase transfers, and finally an algorithm allowing to consider particle-particle or droplet-droplet interactions. The single elements may be developed in a decoupled manner. First, the fluid is computed, then the interphase transfers are accounted for, then the particulate phase is computed and particle-particle or droplet-droplet interactions are handled.

These four elements are introduced in this chapter. To perform these simulations an in-house DNS solver (JADIM[1]) is used that accounts for a monodisperse particulate phase. As coalescence is a polydisperse problem, as presented in chapter 2, this code needs to be adapted accordingly. No modifications to the DNS solver are necessary. The interphase transfer routines need to be accorded to a new polydisperse particulate phase. The collision detection algorithm as well as the collision handling are developed within this work. Finally, it is integrated into the DNS solver, adapted to the vectorial structure of the used supercomputer and validated.

[1] JADIM solves the incompressible unsteady Navier-Stokes equations. It uses a finite volume method on a structured mesh of second order in time and third order in space.

In section 3.1 the fundamentals of Direct Numerical Simulations are explained in regard to the configuration of a forced Homogeneous Isotropic Turbulence (HIT) applied within this work. In section 3.2 the Discrete Particle Simulation is explained as well as the interaction between fluid and particulate phase. In section 3.3 the phenomenon of particle collisions is introduced and an overview of collision detection algorithms is given. Eventually, the novel collision detection algorithm is detailed in section 3.4.

3.1 Direct Numerical Simulation of fluid turbulence

The fluid turbulent motion is solved by means of Direct Numerical Simulation (DNS). The incompressible Navier-Stokes equations (3.2) of a Newtonian fluid are solved without any turbulence modeling. This means that all scales of fluid turbulence, from the integral length scale L_f that carries most of the fluid energy, to the smallest dissipative scales (the Kolmogorov length scale η_K) are resolved. The mass conservation equation and Navier-Stokes equations are given in (3.1) and (3.2).

$$\frac{\partial u_{f,i}}{\partial x_i} = 0 \tag{3.1}$$

$$\frac{\partial u_{f,i}}{\partial t} + u_{f,j}\frac{\partial u_{f,i}}{\partial x_j} = -\frac{1}{\rho_f}\frac{\partial p}{\partial x_i} + \nu_f \frac{\partial^2 u_{f,i}}{\partial x_j \partial x_j} + F_i \tag{3.2}$$

The mass conservation for an incompressible Newtonian fluid writes as given in (3.1), because the density ρ_f of such a fluid is constant. The terms on the left-hand side of (3.2) express the unsteady and convective acceleration of the fluid. The first term on the right-hand side of (3.2) stands for the pressure gradient, the second expresses viscosity. The last term summarizes all other body forces, such as gravity. This last term is omitted within this work.

3.1.1 Characteristic scales of turbulence

Above the integral length scale L_f and the Kolmogorov length scale η_K are mentioned as largest, respectively smallest scale of turbulence. A short definition of these scales will be given in the following. The simplest statistic that contains information on the spatial structure of a turbulent field is the two-point velocity correlation tensor, given as [102]:

$$\mathbf{R}_{ij}(\mathbf{r}, t) \equiv \langle u_i(\mathbf{x}, t) u_j(\mathbf{x} + \mathbf{r}, t) \rangle \tag{3.3}$$

Thus it is possible to define Eulerian auto-correlation functions in longitudinal $f(r)$ and transversal directions $g(r)$ in homogenous isotropic turbulence without summation over index i as follows

$$f(r) = \frac{\langle u_i(\mathbf{x}) u_i(\mathbf{x} + r\mathbf{e}_i)\rangle}{u'^2} \tag{3.4}$$

$$g(r) = \frac{\langle u_i(\mathbf{x}) u_i(\mathbf{x} + r\mathbf{e}_j)\rangle}{u'^2} \quad \text{with} \quad i \neq j \quad , \tag{3.5}$$

where $u^{'}$ is the characteristic turbulent fluid velocity defined as

$$u^{'} = \sqrt{\frac{2}{3} q_f^2} \quad . \tag{3.6}$$

With the auto-correlation functions it is then possible to define integral length scales in longitudinal (L_f) and transversal (L_g) direction. They are given by

$$L_f = \int_0^\infty f(r)\mathrm{d}r \ , \qquad L_g = \int_0^\infty g(r)\mathrm{d}r \quad . \tag{3.7}$$

Before writing the Kolmogorov length scale η_K another length scale is introduced that is based on the auto-correlation functions $f(r)$ and $g(r)$, the Taylor length scales. The Taylor length scales are useful for the characterization of small scales of turbulence. They are written as

$$\lambda_f = \left[-\frac{1}{2} \frac{\mathrm{d}^2}{\mathrm{d}r^2} f(r=0) \right]^{-\frac{1}{2}} \qquad \lambda_g = \left[-\frac{1}{2} \frac{\mathrm{d}^2}{\mathrm{d}r^2} g(r=0) \right]^{-\frac{1}{2}} \quad . \tag{3.8}$$

The question about the smallest scale of turbulence was answered by Kolmogorov [65] by introducing three hypotheses. These hypotheses are explained for example in [102]. Based on the dissipation rate of turbulent kinetic energy ϵ and the kinematic viscosity of the fluid ν_f a length η_K, time τ_η and velocity scale u_η are written, describing the smallest scale of turbulence

$$\eta_K \equiv \left(\frac{\nu_f^3}{\epsilon} \right)^{\frac{1}{4}} \quad , \tag{3.9}$$

$$\tau_\eta \equiv \left(\frac{\nu_f}{\epsilon} \right)^{\frac{1}{2}} \quad , \tag{3.10}$$

$$u_\eta \equiv (\nu_f \epsilon)^{\frac{1}{4}} \quad . \tag{3.11}$$

The relation of the longitudinal and transversal integral and Taylor scales can be given using the relations of von Karman and Howarth [131] in the case of homogeneous isotropic

turbulence by

$$\frac{L_f}{L_g} = 2 \qquad \frac{\lambda_f}{\lambda_g} = \sqrt{2} \quad . \tag{3.12}$$

3.1.2 Forcing of homogeneous isotropic turbulence (HIT)

In order to maintain a statistically stationary turbulent flow field, the production of kinetic energy needs to balance the dissipation of energy. Two main types of models exist to maintain a homogeneous isotropic turbulence: first, models using a deterministic approach (see for example [28] and [96]), and second, models using a stochastic approach [39].

In the deterministic approach the turbulence spectrum is adjusted in comparison with a reference spectrum over all wave numbers. This approach provides good spatial properties, although there is a risk to introduce energy always at the same wave number. A drawback of the deterministic forcing is that the scheme directly corrects the fluid velocity field, thus it does not allow modifications of turbulence by external forces, like particles. Therefore, it can not be used if the influence of the particle on the fluid is taken into consideration.

In the stochastic approach proposed by Eswaran and Pope [39] a random force is applied on the large scales of turbulence (smallest wave numbers), such that it satisfies the space-time properties of the forced scales. In the approach, which is implemented in the here used DNS solver by Février [47], the force is applied in the phase space. This approach was chosen by Février as it allows to control the characteristics of the large scales of forced turbulent field and as a modification of the turbulence by a external force field is possible.

The random force $\mathbf{a}^F(\kappa, t)$ is applied on the smallest wave numbers. Initially, Eswaran and Pope [39] apply the force on the range $]0, \kappa_{max}]$, where κ_{max} is the largest forced wavenumber equal to $2\kappa_0$. The smallest computed wave number κ_0 is a function of the computation domain and is calculated as $\kappa_0 = 2\pi/L_b$, where L_b is the length of the computation domain. In a more general manner and for reasons of statistics [47], the forcing is applied on a range from $[\kappa_{min}, \kappa_{max}]$, with κ_{min} the smallest wave number forced. Considering the random force, the momentum equations write in phase space as follows

$$\frac{\partial u_i}{\partial t}(\kappa, t) = a_i(\kappa, t) + a_i^F(\kappa, t) \quad , \tag{3.13}$$

where $a_i(\kappa, t)$ are the Fourier transforms of the sum of advection terms, pressure gradient, viscosity and external forces from the Navier-Stokes equations (3.2). The three components of the random acceleration $a_i^F(\kappa, t)$ are composed of a real and imaginary part, which results in six components for each wave number. The six components are determined independently from each other by a stochastic process of Ornstein-Uhlenbeck type forming a random

complex vector $\mathbf{b}(\kappa, t)$. The real $\Re$ and imaginary $\Im$ part write as follows

$$\Re\left(b_i(t+\Delta t)\right) = \frac{1-\Delta t}{T_F}\Re\left(b_i(t)\right) + \Gamma\sqrt{\frac{2\sigma_F^2\Delta t}{T_F}} \quad , \tag{3.14}$$

$$\Im\left(b_i(t+\Delta t)\right) = \frac{1-\Delta t}{T_F}\Im\left(b_i(t)\right) + \Gamma\sqrt{\frac{2\sigma_F^2\Delta t}{T_F}} \quad , \tag{3.15}$$

where Γ is a Gaussian random number with zero mean and unit variance, T_F is the characteristic time of forcing and σ_F the amplitude of forcing. The random force $\mathbf{a}^F(\kappa, t)$ is linked to the stochastic vector $\mathbf{b}(\kappa, t)$ by the following equation

$$a_i^F(\kappa, t) = b_i(\kappa, t) - \frac{b_j(\kappa, t)\kappa_j}{\kappa^2}\kappa_i \quad . \tag{3.16}$$

In order to obtain a more regular spectrum, the random acceleration is filtered in phase space for the largest wave numbers forced [47]. The filter function used is proposed by Overholt and Pope [96]

$$f\left(\kappa, \kappa_{max}\right) = \tanh\left(\frac{\kappa_{max}-\kappa}{\xi\kappa_{max}}\right) H\left(\kappa_{max}-\kappa\right) \quad \text{with} \quad \xi = 0.2 \quad , \tag{3.17}$$

where H stands for the Heaviside function.

3.1.3 Parameterization of forced HIT

With the stochastic forcing scheme used here, three parameters allow to change the forced homogeneous isotropic turbulence. These are the characteristic forcing time T_F, the forcing amplitude σ_F and the range of forced wave numbers $[\kappa_{min}, \kappa_{max}]$. Février [47] shows that the smallest scales of turbulence are hardly influenced by this parameter. The large scales, however, change significantly with the inserted energy. Following the recommendations of Février [47] the following range is used in this work: $[2\kappa_0, 6\kappa_0]$. The forcing amplitude σ_F allows to control the injected energy and thus the turbulent kinetic energy of the fluid. The characteristic forcing time T_F acts directly on the Eulerian time scale of the turbulence T_E, but it has no influence on the Lagrangian time scale and the eddy turn over time. As the turbulence simulated depends on parameters of forcing, a physical criterion for a good parameterization of the turbulence is difficult to define. Février [47] proposes as criterion the ratio of the Eulerian time scale to the eddy turn over time to be equal to 1. This corresponds to a turbulence in which the large scales propagate with the characteristic turbulent fluid velocity u'.

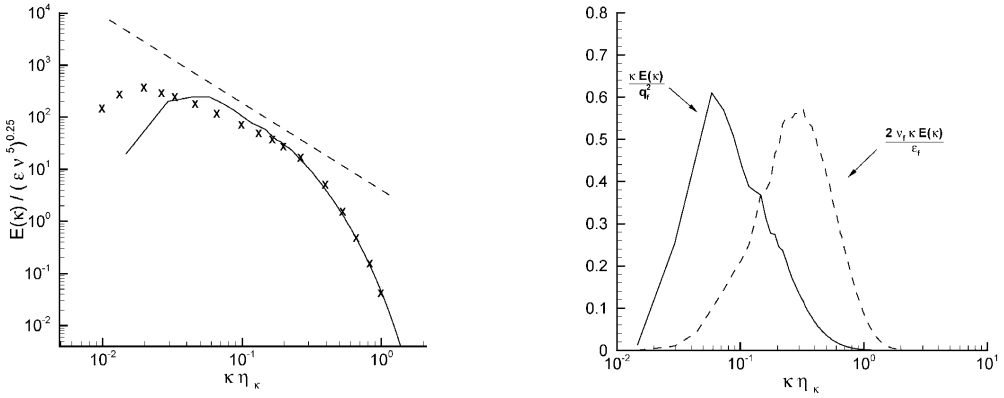

Figure 3.1: (Left) Example for three-dimensional energy spectrum normalized by the Kolmogorov length scale η_K for a simulation with $Re_\lambda = 60.5$ (solid line —). The dashed line − − − represents the gradient $\kappa^{-\frac{5}{3}}$. The symbols represents experimental values from Comte-Bellot and Corrsin [23] for $Re_\lambda = 60.7$. (Right) Energy spectrum $\frac{\kappa E(\kappa)}{q_f^2}$ (solid line —) and dissipation $\frac{2\nu_f \kappa^3 E(\kappa)}{\epsilon_f}$ (dashed line − − −) for simulation with $Re_\lambda = 60.5$.

An example for a forced energy spectrum in comparison with an experimental spectrum is shown in fig. 3.1 (left). Figure 3.1 (right) shows a comparison of energy and dissipation spectra, where it is seen that all dissipative scales are represented by the simulation parameters chosen. The initialization of the turbulent flow fields is given in more details in chapter 5.

3.2 Discrete Particle Simulation

The handling of the dispersed phase is done by means of Discrete Particle Simulation, which is, as its name already indicates, a deterministic Lagrangian method. Whereas the resolution of the fluid turbulence is done in an Eulerian framework. It means that the trajectories of all particles are followed individually and no fixed grid exists for the particles. The interaction with the fluid is accounted for at the position of the dispersed phase elements obtained by interpolation (see section 3.2.3). The integration of particle-particle collisions and their treatment are handled in a very natural way (natural to the particles) applying the deterministic Lagrangian method, as it is shown in section 3.3. Within this work the influence of the particles on the fluid is not accounted for, as the interest of this study lies on the influence of fluid turbulence on droplet coalescence.

The hard sphere model is applied to the droplets. The droplets are modeled as rigid, non-deformable spheres. They interact only at collision, where the rotation of the particles is neglected. They are characterized by their density ρ_p, surface tension σ (which are constants), and their diameter d_p. They possess a position vector $\mathbf{x}_p$ and a velocity vector $\mathbf{v}_p$. The motion of each of these particles is given by an equation of motion in-between collision, which is described in section 3.2.2. The collisions are handled separately from the droplet trajectories at discrete instants, where the collision changes the velocity of the colliding droplets.

The equations solved in-between collision of a droplet, write as

$$\frac{d\mathbf{x}_p}{dt} = \mathbf{v}_p \quad , \tag{3.18}$$

$$\frac{d\mathbf{v}_p}{dt} = \frac{\mathbf{F}_i}{m_{p,i}} + \sum_{\alpha=1,\beta\neq\alpha}^{N_p} \mathbf{F}_{p,\alpha\beta} \quad , \tag{3.19}$$

where $\frac{\mathbf{F}_i}{m_{p,i}}$ represent the sum of external forces on the particle, such as gravity, drag force or others. The term $\sum_{i=1,j\neq i}^{N_p} \mathbf{F}_{p,\alpha\beta}$ in (3.19) represents the impulsive force resulting from instantaneous droplet-droplet collisions.

3.2.1 Summary of working hypotheses

The working hypotheses are summarized here.

- Hard sphere model: droplets are rigid, non-deformable spheres.
- Droplet diameter smaller than Kolmogorov length scale.
- Particle-fluid density ratio is large: only drag force on droplets considered.
- No influence of droplets on fluid turbulence.
- No rotation of droplets and no friction at droplet collision.

3.2.2 Particle trajectory between collisions

At the very beginning Stokes [126] investigated the drag of different geometrical bodies which are both moving in an oscillating way and uniformly moving in a laminar fluid. Boussinesq [18], Basset [9] and Oseen [95] studied the motion of settling spheres under gravity in a fluid at rest. Tchen [129] extended this work to a sphere settling under gravity in an unsteady and nonuniform flow. Corrsin and Lumley [25] and later Maxey and Riley [87]

pointed out some errors in Tchen's extension and are giving equations for the motion of small rigid spheres in nonuniform flows. The diameter of these spheres is smaller than the Kolmogorov length scale ($d_p < \eta_K$). Gatignol [49] writes a formulation which allows to account for particles of the same order as the Kolmogorov length scale ($d_p \approx \eta_K$).

The force acting on the particle can be split into two separate parts: the first part locally undisturbed by the presence of the particle $\mathbf{F}^{ud}$ and the second part disturbed by the presence of the particle $\mathbf{F}^{d}$. The equation of motion can then be written as

$$m_p \frac{dv_{p,i}}{dt} = F_i^{ud} + F_i^{d} \quad . \tag{3.20}$$

The operator $\frac{D}{Dt}$ is used as the time derivative following a fluid element and the operator $\frac{d}{dt}$ as the time derivative following a particle path

$$\frac{D}{Dt} \equiv \frac{\partial}{\partial t} + u_j \frac{\partial}{\partial x_j} \qquad \text{and} \qquad \frac{d}{dt} \equiv \frac{\partial}{\partial t} + v_j \frac{\partial}{\partial x_j} \quad . \tag{3.21}$$

An important assumption to make is that the particle Reynolds number must be much smaller than one

$$Re_p = \frac{d_p \left| \mathbf{v}_p - \mathbf{u}_{f@p} \right|}{\nu_f} << 1 \quad . \tag{3.22}$$

In this case the operators $\frac{D}{Dt}$ following a fluid element and $\frac{d}{dt}$ following a particle do not differ significantly.

While Maxey and Riley [87] treat particles smaller than the Kolmogorov length scale, it is possible to use the locally undisturbed fluid velocity at the particle position $\mathbf{u}_{f@p}$. Gatignol [49] extended the equations to particles of the same order as the Kolmogorov length scale, which demands to introduce fluid velocities averaged over the volume V_p and the surface S_p of the particle, in order to account correctly for the forces on the particle. These velocities are given respectively as

$$\mathbf{u}_{f@p}^{V} = \frac{1}{V_p} \int_{|\mathbf{r}| \leq d_p} \mathbf{u}_{f@p}\left(\mathbf{x}, t\right) \mathrm{d}\mathbf{r} \quad , \tag{3.23}$$

$$\mathbf{u}_{f@p}^{S} = \frac{1}{S_p} \int_{|\mathbf{r}| = d_p} \mathbf{u}_{f@p}\left(\mathbf{x}, t\right) \mathrm{d}\mathbf{r} \quad . \tag{3.24}$$

In this work, as already mentioned, only particles with a diameter smaller than the Kolmogorov length scale are considered. Thus, the locally undisturbed fluid velocity at the particle position $\mathbf{u}_{f@p}$ is used introducing the following simplifications: $\mathbf{u}_{f@p}^{V} \approx \mathbf{u}_{f@p}$ and $\mathbf{u}_{f@p}^{S} \approx \mathbf{u}_{f@p}$. Following Gatignol [49] a power series expansion around the center of the

particle gives

$$\mathbf{u}^V_{f@p} = \mathbf{u}_{f@p} + \frac{d_p^2}{40}\Delta\mathbf{u}_{f@p} + \mathcal{O}\left(d_p^4\Delta\mathbf{u}^2_{f@p}\right) \quad , \tag{3.25}$$

$$\mathbf{u}^S_{f@p} = \mathbf{u}_{f@p} + \frac{d_p^2}{24}\Delta\mathbf{u}_{f@p} + \mathcal{O}\left(d_p^4\Delta\mathbf{u}^2_{f@p}\right) \quad . \tag{3.26}$$

If particle Reynolds numbers such as $Re_p > 1$ are considered, the operators $\frac{D}{Dt}$ following a fluid element and $\frac{d}{dt}$ following a particle path are not equivalent anymore. Following a similar approach in this case is mathematically not as rigorously sound as in the case of $Re_p << 1$. Nevertheless, several authors derive expression for the individual force components in (3.20). The second component $\mathbf{F}^d$, which expresses the forces by the fluid field disturbed by the presence of the particles, is subdivided into three components: the added-mass force $\mathbf{F}_A$, the Basset force $\mathbf{F}_B$ and the drag force $\mathbf{F}_D$. (3.20) writes then

$$m_p\frac{dv_{p,i}}{dt} = F_i^{ud} + F_{A,i} + F_{B,i} + F_{D,i} \quad . \tag{3.27}$$

All these force terms need to be written in the general form using the volume average $\mathbf{u}^V_{f@p}$ or surface averaged $\mathbf{u}^S_{f@p}$ fluid velocity. The explicit expressions for the force terms are given below.

The **undisturbed force $\mathbf{F}^{ud}$** is composed of the force from a pressure gradient and gravity. This force corresponds to the fluid stress on a volume element that would be at the position of the particle. It can be obtained from the Navier-Stokes equations and can be written in terms of fluid acceleration and gravity as follows

$$\mathbf{F}^{ud} = V_p\rho_f\frac{D\mathbf{u}^V_{f@p}}{Dt} + (\rho_p - \rho_f)\,V_p\mathbf{g} \quad . \tag{3.28}$$

The **added-mass force $\mathbf{F}_A$** is added to the system because an accelerating body also accelerates a certain volume of surrounding fluid, as the object displaces the fluid at its position. Auton *et al.* [6] propose a general expression for the added mass force on a body of simple shape moving through an inviscid fluid with an unsteady non-uniform rotational velocity field

$$\mathbf{F}_A = V_p\rho_f C_A\left(\frac{D\mathbf{u}^V_{f@p}}{Dt} + \frac{d\mathbf{v}_p}{dt}\right) \quad . \tag{3.29}$$

C_A is the added mass coefficient, which equals $C_A = 0.5$ for a Stokes flow. This result is confirmed by means of numerical simulations by Magnaudet *et al.* [79].

The **Basset force $\mathbf{F}_B$** represents a second force after the added-mass force which results

from acceleration of the relative velocity of a body in a fluid. This force is also known as 'history force'. Michaelides and Feng [89] show that is best to apply the operator $\frac{d}{dt}$ following the particle trajectory

$$\mathbf{F}_B = V_p \rho_f \frac{9}{d_p} \sqrt{\frac{\nu_f}{\pi}} \int_{-\infty}^{t} \frac{d}{dt} \left[\mathbf{u}^S_{f@p} - \mathbf{v}_p \right] \frac{d\tau}{\sqrt{t-\tau}} \quad . \tag{3.30}$$

The **drag force** $\mathbf{F}_D$ is the force, which the fluid opposes to a moving body. It can be written following Clift *et al.* [22]

$$\mathbf{F}_D = -V_p \rho_f \frac{3}{4} \frac{C_D}{d_p} \left| \mathbf{v}_p - \mathbf{u}^S_{f@p} \right| \left(\mathbf{v}_p - \mathbf{u}^S_{f@p} \right) \quad . \tag{3.31}$$

The general equation of motion for a particle can be written with (3.25) as

$$\frac{d\mathbf{x}_p}{dt} = \mathbf{v}_p \quad , \tag{3.32}$$

$$\begin{aligned} \frac{d\mathbf{v}_p}{dt} &= \frac{\rho_f}{\rho_p} \frac{D\mathbf{u}_{f@p}}{Dt} + \frac{(\rho_p - \rho_f)}{\rho_p} \mathbf{g} \\ &+ \frac{\rho_f}{\rho_p} C_A \left(\frac{D\mathbf{u}_{f@p}}{Dt} + \frac{d\mathbf{v}_p}{dt} \right) \\ &+ \frac{\rho_f}{\rho_p} \frac{9}{d_p} \sqrt{\frac{\nu_f}{\pi}} \int_{-\infty}^{t} \frac{d}{dt} \left[\mathbf{u}_{f@p} - \mathbf{v}_p \right] \frac{d\tau}{\sqrt{t-\tau}} \\ &- \frac{\rho_f}{\rho_p} \frac{3}{4} \frac{C_D}{d_p} \left| \mathbf{v}_p - \mathbf{u}_{f@p} \right| \left(\mathbf{v}_p - \mathbf{u}_{f@p} \right) \quad . \end{aligned} \tag{3.33}$$

The drag coefficient C_D depends on the particle Reynolds number Re_p and is given as follows

$$C_D = \frac{24}{Re_p} \qquad \text{for} \qquad Re_p < 1 \tag{3.34}$$

$$C_D = \frac{24}{Re_p} \left(1 + 0.15 Re_p^{0.687} \right) \qquad \text{for} \qquad Re_p < 1000 \tag{3.35}$$

$$C_D = 0.44 \qquad \text{for} \qquad 1000 < Re_p < 2.5 \cdot 10^5 \quad . \tag{3.36}$$

For higher particle Reynolds numbers ($Re_p < 1000$) inertial effects become more important and the flow around the particle becomes instable. Schiller and Naumann [113] give the drag coefficient correlation (3.35). For a particle Reynolds number $1000 < Re_p < 2.5 \cdot 10^5$ the wake does not change anymore and the drag coefficient stays nearly constant. For particle Reynolds numbers larger than $Re_p > 2.5 \cdot 10^5$ the boundary layer flow changes from laminar to turbulent, which implicates a sudden drag reduction.

In this work the main interest lies on the modification of particle properties by collision and coalescence and on the interaction with the fluid. With a particle-fluid density ratio $\frac{\rho_p}{\rho_f} >> 1$, and assuming that $\frac{D\mathbf{u}_{f@p}}{Dt}$ is negligible compared to the drag force, the resolved equations simplify to

$$\frac{d\mathbf{x}_p}{dt} = \mathbf{v}_p \quad , \tag{3.37}$$

$$\frac{d\mathbf{v}_p}{dt} = -\frac{\rho_f}{\rho_p}\frac{3}{4}\frac{C_D}{d_p}\left|\mathbf{v}_p - \mathbf{u}_{f@p}\right|\left(\mathbf{v}_p - \mathbf{u}_{f@p}\right) \quad . \tag{3.38}$$

If finally collisions are taken into account another term has to be added to (3.38), considering the change in velocity by collision.

3.2.3 Numerical resolution

With (3.37) and (3.38) the question comes up how to determine the locally undisturbed fluid velocity at the particle position $\mathbf{u}_{f@p}$. The fluid is, as already mentioned, solved on an Eulerian grid, whereas the particles are treated in a Lagrangian manner. The fluid velocity at the particle position at a given time is therefore unknown, as it exists only on discrete points of the Eulerian grid. An interpolation of the fluid velocity at the particle position suggests itself.

Based on the work of Balachandar and Maxey [8], Février [47] implemented a method called 'Shape Function Method' (SFM) into the solver used here. This method uses 32 grid points for the fluid velocity around the particle for interpolation. It has a good performance in terms of calculation time and it is a second-order accurate scheme. Fede [41] implemented a third-order accurate scheme named 'cubic spline' using 64 grid points for interpolation. Fede [41] validates the accuracy of cubic spline, SFM and linear interpolation schemes in direct numerical simulations on a 128^3 grid for different Reynolds numbers. The cubic spline scheme 'costs' approximately 30% more in terms of calculation time than the SFM scheme in the performed direct numerical simulations. The performance in terms of accuracy is very satisfying for either cubic spline and SFM. The greatest advantage of the cubic spline scheme lies in its accuracy at large wave numbers. Within this work the SFM is applied.

The time integration of the motion of (3.37) and (3.38) is done applying a second-order Runge-Kutta scheme with the same time step, which is used for the direct numerical simulation of the fluid flow. The particles are moving on straight lines during one time step.

3.3 Particle-Particle and droplet-droplet interaction

The last missing elements for the deterministic simulation of two-phase flows with particle-particle interactions are the detection and treatment of collisions and coalescence. The development of a new detection algorithm is necessary, since in the used DNS solver implemented existing algorithms cannot account for poly-dispersion. As coalescence phenomena necessarily lead to a poly-dispersion of particle diameters, the development of a suitable collision detection algorithm is described below.

Two main questions arise here. First, how to detect rigorously and in an efficient way particle-particle collisions under the aspect of coupling with a fluid flow simulation. Second, how to model collisions between particles on a microscopic level, respecting the most physical behavior and introducing the least possible of modeling assumptions. These two questions are answered in this section.

The first question, which is concerned with a rigorous and computation cost[2] efficient detection of particle-particle collisions, might find different optimal answers in function of the kind of simulations one wishes to perform. Two basically different ideas of collision detection algorithms exist. The Event Driven (ED) approach, in which the particles in the system are usually asynchronous in time and collisions (or more general 'events') are treated following a priority list (see section 3.3.1). The second approach is the Time Driven (TD) approach, where all particles are moved applying the same time step. Thus they are synchronous in time and collisions are treated after the displacement of the particles (see section 3.3.2). The algorithm implemented here is part of the second class of algorithms, the time driven algorithms.

Collisions lead to a sudden change in the state of two particles. Although it is possible to imagine a collision of three or more particles, the probability of such a collision is very small. Very small changes to such a configuration will transform a collision between more than two particles into a series of binary collisions. Therefore in general as well as in this work every collision of three or more particles is replaced by a series of binary collisions. Consequently only the interaction of two particles is searched for. The position vector $\mathbf{x}_p$ and velocity vector $\mathbf{v}_p$ for each particle are known. Thus the exact collision time[3] t_c between two particles can be determined if the particles are moving on straight lines, from the time the collision time t_c is calculated to the moment of collision. This is the case in several different flow configurations. If only a dispersed phase exists and no fluid flow is

[2] In the following the computation cost is simply referred to as cost

[3] The collision time t_c introduced here is not to be confused with the mean particle collision time τ_c, which describes a statistical property and is introduced in chapter 4. The collision time t_c used here is a deterministic value for a pair of particles

present, similar to the movement of molecules in a rarefied gas, the particles always move on a straight line and the only reason to change their velocity is a collision with another particle or with a wall if existing. This flow configuration is also referred to as dry granular flow. In turbulent two-phase flows the particles are usually advanced on a straight line within one time step. Therefore, the exact collision time plays a role in both dry granular flows as well as in turbulent two-phase flows, and independently of the type of detection algorithm used (ED or TD).

A collision takes place if the two particles are touching. In this case the distance between the centers of the particles equals the sum of their radii and (3.39) is verified

$$|\mathbf{x}_q(t_c) - \mathbf{x}_p(t_c)| = \frac{d_p + d_q}{2} \quad , \tag{3.39}$$

where the position of two spherical particles $\mathbf{x}_q(t_c)$ and $\mathbf{x}_p(t_c)$ is given as

$$\mathbf{x}_p(t_c) = \mathbf{x}_{p,0} + \mathbf{v}_p \cdot t_c \qquad \text{and} \qquad \mathbf{x}_q(t_c) = \mathbf{x}_{q,0} + \mathbf{v}_q \cdot t_c \quad . \tag{3.40}$$

If (3.39) is squared and $\Delta\mathbf{x} = \mathbf{x}_{p,0} - \mathbf{x}_{q,0}$, $\Delta\mathbf{v} = \mathbf{v}_q - \mathbf{v}_p$ and $\sigma_{pq} = \frac{d_p+d_q}{2}$ are introduced, where q_p and q_q are the position of particles p and q at a given time, a quadratic equation can be written

$$|\Delta\mathbf{v}|^2 t_c^2 + 2(\Delta\mathbf{v}\Delta\mathbf{x})\, t_c + |\Delta\mathbf{x}|^2 = \sigma_{pq}^2 \quad . \tag{3.41}$$

The exact collision time t_c is the smaller of the two positive solutions of (3.41). If (3.41) has no real positive solution the particles are not colliding. The configuration of a positive and a negative solution for t_c is somewhat more specific in our case and will be explained in detail in section 3.4.1. From a geometrical point of view, this means that the particles are overlapping at the moment the collision time is calculated. For the sake of completeness it is mentioned that one solution corresponds to the case in which the two particles are touching tangentially, but do not collide.

With the notion of the exact collision time t_c, the two different types of collision detection algorithms, event driven and time driven, can be introduced.

3.3.1 Event driven collision detection algorithms

The first class of collision detection algorithms is event driven. All events are sorted in a priority list with the next event in time to be treated first and handled following the order of this list. The biggest advantage of this type of algorithms is that they are absolutely rigorous. All collisions are treated. It appears that this type of algorithm performs best, if the trajectories of the particles are known in advance. This is the case, if the possibility of

a collision with another particle other than the particle the collision time is calculated for is excluded, which means that the collision time t_c calculated represents the next collision of each particle. Dry granular flows are the most evident flow configuration for this type of detection algorithm. But also in particle-laden flows it is possible to apply this type of algorithm, if the particles move on straight lines during a given time interval. Introducing turbulence into the fluid flow, the time interval during which the particles move on a linear trajectory decreases with increasing turbulence. In the simulations performed within this work, the particles move on a linear trajectory only during one time step. It would be possible to apply an event driven algorithm during each time step. This would, however, lead to a huge effort of synchronization of the dispersed phase with fluid at the end of each time step, and the event driven detection algorithm loses its advantage over time driven algorithms that it possesses in dry granular flows.

The first algorithm describing an event driven simulation of hard spheres moving on straight lines was developed by Alder and Wainwright [2] in the case of dry granular flows of less than 500 particles. They started with a simple first algorithm:

Step 1 Compute the time of the next collision t_m in the system.

Step 2 Advance all the particles in the system to t_m.

Step 3 Handle the collision of the two particles.

Applying the algorithm in the above given form seems not to be very efficient. An event driven algorithm needs to perform at least as many operations as the number of collisions, denoted by N_c. Determining the next collision time requires to compare each particle with every other particle in the domain, where N_p is the number of particles in the domain. The cost will be of the order of $\mathcal{O}\left(N_c N_p^2\right)$ operations. For a very small number of particles this algorithm might perform well.

This algorithm can be significantly improved in terms of computation cost. Sigurgeirsson *et al.* [115] show that the operation cost can be reduced from the order of $\mathcal{O}\left(N_c N_p^2\right)$ to $\mathcal{O}\left(N_c log\left(N_p\right)\right)$. The first possibility to reduce cost is to save the calculated collision times for the particles. Alder and Wainwright [2] note that most collision times on two consecutive time steps are the same, as a single collision is not likely to affect collisions between particles distant from the location of this collision. If the collision times of the particles are stored in a list, the cost to recalculate the collision times is not of the order $\mathcal{O}\left(N_p^2\right)$ anymore as only the collision times of the two particles involved in the collision need to be recalculated. Therefore the cost reduces to the order of $\mathcal{O}\left(2N_p - 3\right)$. Furthermore, as very distant particles are not very likely to collide, Alder and Wainwright [2] propose to subdi-

vide the computation domain into cubes, which are referred to as 'cells' in the following. After introducing the cells, collisions are only considered between particles in neighboring cells. Each cell contains a list of the particles assigned to it, introducing a new event, which is the transfer of the particle from one cell to another. This transfer assures not to miss a collision. Another potential improvement lies in step 2 in the above given algorithm. If step 2 is executed only for the particles involved in the event, the cost reduces from the order $\mathcal{O}(N_p)$ to constant per event [36]. This turns the algorithm asynchronous and the position $\mathbf{x}_p$ and velocity $\mathbf{v}_p$ vectors represent now the state at the moment of the last event of each particle.

As it was already mentioned the next event is stored for each particle in a priority list. The big question that arises here is: how to maintain such a list in an efficient manner? After each event, the next event must be determined. Therefore, the data structure of the priority list should allow to extract this next event. If all the next collisions are kept this priority list has to handle $\mathcal{O}(N_p(N_p-1)/2)$ data points. Lubachevsky [76] remarks that it is sufficient to store one event per particle, since once a particle is involved into a collision, all the other events become invalid. This reduces the size of the priority list, but its implementation is still up for discussion. Rapaport [105] proposes to use a binary search tree, which allows to perform the search with a number of steps s in the order of $\mathcal{O}(log(s))$. Other possibilities to implement the priority list are given by Cormen *et al.* [24] or Marin *et al.* [83].

The event driven algorithm of Sigurgeirsson *et al.* [115], which performs in the order of $\mathcal{O}(N_c log(N_p))$ and incorporates the above mentioned optimizations, works according to the below scheme:

Step 1 Find the next event in the priority list.

Step 2 Handle the event.

Step 3 Compute next transfer time for particles included in the event.

Step 4 Compute next collision time with particles in the vicinity.

Step 5 Adjust the event's and its partner's position in the priority list.

Step 6 Return to step 1.

Donev *et al.* [32] implemented a similar algorithm for the use in jammed flows of spherical particles and using additionally a neighbor list for the particles in the case of aspherical ellipsoidal particles [30] and [31].

As only a few collisions occur per time step in simulations of turbulent two-phase flows and a synchronization of the particles at each time step is required, this kind of algorithm does not seem to be the appropriate choice for the simulations performed in this work. Furthermore, the detection collision algorithm needs to be implemented into the vectorized structure of the DNS solver. A vectorization of the priority list appears to add another degree of complexity to the algorithm.

3.3.2 Time driven collision detection algorithms

The second class of collision detection algorithms are time driven. They are originally inspired by simulations of smooth disks and then adapted to hard particle systems. Time driven algorithms are less complex and much simpler to implement than an event driven algorithm. They are developed for example by Hopkins and Louge [57] for studying rapid granular flows of smooth disks. Sundaram and Collins [127] investigated turbulent suspensions of finite volume particles. Hopkins and Louge [57] introduce a detection cell structure, similar to the one described in section 3.3.1 with the difference that here the 'cell' does not contain a list of the particles in its volume. These detection algorithms are developed for a monodisperse particle phase and the detection cell is adapted for exactly this one particle diameter only: fact that does not permit to apply these detection algorithms without modifications in this work. The idea for the introduction of the detection cells is the same: two very distant particles are not very likely to collide, therefore, collision partners are only checked for in the vicinity of the corresponding particle. This reduces the cost for detection from the order $\mathcal{O}\left(N_p\left(N_p-1\right)/2\right)$ to $\mathcal{O}\left(N_p\right)$ per time step.

It is assumed that each particle may collide only once per time step, as multiple collisions of the same particle during one time step can create inaccurate collision frequencies. The time step needs to be adapted to the flow configuration. Another problem that might arise applying time driven detection algorithms is that this kind of algorithm is not rigorous. It can not be excluded that collisions are missed. This is a problem intrinsic to time driven algorithms. Particle collisions are usually detected by checking for an overlap of two particles after they were forwarded in time by one time step. This means that the distance between the center of two particles is smaller than the sum of their radii. This of course represents a non-physical state for hard spheres, but is not obstructive for the treatment of collisions. The problem comes with the time step. The larger the time step the farther a particle moves, which is consequential. For a mono-disperse particle phase, if the distance that is covered by a particle during one time step exceeds a large portion of the particle diameter, a high risk exists to miss a collision, since a particle collision is discovered by

overlap of the two particles. During one time step a particle pair might collide, overlap and separate again. This collision would then not be detected and, as the overlapping distance of two particles decreases if the impact parameter increases, there is a very high risk to miss grazing collisions. Therefore, a small time step is needed. In simulations performed with such a detection algorithm, the criterion on the time step was the more stringent compared with the stability criteria for the DNS. In a poly-disperse particulate flow, the time step criterion for the particulate phase needs of course be oriented on the smallest diameter in the system.

In the time driven detection algorithm developed here for a poly-dispersed particulate phase, a second detection criterion additional to the overlap criteria is introduced in order to increase the time step and simultaneously turn the detection algorithm more accurate. The algorithm developed is detailed in the following section 3.4

3.4 Novel collision detection algorithm for poly-disperse particulate phase

The simplest but also most inefficient algorithm compares all possible particle pairs in the computation domain, leading to a detection cost of the order of $\mathcal{O}\left(N_p\left(N_p-1\right)/2\right)$. As the probability of collision between two sufficiently distant particles during one time step is very small if not zero, it is not necessary to check for a particle of reference with all other particles in the domain. It is sufficient to search for possible collision partners in an adequately large vicinity around this reference particle. To search in the vicinity of a particle, the computation domain is subdivided into cells, which contain a number of particles of the order of $\mathcal{O}\left(1\right)$. If the number of particles per cell is sufficiently low the cost of checking for collisions can be reduced to the order of $\mathcal{O}\left(N_p\right)$, as for each particle only a constant number of particle pairs need to be checked. Therefore, the computation domain is subdivided into cells in such a way that the least particles possible are found in one cell. A higher number of Lagrangian particles per detection cell will increase the computation time. On the other hand the detection cell edge length must be greater than the largest particle diameter in order to ensure a correct detection of all colliding particle pairs. The vicinity to be searched for potential colliding pairs is composed of 27 cubic cells. However, checking half of this neighborhood is sufficient, as it is searched for particle pairs. Searching in the entire neighborhood would lead to double check every particle pair. Hence, only 14 cells need to be checked per particle and computation time can be reduced by half for checking particle pairs. A two-dimensional representation of this vicinity is given in fig. 3.2.

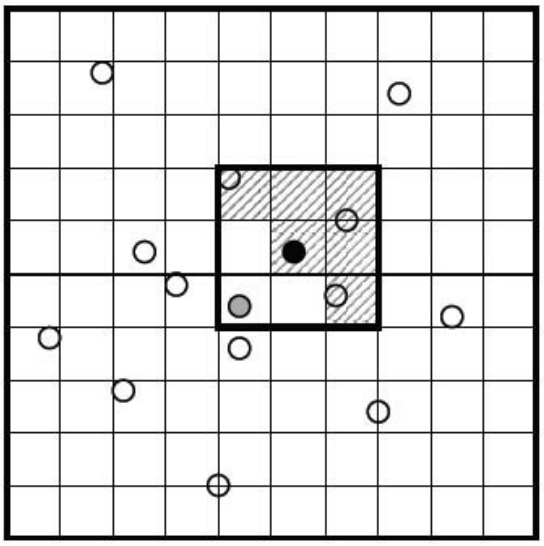

Figure 3.2: Sketch of the particle-particle collision detection vicinity. The black particle is the reference particle.

3.4.1 Detection criteria

Once the domain in which to check for particle-particle collisions is defined, collision detection criteria need to be given. The standard approach is checking for overlap of two particles. As already mentioned this represents a non-physical state for hard spheres, but is not obstructive here. Checking for overlap only, introduces a time step criterion, which is intended for avoiding particles passing through one another during one time step. Consequently they do not overlap at the end of the time step although they collided. A second detection criterion is introduced here in order to increase the time step and to detect more rigorously collisions with a large impact parameter.

Overlap criterion

In a time driven algorithm all particles are moved by the distance each one covers in the given time step. Collisions of two particles are detected checking for an overlap of two particles. Only particles that approach each other are impacting. It is simultaneously checked for overlap of the two particles, which is expressed by (3.42). This means that in case of overlap, the distance of the centers of the two colliding particles is smaller than the sum of their radii. The fact that two particles are approaching each other (3.43) can

be given by the scalar product of the particle relative velocity $\mathbf{w}_{pq}$ and the particle center connecting vector $\mathbf{k}$ as they are defined in fig. 2.1.

$$|\mathbf{x}_q(t_c) - \mathbf{x}_p(t_c)| < \frac{d_p + d_q}{2} \tag{3.42}$$

$$\mathbf{w}_{pq}.\mathbf{k} < 0 \tag{3.43}$$

Second additional criterion

The second detection criterion compares the relative position of two particles in a vicinity in case they do not overlap at the end of the time step. This means that they changed their relative position, if they are approaching at time step t_{n-1} and veering away from each other at time step t_n. This behavior can be expressed in terms of the scalar product of the particle relative velocity $\mathbf{w}_{pq}$ and the particle center connecting vector $\mathbf{k}$. If it is negative the particles are approaching as given already in (3.43). If it is positive they are veering away from each other

$$\mathbf{w}_{pq}.\mathbf{k}|_{n-1} < 0 \qquad \text{and} \qquad \mathbf{w}_{pq}.\mathbf{k}|_n > 0 \quad , \tag{3.44}$$

where $\mathbf{w}_{pq}$ and $\mathbf{k}$ are defined as

$$\mathbf{w}_{pq} = v_q - v_p \qquad \text{and} \qquad \mathbf{k} = \mathbf{x}_q - \mathbf{x}_p \tag{3.45}$$

To decide whether two particles, which are detected in this way, collided, (3.41) is solved. If this equation has two positive real solutions, the smaller one is the collision time t_c. If it has no real solution the cylinders created by the particle diameters on the particle trajectories are skew. The particles changed their relative position, but in a distance always larger than or equal to the sum of their radii. A schematic of the collision detection algorithm is given in fig. 3.3. After the detection of the colliding particle pairs, the collision of the particles or occurring coalescence phenomena need to be handled. The treatment of particle-particle collisions is described in section 3.4.2 and the treatment of the corresponding coalescence phenomena in section 3.4.5.

3.4.2 Collision handling

In the particle-particle collision modeling neither friction nor rotation of the particles are taken into account. If friction were taken into consideration, then also rotation should be considered, as friction at the moment of collision induces rotation in the particles. Furthermore, if one is interested in these phenomena, the interphase transfer law between the fluid

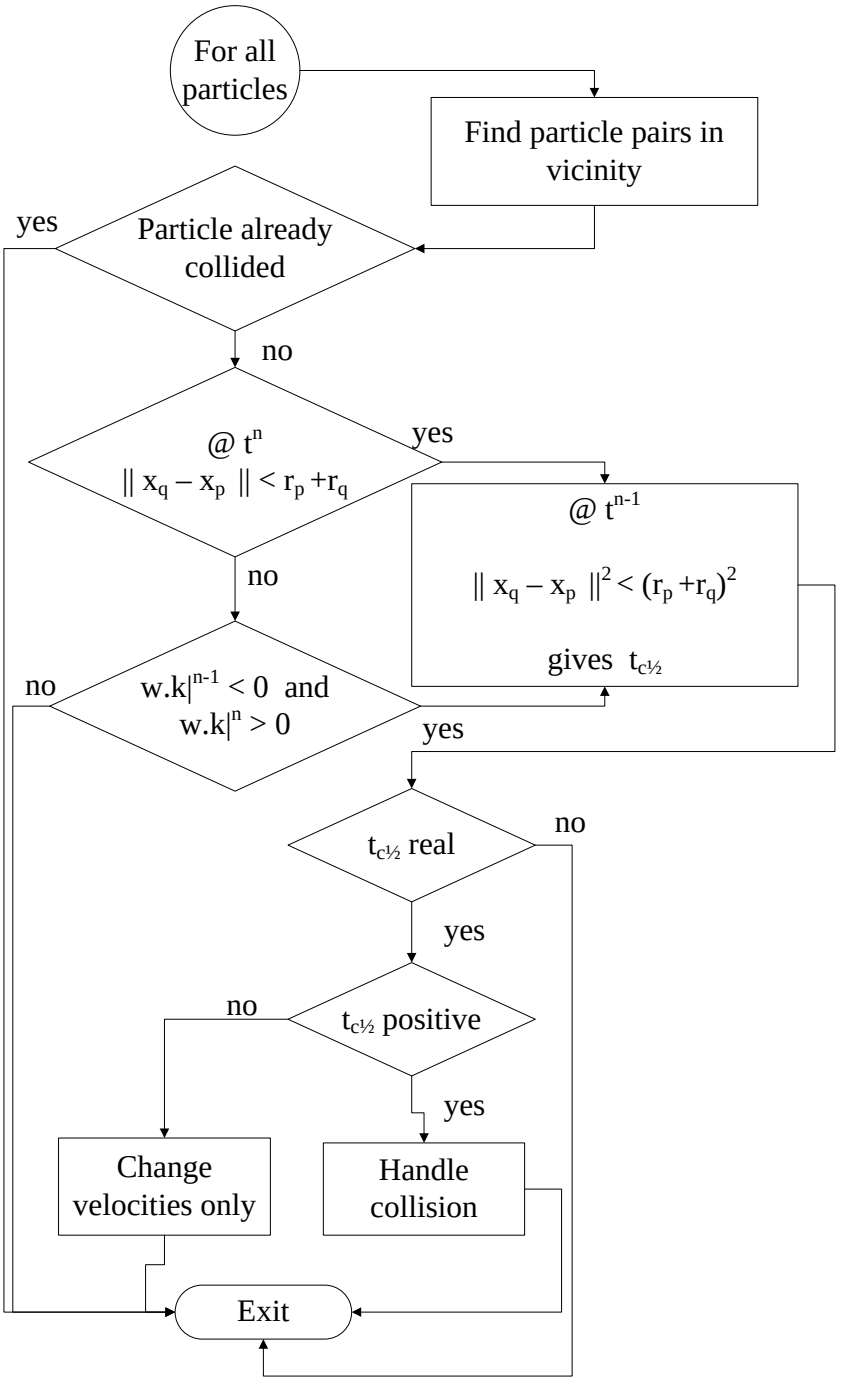

Figure 3.3: Schematic of the collision detection algorithm developed.

and the particles needs to be adapted.

Once particle-particle collisions are detected by either the overlap criterion or the second criterion they are handled equally. One exception is given in the case that (3.41) has a positive and a negative real solution. This case is detailed at the end of this section.

All detected particle pairs are found at their current state t_n. To determine the time of collision and handle it accurately, (3.41) is solved for all detected particle pairs at time step t_{n-1}. This means in other words that the particles are moved backwards in time at their position at the beginning of the time step and then advanced to the exact moment of collision. If (3.41) has only complex solutions - which is only possible if the particle pair was found by the second detection criterion - the particles did not collide during the time step but passed near one another at a distance superior to the sum of their radii. If (3.41) has two real positive solutions, the smaller value is the time of collision t_c. In case (3.41) has only one real solution the particles touch but do not collide as the scalar product $\mathbf{w}_{pq}.\mathbf{k}$ equals zero and the velocity components are not altered. If any negative real solution of (3.41) exists the particles are overlapping at t_{n-1}. Once the time of collision t_c is found the particles are moved forward in time until $(t_{n-1} + t_c)$. The particles now touch and the collision can be handled applying the following equations. First, the general mechanical shock equations for the translational momentum are given by

$$\mathbf{v}_p^{\#} = \mathbf{v}_p + \frac{1}{m_p}\mathbf{J} \tag{3.46}$$

$$\mathbf{v}_q^{\#} = \mathbf{v}_q - \frac{1}{m_q}\mathbf{J} \quad , \tag{3.47}$$

where $\mathbf{J}$ is the momentum vector and the dot denotes the values after the collision. The equations (3.46) and (3.47) lead to the definition of the following relation for the relative velocity $\mathbf{w}_{pq}$

$$\mathbf{w}_{pq}^{\#} = \mathbf{w}_{pq} - \frac{1}{m_{pq}}\mathbf{J} \quad , \tag{3.48}$$

where $m_{pq} = \frac{m_p m_q}{m_p + m_q}$ is the reduced mass. By introduction of an elasticity coefficient e_c, which verifies the following relation,

$$(\mathbf{w}_{pq}\mathbf{k})^{\#} = -e_c\,(\mathbf{w}_{pq}\mathbf{k}) \quad , \tag{3.49}$$

the kinematic shock equations can be written as given in (3.50) and (3.51), expressing the particle velocity after collision in terms of the particle velocity before collision, the relative velocity of the particles, the masses of the particles, the center connecting vector and the

elasticity coefficient by

$$\mathbf{v}_p^{\#} = \mathbf{v}_p + \frac{m_q}{m_p + m_q}(1 + e_c)(\mathbf{w}_{pq}.\mathbf{k})\,\mathbf{k} \tag{3.50}$$

$$\mathbf{v}_q^{\#} = \mathbf{v}_q - \frac{m_p}{m_p + m_q}(1 + e_c)(\mathbf{w}_{pq}.\mathbf{k})\,\mathbf{k} \quad . \tag{3.51}$$

Now the particles are moved forward in time with the new velocities $\mathbf{v}_p^{\#}$ and $\mathbf{v}_q^{\#}$ obtained by (3.50) and (3.51) respectively, until the end of the time step. The remaining time until the end of the time step is calculated as $(t_n - (t_{n-1} + t_c))$. The particles are marked in order to prevent that a second collision during the same time step is handled. Displacing particles after the collisions could indeed lead to a new problem if by doing so an overlap with a third particle is created. This new overlapping particle pair could then be treated as another collision during the same time step if not inhibited. This collision might be one that takes place during the current time step. In this case the collision is missed, but it might also be a collision that never occurs as the third particle collided before with another particle, or a collision which has not been treated yet, or it might be a collision that occurs outside the current time step. The difficulties involved with allowing another collision for a particle during the same time step are much more important than the disadvantage of missing a single collision. Note that one of the fundamental assumptions is that only binary collisions occur, which is justified if the time step is not too large. A time step criterion will be shown in section 3.4.3, which guarantees an appropriate error control in the statistics measured as function of the mean particle collision time.

Due to the particle displacement after collision or the initial distribution of particles especially in dense systems, an overlap of particles at t_{n-1} is possible. To be able to simulate a system over a wide range of particle volume fractions α_p, collisions are treated differently if the particles overlap at t_{n-1} and t_n under the condition that they are approaching one another at t_n. In this case, only the velocity components are altered following (3.50) and (3.51), while particles are not displaced to t_c neither to the end of the time step. This case is represented in the solution of (3.41) by a positive and negative real value for t_c. As the particles are overlapping one of the solutions for which the particle surfaces coincide following their relative velocity represents in (3.41) the moment the particles collided (the negative value in the past) and the second solution represents the moment in which the particles are separating again. The reader may be reminded that the goal of this study is mainly coalescence and thus volume fractions superior to $\alpha_p > 1\%$ will not be treated. Under these conditions the case of an overlap at the two consecutive time steps is practically limited to the initial conditions of the particles. After a few time steps the particles moved

out of this state of permanent overlap.

One drawback of not displacing particles after collisions could lead to an alteration of statistical results in non-homogeneous flow configurations. In strong shear flows or close to walls small differences in particle positions might lead to different results. In homogeneous isotropic flow conditions the different collision treatments, displacing the particles after collision or not, are not expected to significantly alter the statistical results of the dispersed phase.

3.4.3 Validation of detection algorithm

The algorithm is validated performing dry granular flow simulations of a mono-dispersed particle mixture. In section 3.4.4 simulations of a bi-dispersed particle mixture are presented. The results presented here, which are comparing the statistics obtained in dry granular flows with predictions originating from the kinetic theory of rarefied gases, can equally be considered as a validation of the collision detection algorithm in a poly-dispersed particle mixture. As only binary collisions are treated, a bi-dispersed simulation validates the case of a poly-dispersed mixture. These results are nevertheless given in section 3.4.4 in order to keep them in the context of model validation in the case of bi-dispersed simulations. The validation is conducted in dry granular flows as the statistical properties that should represent the particulate system are known from the theory of rarefied gases. It is therefore possible to conduct simulation without the 'disturbing influence' of a fluid phase. All changes in the particle trajectories are exclusively related to particle-particle collisions. This configuration of dry granular flow offers therefore ideal conditions for the validation of the collision detection algorithm.

Furthermore, a number of statistical quantities is needed here, which are introduced in chapter 4. Only the final formulations are given and it is referred to chapter 4 for the derivation of these quantities. These quantities are the probability density functions of the particle relative velocity at the moment of collisions, the particle collision angle and the collision frequency. These statistics are based on the assumption of molecular chaos, which comes from the kinetic theory of rarefied gases and expresses that the velocities of the interacting particles are uncorrelated before the collision. This is correct in rarefied gases and per analogy in dry granular flows. In dry granular flows the particle volume fraction α_p might exceed and often does exceed the range typical for rarefied gases. This introduces a problem in the modeling of the collision frequency of particles. While the mean free path in rarefied gases is usually much larger than the particle diameter, this is not necessarily the case in dry granular flows. Many more particles are found in an infinite

volume than the theory of rarefied gases predicts. Consequently the collision frequency of the particulate phase is higher than the predictions of the theory of rarefied gases. In order to predict correctly the collision frequency and all other particle statistics several authors introduced a correction factor, the radial distribution function g_0. The statistics needed are given in their final form, which is used for the validation of the detection algorithm and of the collision handling. The exact distributions for the collision angle N_θ and the relative velocity at the moment of collision $N_{\mathbf{w}_{pq}}$ are written as

$$N_\theta(\theta) = \begin{cases} -4n_p^2 d_p^2 \sqrt{\pi T_p}\ sin(2\theta) & \text{if} \quad \theta \in \left[\frac{\pi}{2};\pi\right] \\ 0 & \text{else} \end{cases} \tag{3.52}$$

$$N_{\mathbf{w}_{pq}}(\mathbf{w}_{pq}) = 4n_p^2 d_p^2 \sqrt{\pi T_p} \frac{1}{8T_p^2} \mathbf{w}_{pq}^3 \exp\left(-\frac{\mathbf{w}_{pq}^2}{4T_p}\right) \quad , \tag{3.53}$$

where $T_p = \frac{1}{3}\left(\left\langle v'_{p,x} v'_{p,x}\right\rangle + \left\langle v'_{p,y} v'_{p,y}\right\rangle + \left\langle v'_{p,z} v'_{p,z}\right\rangle\right)$ is the particle agitation. If the particulate system is in an equilibrium state, the particle agitation can be written as $T_p = \left\langle v'_{p,x} v'_{p,x}\right\rangle = \left\langle v'_{p,y} v'_{p,y}\right\rangle = \left\langle v'_{p,z} v'_{p,z}\right\rangle$. With the mean relative velocity written as $\frac{3}{2}\sqrt{\pi T_p}$, the mean propagation of the particulate system during one time step Δt can be written as $\delta l = \frac{3}{2}\sqrt{\pi T_p}\Delta t$. In the following the ratio $\frac{\delta l}{d_p}$ will be used to investigate the performance of the algorithm. It expresses the mean propagation of the particulate system in terms of the particle diameter.

A last term needed for the evaluation of the collision detection algorithm and of the collision handling is the theoretical collision frequency f_{pq}^κ. It is also based on the kinetic theory of rarefied gases and writes as

$$f_{pq}^\kappa = g_0 n_p n_q \pi \left(\frac{d_p + d_q}{2}\right)^2 \sqrt{\frac{16}{\pi}\frac{1}{2}(T_p + T_q)} \quad . \tag{3.54}$$

Several models exist for the radial distribution function g_0. Carnahan and Starling [20] propose a relation that depends on the particle volume fraction α_p. It is given by

$$g_0(\alpha_p) = \frac{1}{1-\alpha_p} + \frac{3}{2}\frac{\alpha_p}{(1-\alpha_p)^2} + \frac{1}{2}\frac{\alpha_p^2}{(1-\alpha_p)^3} \quad . \tag{3.55}$$

Lun and Savage [78] propose another model in function of the particle volume fraction α_p and of the maximum particle volume fraction for random uniformly distributed rigid spheres $\alpha_{p,max}$. This model is especially interesting for very high particle volume fraction, as it tends to infinity if $\alpha_p \to \alpha_{p,max}$, while the model of Carnahan and Starling reaches a

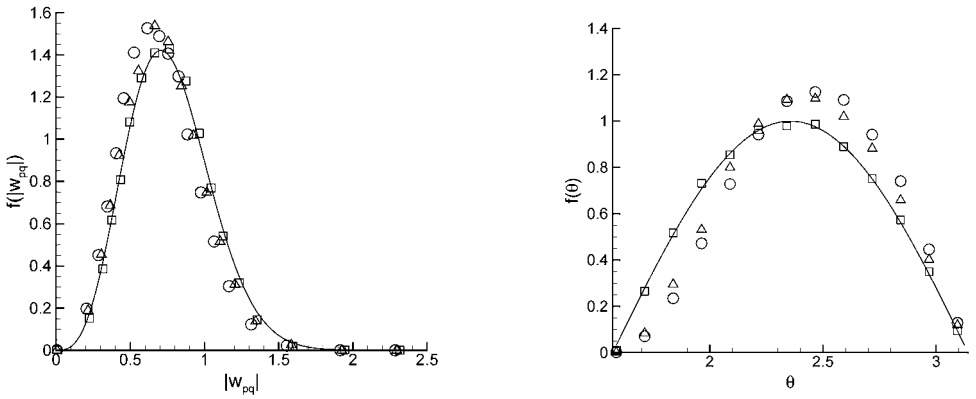

Figure 3.4: (Left) Relative velocity at moment of collision $\mathbf{w}_{pq}$. (Right) Collision angle in dependence of ratio $\frac{\delta l}{d_p}$, using a pure overlap algorithm. $\square$: $\frac{\delta l}{d_p} = 0.13$, Δ : $\frac{\delta l}{d_p} = 1.3$, $\bigcirc$: $\frac{\delta l}{d_p} = 1.9$, — theory

finite value. The model of Lun and Savage [78] writes like

$$g_0\left(\alpha_p\right) = \left(1 - \frac{\alpha_p}{\alpha_{p,max}}\right)^{-2.5\alpha_{p,max}} \quad , \tag{3.56}$$

where α_p obeys $\rho_p \alpha_p = n_p m_p$ and $\alpha_{p,max} = 0.64$.

As mentioned above, a pure overlap detection algorithm requires a time step criterion that limits the forward motion of the particles during a time step in order not to miss particle-particle collisions, especially for large impact parameters (grazing collisions). As for grazing collisions the penetration length of the two particles is smaller than for head-on collisions, these are most likely to be missed. This limiting criterion is expressed as

$$\frac{\delta l}{d_p} = \frac{3}{2}\sqrt{\pi T_p}\frac{\Delta t}{d_p} \quad . \tag{3.57}$$

In a previous work [111] a pure overlap detection algorithm was used. Its accuracy in regard to missing grazing collisions was expressed by plotting the collision angle and relative velocity PDF's with respect to the ratio $\frac{\delta l}{d_p}$ (3.57). A ratio of one for $\frac{\delta l}{d_p}$ means that a particle moves on average exactly one particle diameter forward during one time step. The same criterion is used here. As clearly seen in fig. 3.4 a sufficient algorithm performance is achieved when the particle propagation is limited to about 13% of a particle diameter, thus for a ratio $\frac{\delta l}{d_p} = 0.13$. Table 3.1 shows the properties of simulations used in evaluation of

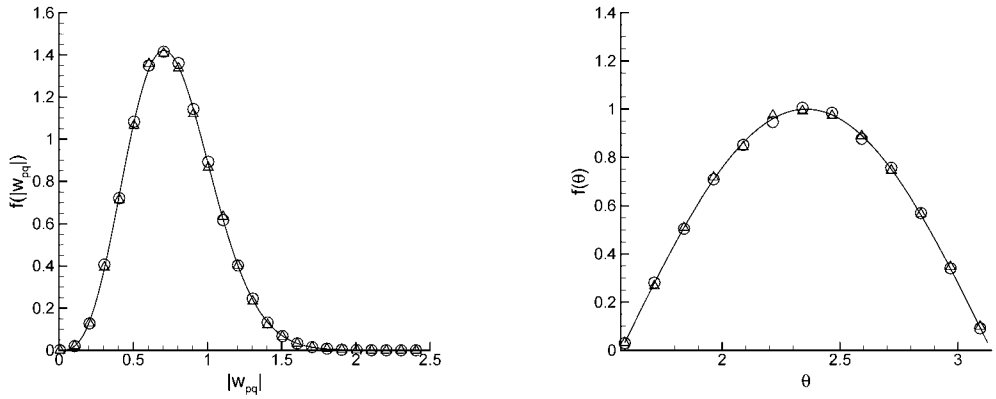

Figure 3.5: (Left) Relative velocity at moment of collision $\mathbf{w}_{pq}$. (Right) Collision angle in dependence of ratio $\frac{\delta l}{d_p}$, using an overlap and the second additional criterion. $\square : \frac{\delta l}{d_p} = 0.13$, $\bigcirc : \frac{\delta l}{d_p} = 1.9$, — theory

the detection criteria. For ratios $\frac{\delta l}{d_p}$ larger than this value the simulation results deviate from the prediction based on the kinetic theory of rarefied gases. In dependence of the flow configuration in DNS/DPS simulations of turbulent two-phase flows the criterion $\frac{\delta l}{d_p}$ can be more stringent than the CFL number of the DNS, which is disadvantageous as the DNS of the continuous phase then needs to be solved applying a time step which is not optimal. In fig. 3.4 (left) it is seen that with an increasing ratio of $\frac{\delta l}{d_p}$ more and more particle-particle collisions are missed between particles with a high relative velocity. This appears logic as faster particles cover a larger distance during a fixed time step than slower ones. Consequently fig. 3.4 (right) shows that the grazing collisions are more sensitive to a

Table 3.1: Properties of simulations for validation of collision algorithm.

Symbol	$\frac{\delta l}{d_p} = 0.13$	$\frac{\delta l}{d_p} = 1.3$	$\frac{\delta l}{d_p} = 1.9$
N_p	100000	100000	100000
α_p	$1\ 10^{-3}$	$1\ 10^{-3}$	$1\ 10^{-3}$
d_p	$3.421\ 10^{-4}$	$3.421\ 10^{-4}$	$3.421\ 10^{-4}$
ρ_p	234	234	234
q_p^2	$8.32\ 10^{-2}$	$8.32\ 10^{-2}$	$8.32\ 10^{-2}$
Δt	$5.8\ 10^{-5}$	$5.8\ 10^{-4}$	$8.48\ 10^{-4}$

higher ratio of $\frac{\delta l}{d_p}$. A correct prediction of the collision angle is even harder to achieve than a correct prediction of the relative velocity as it can be seen for a ratio of $\frac{\delta l}{d_p} = 0.13$ in fig. 3.4, where a slight deviation appears even for this low ratio. To remedy this restriction the above described second particle pair detection criterion is introduced into the algorithm developed here. Figure 3.5 shows results from simulations using the second detection criterion. Also here the relative velocity of colliding particles and the collision angle are represented with respect to criterion $\frac{\delta l}{d_p}$. However, only the limit cases with $\frac{\delta l}{d_p} = 0.13$ and $\frac{\delta l}{d_p} = 1.9$ are shown. It is obvious that both the relative velocity and the collision angle are very well represented even with a ratio of $\frac{\delta l}{d_p}$ as large as $\frac{\delta l}{d_p} = 1.9$. This corresponds to an increase of the time step by a factor of more than 14 for the simulations performed here. In practice, this is a significant advantage as the time step criterion on the dispersed phase is still more stringent than the one on the fluid phase and therefore corresponds to a net increase of the time step by this factor in gas-droplet flows.

Before continuing with the validation of the collision detection algorithm, the cost of this second additional detection criterion is discussed. It seems obvious that the introduction of a second detection criterion leads to an increase of computation time per time step. At the same time a significant increase in the time step can be reached applying this second criterion. Figure 3.6 (left) shows the normalized computation time used for one time step, applying the pure overlap detection and the two detection criteria respectively. It is seen that the computation time increases in the order of 10% by introduction of the second detection criterion. Figure 3.6 (right), however, shows that application of the second detection criterion leads to a decrease in the order of 90% of computation time for $0.1s$ physical seconds.

Representing correctly the relative velocity and collision angle distributions is not sufficient for the validation of the detection algorithm. If for example a systematic error in the detection algorithm persists that affects random particles, the distribution PDF's exhibit a correct behavior, but the collision frequency is not correctly represented. A correct prediction of the collision frequency is crucial. It is the most important statistic of the dispersed phase. As will be shown in chapter 4 the influence of collisions on any quantity is written as the change in the quantity by the collision multiplied with the collision frequency. Therefore, the collision frequency measured is compared to the predictions of the theoretical collision frequency in (3.54). Figure 3.7 compares the radial distribution function g_0 measured to theoretical predictions with respect to the particle volume fraction α_p varying from 0.001 to 0.5. As can be seen in fig. 3.7 the simulation results correspond very well with the theoretical predictions for the collision frequency corrected by the model for the radial distribution function of Carnahan and Starling [20].

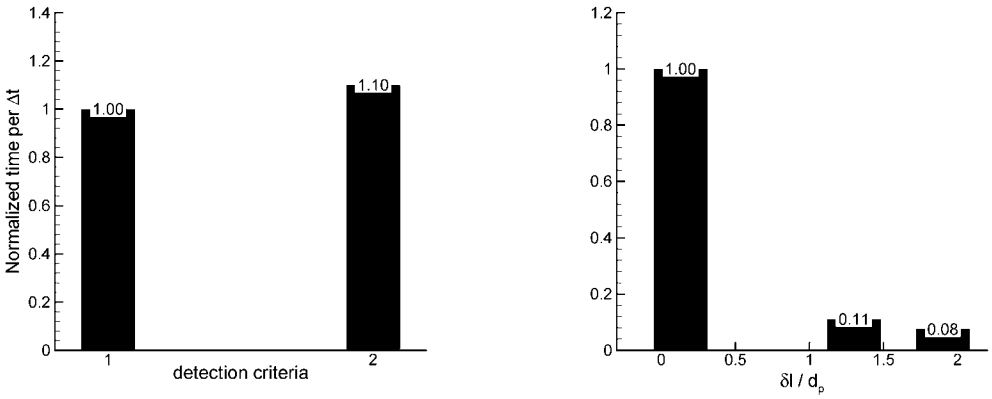

Figure 3.6: (Left) Normalized computation time per time step normalized by the time used applying the overlap criterion only. (Right) Normalized computation time for $0.1s$ physical seconds, using $\frac{\delta l}{d_p} = 0.13$, $\frac{\delta l}{d_p} = 1.3$ and $\frac{\delta l}{d_p} = 1.9$.

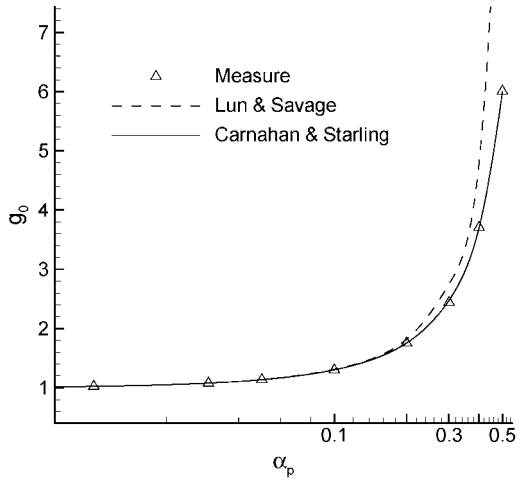

Figure 3.7: Comparison of the radial distribution function g_0 measured to theoretical predictions with respect to the particle volume fraction α_p.

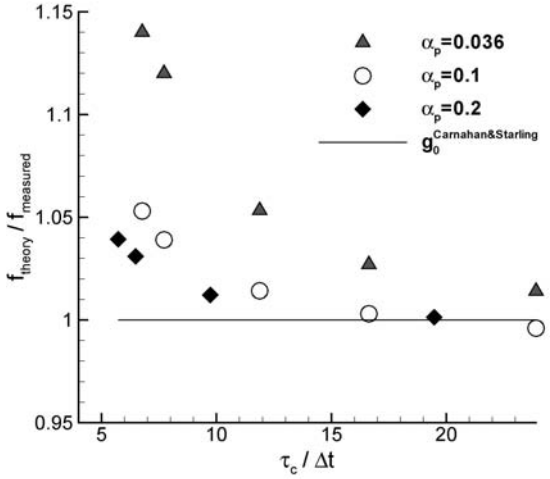

Figure 3.8: Ratio of theoretical to measured collision frequency over time step criterion $\frac{\tau_c}{\Delta t}$.

The mono-dispersed simulations pointed out another characteristic, which is intrinsic to the statistical nature of the mean particle collision time, defined as $\tau_c = \frac{n_p}{f_c}$, leading to a second time step criterion which needs to be respected for high particle volume fractions α_p. With an increasing particle volume fraction α_p the collision frequency increases and thus the mean particle collision time decreases. First calculations were conducted only respecting $\frac{\delta l}{d_p}$ as time step criterion, which led to significant deviations from the theoretical predictions for the collision frequency for particle volume fractions larger than $\alpha_p = 0.2$, while agreeing very well for smaller particle volume fractions. As shown in fig. 3.8 the ratio between the mean particle collision time and the time step must respect a certain value in order to predict correctly the collision frequency. The continuous line in fig. 3.8 represents the ratio between the theoretical predictions of the collision frequency - applying the model of Carnahan and Starling [20] - and the measured collision frequency. The closer the symbols to the continuous line, the smaller the error. Calculations were performed over a range of time steps and for several particle volume fractions α_p. It is clearly shown in fig. 3.8 that numerical predictions are improving with a diminishing time step Δt and hence an increasing ratio of $\frac{\tau_c}{\Delta t}$. This might on a first sight, contradict the validity of the increase of the time step gained by introducing the second detection criterion (3.44) and challenge its validity. But as mentioned before, this behavior is explained by the nature of the mean particle collision time, which is a statistical mean value of a Poisson-like distribution. This means that if the time step is of the order of the mean particle collision time, hence, the ratio $\frac{\tau_c}{\Delta t} = 1$, too many particles exist in the system with a collision time much smaller

than the mean value and thus have a high probability to collide more than once per time step. The reader may keep in mind that only one single collision per particle is allowed by the fundamental work hypothesis. As a consequence collisions that physically occur are suppressed by the algorithm and thus the collision frequency is underestimated. The ratio of $\frac{\tau_c}{\Delta t}$ for which a certain deviation from the theoretical predictions is achieved varies with respect to the particle volume fractions α_p. It can be seen that the smaller α_p, the higher the necessary ratio of $\frac{\tau_c}{\Delta t}$. This is explained by the possible propagation of the particles during a time step, which corresponds to the mean particle collision time τ_c. The denser a system the smaller the distance a particle covers, as the mean particle collision time decreases with increasing particle volume fraction α_p.

Thus, two time step criteria need to be respected, the first $\frac{\delta l}{d_p}$, which could be increased by a factor of ten, and a second criterion, which becomes necessary when introducing the second detection criterion. Those two criteria always lead to a larger time step as in the case of pure overlap algorithm, or for very dense systems at least to the same time step obtaining the same accuracy. The second time step criterion does not play a significant role in dilute systems, on which this work focuses primarily.

3.4.4 Bi-disperse simulations

Simulations of bi-disperse particle mixtures are crucial on the way towards poly-disperse mixture simulations, as the bi-dispersed case offers a manageable amount of validation data and gives the chance to test models for different particle diameters. As each collision in a poly-disperse particle mixture consists of the collision of two particles (with different diameters), the bi-disperse case can equally be considered as a validation of the detection algorithm for a poly-disperse particle mixture. In this chapter, first DPS of bi-disperse particle mixtures are performed, validating the detection algorithm for the collision of unequal-sized particles. It is shown that the system reaches an equilibrium state. Model predictions for the radial distribution function g_0 in the case of bi-disperse particle mixture are compared with results from DPS simulations. In a second part, a collision model for particle kinetic stresses [42] is tested for a bi-disperse non-equilibrium mixture of particles.

Homogeneous system

One of the main differences with a system of a mono-disperse mixture is the fact that in a bi-disperse particle mixture the energy levels for each particle class are not the same in the thermal equilibrium state. Heavier particles do not show the same particle agitation in the equilibrium state as lighter particles. This equilibrium state of the particle agitation can

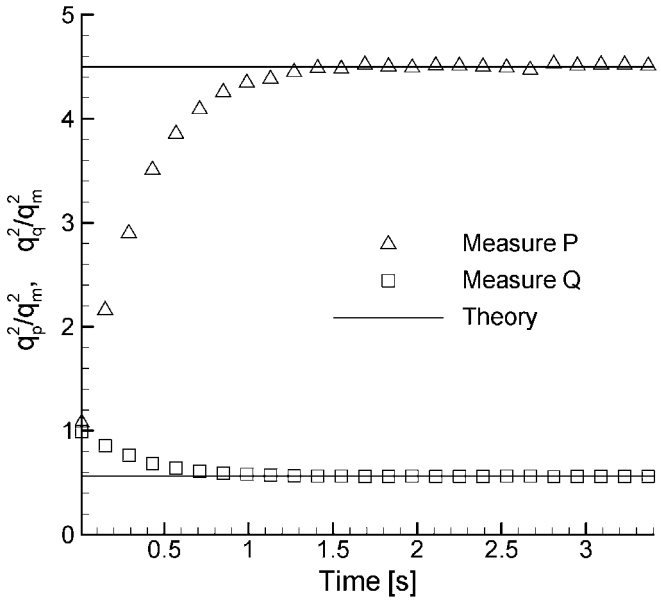

Figure 3.9: Comparison of particle kinetic energy ratios $\frac{q_p^2}{q_m^2}$ and $\frac{q_q^2}{q_m^2}$ measured in DPS simulations to predictions from the equilibrium theory.

be expressed by the following relation

$$m_p q_p^2 = m_q q_q^2 \quad . \tag{3.58}$$

If the particle collisions are elastic, the particle agitation of the bi-disperse mixture q_m^2 can be written as

$$q_m^2 = \frac{n_p m_p q_p^2 + n_q m_q q_q^2}{n_p m_p + n_q m_q} \quad . \tag{3.59}$$

The relations in (3.58) and (3.59) allow to write the particle agitation for each class in function of the particle agitation of the mixture

$$q_p^2 = \frac{n_p m_p + n_q m_q}{m_p (n_p + n_q)} q_m^2 \tag{3.60}$$

$$q_q^2 = \frac{n_p m_p + n_q m_q}{m_q (n_p + n_q)} q_m^2 \quad . \tag{3.61}$$

Now it is possible to find an expression for the ratio of $\frac{q_p^2}{q_m^2}$ and $\frac{q_q^2}{q_m^2}$, which only depends on the mass of the particle classes m_p and m_q as well as on their number densities n_p and n_q. The same values can be measured in the DPS simulations. A comparison of the measured

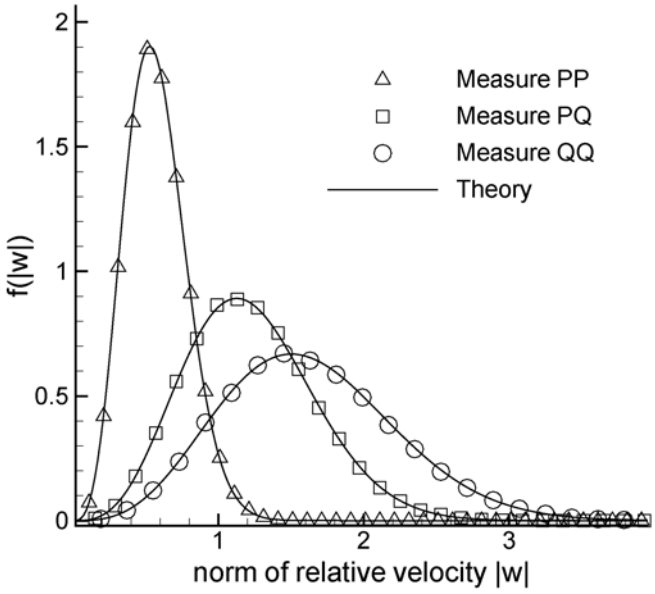

Figure 3.10: Particle relative velocity at the moment of collision. Comparison between theoretical predictions and measurements in DPS.

values to the predictions of the equilibrium theory is given in fig. 3.9. Figure 3.9 shows that the particle kinetic energies converge around their respective theoretical values. This is due to the transfer of particle kinetic energy by collisions, as will be regarded in more detail in section 3.4.4. The same statistics gained in simulations of a mono-disperse mixture, can also be obtained in the case of a bi-disperse mixture. However, in a bi-disperse mixture more than one distribution is obtained, as the statistics for collisions $p-p$, $q-q$ and $p-q$ are not necessarily the same. The collision angle distribution however is the same for all collisions between particles $p-p$, $q-q$ or $p-q$, as in dry granular flows there is no reason that the collision angle distribution is influenced by the particle diameter or mass. The particle relative velocity distribution at the moment of collision exhibits different behaviors for particle collisions $p-p$, $q-q$ or $p-q$. In the case of collisions $p-p$ or $q-q$ the expression in (3.53) remains unaltered, for reasons of readability it is re-typed in this chapter (3.62).

$$N_{\mathbf{w}_{pq}}(\mathbf{w}_{pq}) = 4n_p^2 d_p^2 \sqrt{\pi \frac{2}{3} q_p^2} \frac{1}{8\left(\frac{2}{3}q_p^2\right)^2} \mathbf{w}_{pq}^3 \exp\left(-\frac{\mathbf{w}_{pq}^2}{4\frac{2}{3}q_p^2}\right) \tag{3.62}$$

The theoretical distribution in (3.53) can be written for the case of collisions between particles $p-q$ as

$$N_{\mathbf{w}_{pq}}\left(\mathbf{w}_{pq}\right)=4n_p^2\left(\frac{d_p+d_q}{2}\right)^2\sqrt{\pi\left(\frac{\frac{2}{3}q_p^2+\frac{2}{3}q_q^2}{2}\right)}\frac{1}{8\left(\frac{\frac{2}{3}q_p^2+\frac{2}{3}q_q^2}{2}\right)^2}\mathbf{w}_{pq}^3\exp\left(-\frac{\mathbf{w}_{pq}^2}{2\left(\frac{2}{3}q_p^2+\frac{2}{3}q_q^2\right)}\right) \quad . \tag{3.63}$$

Figure 3.10 compares measurements from DPS to theoretical predictions of the relative velocity from (3.62) and (3.63). It is seen that the simulation results agree well with the theoretical predictions.

A correct prediction of the collision frequency remains important in the case of bi-disperse simulations. In regard to coalescence it is the most important quantity to predict correctly. A theoretical value for the collision frequency for each type of collision ($p-p$, $q-q$ or $p-q$) can be derived and written as

$$f_{pq}^{\kappa}=g_0^{pq}n_pn_q\pi\left(\frac{d_p+d_q}{2}\right)^2\sqrt{\frac{16}{\pi}\frac{1}{2}\left(\frac{2}{3}q_p^2+\frac{2}{3}q_q^2\right)} \quad . \tag{3.64}$$

Consequently, three different collision frequencies are obtained in the case of a bi-disperse simulation. However, another model for the radial distribution function g_0^{pq} is necessary compared with the mono-disperse case. Two models for the radial distribution function are compared here to the measurements in DPS. The first is the model of Mansoori *et al.* [80] and the second model is introduced by Patino and Simonin [98]. The model of Mansoori *et al.* [80] writes

$$g_0^{pq}\left(\alpha_m\right)=\frac{1}{1-\alpha_m}+\frac{3}{2}\left(\frac{d_pd_q}{d_p+d_q}\right)\frac{\xi_{pq}}{\left(1-\alpha_m\right)^2}+\frac{1}{2}\left(\frac{d_pd_q}{d_p+d_q}\right)^2\frac{\xi_{pq}^2}{\left(1-\alpha_m\right)^3} \quad , \tag{3.65}$$

where

$$\alpha_m=\sum_{i=p,q}\alpha_i \qquad \text{and} \qquad \xi_{pq}=2\sum_{i=p,q}\frac{\alpha_i}{d_i} \quad . \tag{3.66}$$

One characteristic of the model of Mansoori *et al.* [80] is that it tends to a finite value if the particle volume fraction approaches the maximum particle volume fraction possible. This can lead to an under-prediction of the collision frequency in very dense systems. These dense configurations are not at the focus of this work, but there is an interested in model validation in comparison with the DPS simulations performed here. Patino and Simonin [98] introduce another model for the particle volume fraction, which tends to ∞ for particle volume fractions approaching the maximum value. This model is based on the

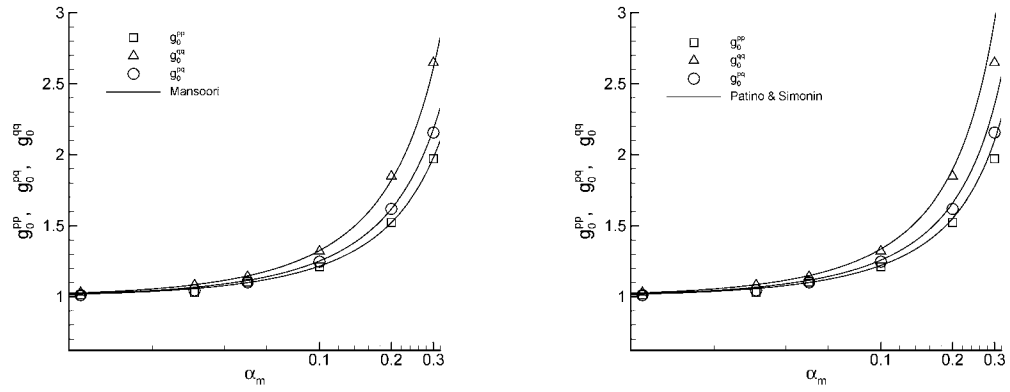

Figure 3.11: (Left) Comparison of radial distribution function measured in DPS simulations to predictions of the model by Mansoori *et al.* [80]. (Right) Comparison of radial distribution function measured in DPS simulations to predictions of the model by Patino and Simonin [98].

work of Lun and Savage [78] and is written as

$$g_0^{pq}(\alpha_m) = \left(1 - \frac{\alpha_m}{\alpha_{p,max}}\right)^{-\gamma_{pq}\ \alpha_{p,max}} \quad , \tag{3.67}$$

with

$$\gamma_{pq} = 1 + \frac{3}{2}\left(\frac{d_p d_q}{d_p + d_q}\right)\frac{\xi_{pq}}{\alpha_m} \quad . \tag{3.68}$$

Figure 3.11 (left) compares the radial distribution function measured in DPS simulations to predictions of the model by Mansoori *et al.* [80]. It is seen that the predictions of the model and measurements in DPS coincide well. Figure 3.11 (right) compares also the radial distribution function measured in DPS simulations to predictions, but by the model of Patino and Simonin [98]. This model also predicts well for small particle volume fractions ($\alpha_p < 0.1$) and less for the more elevated particle volume fractions investigated here. As mentioned above it was introduced for very dense systems and this is where it has its advantages, as it respects the limit of $g_0^{pq} \to \infty$ for a particle volume fraction $\alpha_p \to \alpha_{p,max}$.

Anisotropic system

In order to validate a collision model for particle kinetic stresses simulations of a homogeneous bi-disperse particle mixture are performed, whose particle velocity fluctuating components are altered to anisotropy at the beginning of the simulation in order to account for

Table 3.2: Initial isotropic properties for simulations with anisotropic components.

Symbol	**Particles** p	**Particles** q
N_p	100000	12500
α_p	0.05	0.05
d_p	$9.847\ 10^{-3}$	$1.969\ 10^{-2}$
ρ_p	1000	1000
q_p^2	$1.475\ 10^{-1}$	$1.887\ 10^{-2}$

the transfer of anisotropy between the velocity components of the different particle classes. The collision model for the particle kinetic stresses is presented in details in Fede [41] and in Fede and Simonin [42] and the equations used are given in appendix A.

The simulation data for the initial isotropic phase are given in tab. 3.2. The velocity components are altered anisotropic as given below.

Three test cases are presented here. In the first, only the velocity components of one particle class are turned anisotropic. In the second, the velocity components of both particle classes are turned anisotropic, and in the third test case the thermal equilibrium is disturbed in addition to the creation of anisotropy in the velocity fluctuating components. An overview of the parameters of the test cases is given in (3.73) to (3.78). The modification to the velocity fluctuating components is done by

$$\mathbf{v}_{p,i} = \alpha_i \mathbf{v}_{p,i}^{homogeneous} \tag{3.69}$$

$$\mathbf{v}_{q,i} = \beta_i \mathbf{v}_{q,i}^{homogeneous} \quad , \tag{3.70}$$

where α_i and β_i verify the following relation in order to conserve the thermal equilibrium

$$\alpha_1^2 + \alpha_2^2 + \alpha_3^2 = 3 \qquad \text{and} \qquad \beta_1^2 + \beta_2^2 + \beta_3^2 = 3 \quad . \tag{3.71}$$

These equations guarantee the conservation of the thermal equilibrium due to

$$q_p^2 = \frac{\alpha_1^2 + \alpha_2^2 + \alpha_3^2}{3}\ q_p^{2,homogeneous} \quad . \tag{3.72}$$

If the thermal equilibrium is disturbed the relations in (3.71) do not equal three anymore and the system will converge around a new equilibrium state. The three test cases performed are the following.

Test case 1:

$$\alpha_1 = 0.4; \qquad \alpha_2 = 1.0; \qquad \alpha_3 = \sqrt{3 - \alpha_1^2 - \alpha_2^2} \approx 1.3565 \tag{3.73}$$

$$\beta_1 = 1.0; \qquad \beta_2 = 1.0; \qquad \beta_3 = \sqrt{3 - \beta_1^2 - \beta_2^2} = 1.0 \tag{3.74}$$

Test case 2:

$$\alpha_1 = 0.4; \qquad \alpha_2 = 1.0; \qquad \alpha_3 = \sqrt{3 - \alpha_1^2 - \alpha_2^2} \approx 1.3565 \tag{3.75}$$

$$\beta_1 = 0.6; \qquad \beta_2 = 1.0; \qquad \beta_3 = \sqrt{3 - \beta_1^2 - \beta_2^2} = 1.2806 \tag{3.76}$$

Test case 3:

$$\alpha_1 = 0.4; \qquad \alpha_2 = 1.0; \qquad \alpha_3 = \sqrt{1.5 - \alpha_1^2 - \alpha_2^2} \approx 0.583 \tag{3.77}$$

$$\beta_1 = 0.6; \qquad \beta_2 = 1.0; \qquad \beta_3 = \sqrt{2.5 - \beta_1^2 - \beta_2^2} \approx 1.06 \tag{3.78}$$

The following specifications are used in the DPS simulations. The particle diameter ratio is $\frac{d_p}{d_q} = 2$ with a particle volume fraction ratio of $\frac{\alpha_p}{\alpha_q} = 1$. The total particle volume fraction adds to $\alpha_m = \alpha_p + \alpha_q = 0.1$. For evaluation purposes the particle kinetic stress tensor with trace zero $\hat{R}_{p,ij}$ and the normalized anisotropy tensor $b_{p,ij}$ are used. They are defined as follows

$$\hat{R}_{p,ij} = \left\langle v'_{p,i} v'_{p,j} \right\rangle_p - \frac{2}{3} q_p^2 \tag{3.79}$$

$$b_{p,ij} = \frac{\hat{R}_{p,ij}}{\frac{2}{3} q_p^2} = \frac{\left\langle v'_{p,i} v'_{p,j} \right\rangle_p}{\frac{2}{3} q_p^2} - \delta_{ij} \quad . \tag{3.80}$$

Results from test cases

Test case 1: Figure 3.12 shows that the model [42] predictions are in good agreement with the numerical simulation results. While the altered velocity components in class p returns to isotropy as expected and predicted by the model, the initially un-altered component of class p remains zero. However, the second particle class q, which was not altered, neither exhibits a creation of anisotropy in those velocity fluctuation components that were turned to anisotropy for class p. This can mainly be explained by a transfer of anisotropy from class p to class q by collisions $p - q$ between these two classes. A second effect, which is production of anisotropy in class q, is identified by Fede [41], but is stated to be neither very important nor very persistent as the redistribution of anisotropy by transfer is much

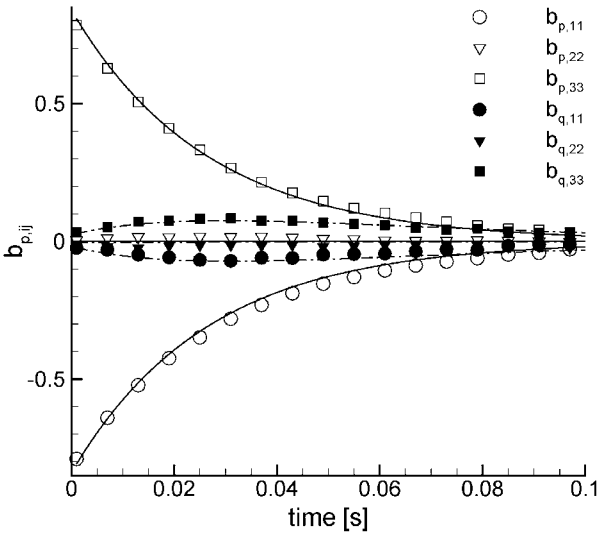

Figure 3.12: **Test case 1**: Normalized anisotropy tensor $b_{p,ij}$ measured in DPS in comparison with model predictions [42]. The solid line — represents model predictions of class p, the dashed line - - - model predictions of class q.

more important.

Test case 2

Figure 3.13 shows the effect of redistribution of anisotropy within the same particle class. Both, particle class p and q are initially altered to anisotropy in this test case. The return to isotropy is here mainly due to collisions within the same particle class, thus collisions $p-p$ and $q-q$.

Test case 3

In this last test case, the thermal equilibrium is disturbed by not respecting relations in (3.71). Figure 3.14 shows that the model predicts the correct return to isotropy. It is interesting to note that the crossing paths over time for the velocity components of class q are well represented by the model. In order to underline the effect of finding a new equilibrium state, if the thermal equilibrium is initially disturbed as in this third test case, fig. 3.15 compares the measurements in DPS of the particle kinetic stress tensor with trace zero $\hat{R}_{p,ij}$ to the model predictions. Figure 3.15 shows that the particulate system converges around the new equilibrium state and that the model predictions agree with the measurements. It needs to be mentioned that in fig. 3.15 different properties of the particle mixture are used in order to present a netter effect.

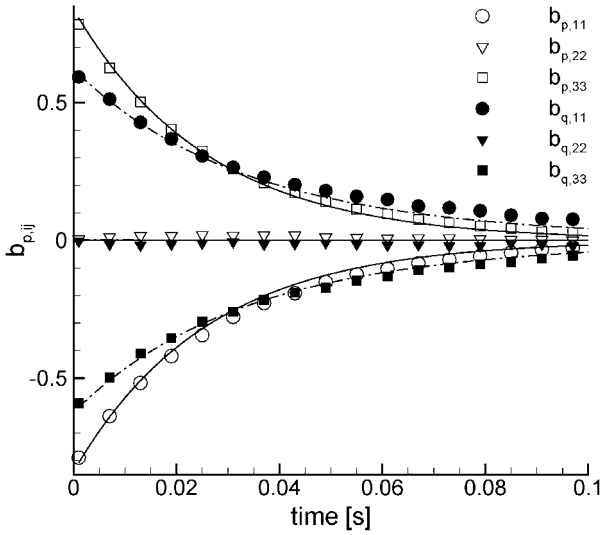

Figure 3.13: **Test case 2**: Normalized anisotropy tensor $b_{p,ij}$ measured in DPS in comparison with model predictions [42]. The solid line — represents model predictions of class p, the dashed line - - - model predictions of class q.

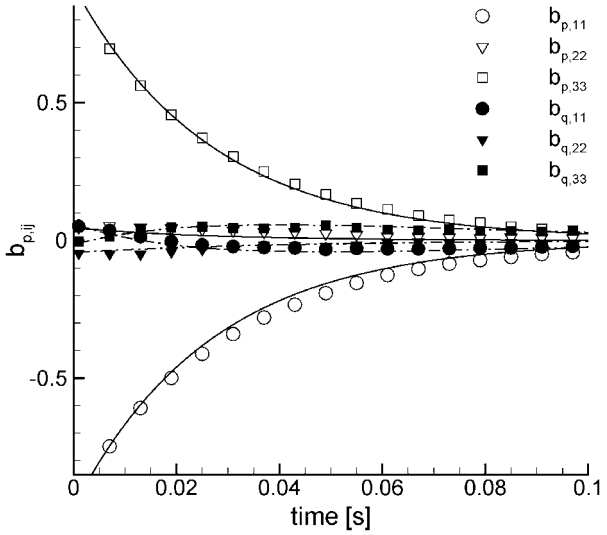

Figure 3.14: **Test case 3**: Normalized anisotropy tensor $b_{p,ij}$ measured in DPS in comparison with model predictions [42]. The solid line — represents model predictions of class p, the dashed line - - - model predictions of class q.

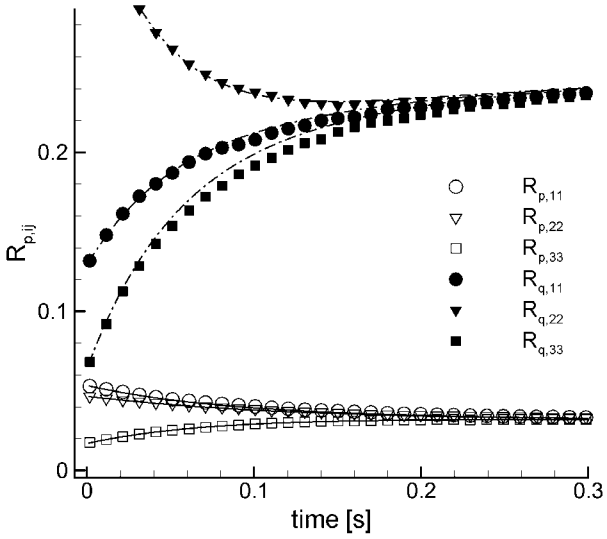

Figure 3.15: **Test case 3**: Particle kinetic stress tensor with trace zero $\hat{R}_{p,ij}$ measured in DPS in comparison with model predictions [42]. The solid line — represents model predictions of class p, the dashed line - - - model predictions of class q.

3.4.5 Coalescence handling

The collision detection algorithm is validated in dry granular flows with particle-particle collisions as explained in section 3.4.3. The droplet pair detection in case of other collision outcomes than rebounds, such as permanent coalescence, reflexive or stretching separation, remains the same in the case of gas-liquid flows. The droplet collision handling is altered only. As described in chapter 2 the collision outcome for colliding droplets is basically described by two dimensionless quantities, the Weber number (see (2.2)) and the impact parameter X (see (2.4)).

In a first step in this work, coalescence phenomena are modeled representing a pure coalescence regime for the sake of distinctness. This means that each collision leads to permanent coalescence and no other collision outcomes exist. Permanent coalescence is modeled applying mass and momentum conservation

$$\begin{aligned} m^* &= m_p + m_q \\ m^*\mathbf{v}^* &= m_p\mathbf{v}_p + m_q\mathbf{v}_q \quad , \end{aligned} \tag{3.81}$$

with m_p and m_q the mass of the particles before coalescence and m^* after. Analogous for the particle velocities $\mathbf{v}_p, \mathbf{v}_q$ and $\mathbf{v}^*$. The corresponding particle diameter is directly

deductible from the mass conservation equations as the particle density is constant and the particles are modeled as rigid spheres, as mentioned above. The position of the new particle that arises from coalescence is given as

$$\mathbf{x}^* = \frac{d_p^3 \mathbf{x}_p + d_q^3 \mathbf{x}_q}{d^{*3}} \tag{3.82}$$

with $\mathbf{x}^*$ the position of the new particle and d_p, d_q and d^* the particle diameters.

In order to introduce other coalescence outcomes as permanent coalescence, boundary limits introduced in chapter 2 for the different regimes are used. These depend on the Weber number We and the impact parameter X. The particle density ρ_p and its surface tension σ are constants. Thus, only the diameter of the smaller particle d_q and the relative velocity at the moment of collision $\mathbf{w}_{pq}$ change from one collision to another. It is possible to determine a theoretical probability density function (PDF) for both the Weber number and the impact parameter. The PDF of the Weber number can be expressed as a function of the relative velocity at the moment of collision by the following relation

$$N_{We}\left(We\right) dWe = N_{\mathbf{w}_{pq}}\left(\mathbf{w}_{pq}\right) d\mathbf{w}_{pq} \quad . \tag{3.83}$$

The distribution for the particle relative velocity is given in (3.53). The final form of the distribution function for the Weber number, after some short calculations based on the normalized distribution function of the particle relative velocity, is found to verify

$$N_{We}\left(\mathbf{w}_{pq}\right) = \frac{1}{16 T_p^2} \frac{\sigma}{\rho_p d_p} \mathbf{w}_{pq}^2 \exp\left(-\frac{\mathbf{w}_{pq}^2}{4T_p}\right) \quad . \tag{3.84}$$

This form is very similar to the PDF of the particle relative velocity with additionally factors accounting for the density and surface tension of the droplet. These two values however are used in the deterministic simulations conducted in this work for parameterization purposes of the two-phase flow and thus not necessarily physical, since priority is given to the dimensionless numbers characterizing turbulent two-phase flows. For validation purposes, the PDF of the particle relative velocity is used instead of the PDF of the Weber number, although it can be obtained without difficulty.

A distribution function can equally be derived for the impact parameter X. This is a purely geometrical quantity, which can be calculated as a function of the collision angle PDF given in (3.52). Again, it can be written

$$N_X\left(X\right) dX = N_\theta\left(\theta\right) d\theta \quad . \tag{3.85}$$

This leads to

$$N_X(X) = \frac{N_\theta(\theta)}{\left|\frac{dX}{d\theta}\right|} \quad , \tag{3.86}$$

where the impact parameter X can be written as

$$X = sin(\pi - \theta) \quad . \tag{3.87}$$

The expression in (3.86) can then be written as function of θ

$$N_X(\theta) = \frac{N_\theta(\theta)}{\left|\frac{dX}{d\theta}\right|} = \frac{-sin(2\theta)}{|-cos(\pi - \theta)|} \quad . \tag{3.88}$$

This equation can be transformed applying trigonometric rules in the interval $\theta \in \left[\frac{\pi}{2}, \pi\right]$, which is the interval of collision angles as it is defined here. It writes then

$$N_X(\theta) = 2sin(\theta) \quad , \tag{3.89}$$

which, expressed in terms of the impact parameter and applying $\theta = \pi - arcsin(X)$, gives the final form for the PDF of the impact parameter after short manipulation

$$N_X(\theta) = 2X \quad . \tag{3.90}$$

The PDF of the impact parameter therefore describes a straight line through the origin. A comparison with measurements from DPS on a dry permanent coalescence flow is given in fig. 3.16. The statistics verify this theoretical prediction of the impact parameter, although the statistics are moderate, which is due to the lack of events that can be taken into consideration. The number of particles finds its maximum at the beginning of the simulation and decreases then with each single collision. Therefore, collisions are limited in number.

A difficulty might arise at the limits of the collision angle θ that occurs, where θ lies as mentioned above in the interval $\theta \in \left[\frac{\pi}{2}, \pi\right]$. In (3.88) it can be seen that the value at $\theta = \frac{\pi}{2}$ is not clear (this case corresponds to a grazing collision at an impact parameter $X = 1$). Introducing an infinitesimal quantity ϵ the limiting case for $\lim_{\epsilon \to 0}\left(\frac{\pi}{2} + \epsilon\right)$ can be calculated. It can be written

$$N_X\left(\theta = \frac{\pi}{2} + \epsilon\right) = \frac{-sin(\pi + 2\epsilon)}{\left|-cos\left(\frac{\pi}{2} - \epsilon\right)\right|} = 2\ cos(\epsilon) \quad . \tag{3.91}$$

And finally

$$\lim_{\epsilon \to 0}(2\ cos(\epsilon)) = 2 \quad . \tag{3.92}$$

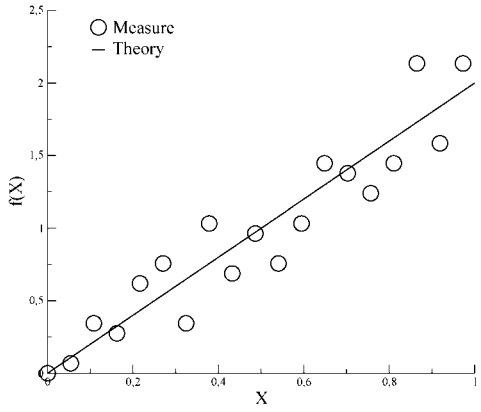

Figure 3.16: Comparison of measured impact parameter X in dry coalescence to predictions from theory.

After verifying that the Weber number We (via the particle relative velocity PDF) and the impact parameter X are correctly represented, the models for the transition between the different regimes introduced in chapter 2 can be used. Only the collision outcomes of permanent coalescence, reflexive separation and stretching separation are regarded in this work. Figure 3.17 shows the critical values of the Weber number for a transition from permanent coalescence to reflexive separation and the impact parameter for a transition from permanent coalescence to stretching separation. The corresponding boundary relations from Ashgriz and Poo [4] are used: (2.9) to (2.11) for the transition to the stretching separation regime and (2.12) to (2.14) for the transition to the reflexive separation regime. As both limiting curves are relations of the Weber number and the impact parameter, the choice to name one the critical Weber number curve and the other one the critical impact parameter curve is freely chosen and could be inverted. However, it appears logic in respect to the transition from permanent coalescence to reflexive separation. As a matter of fact the limiting curve from permanent coalescence to reflexive separation (here called critical Weber number) becomes negative if it exceeds a certain value for the impact parameter, the function has a discontinuity at this value of X (horizontal solid line in fig. 3.17). In order to account correctly for permanent coalescence also for a larger impact parameter the $We - X$-domain is subdivided into four sections. The criteria for these four sections and the consequent collision outcome are given below

$$
\begin{array}{lll}
We & < We_{crit} & \& \; X < X_{crit} \qquad \text{permanent coalescence (1)} \\
We_{crit} & < 0 & \& \; X < X_{crit} \qquad \text{permanent coalescence (2)}
\end{array}
$$

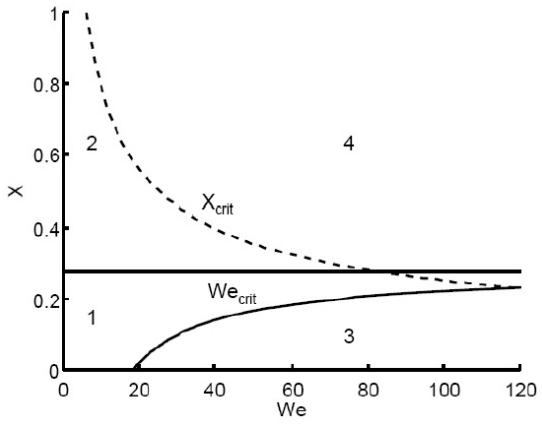

Figure 3.17: Boundary limits from Ashgriz and Poo [4] for critical Weber number We_{crit} — and impact parameter X_{crit} - - - for a particle diameter ratio of $\Delta = 1$.

$$\begin{array}{llll} We & > We_{crit} & \& \; We_{crit} > 0 \quad \& \; X < X_{crit} & \text{reflexive separation (3)} \\ X & > X_{crit} & & \text{stretching separation (4)} \quad . \end{array}$$

The collision handling in case of reflexive and stretching separation needs now to be defined. These two regimes are physically complex and difficult to model within the frame of the hard-sphere model. The modeling concentrates on the main effects and neglects many others as will be shown for the sake of distinctness.

Reflexive separation is treated as a particle-particle collision following (3.50) and (3.51). An elasticity coefficient can be introduced in order to account for dissipation of kinetic energy due to the reflexive separation. In reflexive separation two droplets collide, coalesce and separate again. The modeling of reflexive separation by these elastic collision equations seems fair.

Stretching separation represents a very complex collision outcome with usually the creation of satellite droplets very small in comparison with the droplet diameters. The creation of satellite droplets is therefore numerically very challenging in DNS/DPS simulations and their treatment is not feasible within this work. Droplets that undergo stretching separation, basically continue on their initial trajectories after separation. As explained in chapter 2 this collision phenomenon introduces rotation in the particles. As rotation is not considered in the frame of this study, only the two separated particles persist, following a similar trajectory as before the collision. Although kinetic energy is dissipated due to the deformation and coalescence of the droplets, this dissipation is not regarded here. There-

fore, the modeling of stretching separation consists in not altering the particle properties if this event occurs. This seems crude, but represents the essential properties of the two droplets after collision.

3.4.6 Comparison of deterministic permanent coalescence treatment to Monte-Carlo predictions in dry granular flows

In this section measures of the coalescence rate in DPS simulations of dry coalescence, where permanent coalescence is the only possible collision outcome, are compared to predictions of Monte-Carlo simulations. The principle of Monte-Carlo simulations is presented in chapter 4. This simulations are considered to be exact in dry granular flows and a correct measure of the coalescence rate and particle kinetic energy in the system is qualified by agreement with the Monte-Carlo predictions. First, the influence of the initial value of the particle kinetic energy on the coalescence rate is presented, which is also important for a correct understanding of later results in turbulent two-phase flows. Second, these comparisons to predictions of Monte-Carlo simulations are used to revalidate the algorithm after it is adapted to different platforms.

Influence of initial particle kinetic energy

In the simulations presented here the DPS simulations are initialized with values obtained from Monte-Carlo predictions. This means the Monte-Carlo simulations were performed first and DPS simulations were adapted. This way it is possible to investigate the influence of the initial value for the particle kinetic energy q_p^2. As in dry granular flows the particle kinetic energy is conserved if collisions but not coalescence are treated, two different simulations are performed. First, the initial value for the particle kinetic energy q_p^2 is determined as the mean in time over a period in which q_p^2 is already stationary in the Monte-Carlo simulations as shown in fig. 3.18. This value is used for the DPS simulations. The initialization of the Monte-Carlo simulations is done with an underlying fluid flow field which brings the particulate phase into a stationary state. At the moment coalescence is started the fluid flow is turned off and thus the configuration of dry granular flows is produced. Figure 3.18 (left) shows that the particle number (or therefore the coalescence rate) is correctly represented. The particle kinetic energy q_p^2 in fig. 3.18 (right) however shows a small deviation between the measures in DPS and the predictions of the Monte-Carlo simulations, which should not exist. If the initial value for the particle kinetic energy q_p^2 in the DPS simulations is chosen to be the instantaneous value of q_p^2 at the moment coalescence is started in the Monte-Carlo simulations, this difference in the particle kinetic

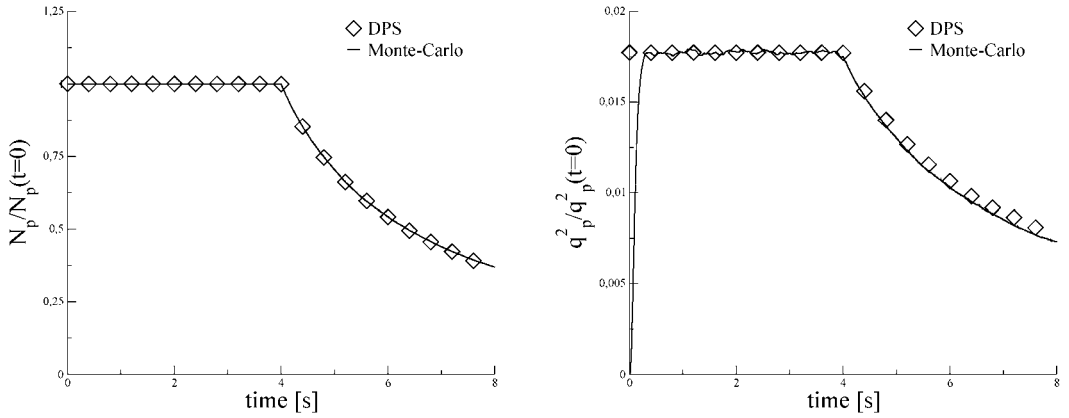

Figure 3.18: (Left) Particle number N_p measured in DPS in comparison with predictions from Monte-Carlo simulations. (Right) Particle kinetic energy q_p^2 measured in DPS in comparison with predictions from Monte-Carlo simulations, initialized with the mean of q_p^2 before coalescence starts.

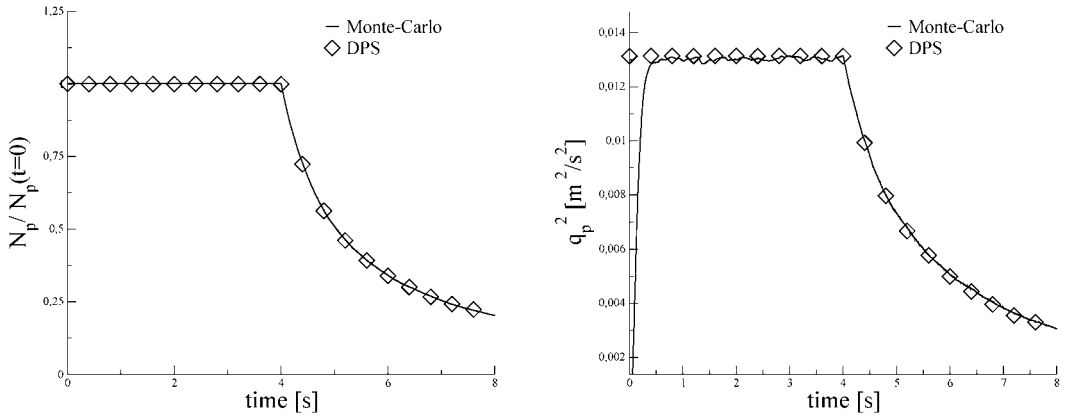

Figure 3.19: (Left) Particle number N_p measured in DPS in comparison with predictions from Monte-Carlo simulations. (Right) Particle kinetic energy q_p^2 measured in DPS in comparison with predictions from Monte-Carlo simulations, initialized with the instantaneous value of q_p^2 before coalescence starts.

Table 3.3: Properties of simulations for comparison with Monte-Carlo.

Symbol	**Particles** p
N_p	24000
α_p	$7.5\ 10^{-6}$
d_p	$5.0\ 10^{-4}$
ρ_p	234
q_p^2	$1.32\ 10^{-2}$

energy vanishes as seen in fig. 3.19. As there is no memory of particulate phase in the Monte-Carlo simulations, the instantaneous value is decisive.

In later simulations of turbulent two-phase flows, the Monte-Carlo simulations will be initialized with values obtained from the deterministic DNS/DPS simulations. These initial values are usually mean values and the instantaneous values are fluctuating in time. An exact prediction of the particle kinetic energy seems therefore very challenging.

Code validation on different platforms

After being developed, the collision detection algorithm and collision treatment needed to be integrated into the DNS solver and adapted to its structure. Finally, the algorithm needed to be vectorized due to the vectorial structure of the NEC-SX-8 on which the DNS/DPS simulations were performed. Of course a re-validation is necessary in order to assure not to introduce errors by these modifications. Besides the validations presented above, while validating the collision algorithm, also the coalescence rate and the particle kinetic energy in the coalescing regime are compared. The results are presented in fig. 3.20. It is seen that the particle number as well as the particle kinetic energy are well represented and correspond to one another in the different stages of the code and on different platforms. Table 3.3 summarizes the simulation data used for validation with coalescence.

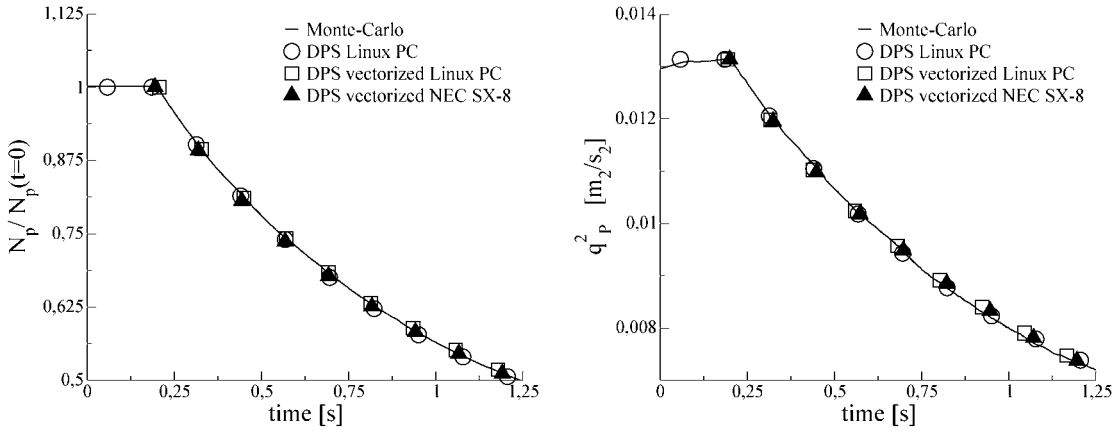

Figure 3.20: (Left) Particle number N_p measured in DPS in comparison with predictions from Monte-Carlo simulations comparing vectorized and non-vectorized versions of the code and different platforms. (Right) Particle kinetic energy q_p^2 measured in DPS in comparison with predictions from Monte-Carlo simulations comparing vectorized and non-vectorized versions of the code and different platforms.

Chapter 4

Statistical description of gas-droplet flows

The description of the dispersed phase in turbulent two-phase flows is often based on the kinetic theory of rarefied gases due to the analogy between the motion of molecules in a gas and the random motion of particles or droplets in turbulent two-phase flows. Several authors developed approaches based on this kinetic theory of rarefied gases [91], [107], [144]. In the first part the basics of the PDF approach are presented and a transport equation for a PDF is derived in a general way. Then the transport equation of the particle velocity PDF f_p and the joint fluid-particle PDF f_{fp} accounting for the interaction of fluid and particulate phase are outlined. In the second part the stochastic Lagrangian approach for a direct resolution of the derived transport equation is presented. In the following part the moment method approach is introduced and the transport equation for the respective moments are given. Finally, the Direct Quadrature Method of Moments (DQMOM) for coalescence based on the joint fluid-particle velocity PDF is introduced.

4.1 Derivation of the PDF transport equation: Boltzmann-type equation

The fundamentals of the kinetic theory of rarefied gases are given in several works [21], [46]. The dispersed phase in turbulent two-phase flows is described by the Lagrangian coordinates of all particles in the system at all times in analogy to the kinetic theory of rarefied gases. If a Cartesian coordinate system is introduced the position in physical space of each particle can be expressed as $\mathbf{x} = (x_x, x_y, x_z)$. In turbulent dispersed two-phase flows a variety of different variables is used in general to describe its physical properties, while in the frame

of the theory of rarefied gases often only the particle velocity vector $\mathbf{c}_p$ is taken into account as variable. A phase space can be introduced that contains all these physical properties of the dispersed phase. Thus it is possible to summarize all properties of the N_p particles in a vector $\boldsymbol{\xi} = \left(\boldsymbol{\xi}_1, ..., \boldsymbol{\xi}_n, ..., \boldsymbol{\xi}_{N_p}\right) = \left(\mathbf{x}_1^*, \mathbf{c}_1, \mu_1, ..., \mathbf{x}_n^*, \mathbf{c}_n, \mu_n, ..., \mathbf{x}_{N_p}^*, \mathbf{c}_{N_p}, \mu_{N_p}\right)$, where $\mathbf{x}_n^*$ stand for the position of particle n, $\mathbf{c}_n$ stand for the particle velocity of particle n and μ_n for the particle mass of particle n. Any other relevant property can be added if necessary.

The **fine grained** number density function $W\left(\boldsymbol{\xi}; t, \mathcal{H}_{fp}\right)$ represents the particle properties at time t for one given two-phase flow realization $\mathcal{H}_{fp}$. It can be written

$$W\left(\boldsymbol{\xi}; t, \mathcal{H}_{fp}\right) = \sum_{n=1}^{N_p} \delta\left(\mathbf{x}_n^* - \mathbf{x}_n\left(t\right)\right) \delta\left(\mathbf{c}_n - \mathbf{v}_n\left(t\right)\right) \delta\left(\mu_n - m_n\left(t\right)\right) \quad , \tag{4.1}$$

where W satisfies

$$\int W\left(\boldsymbol{\xi}; t, \mathcal{H}_{fp}\right) d\boldsymbol{\xi} = N_p\left(t, \mathcal{H}_{fp}\right) \quad . \tag{4.2}$$

A vector $\boldsymbol{\zeta}\left(t\right)$ is introduced that contains the particle cloud properties in physical space for the given two-phase flow realization $\mathcal{H}_{fp}$.

$$\boldsymbol{\zeta}\left(t\right) = \left(\boldsymbol{\zeta}_1\left(t\right), ..., \boldsymbol{\zeta}_n\left(t\right), ..., \boldsymbol{\zeta}_{N_p}\left(t\right)\right) \tag{4.3}$$

$$\text{with} \qquad \boldsymbol{\zeta}_n\left(t\right) = \left(\mathbf{x}_n\left(t\right), \mathbf{v}_n\left(t\right), m_n\left(t\right)\right) \quad . \tag{4.4}$$

The chain rule applied on the definition of $W\left(\boldsymbol{\xi}; t, \mathcal{H}_{fp}\right)$ gives directly

$$\frac{\partial W}{\partial t} = -\sum_{n=1}^{N_p} \frac{\partial W}{\partial \boldsymbol{\xi}_n} \cdot \left(\frac{d\boldsymbol{\zeta}_n}{dt}\right)_{\boldsymbol{\zeta}=\boldsymbol{\xi}} \tag{4.5}$$

The fine grained number density function W obeys then the following Liouville equation

$$\frac{\partial W}{\partial t} + \sum_{n=1}^{N_p} \left[\frac{\partial W}{\partial x_{n,j}^*} \left(\frac{dx_{n,j}}{dt}\right)_{\boldsymbol{\zeta}=\boldsymbol{\xi}} + \frac{\partial W}{\partial c_{n,j}} \left(\frac{dv_{n,j}}{dt}\right)_{\boldsymbol{\zeta}=\boldsymbol{\xi}} + \frac{\partial W}{\partial \mu_n} \left(\frac{dm_n}{dt}\right)_{\boldsymbol{\zeta}=\boldsymbol{\xi}} \right] = 0 \tag{4.6}$$

The statistical averaging may be defined as an arithmetic mean of $N_{\mathcal{H}_{fp}}$ $\left(N_{\mathcal{H}_{fp}} \to \infty\right)$ independent identical realizations as

$$\left\langle . \right\rangle = \lim_{N_{\mathcal{H}_{fp}} \to \infty} \left[\frac{1}{N_{\mathcal{H}_{fp}}} \sum_{N_{\mathcal{H}_{fp}}} \left(.\right) \right] \quad . \tag{4.7}$$

The corresponding ensemble number density function is then written as

$$\mathcal{F}_p\left(\boldsymbol{\xi};t\right)=\left\langle W\left(\boldsymbol{\xi};t,\mathcal{H}_{fp}\right)\right\rangle \quad , \tag{4.8}$$

which satisfies:

1. Non-negativity

$$\mathcal{F}_p\left(\boldsymbol{\xi};t\right)\geq 0 \quad . \tag{4.9}$$

2. Normalization of the PDF

$$\int \mathcal{F}_p\left(\boldsymbol{\xi};t\right)d\boldsymbol{\xi}=\overline{N}_p\left(t\right) \quad . \tag{4.10}$$

3. The probability has to be 0 for $|\xi|\rightarrow\infty$

$$\lim_{|\boldsymbol{\xi}|\rightarrow\infty}\mathcal{F}_p\left(\boldsymbol{\xi};t\right)=0 \quad . \tag{4.11}$$

The one-particle number density function $f_p^{(1)}$ (Boltzmann distribution function) can be computed from $\mathcal{F}_p$ as

$$f_p^{(1)}\left(\mathbf{x}_1^*,\mathbf{c}_1,\mu_1;t\right)=\int \mathcal{F}_p\left(\mathbf{x}_1^*,\mathbf{c}_1,\mu_1...,\mathbf{x}_{N_p}^*,\mathbf{c}_{N_p},\mu_{N_p};t\right)\prod_{n=2}^{N_p}d\mathbf{x}_n^*d\mathbf{c}_nd\mu_n \quad . \tag{4.12}$$

The $f_p^{(1)}$ governing equation may be derived from (4.6) by application of the averaging operator (4.7) and integration over $n=2$ to N_p particle properties $\mathbf{x}_n^*,\mathbf{c}_n,\mu_n$

$$\frac{\partial f_p^{(1)}}{\partial t}+v_{p,j}\frac{\partial f_p^{(1)}}{\partial x_j}+\frac{\partial}{\partial c_{p,j}}\left(\left\langle\frac{dv_{p,j}}{dt}\left|\boldsymbol{\zeta}_p=\boldsymbol{\xi}_p\right.\right\rangle f_p^{(1)}\right)+\frac{\partial}{\partial\mu_p}\left(\left\langle\frac{dm_p}{dt}\left|\boldsymbol{\zeta}_p=\boldsymbol{\xi}_p\right.\right\rangle f_p^{(1)}\right)=0 \quad . \tag{4.13}$$

Using the acceleration equation (3.19), (4.13) can be written if the external forces on the particle and the collision forces are split as

$$\frac{\partial f_p}{\partial t}+v_{p,j}\frac{\partial f_p}{\partial x_j}+\frac{\partial}{\partial c_{p,j}}\left(\left\langle\frac{F_{D,j}}{m_p}\left|\boldsymbol{\zeta}_p=\boldsymbol{\xi}_p\right.\right\rangle f_p\right)=\left(\frac{\partial f_p}{\partial t}\right)_{coll} \quad , \tag{4.14}$$

where $\left(\frac{\partial f_p}{\partial t}\right)_{coll}$ expresses the change in f_p due to collisions. As no evaporation is considered the change in mass appears in the collision operator only. (4.14) is a Boltzmann-type equation.

4.1.1 Modeling of the undisturbed fluid characteristics

A major closure problem in the (3.33), accounting for the droplet acceleration, is related to the modeling of the undisturbed fluid characteristics at the particle position such as the locally undisturbed fluid velocity at the particle position $\mathbf{u}_{f@p}$ [117]. The conditional expectation of the drag force $F_{D,i}$ in the transport equation of f_p can be written in a simplified manner as

$$\begin{aligned} \left\langle \frac{F_{D,j}}{m_p} \right\rangle &= -\frac{1}{\tau_{fp}^F} \left\langle [v_{p,j} - u_{f@p,j}] \mid \mathbf{c}_p \right\rangle \\ &= -\frac{1}{\tau_{fp}^F} \left[c_{p,j} - U_{f,j} - \left\langle u'_{f@p,j} \mid \mathbf{c}_p \right\rangle \right] \quad ; \end{aligned} \tag{4.15}$$

this way the closure problem is related to the conditional expectation of the undisturbed fluid velocity fluctuation $u'_{f@p,j}$. The mean particle relaxation time τ_{fp}^F, is proposed by Deutsch and Simonin [29] in order to linearize the particle momentum equation for higher particle Reynolds numbers. The mean particle relaxation time τ_{fp}^F is defined by

$$\tau_{fp}^F = \frac{4}{3} \frac{\rho_p}{\rho_f} \frac{d_p}{\langle C_D \rangle \langle |v_{p,j} - u_{f@p,j}| \rangle} \quad , \tag{4.16}$$

where the mean drag coefficient $\langle C_D \rangle$ is given by

$$\langle C_D \rangle = \frac{24}{\langle Re_p \rangle} \left(1 + 0.15 \langle Re_p \rangle^{0.687} \right) \quad , \tag{4.17}$$

and the mean particle Reynolds number given by

$$\langle Re_p \rangle = \frac{d_p \left| v_{p,j} - u_{f@p,j} \right|}{\nu_f} \quad . \tag{4.18}$$

The undisturbed fluid velocity fluctuation $u'_{f@p,j}$ can be expressed in terms of the conditional fluid velocity distribution function $f_f(\mathbf{c}_f \mid \mathbf{c}_p, \mathbf{x}; t)$ as

$$\left\langle u'_{f@p,j} \mid \mathbf{c}_p \right\rangle = \int \left[c_{f,j} - U_{f,j} \right] f_f(\mathbf{c}_f \mid \mathbf{c}_p, \mathbf{x}; t) \, d\mathbf{c}_f \quad . \tag{4.19}$$

In general the fluid velocity and the fluid velocity following the particle path are random but correlated and the conditional fluid velocity distribution function $f_f(\mathbf{c}_f \mid \mathbf{c}_p, \mathbf{x}; t)$ does not equal the standard fluid velocity distribution function $f_f(\mathbf{c}_f, \mathbf{x}; t)$. It is

$$f_f(\mathbf{c}_f \mid \mathbf{c}_p, \mathbf{x}; t) \neq f_f(\mathbf{c}_f, \mathbf{x}; t) \quad . \tag{4.20}$$

Several authors developed closure models for $\left\langle u'_{f@p,j} \mid \mathbf{c}_p \right\rangle$. Derevich and Zaichik [27] propose a model assuming a Gaussian random field for the turbulent fluid velocities using an exponential approximation for the Lagrangian fluid correlation function $\langle R_f(\tau) \rangle_p$. Later Zaichik *et al.* [143] propose an extension to their original model which remedies an inconsistency in the asymptotic behavior in the scalar limit case (for particles with very low inertial). Reeks [108] [109] developed a turbulent driving force closure model based on Kraichnan's Lagrangian history direct interaction approximation [66].

Simonin *et al.* [118] propose the derivation of a closure model for the particle kinetic equation based on the stochastic Lagrangian description of the fluid turbulence. Several methods were developed based on this approach in order to model the instantaneous fluid velocity along the particle path ([94], [13], [90]). For example Gosman and Ioannides [51] introduce the so-called eddy life time concept, which assumes that particles interact with a sequence of turbulent eddies. This approach can lead to inconsistent behavior for very low particle inertia. Therefore, Simonin *et al.* [118] propose an approach of Langevin-type, which allows a consistency with the single-phase turbulence [101]. This approach consists of generating directly the fluid velocities following the particle path, by modeling the decorrelation induced by the mean and turbulent fluid-particle relative motion, which is the so-called crossing trajectory effect [99], [118].

Langevin equation for the fluid velocity along the particle path

By analogy with the approach of Pope [101], Simonin *et al.* [118] write the Langevin equation for the locally undisturbed fluid velocity increment measured along the particle path as

$$\begin{aligned} u_{f@p,i}(\mathbf{x}+\mathbf{v}_p\delta t, t+\delta t) - u_{f@p,i}(\mathbf{x},t) &= g_i\delta t - \frac{1}{\rho_f}\frac{\partial P_f}{\partial x_i}\delta t + \frac{\partial}{\partial x_j}\left[\nu_f \frac{\partial U_{f,i}}{\partial x_j}\right]\delta t \\ &+ \left[v_{p,j} - u_{f@p,j}\right]\frac{\delta U_{f,i}}{\delta x_j}\delta t \\ &+ G_{fp,ij}\left[u_{f@p,j} - U_{f,j}\right]\delta t + C_{fp}\delta W_{fp,i} \quad . \end{aligned} \tag{4.21}$$

Effects of viscosity, fluctuating pressure gradient and crossing trajectories on the fluid turbulent velocity fluctuations viewed by the particles are taken into account by the terms $G_{fp,ij}$ and $C_{fp}\delta W_{fp,i}$. C_{fp} is a model coefficient, which depends on the small-scale turbulence statistics and $\delta W_{fp,i}$ is a stochastic Wiener process. As a Wiener process it is a random vector with zero mean and isotropic covariance matrix. It is:

$$\langle \delta W_{fp,i} \rangle = 0$$

$$\begin{aligned} \left\langle u_{f@p,i}\left(t'\right)\delta W_{fp,j}\left(t\right)\right\rangle &= 0 \qquad \text{with} \qquad t' \leq t \\ \left\langle \delta W_{fp,i}\delta W_{fp,j}\right\rangle &= \delta_{ij}\delta t \end{aligned} \tag{4.22}$$

$G_{fp,ij}$ is a second-order tensor for the statistics of the fluid velocity field along the particle path consistent with the single-phase approach (Simonin *et al.* [118]).

4.1.2 Transport equation for joint fluid-particle velocity PDF f_{fp}

The modeling approach proposed by Simonin *et al.* [118], presented in section 4.1.1 allows to close directly the transport equation of a probability density function that includes the fluid velocity at the particle position. This transport equation for the joint fluid-particle velocity PDF $f_{fp}\left(\mathbf{x},\mathbf{c}_f,\mathbf{c}_p,\mu_p;t\right)$ is given next. The transport equation for $f_{fp}\left(\mathbf{x},\mathbf{c}_f,\mathbf{c}_p,\mu_p;t\right)$ is a Boltzmann-type equation and writes as

$$\begin{aligned} \frac{\partial f_{fp}}{\partial t} + c_{p,j}\frac{\partial f_{fp}}{\partial x_j} &+ \frac{\partial}{\partial c_{p,j}}\left(\left\langle \frac{F_{D,j}}{m_p}|\mathbf{c}_f,\mathbf{c}_p,\mu_p\right\rangle f_{fp}\right) \\ &+ \frac{\partial}{\partial c_{f,j}}\left(\left\langle \frac{du_{f@p,j}}{dt}|\mathbf{c}_f,\mathbf{c}_p,\mu_p\right\rangle f_{fp}\right) \\ &= \left(\frac{\partial f_{fp}}{\partial t}\right)_{coll} \quad . \end{aligned} \tag{4.23}$$

It is reminded that the term $\frac{du_{f@p,j}}{dt}$ does not express the acceleration of the fluid, but the Lagrangian derivative of the fluid velocity following the particle path.

Some definitions with respect to the relation between the particle velocity PDF f_p and the joint fluid-particle velocity PDF f_{fp} are given. The particle velocity PDF f_p can be obtained from the joint fluid-particle velocity PDF f_{fp} by integration over the fluid velocity vector $\mathbf{c}_f$. It can thus be written

$$f_p\left(\mathbf{x},\mathbf{c}_p,\mu_p;t\right) = \int f_{fp}\left(\mathbf{x},\mathbf{c}_f,\mathbf{c}_p,\mu_p;t\right)d\mathbf{c}_f \quad . \tag{4.24}$$

Moreover a conditional PDF can be defined, $f_{f|p}\left(\mathbf{x},\mathbf{c}_f|\mathbf{c}_p,\mu_p;t\right)$, which verifies

$$f_f\left(\mathbf{x},\mathbf{c}_f|\mathbf{c}_p,\mu_p;t\right) = \frac{f_{fp}\left(\mathbf{x},\mathbf{c}_f,\mathbf{c}_p,\mu_p;t\right)}{f_p\left(\mathbf{x},\mathbf{c}_p,\mu_p;t\right)} \quad . \tag{4.25}$$

And a last important relation with respect to the closure of the collision terms in turbulent two-phase flows is that the fluid velocity at the particle position $\mathbf{u}_{f@p}$ and the particle velocity $\mathbf{v}_p$ at the same position are in general random but correlated variables. Therefore,

it must be written

$$f_{fp}\left(\mathbf{x},\mathbf{c}_f,\mathbf{c}_p;t\right) \neq f_f\left(\mathbf{x},\mathbf{c}_f;t\right) f_p\left(\mathbf{x},\mathbf{c}_p;t\right) \quad . \tag{4.26}$$

Closure of the external force terms in the transport equation of f_{fp}

The derivative with respect to $\mathbf{c}_f$ of $\frac{du_{f@p,j}}{dt}$ can now be written directly with the use of (4.21) as

$$\begin{aligned}\frac{\partial}{\partial c_{f,j}}\left(\left\langle \frac{du_{f@p,j}}{dt} \mid \mathbf{c}_f,\mathbf{c}_p,\mu_p \right\rangle f_{fp}\right) \quad = \\ \frac{\partial}{\partial c_{f,j}}\left[\left(g_j - \frac{1}{\rho_f}\frac{\partial P_f}{\partial x_i} + \frac{\partial}{\partial x_m}\left[\nu_f \frac{\partial U_{f,j}}{\partial x_m}\right]\right) f_{fp}\right] \\ + \frac{\partial}{\partial c_{f,j}}\left[\left(\left[c_{p,m} - c_{f@p,m}\right]\frac{\delta U_{f,j}}{\delta x_m} + G_{fp,jm}\left[c_{f@p,m} - U_{f,m}\right]\right) f_{fp}\right] \\ - \frac{\partial}{\partial c_{f,j}}\left[\frac{\partial}{\partial c_{f,j}}\left(\frac{1}{2} C_{fp} f_{fp}\right)\right] \quad .\end{aligned} \tag{4.27}$$

The terms $G_{fp,jm}$ and C_{fp} are modeled by means of local mean fluid quantities [117].

It shall be noticed that the term $\frac{\partial}{\partial c_{p,j}}\left(\left\langle \frac{dv_{p,j}}{dt} | \mathbf{c}_f,\mathbf{c}_p,\mu_p \right\rangle f_{fp}\right)$ does not differ from the one written for a transport equation for the PDF f_p in the case of gas-particle or gas-droplet flows. As long as the relation for the density ratio, $\frac{\rho_p}{\rho_f} >> 1$, is justified, the Lagrangian derivative of the fluid following the particle path does not contribute to any quantity that depends only on the particle velocity $\mathbf{c}_p$.

4.1.3 Collision operator in PDF transport equations of f_p and f_{fp}

The last two terms in the PDF transport equations of f_p and f_{fp} that need to be closed are the collision operators $\left(\frac{\partial f_p}{\partial t}\right)_{coll}$ and $\left(\frac{\partial f_{fp}}{\partial t}\right)_{coll}$. This represents one of the key elements in modeling turbulent two-phase flows. All fundamental works on the collision operators is done in the frame of the kinetic theory of rarefied gases, as this approach for turbulent two-phase flows is based on this theory as mentioned above. The collision models originating from the theory of rarefied gases can therefore be expected to perform well in diluted dry granular flows, and with some correction accounting for the increased volume fraction of the particles, it is possible to achieve very good performances of these terms even in dense dry granular flows, as it is shown in section 3.4.4. In turbulent two-phase flows some difficulties should be expected, since the inertial particles possess a response time to the fluid forces on the particles. If this response time is large (for highly inertial particles) the collision models from the kinetic theory of rarefied gases might still be justifiable [1]. In case that their response time is smaller or of the order of the integral turbulent time scale, these models

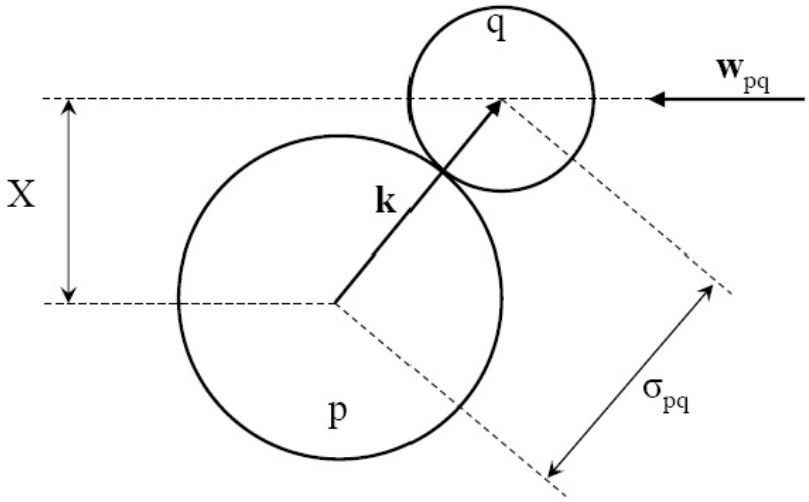

Figure 4.1: Geometry of a binary collision

are not valid anymore. Nevertheless, the models originating from the theory of rarefied gases are still the standard model.

Collision outcomes like coalescence can be considered as another type of collision. Collisions or coalescence has an influence on the different quantities of the dispersed phase.

Collision operator for f_{fp}

In turbulent two-phase flows the properties of the two particles involved in the collision can not always be considered as independent, in contrast to the kinetic theory of rarefied gases and therefore, the probability to find two particles at contact can not be expressed by two single-particle PDFs f_{fp}, but needs to be written as a two-particle pair distribution function $f_{fp}^{(2)}$.

The distance between the centers of the two particles, as it is seen in fig. 4.1, is given as

$$\sigma_{pq} = \frac{d_p + d_q}{2} \quad . \tag{4.28}$$

In order to collide two particles must be distant by the sum of their radii, thus σ_{pq}. In this case the the position of the second particle q is written as

$$\mathbf{x} = \mathbf{x} + \sigma_{pq}\mathbf{k} \quad . \tag{4.29}$$

And eventually the particles need to approach each other in order to collide. This can be written in terms of the scalar product of the particle relative velocity $\mathbf{w}_{pq} = \mathbf{v}_q - \mathbf{v}_p$ and the normalized center connecting vector $\mathbf{k} = \mathbf{x}^{(q)} - \mathbf{x}^{(p)}$. It needs to verify

$$\mathbf{w}_{pq}.\mathbf{k} < 0 \quad . \tag{4.30}$$

The change in the number of particles in $d\mathbf{x}d\mathbf{c}_p d\mathbf{c}_f d\mu_p dt$ is written as

$$\left(\frac{\partial f_{fp}}{\partial t}\right)_{coll} d\mathbf{x}d\mathbf{c}_p d\mathbf{c}_f d\mu_p dt \quad . \tag{4.31}$$

This variation is split into a gain (or "birth") and loss (or "death") term. In order to be consistent throughout this work, the names "birth" and "death" are used, as they are intuitive in the coalescence modeling. Thus, it can be written

$$\left(\frac{\partial f_{fp}}{\partial t}\right)_{coll} d\mathbf{x}d\mathbf{c}_p d\mathbf{c}_f d\mu_p dt = \left[\left(\frac{\partial f_{fp}}{\partial t}\right)^{+}_{coll} - \left(\frac{\partial f_{fp}}{\partial t}\right)^{-}_{coll}\right] d\mathbf{x}d\mathbf{c}_p d\mathbf{c}_f d\mu_p dt \quad . \tag{4.32}$$

The "Birth" and "Death" terms write

$$\begin{aligned}\left(\frac{\partial f_{fp}}{\partial t}\right)^{+}_{coll} &= \frac{1}{2}\int_{\mathbf{w}_{pq}.\mathbf{k}<0} \sigma_{pq}^2 \mathbf{w}_{pq}.\mathbf{k} f_{fp}^{(2)}\left(\mathbf{x}, \mathbf{c}_{f@p}, \mathbf{c}_p, \mu_p, \mathbf{x}+\sigma_{pq}\mathbf{k}, \mathbf{c}_{f@q}, \mathbf{c}_q, \mu_q, t\right) \\ &\quad \times d\mathbf{k} d\mathbf{c}_{f@q} d\mathbf{c}_q d\mu_q \quad , \end{aligned} \tag{4.33}$$

$$\begin{aligned}\left(\frac{\partial f_{fp}}{\partial t}\right)^{-}_{coll} &= \int_{\mathbf{w}_{pq}.\mathbf{k}<0} \sigma_{pq}^2 \mathbf{w}_{pq}.\mathbf{k} f_{fp}^{(2)}\left(\mathbf{x}, \mathbf{c}_{f@p}, \mathbf{c}_p, \mu_p, \mathbf{x}+\sigma_{pq}\mathbf{k}, \mathbf{c}_{f@q}, \mathbf{c}_q, \mu_q, t\right) \\ &\quad \times d\mathbf{k} d\mathbf{c}_{f@q} d\mathbf{c}_q d\mu_q \quad . \end{aligned} \tag{4.34}$$

Collision operator for f_p for rigid particle collisions

Laviéville [73] uses the hard sphere model for the derivation of the collision terms $\left(\frac{\partial f_p}{\partial t}\right)^{-}_{coll}$ and $\left(\frac{\partial f_p}{\partial t}\right)^{+}_{coll}$, for collision of solid particles. The change in the number of particles in $d\mathbf{x}d\mathbf{c}_p dt$ is written as

$$\left(\frac{\partial f_p}{\partial t}\right)_{coll} d\mathbf{x}d\mathbf{c}_p dt \quad . \tag{4.35}$$

This variation is split into a gain (or "birth") and loss (or "death") term. In order to be consistent throughout this work, the names "birth" and "death" are used, as they are

intuitive in the coalescence modeling. Thus, it can be written

$$\left(\frac{\partial f_p}{\partial t}\right)_{coll} d\mathbf{x}d\mathbf{c}_p dt = \left[\left(\frac{\partial f_p}{\partial t}\right)^{+}_{coll} - \left(\frac{\partial f_p}{\partial t}\right)^{-}_{coll}\right] d\mathbf{x}d\mathbf{c}_p dt \quad . \tag{4.36}$$

These "birth" and "death" terms appear, since the collision between two particles is treated applying (3.46). A particle with a velocity $\mathbf{c}_p$ has the velocity $\mathbf{c}_p^{\#}$ after the collision. Thus, a particle with the velocity $\mathbf{c}_p$ is not contained in the volume $d\mathbf{x}_p d\mathbf{c}_p dt$ anymore after collision.

I The "birth" and "death" terms can be written as

$$\left(\frac{\partial f_p}{\partial t}\right)^{-}_{coll} = -\left[\int_{\mathbf{w}_{pq}.\mathbf{k}<0} \sigma_{pq}^2 \mathbf{w}_{pq}.\mathbf{k}\; f_p^{(2)}\left(\mathbf{x}_p, \mathbf{c}_p, \mathbf{x}_p + \sigma_{pq}\mathbf{k}, \mathbf{c}_q, t\right) d\mathbf{c}_q d\mathbf{k}\right] \tag{4.37}$$

$$\left(\frac{\partial f_p}{\partial t}\right)^{+}_{coll} = -\left[\int_{\mathbf{w}_{pq}.\mathbf{k}<0} \sigma_{pq}^2 \mathbf{w}_{pq}.\mathbf{k}\; \frac{f_p^{(2)}\left(\mathbf{x}_p, \mathbf{c}_p^{\#}, \mathbf{x}_p + \sigma_{pq}\mathbf{k}, \mathbf{c}_q^{\#}, t\right)}{e_c^2} d\mathbf{c}_q d\mathbf{k}\right] \quad , \tag{4.38}$$

where the velocities $\mathbf{c}_p^{\#}$ and $\mathbf{c}_q^{\#}$ are given by

$$\mathbf{c}_p^{\#} = \mathbf{c}_p + \frac{m_q}{m_p + m_q}\left(1 + e_c\right)\left(\mathbf{w}_{pq}.\mathbf{k}\right)\mathbf{k} \tag{4.39}$$

$$\mathbf{c}_q^{\#} = \mathbf{c}_q - \frac{m_p}{m_p + m_q}\left(1 + e_c\right)\left(\mathbf{w}_{pq}.\mathbf{k}\right)\mathbf{k} \quad . \tag{4.40}$$

These formulations are used within chapter 3 for the validation of the collision detection algorithm.

It should be mentioned, that the following relation between $\left(\frac{\partial f_p}{\partial t}\right)_{coll}$ and $\left(\frac{\partial f_{fp}}{\partial t}\right)_{coll}$ is valid

$$\left(\frac{\partial f_p}{\partial t}\right)_{coll} = \left(\frac{\partial \int f_{fp} d\mathbf{c}_f}{\partial t}\right)_{coll} = \int \left(\frac{\partial f_{fp}}{\partial t}\right)_{coll} d\mathbf{c}_f \tag{4.41}$$

Closure of pair distribution functions $f_p^{(2)}$ and $f_{fp}^{(2)}$

In the above given formulations for the collision/coalescence operators $\left(\frac{\partial f_p}{\partial t}\right)_{coll}$ and $\left(\frac{\partial f_{fp}}{\partial t}\right)_{coal}$ pair distribution functions $f_p^{(2)}$ and $f_{fp}^{(2)}$ appear. These pair distribution functions are not closed. Two different types of closure model are presented in this section[1]. The first is the "molecular-chaos" assumptions. This closure originates from the kinetic theory of rarefied

[1] $\mathbf{x}_p$ and $\mathbf{x}_q$ are used in this section, in order to distinguish between particles of class p and q. This is in contrast to the notation used so far.

gases and implies that the particle velocities are not correlated before the collision. While this is true in the domain in which the kinetic theory of rarefied gases applies, as well as in dry granular flows, it is not correct in turbulent two-phase flows for small or intermediate droplet Stokes numbers. In turbulent two-phase flows the particle velocities of two impacting particles are correlated by the fluid velocity at the position of the particles. In order to account for this correlation a second closure model is presented that takes into account the correlations in the particle velocities by the fluid turbulence.

Molecular-chaos assumption

The molecular-chaos assumption closure is first regarded for the particle pair distribution function $f_p^{(2)}$, which does not account for the fluid velocity at the particle position. If the velocities of the two impacting particles are not correlated at all, the pair distribution function can be written as the product of two single-particle distribution functions

$$f_p^{(2)}\left(\mathbf{x}_p, \mathbf{c}_p, \mathbf{x}_q, \mathbf{c}_q; t\right) = g_0^{pq}\ f_p\left(\mathbf{x}_p, \mathbf{c}_p; t\right)\ f_q\left(\mathbf{x}_q, \mathbf{c}_q; t\right) \quad , \tag{4.42}$$

where g_0^{pq} is the radial distribution function, which will be explained at the end of this section.

This closure can also be applied if the joint fluid-particle velocity PDF is used. The pair distribution of the joint fluid-particle velocity PDF $f_{fp}^{(2)}$ can be modeled applying the molecular-chaos assumption, if the particle pair distribution function $f_p^{(2)}$ is first obtained by integration over the velocity space

$$f_p^{(2)}(\mathbf{c}_p, \mathbf{x}_p, \mathbf{c}_q, \mathbf{x}_q; t) = \int\int f_{fp}^{(2)}(\mathbf{c}_{f@p}, \mathbf{c}_p, \mathbf{x}_p, \mathbf{c}_{f@q}, \mathbf{c}_q, \mathbf{x}_q; t) d\mathbf{c}_{f@p} d\mathbf{c}_{f@q} \quad . \tag{4.43}$$

Now, (4.42) can be applied again and it is formally possible to apply the molecular-chaos assumption if the joint fluid-particle velocity PDF is used. The closure of the pair distribution function based on the molecular-chaos assumption is still the standard approach in modeling turbulent two-phase flows. Next a closure is introduced that accounts for the correlations of the particle velocities by the fluid turbulence [73].

Closure with particle velocities correlation model

Laviéville proposes a closure of $f_{fp}^{(2)}$ that takes the correlation of the particle velocities by the fluid turbulence into account, also Villedieu and Simonin [130] introduce a coalescence model that accounts for the correlation of droplet velocities induced by the fluid turbulence.

Until the end of this section the dependencies on $\mathbf{x}_p$, $\mathbf{x}_q$ and t are dropped for the sake of clarity. First, $f_{fp}^{(2)}$ is written in an exact manner as

$$\begin{aligned} f_{fp}^{(2)}\left(\mathbf{c}_p, \mathbf{c}_{f@p}, \mathbf{c}_{f@q}, \mathbf{c}_q\right) &= \\ g_0^{pq}\ f_f^{(2)}\left(\mathbf{c}_{f@p}, \mathbf{c}_{f@q}\right)\ f_p\left(\mathbf{c}_p \mid \mathbf{c}_{f@p}, \mathbf{c}_{f@q}\right)\ f_q\left(\mathbf{c}_q \mid \mathbf{c}_p, \mathbf{c}_{f@p}, \mathbf{c}_{f@q}\right) &\quad . \end{aligned} \tag{4.44}$$

The key element of the modeling is the assumption that the particle velocities are principally conditioned by the the fluid velocities $\mathbf{c}_{f@p}$ and $\mathbf{c}_{f@q}$ seen at their position. This assumption gives the following simplification

$$f_p\left(\mathbf{c}_p \mid \mathbf{c}_{f@p}, \mathbf{c}_{f@q}\right) \approx f_p\left(\mathbf{c}_p \mid \mathbf{c}_{f@p}\right) \tag{4.45}$$

$$f_q\left(\mathbf{c}_q \mid \mathbf{c}_p, \mathbf{c}_{f@p}, \mathbf{c}_{f@q}\right) \approx f_q\left(\mathbf{c}_q \mid \mathbf{c}_{f@q}\right) \quad . \tag{4.46}$$

It can then be written

$$\begin{aligned} f_{fp}^{(2)}\left(\mathbf{c}_p, \mathbf{c}_{f@p}, \mathbf{c}_{f@q}, \mathbf{c}_q\right) &= \\ g_0^{pq}\ f_f^{(2)}\left(\mathbf{c}_{f@p}, \mathbf{c}_{f@q}\right)\ f_p\left(\mathbf{c}_p \mid \mathbf{c}_{f@p}\right)\ f_q\left(\mathbf{c}_q \mid \mathbf{c}_{f@q}\right) &\quad , \end{aligned} \tag{4.47}$$

with the relation valid for both particles p and q

$$f_p\left(\mathbf{c}_p \mid \mathbf{c}_{f@p}\right) = \frac{f_{fp}\left(\mathbf{c}_p, \mathbf{c}_{f@p}\right)}{f_f\left(\mathbf{c}_{f@p}\right)} \quad . \tag{4.48}$$

The closure in (4.47) can be simplified in the case in which the two colliding particles are sufficiently small and the centers are sufficiently close to each other, such that $\sigma_{pq} < \eta_K$ is valid. In this case the two particles see the same fluid velocity and (4.47) can then be written as

$$f_{fp}^{(2)}\left(\mathbf{c}_p, \mathbf{c}_{f@p}, \mathbf{c}_{f@q}, \mathbf{c}_q\right) = g_0^{pq}\ \frac{\delta\left(\mathbf{c}_{f@p} - \mathbf{c}_{f@q}\right)}{f_f\left(\mathbf{c}_{f@p}\right)} f_{fp}\left(\mathbf{c}_p, \mathbf{c}_{f@p}\right)\ f_{fq}\left(\mathbf{c}_q, \mathbf{c}_{f@q}\right) \quad . \tag{4.49}$$

The last term not defined in (4.49) is the radial distribution function g_0^{pq}. In chapter 3 models for a mono-disperse particle distribution are given and in section 3.4.4 models are given for the case of a bi-disperse particle distribution. It is a function, that is initially proposed for a dense gas and accounts for the increase in collisions with the particle volume fraction α_p, applying the principles of the kinetic theory of rarefied gases, but in a volume fraction range, where kinetic theory of rarefied gases is not valid anymore without correction. Thus, the radial distribution function g_0^{pq} is introduced to correct the molecular-chaos assumption

in the case of a dense gas as given in (4.42) as

$$f_p^{(2)}\left(\mathbf{x}_p, \mathbf{c}_p, \mathbf{x}_q, \mathbf{c}_q, t\right) = g_0^{pq}\ f_p\left(\mathbf{x}_p, t; \mathbf{c}_p\right)\ f_q\left(\mathbf{x}_q, t; \mathbf{c}_q\right) \quad , \tag{4.50}$$

where the integral over the velocity space (4.50) writes

$$n_p^{(2)}\left(\mathbf{x}_p, \mathbf{x}_q, t\right) = g_0^{pq}\ n_p\left(\mathbf{x}_p, t\right)\ n_q\left(\mathbf{x}_q, t\right) \tag{4.51}$$

and finally g_0^{pq} writes

$$g_0^{pq} = \frac{n_p^{(2)}\left(\mathbf{x}_p, \mathbf{x}_q, t\right)}{n_p\left(\mathbf{x}_p, t\right)\ n_q\left(\mathbf{x}_q, t\right)} \quad . \tag{4.52}$$

With g_0^{pq} all elements of (4.49) are known. However, no information is given about the shape of the PDFs f_p and f_{fp}. Two different possibilities exist to express a these PDFs. First, the real distribution is know and there is no difficulty and second, which is the choice in this work, the shape of the PDF is assumed.

Assumed shape for particle velocity PDF

In the kinetic theory of rarefied gases, the evolution of the system is described by the Boltzmann equation (4.13). It can be shown [21], [46] that the Maxwell distribution is solution of the Boltzmann equation. Thus, the shape of the velocity PDF f_p in a flow that corresponds to the regime of a rarefied gas or in dry granular flows can be assumed as Maxwellian. Chapman and Cowling [21] propose a "one-temperature model" that is centered over the mean velocity $\mathbf{U}_m$ of the particle mixture. Fede [41] compares this "one-temperature model" with a "two-temperature model" proposed by Goldman and Sirovich [50]. Following Gourdel *et al.* [52] and Lathouwers and Bellan [68] a turbulent two-phase flow is rarely at a global equilibrium state, as the turbulence holds particles in a local equilibrium. Fede [41] showed by means of DNS/DPS of a turbulent two-phase flow that the "two-temperature model" predicts the velocity distribution correctly in a system, which is out of the thermal equilibrium, while the "one-temperature model" fails to do so. In this "two temperature model" the velocity distributions are centered over the granular temperature of each class. The model is given by

$$f_p\left(\mathbf{c}_p\right) = \frac{n_p}{\left(2\pi T_p\right)^{\frac{2}{3}}} \exp\left[-\frac{\left(\mathbf{c}_p - \mathbf{U}_p\right)^2}{2T_p}\right] \quad , \tag{4.53}$$

where the particle granular temperature T_p is written as

$$T_p = \frac{1}{3}\left\langle\left(\mathbf{c}_p - \mathbf{U}_p\right)^2\right\rangle \quad . \tag{4.54}$$

Assumed shape for fluid velocity PDF

In homogeneous isotropic flows the velocity distribution of the fluid is usually assumed as a Maxwellian distribution and f_f writes

$$f_{f@p}\left(\mathbf{c}_{f@p}\right) = \frac{1}{\left(\frac{4}{3}\pi q_{f@p}^2\right)^{\frac{2}{3}}} \exp\left[-\frac{\mathbf{c}_f^2}{4q_{f@p}^2}\right] \quad . \tag{4.55}$$

Assumed shape for joint fluid-particle velocity PDF

In the frame of modeling turbulent two-phase flows with the joint fluid-particle velocity PDF f_{fp} a shape for this PDF needs to be assumed either. Laviéville [73] proposes for f_{fp}, in the case of a homogeneous isotropic turbulence, the following form

$$f_{fp}\left(\mathbf{c}_f, \mathbf{c}_p\right) = n_p A_{fp} \exp\left[-B_f \mathbf{c}_f^2 - B_p \mathbf{c}_p^2 + B_{fp} \mathbf{c}_f \mathbf{c}_p\right] \quad , \tag{4.56}$$

where A_{fp}, B_f, B_p and B_{fp} are obtained by respecting the following relations

$$\int\int f_{fp}\left(\mathbf{c}_f, \mathbf{c}_p\right) d\mathbf{c}_f d\mathbf{c}_f = n_p \tag{4.57}$$

$$\int\int c_{p,i} c_{p,j}\ f_{fp}\left(\mathbf{c}_f, \mathbf{c}_p\right) d\mathbf{c}_f d\mathbf{c}_f = n_p \frac{2}{3} q_p^2 \delta_{ij} \tag{4.58}$$

$$\int\int c_{f,i} c_{f,j}\ f_{fp}\left(\mathbf{c}_f, \mathbf{c}_p\right) d\mathbf{c}_f d\mathbf{c}_f = n_p \frac{2}{3} q_{f@p}^2 \delta_{ij} \tag{4.59}$$

$$\int\int c_{f,i} c_{p,j}\ f_{fp}\left(\mathbf{c}_f, \mathbf{c}_p\right) d\mathbf{c}_f d\mathbf{c}_f = n_p \frac{1}{3} q_{fp} \delta_{ij} \quad . \tag{4.60}$$

(4.56) is then written with the following values

$$A_{fp} = \left(\frac{1-\xi_{fp}^2}{\frac{4}{3}\pi q_{f@p}^2\ \frac{4}{3}\pi q_p^2}\right)^{\frac{3}{2}} \tag{4.61}$$

$$B_f = \frac{1}{\left(1-\xi_{fp}^2\right)\left(\frac{4}{3} q_{f@p}^2\right)} \tag{4.62}$$

$$B_p = \frac{1}{\left(1-\xi_{fp}^2\right)\left(\frac{4}{3} q_p^2\right)} \tag{4.63}$$

$$B_{fp} = \frac{\xi_{fp}}{\left(1-\xi_{fp}^2\right)\sqrt{\left(\frac{2}{3} q_p^2\ \frac{2}{3} q_{f@p}^2\right)}} \quad , \tag{4.64}$$

where ξ_{fp} is the fluid-particle velocity correlation coefficient defined in the interval $[0, 1]$ as

$$\xi_{fp} = \frac{q_{fp}}{2\sqrt{q_{f@p}^2 \; q_p^2}} \quad . \tag{4.65}$$

By integration of f_{fp} over the fluid velocity $\mathbf{c}_f$ or particle velocity $\mathbf{c}_p$ the above introduced fluid velocity $f_{f@p}$ and particle velocity f_p PDFs are obtained as

$$f_{f@p}\left(\mathbf{c}_f\right) = \int f_{fp}\left(\mathbf{c}_f, \mathbf{c}_p\right) d\mathbf{c}_p \tag{4.66}$$

$$f_p\left(\mathbf{c}_p\right) = \int f_{fp}\left(\mathbf{c}_f, \mathbf{c}_p\right) d\mathbf{c}_f \quad . \tag{4.67}$$

Laviéville [73] introduces also a shape for the particle pair velocity distribution $f_p^{(2)}$ in homogeneous isotropic turbulence. Pigeonneau [100] extends the work of Laviéville [73] to a poly-dispersed particle mixture. Other closures of the particle pair velocity distribution $f_p^{(2)}$ are given for example by Williams and Crane [135], who propose a Lagrangian method related to the particle trajectory history, or by Derevich [26], who writes a transport equation for $f_p^{(2)}$.

All the above introduced shapes for the various PDFs are given for the case of a homogeneous isotropic turbulence. This is a simplified and idealized case, which is not always applicable. However, all studies performed within this work are in homogeneous isotropic turbulence. Nevertheless, it shall be mentioned that it is possible to expand the above given forms for the homogeneous isotropic case to anisotropic and dense cases. The formalisms which are most common to do so usually follow the works of Grad [53] and Jenkins and Richman [62]. The reader may refer to these works or to Laviéville [73], Sakiz [111] or Fede [41], who gives a more exhaustive overview, for more details.

4.2 Direct resolution of Boltzmann-type equation - Stochastic Lagrangian approach

Based on the kinetic theory of rarefied gases Monte-Carlo algorithms have been developed in order to solve the PDF transport equation directly. Several authors ([43], [60]) proposed modified algorithms in order to account for particle-particle collisions in gas-solid turbulent flows. In the so-called Direct Simulation Monte-Carlo (DSMC), the particles N_p in a computation cell are summarized and represented by a given number of numerical particles N_{num}. Based on (4.23), (3.18) and (3.19) are then solved for each of these numerical par-

ticles in two steps. First, in the so-called free-flow phase, the trajectories of the particles are solved without accounting for collisions of droplets. Second, collisions are accounted for. The joint fluid-particle velocity PDF f_{fp} is approximated in this approach as a sum of Dirac functions, which can be written per computation cell as

$$f_{fp}\left(\mathbf{c}_f, \mathbf{c}_p, \mu_p, \mathbf{x}; t\right) \approx \sum_{\alpha=1}^{N_{num}} \omega_\alpha \delta\left(\mathbf{x} - \mathbf{x}_{p,\alpha}\right) \delta\left(\mathbf{c}_p - \mathbf{v}_{p,\alpha}\right) \left(\mathbf{c}_f - \mathbf{u}_{f,\alpha}\right) \delta\left(\mu_p - \mathbf{m}_{p,\alpha}\right) \quad , \quad (4.68)$$

with ω_α the particle density in the computation cell.

Two aspects in the stochastic Lagrangian approach need to be modeled: first, the fluid velocity at the particle position, and second, the collision handling. The modeling of these two issues is given in section 4.2.1 and 4.2.2.

4.2.1 Stochastic simulation of fluid velocity

If the Lagrangian stochastic simulations of the dispersed phase are coupled with RANS simulations only the mean fluid velocity in each computation cell is known. However, in order to calculate the drag force of the particles the instantaneous fluid velocity at the particle position is needed. As detailed in section 4.1.1, a variety of approaches exist to do so. In this work, again the Langevin-type equation of Simonin [117] is used in the following form

$$\begin{aligned} u_{f@p,i}\left(t + \delta t\right) - u_{f@p,i}\left(t\right) &= \left[v_{p,j} - u_{f@p,j}\right] \frac{\delta U_{f,i}}{\delta x_j} \delta t \\ &+ G_{fp,ij}\left[u_{f@p,j} - U_{f,j}\right] \delta t + C_{fp} \delta W_{fp,i} \quad . \end{aligned} \quad (4.69)$$

With the definitions in (4.22) the final form of the Langevin equation used in the simulations to model the fluid velocity at the particle position is written as

$$u'_{f@p,i}\left(t + \Delta t\right) = u'_{f@p,i}\left(t\right) \left(1 - \frac{\Delta t}{\tau^t_{f@p}}\right) + \sqrt{\Delta t} \sqrt{\frac{4}{3} \frac{q^2_{f@p}}{\tau^t_{f@p}}}\, \widehat{x} \quad , \quad (4.70)$$

where $\widehat{x}$ is a Gaussian random number.

4.2.2 Stochastic collision handling

Basically two different types of stochastic collision algorithms exist, the single-particle method and the multiple-particle method.

In the single-particle method (see for example [12], [93], [120]), the collision probability

with another particle, based on the collision frequency originating from the theory of rarefied gases, is determined for each particle. Practically, a uniformly distributed random number is created and compared to the collision probability. If the created number is smaller than the collision probability the collision takes places, otherwise it is rejected. This procedure is the so-called rejection method. The collision probability p_{pq} writes as

$$p_{pq} = f_{pq}^{\kappa} \cdot \Delta t \quad . \tag{4.71}$$

In the multiple particle approach all particles are grouped in pairs. The algorithm used here is part of this class and is developed by Hylkema and Villedieu [60]. Within the multiple particle approach, two sub-types of algorithms can be distinguished, algorithms of the type of Bird [15] and of type Babovsky [7]. In the former, a master equation is solved applying the discretization of the time step. An algorithm of this kind is used for example by Fede [41] and Fede *et al.* [43]. The algorithm used in this work is of the second type, which resolves the PDF transport equation directly and was initially proposed by Nanbu [92] and picked up by Babovsky [7]. The algorithm is structured as follows.

Step 1 All particles are grouped in $\frac{(N_{num})}{2}$ random pairs (in the case that the particle number is odd, $\frac{(N_{num}-1)}{2}$ random particle pairs are built).

Step 2 The collision probability for each pair is calculated with (4.71).

Step 3 A rejection method is used: this means that a random number is created and if it is smaller than the collision probability the collision is handled.

For the creation of both the random particle pairs and the random number used to determine whether a collision takes place or not, a "Substract-and-borrow" random number generator is applied in the algorithm used in this work[2].

Berlemont *et al.* [14] showed that not accounting for the correlations induced by the fluid turbulence on the particle velocities destroys particle kinetic energy, although the particle collisions are elastic. They showed that a standard Monte-Carlo algorithm, which does not account for this correlation leads to the destruction of fluid-particle covariance q_{fp}, which induces a decrease in the particle agitation q_p^2. In order to take into consideration the correlation of the particle velocities by the fluid turbulence, Berlemont *et al.* [12] and Sommerfeld [122] [123] propose algorithms following the single-particle approach. The algorithm of Fede *et al.* [43] also accounts for the correlations in the particle velocities

[2]The generator used was initially proposed by Marsaglia and Zaman [85] and later improved by Lüscher [75], and used here in the form implemented by James [61].

induced by the fluid turbulence. The algorithm used in this work is based on the Babovsky-type algorithm of Hylkema and Villedieu [60], where step one is modified in order to account for the correlations in the particle velocities. The particles are sorted by their fluid velocity and subdivided into several sections, such that particles "seeing" a similar fluid velocity are in the same section. The Babovsky-type algorithm is then applied to each of these sections, ensuring that the only colliding particles are those that see a similar fluid velocity, which represents the correlation effect of the particle velocities by the fluid turbulence.

4.3 Moment methods for PDF approach

The second possibility is to resolve a PDF transport equation for a given number of moments of the distribution. The moments of a distribution f_p or f_{fp} are the mean values of a quantity $\boldsymbol{\psi}$. Thus the derived moment equations contain moments of the distribution function instead of the distribution function. In the following the moments $\langle \boldsymbol{\psi} \rangle$ are given for a distribution f_{fp}, but can also be obtained for a distribution f_p by the relation in (4.24). The dependencies of the variables on $\mathbf{x}, t$ are dropped for the sake of readability.

The mean value of a quantity $\boldsymbol{\psi}(\mathbf{c}_f, \mathbf{c}_p, \mu_p)$ can be obtained by integration over the phase space as

$$\langle \boldsymbol{\psi} \rangle = \frac{1}{n_p} \int \boldsymbol{\psi}(\mathbf{c}_f, \mathbf{c}_p, \mu_p) \; f_{fp}(\mathbf{c}_f, \mathbf{c}_p, \mu_p) \, d\mathbf{c}_f d\mathbf{c}_p d\mu_p \quad , \tag{4.72}$$

where n_p is the 0-order moment of f_{fp}

$$n_p = \int f_{fp}(\mathbf{c}_f, \mathbf{c}_p, \mu_p) \, d\mathbf{c}_f d\mathbf{c}_p d\mu_p \quad . \tag{4.73}$$

In two-phase flows it is often convenient to introduce mass-weighted moments of the dispersed phase [117]. It is written

$$\langle \boldsymbol{\psi} \rangle = \frac{1}{n_p m_p} \int \mu_p \; \boldsymbol{\psi}(\mathbf{c}_f, \mathbf{c}_p, \mu_p) \; f_{fp}(\mathbf{c}_f, \mathbf{c}_p, \mu_p) \, d\mathbf{c}_f d\mathbf{c}_p d\mu_p \quad , \tag{4.74}$$

where $n_p m_p$ is defined as

$$n_p m_p = \int \mu_p \; f_{fp}(\mathbf{c}_f, \mathbf{c}_p, \mu_p) \, d\mathbf{c}_f d\mathbf{c}_p d\mu_p \quad . \tag{4.75}$$

4.3.1 Transport equation for moments of f_{fp}

By integration of the PDF transport equations (here the transport equation for f_{fp}) multiplied with the quantity $\boldsymbol{\psi}$ a moment transport equation for $\boldsymbol{\psi}$ is obtained. The transport equations for first-order moments follow from splitting the instantaneous values of all variables into a mean and fluctuating part and a consequent averaging. This way moments of a higher order $(n+1)$ are introduced. These higher moments need to be closed. Principally, three different possibilities exist to handle these unclosed higher moments. First, they can be neglected if it seems appropriate. Second, a direct modeling is possible, where these terms are set into relation with known mean values (first-order moments). Third, it is possible to write a transport equation the higher unclosed moments. For higher-order moment closure the reader may refer to Simonin [117] or Boëlle [16].

A general equation for the change of a quantity $\boldsymbol{\psi}\left(\mathbf{c}_f, \mathbf{c}_p, \mu_p\right)$ can by derived from the PDF transport equation by integration over the phase space. This equation writes following Enskog

$$
\begin{aligned}
n_p m_p \frac{\partial}{\partial t}\left\langle \boldsymbol{\psi} \right\rangle + n_p m_p \frac{\partial}{\partial x_i}\left\langle c_{p,i} \boldsymbol{\psi} \right\rangle \;=\; & \\
& + \; n_p m_p \left\langle \frac{dv_{p,i}}{dt} \frac{\partial \boldsymbol{\psi}}{\partial c_{p,i}} \right\rangle \\
& + \; n_p m_p \left\langle \frac{du_{f@p,i}}{dt} \frac{\partial \boldsymbol{\psi}}{\partial c_{f,i}} \right\rangle \\
& + \; n_p m_p \left\langle \frac{dm_p}{dt} \left[\frac{\partial \boldsymbol{\psi}}{\partial m_p} + \frac{\boldsymbol{\psi}}{m_p} \right] \right\rangle \\
& + \; \mathcal{C}\left(m_p \boldsymbol{\psi}\right) \quad . \qquad (4.76)
\end{aligned}
$$

To obtain the conservation equation for a specific moment, $\boldsymbol{\psi}$ in (4.76) needs to be replaced by the quantity of interest.

4.3.2 Modeling of moment balance equations of f_{fp}

The moment balance equations which are of interest in this work are given next. The momentum balance equation is also given, even if in homogeneous isotropic turbulence any derivative of the mean velocity equals 0. The particle velocity can be written as $v_{p,i} = V_{p,i} + v'_{p,i}$ and the fluid velocity as $u_{f@p,i} = U_{f@p,i} + u'_{f@p,i}$.

Droplet number balance equation $\left(\boldsymbol{\psi} = \frac{1}{m_p}\right)$

The particle number balance equation is obtained for $\left(\boldsymbol{\psi} = \frac{1}{m_p}\right)$ as

$$\frac{\partial}{\partial t} n_p + \frac{\partial}{\partial x_i} n_p V_{p,i} = -\frac{\partial}{\partial x_i} n_p \overline{m}_p \left\langle \frac{v'_{p,i}}{m_p} \right\rangle + \mathcal{C}\left(1\right) \quad , \tag{4.77}$$

where the first term on the right-hand side represents the change due to turbulent mixing of particles with different diameter, and the second term stands for the change of the droplet number by collision or droplet coalescence/break-up. In order to distinguish the mass of one particle m_p from the mean particle mass $\overline{m}_p$ a bar is introduced over the mean particle mass.

Mass balance equation $(\boldsymbol{\psi} = 1)$

The mass balance equation is obtained for $(\boldsymbol{\psi} = 1)$ as

$$\frac{\partial}{\partial t} n_p \overline{m}_p + \frac{\partial}{\partial x_i} n_p \overline{m}_p V_{p,i} = \mathcal{C}\left(m_p\right) \quad , \tag{4.78}$$

where the right-hand side term accounts for the exchange of mass between particles due to particle break-up or coalescence. If evaporation were considered, it would also be taken into account in this equation. In the case of particle collision the particle mass is conserved and $\mathcal{C}\left(m_p\right) = 0$.

Momentum balance equation $(\boldsymbol{\psi} = v_{p,i})$

The momentum balance equation is obtained for $(\boldsymbol{\psi} = v_{p,i})$ as

$$\begin{aligned} n_p \overline{m}_p \frac{\partial}{\partial t} V_{p,i} + n_p \overline{m}_p V_{p,j} \frac{\partial}{\partial x_j} V_{p,i} = & - \frac{\partial}{\partial x_j} n_p \overline{m}_p \left\langle v'_{p,j} v'_{p,i} \right\rangle \\ & + n_p \overline{m}_p \left\langle \frac{F_{r,i}}{m_p} \right\rangle + \mathcal{C}\left(m_p v'_{p,i}\right) \quad , \end{aligned} \tag{4.79}$$

where the first term on the right-hand side represents the transport of momentum by particle velocity fluctuations. The second term accounts for the mean interphase momentum transfer between the fluid and dispersed phase. It is usually expressed in gas-solid or gas-liquid two-phase flows as the drag force. The second term can be written as

$$n_p \overline{m}_p \left\langle \frac{F_{r,i}}{m_p} \right\rangle = -n_p \overline{m}_p \frac{1}{\tau^F_{fp}} V_{r,i} \quad , \tag{4.80}$$

with $V_{r,i} = (V_{p,i} - U_{f@p,i}) - V_{d,i}$, where $V_{d,i}$ represents the drift velocity.

Droplet kinetic stress balance equation $\left(\boldsymbol{\psi} = v'_{p,i}v'_{p,j}\right)$

The particle kinetic stress balance equation is obtained for $\left(\boldsymbol{\psi} = v'_{p,i}v'_{p,j}\right)$ as

$$\begin{aligned} n_p\overline{m}_p\left[\frac{\partial}{\partial t} + V_{p,m}\frac{\partial}{\partial x_j}\right]\left\langle v'_{p,i}v'_{p,j}\right\rangle = & - \frac{\partial}{\partial x_m}n_p\overline{m}_p\left\langle v'_{p,i}v'_{p,j}v'_{p,m}\right\rangle \\ & - n_p\overline{m}_p\left[\left\langle v'_{p,i}v'_{p,m}\right\rangle\frac{\partial V_{p,j}}{\partial x_m} + \left\langle v'_{p,j}v'_{p,m}\right\rangle\frac{\partial V_{p,j}}{\partial x_m}\right] \\ & + n_p\overline{m}_p\left[\left\langle\frac{F_{r,i}}{m_p}v'_{p,j}\right\rangle + \left\langle\frac{F_{r,j}}{m_p}v'_{p,i}\right\rangle\right] \\ & + \mathcal{C}\left(m_p v'_{p,i}v'_{p,j}\right) \quad . \end{aligned} \tag{4.81}$$

The first term on the right-hand side of (4.81) represents the transport of particle kinetic stress by the particle velocity fluctuations. It may be modeled using a Boussinesq approximation derived from third-order moment transport equations [116]. The second term represents production of particle kinetic stress by the particle mean velocity gradient. The third term results from the interaction of the dispersed phase with fluid turbulence. It can be written as

$$n_p\overline{m}_p\left[\left\langle\frac{F_{r,i}}{m_p}v'_{p,j}\right\rangle + \left\langle\frac{F_{r,j}}{m_p}v'_{p,i}\right\rangle\right] \approx -n_p\overline{m}_p\frac{2}{\tau^F_{fp}}\left[\left\langle v'_{p,i}v'_{p,j}\right\rangle - R_{fp,ij}\right] \quad , \tag{4.82}$$

where the fluid-particle velocity covariance vector $R_{fp,ij}$ is written

$$R_{fp,ij} = \frac{1}{2}\left[\left\langle u'_{f@p,i}v'_{p,j}\right\rangle + \left\langle v'_{p,i}u'_{f@p,j}\right\rangle\right] \quad . \tag{4.83}$$

The last term on the right-hand side of (4.81) accounts for the influence of collisions on the particle kinetic stress.

Fluid-particle covariance balance equation $\left(\boldsymbol{\psi} = u'_{f@p,i}v'_{p,j}\right)$

The fluid-particle covariance balance equation is obtained for $\left(\boldsymbol{\psi} = u'_{f@p,i}v'_{p,j}\right)$ as

$$\begin{aligned} n_p\overline{m}_p\left[\frac{\partial}{\partial t} + V_{p,m}\frac{\partial}{\partial x_j}\right]\left\langle u'_{f@p,i}v'_{p,j}\right\rangle = & \\ & -\frac{\partial}{\partial x_m}n_p\overline{m}_p\left\langle u'_{f@p,i}v'_{p,j}v'_{p,m}\right\rangle \end{aligned}$$

$$
\begin{aligned}
&-n_p\overline{m}_p\left[\left\langle u'_{f@p,i}v'_{p,m}\right\rangle\frac{\partial V_{p,j}}{\partial x_m}+\left\langle v'_{p,j}u'_{f@p,m}\right\rangle\frac{\partial U_{f@p,j}}{\partial x_m}\right]\\
&-n_p\overline{m}_p\frac{1}{\tau_{fp}^F}\left[\left\langle u'_{f@p,i}v'_{p,j}\right\rangle-\left\langle u'_{f@p,i}u'_{f@p,j}\right\rangle\right]\\
&+n_p\overline{m}_pG_{fp,im}\left\langle u'_{f@p,m}v'_{p,j}\right\rangle\\
&+\mathcal{C}\left(m_pu'_{f@p,i}v'_{p,j}\right)\quad .
\end{aligned}
\tag{4.84}
$$

The first term on the right-hand side of (4.84) represents the transport of fluid-particle velocity covariance by the particle velocity fluctuations. The second term on the right-hand side gives the production of covariance by the particle and fluid mean velocity gradients. The third term results from the interaction of the dispersed phase with fluid turbulence. The fourth term accounts for the destruction of covariance due to pressure-strain correlations, viscous dissipation and the crossing trajectory effect. The last term gives the influence of collisions on the the fluid-particle covariance.

4.3.3 Collision source terms $\mathcal{C}\left(m_p\boldsymbol{\psi}\right)$

In section 4.3.2, in the mass-weighted moment balance equations collisional source terms $\mathcal{C}\left(m_p\boldsymbol{\psi}\right)$ appear. These collisional source terms are given in this section for the first-order mass moments $m_p^k\psi$ with $k=1$ for both the case of particle collisions and droplet coalescence. In section 4.4 the moments method for coalescence is described, where higher-order mass moments $m_p^k\psi$ with $k>1$ are needed. The corresponding collisional source terms are given in section 4.4.

The collisional mass-weighted source terms $\mathcal{C}\left(m_p\boldsymbol{\psi}\right)$ can be written as

$$
\mathcal{C}\left(m_p\boldsymbol{\psi}\right)=\int\mu_p\boldsymbol{\psi}\left(\mathbf{c}_f,\mathbf{c}_p,\mu_p\right)\left(\frac{\partial f_{fp}}{\partial t}\right)_{coll}d\mathbf{c}_fd\mathbf{c}_pd\mu_p\quad . \tag{4.85}
$$

The expression in (4.85) can be written respecting the form of the collision operator $\left(\frac{\partial f_{fp}}{\partial t}\right)_{coll}$ given in (4.32) as

$$
\mathcal{C}\left(m_p\boldsymbol{\psi}\right)=\mathcal{B}\left(m_p^{\#}\boldsymbol{\psi}\right)-\mathcal{D}\left(m_p\boldsymbol{\psi}\right)\quad , \tag{4.86}
$$

where $\mathcal{B}\left(m_p\boldsymbol{\psi}^{\#}\right)$ and $\mathcal{D}\left(m_p\boldsymbol{\psi}\right)$ are

$$
\begin{aligned}
\mathcal{D}\left(m_p\boldsymbol{\psi}\right)=\quad&-\frac{1}{2}\int_{\mathbf{w}_{pq}.\mathbf{k}<0}\sigma_{pq}^2\ \mathbf{w}_{pq}.\mathbf{k}\ \mu_p\left[\boldsymbol{\psi}\left(\mathbf{c}_{f@p},\mathbf{c}_p,\mu_p\right)+\boldsymbol{\psi}\left(\mathbf{c}_{f@q},\mathbf{c}_q,\mu_q\right)\right]\\
&\times f_{fp}^{(2)}\left(\mathbf{x}_p,\mathbf{c}_{f@p},\mathbf{c}_p,\mu_p,\mathbf{x}_p+\sigma_{pq}\mathbf{k},\mathbf{c}_{f@q},\mathbf{c}_q,\mu_q,t\right)
\end{aligned}
$$

$$\times d\mathbf{k} d\mathbf{c}_{f@p} d\mathbf{c}_p d\mu_p d\mathbf{c}_{f@q} d\mathbf{c}_q d\mu_q \tag{4.87}$$

$$\begin{aligned}\mathcal{B}\left(m_p\boldsymbol{\psi}^{\#}\right) = \quad & -\frac{1}{2}\int_{\mathbf{w}_{pq}.\mathbf{k}<0} \sigma_{pq}^2\ \mathbf{w}_{pq}.\mathbf{k}\ \mu_p \left[\boldsymbol{\psi}^{\#}\left(\mathbf{c}_{f@p}, \mathbf{c}_p^{\#}, \mu_p^{\#}\right) + \boldsymbol{\psi}^{\#}\left(\mathbf{c}_{f@q}, \mathbf{c}_q^{\#}, \mu_q^{\#}\right)\right] \\ & \times f_{fp}^{(2)}\left(\mathbf{x}_p, \mathbf{c}_{f@p}, \mathbf{c}_p, \mu_p, \mathbf{x}_p + \sigma_{pq}\mathbf{k}, \mathbf{c}_{f@q}, \mathbf{c}_q, \mu_q, t\right) \\ & \times d\mathbf{k} d\mathbf{c}_{f@p} d\mathbf{c}_p d\mu_p d\mathbf{c}_{f@q} d\mathbf{c}_q d\mu_q \quad . \end{aligned} \tag{4.88}$$

In the case of coalescence the birth term writes with $\boldsymbol{\psi}^*$ the property after collision as

$$\begin{aligned}\mathcal{B}\left(m_p\boldsymbol{\psi}^{*}\right) = \quad & -\frac{1}{2}\int_{\mathbf{w}_{pq}.\mathbf{k}<0} \sigma_{pq}^2\ \mathbf{w}_{pq}.\mathbf{k}\ \mu_p \left[\boldsymbol{\psi}^{*}\left(\mathbf{c}_{f@p}^*, \mathbf{c}_p^{*}, \mu_p^{*}\right)\right] \\ & \times f_{fp}^{(2)}\left(\mathbf{x}_p, \mathbf{c}_{f@p}, \mathbf{c}_p, \mu_p, \mathbf{x}_p + \sigma_{pq}\mathbf{k}, \mathbf{c}_{f@q}, \mathbf{c}_q, \mu_q, t\right) \\ & \times d\mathbf{k} d\mathbf{c}_{f@p} d\mathbf{c}_p d\mu_p d\mathbf{c}_{f@q} d\mathbf{c}_q d\mu_q \quad . \end{aligned} \tag{4.89}$$

This can be written as

$$\begin{aligned}\mathcal{C}\left(m_p\boldsymbol{\psi}\right) = \quad & \frac{1}{2}\int_{\mathbf{w}_{pq}.\mathbf{k}<0} \sigma_{pq}^2\ \mathbf{w}_{pq}.\mathbf{k}\ m_p\left[\Delta\boldsymbol{\psi}\right] \\ & \times f_{fp}^{(2)}\left(\mathbf{x}_p, \mathbf{c}_{f@p}, \mathbf{c}_p, \mu_p, \mathbf{x}_p + \sigma_{pq}\mathbf{k}, \mathbf{c}_{f@q}, \mathbf{c}_q, \mu_q, t\right) \\ & \times d\mathbf{k} d\mathbf{c}_{f@p} d\mathbf{c}_p d\mu_p d\mathbf{c}_{f@q} d\mathbf{c}_q d\mu_q \quad , \end{aligned} \tag{4.90}$$

where $[\Delta\boldsymbol{\psi}]$ is written as the quantity after the collision minus the quantity before the collision

$$\begin{aligned}\left[\Delta\boldsymbol{\psi}\right] \quad &= \quad \boldsymbol{\psi}^{\#}\left(\mathbf{c}_{f@p}, \mathbf{c}_p^{\#}, \mu_p^{\#}\right) + \boldsymbol{\psi}^{\#}\left(\mathbf{c}_{f@q}, \mathbf{c}_q^{\#}, \mu_q^{\#}\right) \\ &- \quad \boldsymbol{\psi}\left(\mathbf{c}_{f@p}, \mathbf{c}_p, \mu_p\right) - \boldsymbol{\psi}\left(\mathbf{c}_{f@q}, \mathbf{c}_q, \mu_q\right) \ . \end{aligned} \tag{4.91}$$

The respective collisional source terms for the moment balance equations are given next.

Collision source term in particle number balance equation $\mathcal{C}(1)$

The collisional source term $\mathcal{C}(1)$ is given for both the case of particle-particle collision and droplet coalescence.

Particle-particle collision

The change $[\Delta\boldsymbol{\psi}]$ in the case of particle-particle collisions is written as

$$\begin{aligned} \boldsymbol{\psi}^{\#}\left(\mathbf{c}_{f@p}, \mathbf{c}_p^{\#}, \mu_p^{\#}\right) &= 1 \qquad & \boldsymbol{\psi}\left(\mathbf{c}_{f@p}, \mathbf{c}_p, \mu_p\right) &= 1 \\ \boldsymbol{\psi}^{\#}\left(\mathbf{c}_{f@q}, \mathbf{c}_q^{\#}, \mu_q^{\#}\right) &= 1 \qquad & \boldsymbol{\psi}\left(\mathbf{c}_{f@q}, \mathbf{c}_q, \mu_q\right) &= 1 \quad . \end{aligned} \tag{4.92}$$

If the collision source term $\mathcal{C}(1)$ is expressed as the sum of a "birth" and "death" source term it can be written

$$\mathcal{C}(1) = \mathcal{B}(1) - \mathcal{D}(1) = 0 \quad . \tag{4.93}$$

The terms $\mathcal{B}(1)$ and $\mathcal{D}(1)$ are equal and express the mean collision frequency f_{pq}^{κ} here (see (3.54)).

Droplet coalescence

The change $[\Delta\boldsymbol{\psi}]$ in the case of droplet coalescence is written as

$$\begin{aligned} \boldsymbol{\psi}^{*}\left(\mathbf{c}_{f@p}, \mathbf{c}_p^{*}, \mu_p^{*}\right) &= 1 \qquad & \boldsymbol{\psi}\left(\mathbf{c}_{f@p}, \mathbf{c}_p, \mu_p\right) &= 1 \\ & & \boldsymbol{\psi}\left(\mathbf{c}_{f@q}, \mathbf{c}_q, \mu_q\right) &= 1 \quad . \end{aligned} \tag{4.94}$$

If the coalescence source term $\mathcal{C}(1)$ is expressed as the sum of a "birth" and "death" source term it can be written

$$2\mathcal{B}(1) = \mathcal{D}(1) \quad . \tag{4.95}$$

The term $\mathcal{D}(1)$ expresses the mean collision frequency f_{pq}^{κ} here (see (3.54)). To conclude particle-particle collisions are particle number conservative, whereas droplet coalescence is not particle number conservative.

Collision source term in mass balance equation $\mathcal{C}(m_p)$

The collisional source term $\mathcal{C}(m_p)$ is given for both the case of particle-particle collision and droplet coalescence.

Particle-particle collision

The change $[\Delta\boldsymbol{\psi}]$ in the case of particle-particle collisions is written as

$$\begin{aligned} \boldsymbol{\psi}^{\#}\left(\mathbf{c}_{f@p}, \mathbf{c}_p^{\#}, \mu_p^{\#}\right) &= m_p^{\#} = m_p \qquad & \boldsymbol{\psi}\left(\mathbf{c}_{f@p}, \mathbf{c}_p, \mu_p\right) &= m_p \\ \boldsymbol{\psi}^{\#}\left(\mathbf{c}_{f@q}, \mathbf{c}_q^{\#}, \mu_q^{\#}\right) &= m_q^{\#} = m_q \qquad & \boldsymbol{\psi}\left(\mathbf{c}_{f@q}, \mathbf{c}_q, \mu_q\right) &= m_q \quad . \end{aligned} \tag{4.96}$$

The terms $\mathcal{B}(m_p)$ and $\mathcal{D}(m_p)$ are equal as there is no mass exchange at the moment of collisions. Thus, collisions do not change the mass distribution as $m_p^{\#} = m_p$ and $m_q^{\#} = m_q$ are valid. The collision source terms writes

$$\mathcal{C}(m_p) = \mathcal{B}\left(m_p^{\#}\right) - \mathcal{D}(m_p) = 0 \quad . \tag{4.97}$$

Droplet coalescence

As it is easily understandable from the physics of droplet coalescence, permanent coalescence changes the mass distribution, although the total mass is conserved

$$\begin{aligned} \boldsymbol{\psi}^*\left(\mathbf{c}_{f@p}, \mathbf{c}_p^*, \mu_p^*\right) = m^* = m_p + m_q \qquad & \boldsymbol{\psi}\left(\mathbf{c}_{f@p}, \mathbf{c}_p, \mu_p\right) = m_p \\ & \boldsymbol{\psi}\left(\mathbf{c}_{f@q}, \mathbf{c}_q, \mu_q\right) = m_q \quad . \end{aligned} \tag{4.98}$$

The collisional source term $\mathcal{C}(m_p)$ can be written

$$\mathcal{C}(m_p) = \mathcal{B}(m^*) - \mathcal{D}(m_p) = 0 \quad . \tag{4.99}$$

Collision source term in momentum balance equation $\mathcal{C}(m_p v_{p,i})$

The collisional source term $\mathcal{C}(m_p v_{p,i})$ is given for both the case of particle-particle collision and droplet coalescence.

Particle-particle collision

The change $[\Delta\boldsymbol{\psi}]$ in the case of particle-particle collisions is written as

$$\begin{aligned} \boldsymbol{\psi}^{\#}\left(\mathbf{c}_{f@p}, \mathbf{c}_p^{\#}, \mu_p^{\#}\right) = m_p v_{p,i}^{\#} \qquad & \boldsymbol{\psi}\left(\mathbf{c}_{f@p}, \mathbf{c}_p, \mu_p\right) = m_p v_{p,i} \\ \boldsymbol{\psi}^{\#}\left(\mathbf{c}_{f@q}, \mathbf{c}_q^{\#}, \mu_q^{\#}\right) = m_q v_{q,i}^{\#} \qquad & \boldsymbol{\psi}\left(\mathbf{c}_{f@q}, \mathbf{c}_q, \mu_q\right) = m_q v_{q,i} \quad . \end{aligned} \tag{4.100}$$

The expression $[\Delta(\boldsymbol{\psi} = m_p v_{p,i})]$ is written

$$[\Delta(\boldsymbol{\psi} = m_p v_{p,i})] = m_p\left(\mathbf{v}_{p,i}^{\#} - \mathbf{v}_{p,i}\right) + m_q\left(\mathbf{v}_{q,i}^{\#} - \mathbf{v}_{q,i}\right) \quad , \tag{4.101}$$

with some transformations and relations in (4.39) and (4.40) the collisional source terms is

$$\mathcal{C}(m_p v_{p,i}) = \mathcal{B}\left(m_p v_{p,i}^{\#}\right) - \mathcal{D}(m_p v_{p,i}) = 0 \quad . \tag{4.102}$$

Droplet coalescence

The change $[\Delta\boldsymbol{\psi}]$ in the case of droplet coalescence is written as

$$\begin{aligned} \boldsymbol{\psi}^* \left(\mathbf{c}_{f@p}, \mathbf{c}_p^*, \mu_p^*\right) &= m^* v_{p,i}^* & \boldsymbol{\psi} \left(\mathbf{c}_{f@p}, \mathbf{c}_p, \mu_p\right) &= m_p v_{p,i} \\ & & \boldsymbol{\psi} \left(\mathbf{c}_{f@q}, \mathbf{c}_q, \mu_q\right) &= m_q v_{q,i} \quad , \end{aligned} \tag{4.103}$$

where

$$m^* = m_p + m_q \tag{4.104}$$

$$m^* v_{p,i}^* = m_q v_{p,i} + m_q v_{q,i} \quad . \tag{4.105}$$

The collisional source term $\mathcal{C}\left(m_p v_{p,i}\right)$ can be written

$$\mathcal{C}\left(m_p v_{p,i}\right) = \mathcal{B}\left(m^* v_{p,i}^*\right) - \mathcal{D}\left(m_p v_{p,i}\right) = 0 \quad . \tag{4.106}$$

Collision source term in particle kinetic stress balance equation $\mathcal{C}\left(m_p v'_{p,i} v'_{p,j}\right)$

The collisional source term $\mathcal{C}\left(m_p v'_{p,i} v'_{p,j}\right)$ is given for both the case of particle-particle collision and droplet coalescence.

Particle-particle collision

The change $[\Delta\boldsymbol{\psi}]$ in the case of particle-particle collisions is written as

$$\begin{aligned} \boldsymbol{\psi}^{\#} \left(\mathbf{c}_{f@p}, \mathbf{c}_p^{\#}, \mu_p^{\#}\right) &= m_p v_{p,i}^{\#'} v_{p,j}^{\#'} & \boldsymbol{\psi} \left(\mathbf{c}_{f@p}, \mathbf{c}_p, \mu_p\right) &= m_p v'_{p,i} v'_{p,i} \\ \boldsymbol{\psi}^{\#} \left(\mathbf{c}_{f@q}, \mathbf{c}_q^{\#}, \mu_q^{\#}\right) &= m_q v_{q,i}^{\#'} v_{q,j}^{\#'} & \boldsymbol{\psi} \left(\mathbf{c}_{f@q}, \mathbf{c}_q, \mu_q\right) &= m_q v'_{q,i} v'_{q,i} \end{aligned} \tag{4.107}$$

The expression $\left[\Delta\left(\boldsymbol{\psi} = m_p v'_{p,i} v'_{p,j}\right)\right]$ is written

$$\begin{aligned} \left[\Delta\left(\boldsymbol{\psi} = m_p v'_{p,i} v'_{p,j}\right)\right] &= \frac{m_p m_q}{m_+ m_p} \left(1 + e_c\right) \left(\mathbf{w}_{pk}.\mathbf{k}\right) \\ & \quad \times \left[\left(1 + e_c\right) \left(\mathbf{w}_{pk}.\mathbf{k}\right) k_i k_j - \left(w_{pq,i} k_j + w_{pq,j} k_i\right)\right] \quad . \end{aligned} \tag{4.108}$$

Droplet coalescence

The change $[\Delta\boldsymbol{\psi}]$ in the case of droplet coalescence is written as

$$\begin{aligned} \boldsymbol{\psi}^* \left(\mathbf{c}_{f@p}, \mathbf{c}_p^*, \mu_p^*\right) &= m^* v_{p,i}^{*'} v_{p,j}^{*'} & \boldsymbol{\psi} \left(\mathbf{c}_{f@p}, \mathbf{c}_p, \mu_p\right) &= m_p v'_{p,i} v'_{p,j} \\ & & \boldsymbol{\psi} \left(\mathbf{c}_{f@q}, \mathbf{c}_q, \mu_q\right) &= m_q v'_{q,i} v'_{q,i} \quad , \end{aligned} \tag{4.109}$$

where

$$m^* = m_p + m_q \tag{4.110}$$

$$m^* v^*_{p,i} = m_q v_{p,i} + m_q v_{q,i} \quad . \tag{4.111}$$

The expression $\left[\Delta\left(\boldsymbol{\psi} = m_p v'_{p,i} v'_{p,j}\right)\right]$ is written

$$\left[\Delta\left(\boldsymbol{\psi} = m_p v'_{p,i} v'_{p,j}\right)\right] = -\frac{m_p m_q}{m_p + m_q} w'_{pq,i} w'_{pq,j} \quad . \tag{4.112}$$

It is interesting to note that the expressions in (4.108) and (4.112) are equivalent if particle collisions are handled with a normal restitution coefficient $e_c = 0$.

4.4 Direct Quadrature Method of Moments for coalescence

Droplet coalescence is a poly-disperse problem, as already stated before, which is difficult to account for in classical Eulerian approaches due to the poly-dispersion and interaction of droplets (coalescence). Belt and Simonin [11] recently developed an extension of the DQMOM approach proposed by Marchisio and Fox [82] based on the above presented formalism of the joint-fluid particle velocity PDF f_{fp} by Simonin [117]. This extension, which is presented in this section 4.4, is compared with predictions of droplet coalescence from DNS/DPS simulations.

4.4.1 How to account for poly-dispersion?

In order to correctly describe inter-phase transfers it is necessary to account locally and dynamically for poly-dispersion. In order to do so a given particle diameter (or particle mass) distribution needs to be discretized. This can be done for example by introducing a particle diameter PDF discretization, which foresees the possible development of the initial particle diameter PDF. This means that in case of pure coalescence all future coalesced particles need to fall into one of the pre-allocated classes, which might be zero initially. If droplet break-up or creation of satellite droplets is additionally taken into account, the same needs to be done for all possible smaller droplets. This leads to a large number of particle classes, for which interactions need to be considered. Another possibility is to use the Gauss-Quadrature rule in the frame of moment method approach. The Gauss-Quadrature is a mathematical method to approximate the definite integral of a function as the sum of weighted function values at specific points. The here presented DQMOM approach uses the Gauss-Quadrature rule for the discretization of the diameter PDF.

4.4.2 General DQMOM formalism

Marchisio and Fox [82] propose the DQMOM approach, where the particle distribution f_p is written as a summation of N weighted Dirac functions

$$f_p\left(\mathbf{c}_p, \mu_p; \mathbf{x}, t\right) = \sum_{\alpha=1}^{N} \omega_\alpha\left(\mathbf{x}, t\right) \delta\left(\mu_p - m_{p,\alpha}\left(\mathbf{x}, t\right)\right) \delta\left(\mathbf{c}_p - \mathbf{v}_{p,\alpha}\left(\mathbf{x}, t\right)\right) \quad , \tag{4.113}$$

with $m_{p,\alpha}\left(\mathbf{x}, t\right)$ the particle mass and $\mathbf{v}_{p,\alpha}\left(\mathbf{x}, t\right)$ the particle velocity of a class α. This way Marchisio and Fox [82] associate one single mean velocity with each mass. However, using this definition, it is not possible to derive a particle kinetic-energy balance equation within the moment method approach, since only a particle mean velocity exists. Moreover, collisional effects appear therefore only in the number and mass balance equations using the formalism of Marchisio and Fox [40], [82].

Belt and Simonin [11] developed the DQMOM approach of Marchisio and Fox [82] for the above presented formalism of the joint-fluid particle velocity PDF f_{fp}. The relevant transport equation for f_{fp} is given in (4.23). The joint-fluid particle velocity PDF f_{fp} introduced by Simonin [117] is explained above. It can be written using a velocity PDF conditioned on the particle mass multiplied by a particle mass PDF as

$$f_{fp}\left(\mathbf{c}_f, \mathbf{c}_p, \mu_p; \mathbf{x}, t\right) = n_p\left(\mathbf{x}, t\right) h_{fp}\left(\mathbf{c}_f, \mathbf{c}_p | \mu_p; \mathbf{x}, t\right) g\left(\mu_p; \mathbf{x}, t\right) \quad , \tag{4.114}$$

where $h_{fp}\left(\mathbf{c}_f, \mathbf{c}_p | \mu_p; \mathbf{x}, t\right)$ is the joint fluid-particle velocity PDF at time t, conditioned on the mass m_p to be equal to μ_p, with the center of mass located in the volume $[\mathbf{x}, \mathbf{x} + d\mathbf{x}]$ and a translation velocity $\mathbf{v}_p$ in $[\mathbf{c}_p, \mathbf{c}_p + d\mathbf{c}_p]$, seeing a locally undisturbed fluid velocity $\mathbf{u}_f$ in $[\mathbf{c}_f, \mathbf{c}_f + d\mathbf{c}_f]$. $g\left(\mathbf{x}, \mu_p; t\right)$ is the particle mass PDF at time t with the center of mass located in the volume $[\mathbf{x}, \mathbf{x} + d\mathbf{x}]$ and a mass m_p in $[\mu_p, \mu_p + d\mu_p]$. The PDFs h_{fp} and g verify

$$\int h_{fp}\left(\mathbf{c}_f, \mathbf{c}_p | \mu_p; \mathbf{x}, t\right) d\mathbf{c}_p d\mathbf{c}_f = 1 \quad \forall\ \mu_p \tag{4.115}$$

$$\int g\left(\mu_p; \mathbf{x}, t\right) d\mu_p = 1 \quad . \tag{4.116}$$

A similar description as in (4.114) is found for the case of laminar flows in [69] and [45]. Belt and Simonin [11] write the particle mass PDF g, similar to the approach of Marchisio and Fox [82] in (4.113), as a summation of N weighted Dirac functions with the sum of the

weights ω_α over all classes equal to 1

$$g\left(\mu_p;\mathbf{x},t\right)=\sum_{\alpha=1}^{N}\omega_\alpha\left(\mathbf{x},t\right)\delta\left(\mu_p-m_{p,\alpha}\left(\mathbf{x},t\right)\right) \quad . \tag{4.117}$$

The weights ω_α and the abscissas $m_{p,\alpha}$ in (4.117) are unknown, thus $2N$ unknowns for ω_α and $m_{p,\alpha}$ must be determined. This is achieved by application of the Gauss-Quadrature approximation for the moments of g

$$\int \mu_p^k g\left(\mu_p;\mathbf{x},t\right)d\mu_p \quad = \quad \sum_{\alpha=1}^{N} m_{p,\alpha}^k\left(\mathbf{x},t\right)\ \omega_\alpha\left(\mathbf{x},t\right) \quad . \tag{4.118}$$

Following the DQMOM approach $2N$ transport equations on the low-order mass moments are derived by integration of the PDF transport equation (4.23) multiplied by μ_p^k as

$$\int \mu_p^k\left(\frac{df_{fp}}{dt}\right)d\mathbf{c}_f d\mathbf{c}_p d\mu_p \quad . \tag{4.119}$$

The single source terms, which appear in the above given equations, are directly derived from the formulations given by Simonin [117] and which are reported in section 4.1.2. The exact terms in the frame of DQMOM are given in Belt and Simonin [11].

4.4.3 Number and mass balance equations in DQMOM

The integration of the PDF transport equation (4.23) multiplied by μ_p^k gives, after some manipulation, the number and mass balance equation in the form of the following system, with k ranging from 0 to $2N-1$

$$\begin{aligned}
&\int \mu_p^k\left(\frac{\partial f_{fp}}{\partial t}\right)_{coll} d\mathbf{c}_f d\mathbf{c}_p d\mu_p \\
&= (1-k)\sum_{\alpha=1}^{N} m_{p,\alpha}^k\left[\frac{\partial}{\partial t}\left(n\right)_\alpha+\frac{\partial}{\partial x_j}\left(V_{p,j}n\right)_\alpha\right] \\
&\quad +k\sum_{\alpha=1}^{N} m_{p,\alpha}^{k-1}\left[\frac{\partial}{\partial t}\left(n\ m_p\right)_\alpha+\frac{\partial}{\partial x_j}\left(V_{p,j}n\ m_p\right)_\alpha-n_\alpha\langle\Gamma\rangle_\alpha\right] \quad .
\end{aligned} \tag{4.120}$$

For the sake of readability expressions given in the form $\left(xy\right)_\alpha$ stand for $(x_\alpha y_\alpha)$. Thus, for example $\left(n\right)_\alpha$ means (n_α) or $\left(V_{p,j}n\ m_p\right)_\alpha$ stands for $(V_{p,j,\alpha}n_\alpha m_{p,\alpha})$.

The mean number of particles per unit volume n_α with mass $m_{p,\alpha}$ is defined as $n_\alpha=\omega_\alpha n$. The physical meaning of the weight ω_α appears, in this approach, as the ratio of the number

of droplets per class α to the total number of droplets at $\mathbf{x}_p$ and t. (4.120) gives the values for the N abscissas $m_{p,\alpha}$ and N weights n_α, from which the droplet diameter distribution is reconstructed, in such a way that it shows the correct moments up to the order $2N-1$. The term $n_\alpha\langle\Gamma\rangle_\alpha$ in (4.120) represents the evaporation rate of the droplets, which is 0 throughout this work.

For $N = 1$ (4.120) is identical to the number ($k = 0$) and mass ($k = 1$) transport equations for mono-disperse droplets given in section 4.3.2 and derived by Simonin [117]. (4.120) is also equivalent to the system obtained by Marchisio and Fox [82], if it is written in terms of particle diameter d_p.

(4.120) can be summarized as

$$\mathcal{C}(m_p^k) \;=\; (1-k)\sum_{\alpha=1}^{N} m_{p,\alpha}^k a_\alpha^{(1)} + k\sum_{\alpha=1}^{N} m_{p,\alpha}^{k-1} b_\alpha^{(1)} \quad , \tag{4.121}$$

where $\mathcal{C}(m_p^k) = \int \mu_p^k \left(\frac{\partial f_{fp}}{\partial t}\right)_{coll} d\mathbf{c}_f d\mathbf{c}_p d\mu_p$ is the collision source term in (4.120), and $a_\alpha^{(1)}$ and $b_\alpha^{(1)}$ are the source terms of the number and mass balance equations for particle class α

$$\frac{\partial}{\partial t}(n)_\alpha + \frac{\partial}{\partial x_j}(V_{p,j} n)_\alpha = a_\alpha^{(1)} \tag{4.122}$$

$$\frac{\partial}{\partial t}(n\; m_p)_\alpha + \frac{\partial}{\partial x_j}(V_{p,j} n\; m_p)_\alpha - n_\alpha\langle\Gamma\rangle_\alpha = b_\alpha^{(1)} \quad . \tag{4.123}$$

4.4.4 Momentum balance equation in DQMOM

The integration of the PDF transport equation (4.23) multiplied by $\mu_p^k c_{p,i}$ gives, after some manipulation, the momentum balance equation in the form of the following system with k ranging from 0 to $2N-1$

$$\mathcal{C}(m_p^k v_{p,i}) \;=\; (1-k)\sum_{\alpha=1}^{N} m_{p,\alpha}^k a_\alpha^{(2)} + k\sum_{\alpha=1}^{N} m_{p,\alpha}^{k-1} b_\alpha^{(2)} \quad , \tag{4.124}$$

where $a_\alpha^{(2)}$ is the source term of the transport equation for the velocity, and $b_\alpha^{(2)}$ is the source term for the transport equation of the momentum for particles of class α given by

$$\begin{aligned} \frac{\partial}{\partial t}(n\; V_{p,i})_\alpha \;&+\; \frac{\partial}{\partial x_j}(n\; V_{p,i}V_{p,j})_\alpha \\ &+\; \frac{\partial}{\partial x_j}\left(n_\alpha\langle v'_{p,i}v'_{p,j}\rangle_\alpha\right) - n_\alpha\langle\frac{F_i}{m_p}\rangle_\alpha = a_\alpha^{(2)} \end{aligned} \tag{4.125}$$

$$\begin{aligned}\frac{\partial}{\partial t}\left(n\ m_p V_{p,i}\right)_\alpha &+ \frac{\partial}{\partial x_j}\left(n\ m_p V_{p,i} V_{p,j}\right)_\alpha \\ &+ \frac{\partial}{\partial x_j}\left(n_\alpha m_{p,\alpha}\langle v'_{p,i} v'_{p,j}\rangle_\alpha\right) \\ &- n_\alpha\langle V_{p,i}\Gamma\rangle_\alpha - n_\alpha m_{p,\alpha}\langle\frac{F_i}{m_p}\rangle_\alpha = b_\alpha^{(2)} \quad . \end{aligned} \tag{4.126}$$

(4.126) is equal to the momentum transport equation in the mono-disperse case in the equation framework of Simonin [117].

4.4.5 Droplet kinetic stress balance equation in DQMOM

The integration of the PDF transport equation (4.23) multiplied by $\mu_p^k c_{p,i} c_{p,j}$ gives, after some manipulation, the momentum balance equation in the form of the following system with k ranging from 0 to $2N-1$

$$\begin{aligned}\mathcal{C}\left(m_p^k v'_{p,i} v'_{p,j}\right) + E = \\ (1-k)\sum_{\alpha=1}^{N} m_{p,\alpha}^k a_\alpha^{(3)} + k\sum_{\alpha=1}^{N} m_{p,\alpha}^{k-1} b_\alpha^{(3)} \quad ,\end{aligned} \tag{4.127}$$

where $a_\alpha^{(3)}$ and $b_\alpha^{(3)}$ are the source terms of the following transport equations for particles of class α given by

$$\begin{aligned}\frac{\partial}{\partial t}\left(n_\alpha\langle v'_{p,i} v'_{p,j}\rangle_\alpha\right) &+ \frac{\partial}{\partial x_l}\left(n_\alpha\langle v'_{p,i} v'_{p,j}\rangle_\alpha V_{p,l,\alpha}\right) \\ &+ \frac{\partial}{\partial x_l}\left(n_\alpha\langle v'_{p,i} v'_{p,j} v'_{p,l}\rangle_\alpha\right) \\ &+ n_\alpha\langle v'_{p,i} v'_{p,l}\rangle_\alpha\frac{\partial}{\partial x_l}V_{p,j,\alpha} + n_\alpha\langle v'_{p,j} v'_{p,l}\rangle_\alpha\frac{\partial}{\partial x_l}V_{p,i,\alpha} \\ &- n_\alpha\langle v'_{p,j}\frac{F_i}{m_p}\rangle_\alpha - n_\alpha\langle v'_{p,i}\frac{F_j}{m_p}\rangle_\alpha \quad = \quad a_\alpha^{(3)}\end{aligned} \tag{4.128}$$

$$\begin{aligned}\frac{\partial}{\partial t}\left(n_\alpha m_{p,\alpha}\langle v'_{p,i} v'_{p,j}\rangle_\alpha\right) &+ \frac{\partial}{\partial x_l}\left(n_\alpha m_{p,\alpha}\langle v'_{p,i} v'_{p,j}\rangle_\alpha V_{p,l,\alpha}\right) \\ &+ \frac{\partial}{\partial x_l}\left(n_\alpha m_{p,\alpha}\langle v'_{p,i} v'_{p,j} v'_{p,l}\rangle_\alpha\right) \\ &+ n_\alpha m_{p,\alpha}\langle v'_{p,i} v'_{p,l}\rangle_\alpha\frac{\partial}{\partial x_l}V_{p,j,\alpha}\end{aligned}$$

$$
\begin{aligned}
&+ \quad n_\alpha m_{p,\alpha} \langle v'_{p,j} v'_{p,l} \rangle_\alpha \frac{\partial}{\partial x_l} V_{p,i,\alpha} \\
&- \quad n_\alpha m_{p,\alpha} \langle v'_{p,j} \frac{F_i}{m_p} \rangle_\alpha - n_\alpha m_{p,\alpha} \langle v'_{p,i} \frac{F_j}{m_p} \rangle_\alpha \\
&- \quad n_\alpha \langle \Gamma v'_{p,i} v'_{p,j} \rangle_\alpha \quad = \quad b_\alpha^{(3)} \quad . \qquad (4.129)
\end{aligned}
$$

(4.128) is equal to the particle kinetic stress transport equation in the mono-disperse case in the equation framework of Simonin [117]. In (4.127) an additional term E appears, which is due, following Belt and Simonin [11], to conditional averages on the mass in the integration of the PDF transport equation (4.23) multiplied by $\mu_p^k c_{p,i} c_{p,j}$. In a homogeneous isotropic turbulence it is zerom and it writes in the general case as [11]

$$
\begin{aligned}
E_{ij} \quad = \quad & -\sum_{\alpha=1}^{N} n_\alpha m_{p,\alpha}^k \left[\langle v'_{p,i} v'_{p,l} \rangle_\alpha \left(\frac{\partial V_{p,j}}{\partial x_l} \Big|_\alpha - \frac{\partial V_{p\alpha,j}}{\partial x_l} \right) + \langle v'_{p,i} \Gamma' \rangle_\alpha \frac{\partial V_{p,j}}{\partial \mu_p} \Big|_\alpha \right. \\
& \left. + \langle v'_{p,j} v'_{p,l} \rangle_\alpha \left(\frac{\partial V_{p,i}}{\partial x_l} \Big|_\alpha - \frac{\partial V_{p\alpha,i}}{\partial x_l} \right) + \langle v'_{p,j} \Gamma' \rangle_\alpha \frac{\partial V_{p,i}}{\partial \mu_p} \Big|_\alpha \right] \quad . \qquad (4.130)
\end{aligned}
$$

4.4.6 Fluid-particle covariance balance equation in DQMOM

The integration of the PDF transport equation (4.23) multiplied by $\mu_p^k c_{f,i} c_{p,j}$ gives, after some manipulation, the fluid-particle covariance balance equation in the form of the following system with k ranging from 0 to $2N-1$

$$
\mathcal{C}\left(m_p^k u'_{f,i} v'_{p,j} \right) + E' = (1-k) \sum_{\alpha=1}^{N} m_{p,\alpha}^k a_\alpha^{(4)} + k \sum_{\alpha=1}^{N} m_{p,\alpha}^{k-1} b_\alpha^{(4)} \quad , \qquad (4.131)
$$

where $a_\alpha^{(4)}$ and $b_\alpha^{(4)}$ are the source terms of the following transport equations for particles of class α given by

$$
\begin{aligned}
\frac{\partial}{\partial t} \left(n_\alpha \langle u'_{f,i} v'_{p,j} \rangle_\alpha \right) \quad & + \quad \frac{\partial}{\partial x_l} \left(n_\alpha \langle u'_{f,i} v'_{p,j} \rangle_\alpha V_{p,l,\alpha} \right) \\
& + \quad \frac{\partial}{\partial x_l} \left(n_\alpha \langle u'_{f,i} v'_{p,j} v'_{p,l} \rangle_\alpha \right) \\
& + \quad n_\alpha \langle u'_{f,l} v'_{p,j} \rangle_\alpha \frac{\partial}{\partial x_l} V_{p,i,\alpha} \\
& - \quad n_\alpha \langle u'_{f,j} \frac{F_i}{m_p} \rangle_\alpha - n_\alpha \langle v'_{p,j} A_\beta \rangle_\alpha \quad = \quad a_\alpha^{(4)} \qquad (4.132)
\end{aligned}
$$

$$\begin{aligned}\frac{\partial}{\partial t}\left(n_\alpha m_{p,\alpha}\langle u'_{f,i}v'_{p,j}\rangle_\alpha\right) &+ \frac{\partial}{\partial x_j}\left(n_\alpha m_{p,\alpha}\langle u'_{f,i}v'_{p,j}\rangle_\alpha V_{p,l,\alpha}\right)\\ &+ \frac{\partial}{\partial x_l}\left(n_\alpha m_{p,\alpha}\langle u'_{f,i}v'_{p,j}v'_{p,l}\rangle_\alpha\right)\\ &+ n_\alpha m_{p,\alpha}\langle u'_{f,l}v'_{p,j}\rangle_\alpha\frac{\partial}{\partial x_l}V_{p,i,\alpha}\\ &- n_\alpha m_{p,\alpha}\langle u'_{f,j}\frac{F_i}{m_p}\rangle_\alpha - n_\alpha m_{p,\alpha}\langle v'_{p,j}A_i\rangle_\alpha\\ &- n_\alpha\langle\Gamma u'_{f,i}v'_{p,j}\rangle_\alpha \quad = \quad b_\alpha^{(4)} \quad . \end{aligned} \tag{4.133}$$

(4.132) is equal to the fluid-particle covariance transport equation in the mono-disperse case in the equation framework of Simonin [117]. The term E' in (4.131) equals also 0 in a homogeneous isotropic turbulence.

4.4.7 Collision source terms in DQMOM for coalescence

The collisional source terms needed in the DQMOM approach are the same as the ones given in section 4.3.3 for the case of $k = 0$ and $k = 1$. The collision source terms for $k > 1$ are given in this section and the integrals are solved, and the final form of the collision source term is given. In the case of the collision source term in the particle number and mass balance equation the integrals over the mass and velocity can be solved separately as the joint fluid-particle velocity PDF is split (see (4.114)) into the product of a fluid-particle velocity PDF conditioned on the particle mass and the particle mass PDF, on which the Gauss-Quadrature is applied. The collision source terms are written as

$$\mathcal{C}\left(\boldsymbol{\psi}\right) = \mathcal{B}\left(\boldsymbol{\psi}\right) - \mathcal{D}\left(\boldsymbol{\psi}\right) \tag{4.134}$$

The "death" and "birth" terms are given by

$$\begin{aligned}\mathcal{D}\left(\boldsymbol{\psi}\right) = \quad & \frac{1}{2}\int_{\mathbf{w}_{pq}.\mathbf{k}<0}\sigma_{pq}^2\mathbf{w}_{pq}.\mathbf{k}\ \left[\boldsymbol{\psi}\left(\mathbf{c}_{f@p},\mathbf{c}_p,\mu_p\right)+\boldsymbol{\psi}\left(\mathbf{c}_{f@q},\mathbf{c}_q,\mu_q\right)\right]\\ & \times f_{fp}^{(2)}\left(\mathbf{x},\mathbf{c}_{f@p},\mathbf{c}_p,\mu_p,\mathbf{x}+\sigma_{pq}\mathbf{k},\mathbf{c}_{f@q},\mathbf{c}_q,\mu_q,t\right)\\ & \times d\mathbf{k}d\mathbf{c}_{f@p}d\mathbf{c}_p d\mu_p d\mathbf{c}_{f@q}d\mathbf{c}_q d\mu_q \end{aligned} \tag{4.135}$$

$$\begin{aligned}\mathcal{B}\left(\boldsymbol{\psi}^*\right) = \quad & \frac{1}{2}\int_{\mathbf{w}_{pq}.\mathbf{k}<0}\sigma_{pq}^2\mathbf{w}_{pq}.\mathbf{k}\ \left[\boldsymbol{\psi}^*\left(\mathbf{c}_{f@p}^*,\mathbf{c}_p^*,\mu_p^*\right)\right]\\ & \times f_{fp}^{(2)}\left(\mathbf{x},\mathbf{c}_{f@p},\mathbf{c}_p,\mu_p,\mathbf{x}+\sigma_{pq}\mathbf{k},\mathbf{c}_{f@q},\mathbf{c}_q,\mu_q,t\right)\\ & \times d\mathbf{k}d\mathbf{c}_{f@p}d\mathbf{c}_p d\mu_p d\mathbf{c}_{f@q}d\mathbf{c}_q d\mu_q \quad . \end{aligned} \tag{4.136}$$

The joint fluid-particle velocity PDF f_{fp} can be written, for colliding droplets respecting the definition of f_{fp} and (4.114), as

$$\begin{aligned} f_{fp}^{(2)}\left(\mathbf{x}, \mathbf{c}_{f@p}, \mathbf{c}_p, \mu_p, \mathbf{x}+\sigma_{pq}\mathbf{k}, \mathbf{c}_{f@q}, \mathbf{c}_q, \mu_q, t\right) = \\ \times n_p\left(\mathbf{x}, t\right)\ h_p\left(\mathbf{c}_p \mid \mathbf{c}_{f@p}, \mu_p; \mathbf{x}, t\right)\ g_p\left(\mu_p; \mathbf{x}, t\right) \\ \times n_q\left(\mathbf{x}, t\right)\ h_q\left(\mathbf{c}_q \mid \mathbf{c}_{f@q}, \mu_q; \mathbf{x}, t\right)\ g_q\left(\mu_q; \mathbf{x}, t\right) \\ \times f_{f@p}\left(\mathbf{c}_{f@p}; \mathbf{x}, t\right)\ \delta\left(\mathbf{c}_{f@q}-\mathbf{c}_{f@p}\right) \quad . \end{aligned} \tag{4.137}$$

Within this work the collision source term in the particle number and mass balance equation is mainly considered. The collision source term in the particle kinetic energy balance equation is often neglected. It will be shown that this assumption is often justified, but that such a term also plays a not insignificant role in dry granular flows or high particle inertia two-phase flows (see chapter 6). The collision source term in the momentum balance equation is given for the sake of completeness, but is not used in this work, since the flow configuration used here is a homogeneous isotropic turbulence.

Collision source term for particle number and mass

The collision source terms are given first applying, the molecular-chaos assumption in the collision terms (uncorrelated particle velocity model), and second accounting for the correlation of the particle velocities by the fluid turbulence (correlated particle velocity model) following [100]. The "death" and "birth" terms can thus be written with $\boldsymbol{\psi}_{pq} = \mu_p^k$ as

$$\begin{aligned} \mathcal{D}\left(\boldsymbol{\psi}\right) = \quad & \frac{1}{2}\sigma_{pq}^2 n_p\left(\mathbf{x}, t\right) n_q\left(\mathbf{x}, t\right) \pi \int_{\mathbf{w}_{pq}.\mathbf{k}<0} \mathbf{w}_{pq}.\mathbf{k}\ \left[\boldsymbol{\psi}_{pq}\right] W_r\left(\mu_p, \mu_q; \mathbf{x}, t\right) \\ & \times g_p\left(\mu_p; \mathbf{x}, t\right) g_q\left(\mu_q; \mathbf{x}, t\right) d\mu_p d\mu_q \end{aligned} \tag{4.138}$$

$$\begin{aligned} \mathcal{B}\left(\boldsymbol{\psi}\right) = \quad & \frac{1}{2}\sigma_{pq}^2 n_p\left(\mathbf{x}, t\right) n_q\left(\mathbf{x}, t\right) \pi \int_{\mathbf{w}_{pq}.\mathbf{k}<0} \mathbf{w}_{pq}.\mathbf{k}\ \left[\boldsymbol{\psi}_{pq}^*\right] W_r\left(\mu_p, \mu_q; \mathbf{x}, t\right) \\ & \times g_p\left(\mu_p; \mathbf{x}, t\right) g_q\left(\mu_q; \mathbf{x}, t\right) d\mu_p d\mu_q \quad , \end{aligned} \tag{4.139}$$

where W_r is the mean relative velocity of colliding droplets. It is written applying the uncorrelated particle velocity model as

$$W_r\left(\mu_p, \mu_q; \mathbf{x}, t\right) = \sqrt{\frac{16}{\pi}\frac{1}{3}\left(q_p^2 + q_q^2\right)} \quad , \tag{4.140}$$

and accounting for the correlation of the particle velocities by the fluid turbulence by means of the correlated particle velocity model as

$$W_r\left(\mu_p, \mu_q; \mathbf{x}, t\right) = \sqrt{\frac{16}{\pi}\frac{1}{3}\left(q_p^2 + q_q^2 - 2\xi_{fp}\xi_{fq}\sqrt{q_p^2 q_q^2}\right)} \quad , \tag{4.141}$$

with the fluid-particle correlation coefficients ξ_{fp} and ξ_{fq} given as defined in (4.65).

4.4.8 Resolution of the equation system

The equation systems in (4.121), (4.124), (4.127) and (4.131) have the same structure and thus the resolution can be done alike. The resolution of the equation systems is described in detail by Belt and Simonin [11] and is the same Marchisio and Fox [82] applied. The systems can be solved in two steps. First, the particle number $n_\alpha\left(t_n\right)$ and particle mass $\mu_{p,\alpha}\left(t_n\right)$ per particle class at time t_n are computed based on the source terms $a_\alpha^{(i)}\left(t_{n-1}\right)$ and $b_\alpha^{(i)}\left(t_{n-1}\right)$ at time t_{n-1}. Second, the particle number $n_\alpha\left(t_n\right)$ and particle mass $\mu_{p,\alpha}\left(t_n\right)$ per particle class at time t_n are used to determine the source terms $a_\alpha^{(i)}\left(t_n\right)$ and $b_\alpha^{(i)}\left(t_n\right)$ at time t_n respecting the collisional source terms $\mathcal{C}\left(\boldsymbol{\psi}\right)$.

The systems, which need to be resolved, can be written in matrix notation as

$$\begin{pmatrix} & & \\ M_1 & & M_2 \\ & & \end{pmatrix} \begin{pmatrix} a_1^{(i)} \\ \vdots \\ a_N^{(i)} \\ b_1^{(i)} \\ \vdots \\ b_N^{(i)} \end{pmatrix} = \begin{pmatrix} \mathcal{C}(\boldsymbol{\psi}^0) \\ \\ \vdots \\ \vdots \\ \\ \mathcal{C}(\boldsymbol{\psi}^{2N-1}) \end{pmatrix} \quad . \tag{4.142}$$

(4.142) can be written as $\boldsymbol{M}\boldsymbol{s} = \boldsymbol{c}$, where $\boldsymbol{M}$ is a matrix formed by two $2N \times N$ matrices $\boldsymbol{M}_1$ and $\boldsymbol{M}_2$. The vector $\boldsymbol{s}$ is composed of the source terms and vector $\boldsymbol{c}$ contains the collisional source terms of the 0 to $2N-1$ order mass moments. The exact expressions for the matrices are given in Belt and Simonin [11]. Matrix $\boldsymbol{M}$ is very ill conditioned as it contains the mass of the particle class to the power of k. The values of $\mu_{p,\alpha}^k$ may vary dramatically even for a maximum-minimum diameter ratio of 4. The corresponding mass ratio equals 64 with a constant particle density. The mass of a particle class appears until the power of $2N-1$, which gives for 4 Dirac functions already a ratio of 2^{42}. Belt and Simonin [11] write therefore the systems in (4.121), (4.124), (4.127) and (4.131) in function of the diameter in the case of a constant particle density ρ_p, which is the case in this work. A system on the particle diameter is thus obtained, which is identical for particle number

and mass to the equations of Marchisio and Fox [82]. Belt and Simonin [11] show the equivalence of solving the system either on particle mass or on particle diameter. Using a pre-conditioning of the matrix $\boldsymbol{M}$ and normalization of the equation systems with the particle diameter of class α allows to invert the matrix in an efficient manner.

Another difficulty in the DQMOM approach is pointed out by Fan *et al.* [40]. If two abscissas $\mu_{p,\alpha}$ are to close to each other, matrix $\boldsymbol{M}$ becomes singular. To avoid problems in this case, the diameters of the resolved system are forced to be different by a small number, which is sufficiently large to keep the matrix invertible.

A last point is noted in regard to the invertibility of matrix $\boldsymbol{M}$. Within this work, simulations are conducted with an initial monodisperse particulate phase, which is a problem in DQMOM as the initial abscissas of the chosen Dirac functions can not be equal to another. In this case, the DQMOM simulations are simply started after three different Dirac functions developed in the DNS/DPS simulations.

Chapter 5

Deterministic Simulation of inertial coalescence in homogeneous isotropic turbulence

In order to evaluate the influence of fluid turbulence on the coalescence rate of inertial droplets, direct numerical simulations of the three different turbulent fluid flow fields are computed coupled with five different initially monodisperse droplet phases in a first step. The flow configuration is a homogeneous isotropic turbulence and the droplet phase is in an equilibrium state with the fluid turbulence. In the following the initialization of the fluid-droplet flow fields is detailed and the characteristics of the three different fluid flow fields and five different initially monodisperse droplet phases are given. The fluid flow field with the intermediate turbulent Reynolds number is considered as the reference simulation. Results are given for this fluid flow field only, if it is not necessary to account for the influence of the turbulence intensity, for the cause presented.

5.1 Initialization of fluid-droplet flow

The initialization of the turbulent fluid-droplet flow field is done in several steps. These steps are illustrated in fig. 5.1. In the first step, the fluid turbulent flow field is initialized. The forcing parameters (see section 3.1.2) are chosen such that the target turbulent Reynolds number is achieved, verifying the demanded properties of the fluid flow. In this work a high resolution of the small turbulence scales was aimed for. Three different turbulent flow fields are computed on grids with 80^3, 128^3 and 256^3 cells. The goal was to double the turbulent Reynolds numbers passing from one grid to another, by maintaining a resolution

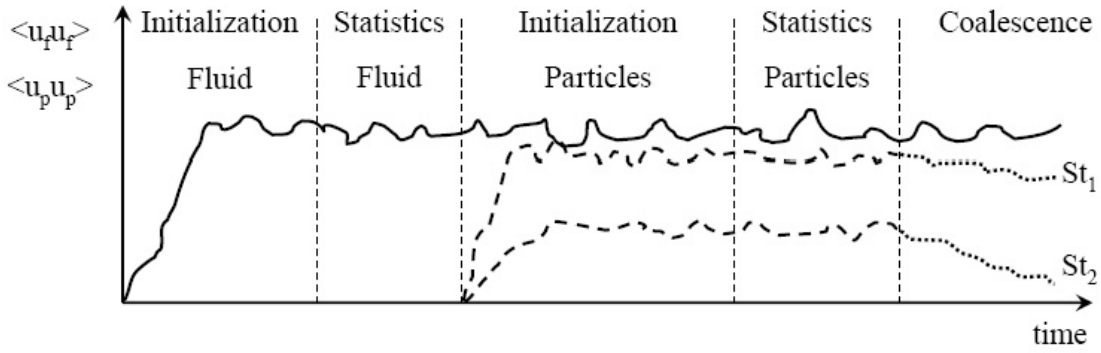

Figure 5.1: Sketch of the initialization of the turbulent fluid-droplet flow fields. The continuous line — represents the fluid velocity covariance and the dashed line − − − the droplet velocity covariance. The dotted line ··· stands for the droplet velocity covariance after coalescence is started from an equilibrium state. The relation between the Stokes numbers is $St_2 > St_1$.

of $\kappa_{max} \cdot \eta_K = 2$, which means that the smallest scale of turbulence, the Kolmogorov length scale η_K, well resolved.

In the second step of the fluid-droplet flow field initialization, relevant statistics are measured on the flow field, in order to decide whether the flow field has reached already the state of a homogeneous isotropic turbulence, with properties in the range aimed for. If this is the case, the droplet phases are added to the flow field. The droplet phase is randomly distributed in space and initialized either with a droplet velocity equal to 0 (as shown in fig. 5.1) or a droplet velocity equal to the one of the fluid flow. The droplets may encounter particle-particle collisions in this phase, but do not coalesce and will find an equilibrium state with the fluid phase. In a last step on the initialization process, the statistics of the droplet phase are verified and if an equilibrium state is established, coalescence is activated. Following this initialization procedure, it is guaranteed that the fluid-droplet flow field is at an equilibrium state.

The properties of the different flow fields are presented in the next section, first for the fluid flow field (section 5.1.1) and second for the dispersed phases (section 5.1.2).

5.1.1 Fluid flow fields

All the fluid flow simulations of homogeneous isotropic turbulence performed within this work are realized in a cubical domain with either 80^3, 128^3 or 256^3 grid points for a physical

Table 5.1: Simulation parameters for Direct Numerical Simulation of the turbulent fluid flow fields, based on grids with 80^3, 128^3 and 256^3 cells.

Quantity	**Symbol**	**Unit**	$\mathbf{80^3}$	$\mathbf{128^3}$	$\mathbf{256^3}$
Box length	L_b	m	0.128	0.128	0.128
Grid points	N_{grid}	1	80^3	128^3	256^3
Min. resolved wave number	κ_0	$1/m$	49.1	49.1	49.1
Max. resolved wave number	κ_{max}	$1/m$	1914.4	3092.5	6234.0
Forcing range			$[2\kappa_0, 6\kappa_0]$	$[2\kappa_0, 6\kappa_0]$	$[2\kappa_0, 6\kappa_0]$
Forcing amplitude σ_F			0.0055	0.02	0.18
Forcing time T_F			0.4	0.2	0.04
Fluid density	ρ_f	kg/m^3	1.17	1.17	1.17
Kinematic viscosity	ν_f	m^2/s	$1.47 \cdot 10^{-5}$	$1.47 \cdot 10^{-5}$	$1.47 \cdot 10^{-5}$

length of the cube of $L_b = 0.128m$ and with periodical boundary conditions. Table 5.1 shows the simulation parameters. The fluid is in all cases air, with a fluid density $\rho_f = 1.17\ kg/m^3$ and kinematic viscosity $\nu_f = 1.47 \cdot 10^{-5}\ m^2/s$.

The statistics measured for the turbulent fluid flow fields are given in table 5.2. The turbulent Reynolds numbers based on the integral Lagrangian length scale are 26.4 on the 80^3 point grid, 61.2 on the 128^3 point grid and 144.3 on the 256^3 point grid. Thus, a doubling of the fluid turbulence Reynolds numbers is achieved, allowing to assess the influence of the fluid turbulence on the coalescence rate. A high resolution of the small scales of turbulence is achieved as can be read from the values of $\kappa_{max} \cdot \eta_K$ in table 5.2. The three-dimensional energy spectrum normalized by the Kolmogorov length scale η_K for the simulation case with turbulent Reynolds number on the Taylor scale of $Re_\lambda = 60.5$ is given in fig. 5.2. The solid line represents the energy spectrum measured in the DNS in comparison with experimental results of Comte-Bellot and Corrsin [23] for a Reynolds number on the Taylor scale $Re_\lambda = 60.7$. The gradient $\kappa^{-\frac{5}{3}}$ is given by the dashed line, indicating the inertial range, in which energy is transferred in the so-called energy cascade and dissipation due to molecular viscosity is negligible. A good agreement can be found for the measured spectrum in comparison with the experimental results of Comte-Bellot and Corrsin [23]. Figure 5.3 shows the energy and dissipation spectra for the simulation case with turbulent Reynolds number on the Taylor scale of $Re_\lambda = 60.5$. The shifting of the two spectra indicates the inertial range. The reader may notice, that the smallest dissipative scales (for very large wave numbers) are well resolved, which is due to the resolution of the

Table 5.2: Turbulent fluid flow statistics of the three simulation grids 80^3, 128^3 and 256^3 computed.

Quantity	**Symbol**	**Unit**	$\mathbf{80^3}$	$\mathbf{128^3}$	$\mathbf{256^3}$
Box length	L_b	m	0.128	0.128	0.128
Reynolds number integr. scale	Re_L	–	26.4	61.2	144.3
Integral longit. length scale	L_f/L_b	–	0.0980	0.1056	0.0852
Integral transv. length scale	L_g/L_b	–	0.0511	0.0491	0.0426
Integral scale ratio	$0.5L_f/L_g$	–	0.96	1.07	1.00
Reynolds number Taylor scale	Re_λ	–	18.1	32.9	60.5
Taylor longit. length scale	λ_f/L_b	–	0.0941	0.0805	0.0507
Taylor transv. length scale	λ_g/L_b	–	0.0674	0.0568	0.0357
Taylor scale ratio	$1/\sqrt{2}\lambda_f/\lambda_g$	–	0.99	1.00	1.00
Kolmogorov length scale	η_K/L_b	–	0.0081	0.0051	0.0023
Kolmogorov time scale	τ_K	s	0.0729	0.0285	0.0061
Kolmogorov velocity scale	u_η	m/s	0.0142	0.0227	0.0492
	$\kappa_{max} \cdot \eta_K$	–	1.98	2.00	1.86
Lagrangian integ. time scale	τ_f^t/T_e	–	0.837	0.704	0.643
Eddy turn over time	T_e	s	0.405	0.203	0.056
Eulerian time scale	T_E/T_e	–	1.047	0.946	1.036
Ratio T_e/T_E	T_e/T_E	–	1.047	1.055	0.972
Fluid kinetic energy	q_f^2	m^2/s^2	0.0015	0.0067	0.0567
Energy dissipation	ϵ_f	m^2/s^3	0.0028	0.0181	0.3995

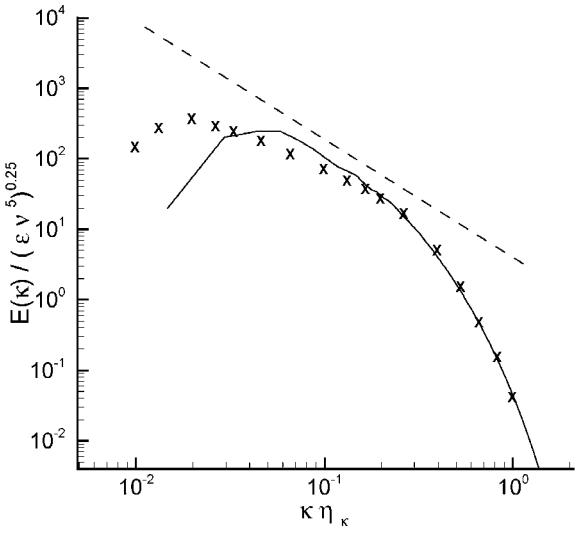

Figure 5.2: Three-dimensional energy spectrum normalized by the Kolmogorov length scale η_K for simulation case with $Re_\lambda = 60.5$ (solid line —). The dashed line − − − represents the gradient $\kappa^{-\frac{5}{3}}$. The symbols represent experimental values from Comte-Bellot and Corrsin [23] for $Re_\lambda = 60.7$.

turbulent fluid flow field with $\kappa_{max} \cdot \eta_K = 1.86$.

The three-dimensional energy spectrum normalized by the Kolmogorov length scale η_K for the simulation case with turbulent Reynolds number on the Taylor scale of $Re_\lambda = 32.9$ is given in fig. 5.4 and the three-dimensional energy spectrum normalized by the Kolmogorov length scale η_K for the simulation case with turbulent Reynolds number on the Taylor scale of $Re_\lambda = 18.1$ is given in fig. 5.6 respectively. Comparing the three-dimensional energy spectra for a Reynolds number on the Taylor scale of $Re_\lambda = 32.9$ in fig. 5.4 and for Reynolds number on the Taylor scale of $Re_\lambda = 18.1$ in fig. 5.6 with the energy spectrum in fig. 5.2 for a Reynolds number on the Taylor scale of $Re_\lambda = 60.5$, it can be noticed that all spectra coincide very well with the experimental results for the higher wave numbers. The inertial range lessens with a decreasing Reynolds number, as clearly seen in fig. 5.2, fig. 5.4 and fig. 5.6. By comparison of the energy and dissipation spectra in fig. 5.3, fig. 5.5 and fig. 5.7, it is seen that the shift of the energy and dissipation spectra decreases with decreasing Reynolds number, likewise indicating a more narrow inertial range. As it is seen in fig. 5.3, also fig. 5.5 and fig. 5.7 show that the smallest dissipative scales are well resolved, which corresponds to resolutions of $\kappa_{max} \cdot \eta_K = 1.98$ for $Re_\lambda = 32.9$ and $\kappa_{max} \cdot \eta_K = 2.00$ for $Re_\lambda = 18.1$.

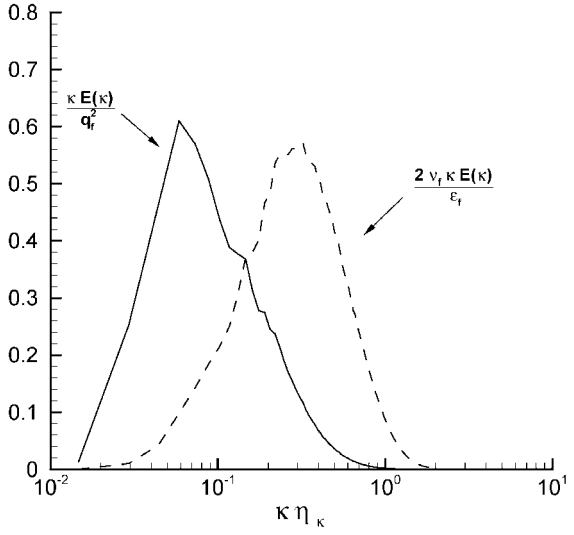

Figure 5.3: Energy spectrum $\frac{\kappa E(\kappa)}{q_f^2}$ (solid line —) and dissipation $\frac{2\nu_f \kappa^3 E(\kappa)}{\epsilon_f}$ (dashed line $- - -$) for simulation case with $Re_\lambda = 60.5$.

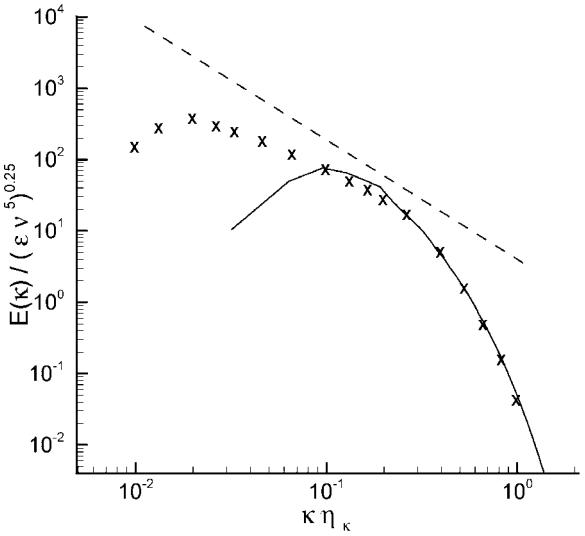

Figure 5.4: Three-dimensional energy spectrum normalized by the Kolmogorov length scale η_K for simulation case with $Re_\lambda = 32.9$ (solid line —). The dashed line $- - -$ represents the gradient $\kappa^{-\frac{5}{3}}$. The symbols represent experimental values from Comte-Bellot and Corrsin [23] for $Re_\lambda = 60.7$.

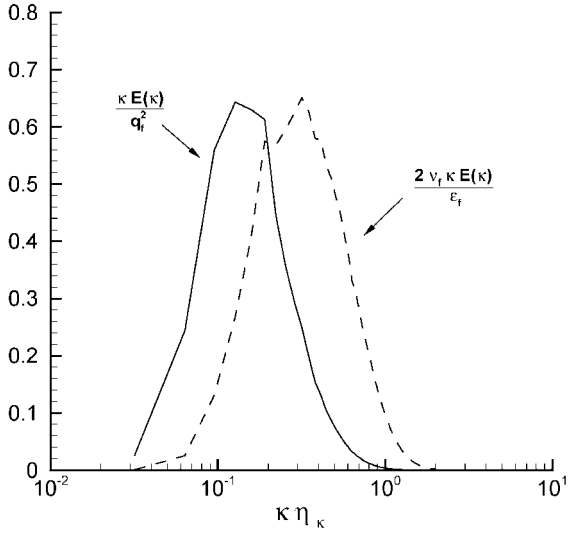

Figure 5.5: Energy spectrum $\frac{\kappa E(\kappa)}{q_f^2}$ (solid line —) and dissipation $\frac{2\nu_f \kappa^3 E(\kappa)}{\epsilon_f}$ (dashed line – – –) for simulation case with $Re_\lambda = 32.9$.

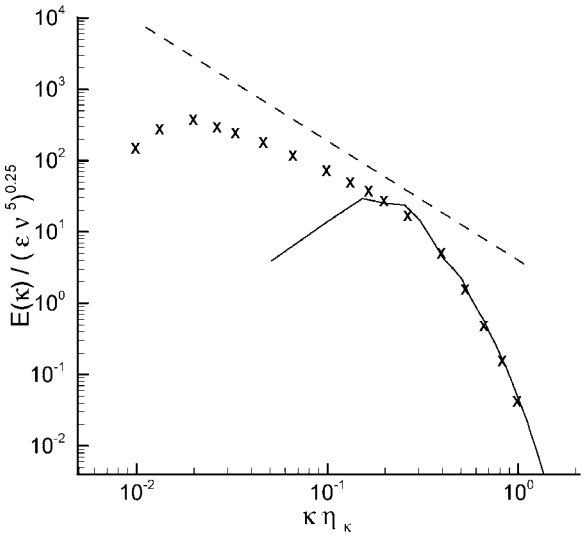

Figure 5.6: Three-dimensional energy spectrum normalized by the Kolmogorov length scale η_K for simulation case $Re_\lambda = 18.1$ (solid line —). The dashed line – – – represents the gradient $\kappa^{-\frac{5}{3}}$. The symbols represent experimental values from Comte-Bellot and Corrsin [23] for $Re_\lambda = 60.7$.

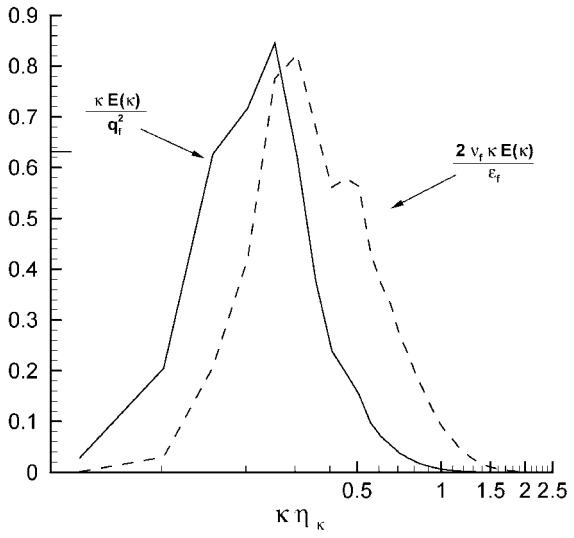

Figure 5.7: Energy spectrum $\frac{\kappa E(\kappa)}{q_f^2}$ (solid line —) and dissipation $\frac{2\nu_f \kappa^3 E(\kappa)}{\epsilon_f}$ (dashed line $- - -$) for simulation case 80^3 with $Re_\lambda = 18.1$.

The Eulerian auto-correlation functions in longitudinal $\square$ and transversal $\triangle$ direction of the fluid velocity are introduced in chapter 3. The shape of the the auto-correlation functions tends to an exponential form with an increasing turbulent Reynolds number. The exponential form of the longitudinal auto-correlation function $f(r)$ is given as [56]

$$f(r) = \exp\left(-\frac{r}{L_f}\right) \quad . \tag{5.1}$$

With the relation of von Karman and Howarth [131], the auto-correlation function in transversal direction $g(r)$ in homogeneous isotropic turbulence can be obtained as

$$g(r) = f(r) + \frac{r}{2}\frac{df(r)}{dr} \quad . \tag{5.2}$$

In low-Reynolds number flows, the exponential shape of the auto-correlation function is not entirely adapted. Most remarkably, the exponential shape of the auto-correlation function does not respect the zero gradient for $r \to 0$. Laviéville [73] proposes a model based on the auto-correlation function introduced by Sawford [112]. The longitudinal auto-correlation

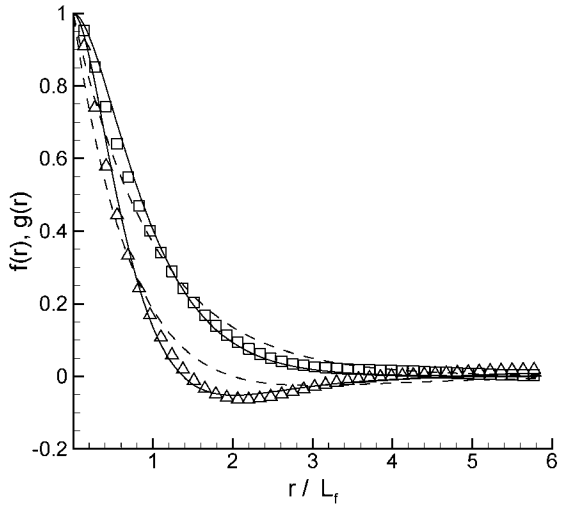

Figure 5.8: Eulerian auto-correlation functions in longitudinal □ and transversal △ direction of the fluid velocity measured in simulation case with $Re_\lambda = 60.5$. The dashed line − − − corresponds to the exponential form of the auto-correlation function and the solid line — to the model for the auto-correlation function proposed by Laviéville [73] based on the work of Sawford [112].

function $f(r)$ is given then as

$$f(r) = \frac{\lambda_g \exp\left(-\frac{r}{\lambda_g}\right) - (L_f - \lambda_g)\exp\left(-\frac{r}{L_f - \lambda_g}\right)}{2\lambda_g - L_f} \quad . \tag{5.3}$$

This form of the auto-correlation function is based on the Taylor micro-scales, which describe correctly the behavior for $r \to 0$

$$\lambda_f = \left[-\frac{1}{2}\frac{\mathrm{d}^2}{\mathrm{d}r^2} f(r=0)\right]^{-\frac{1}{2}} \qquad \lambda_g = \left[-\frac{1}{2}\frac{\mathrm{d}^2}{\mathrm{d}r^2} g(r=0)\right]^{-\frac{1}{2}} \quad . \tag{5.4}$$

Figure 5.8 compares the Eulerian auto-correlation functions in longitudinal □ and transversal △ direction of the fluid velocity measured in simulations with $Re_\lambda = 60.5$ with the predictions of the exponential model in (5.1) and the model based on the Taylor micro-scales in (5.3). Figure 5.8 shows that the form based on the Taylor micro-scales represents the auto-correlation functions $f(r)$ and $g(r)$ better than the exponential model.

Figure 5.9 and fig. 5.10 show the Eulerian auto-correlation functions in longitudinal □

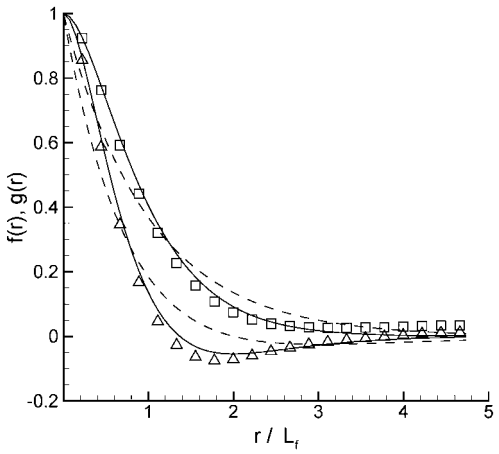

Figure 5.9: Eulerian auto-correlation functions in longitudinal □ and transversal △ direction of the fluid velocity measured in simulation case with $Re_\lambda = 32.9$. The dashed line − − − corresponds to the exponential form of the auto-correlation function and the solid line — to the model for the auto-correlation function proposed by Laviéville [73] based on the work of Sawford [112].

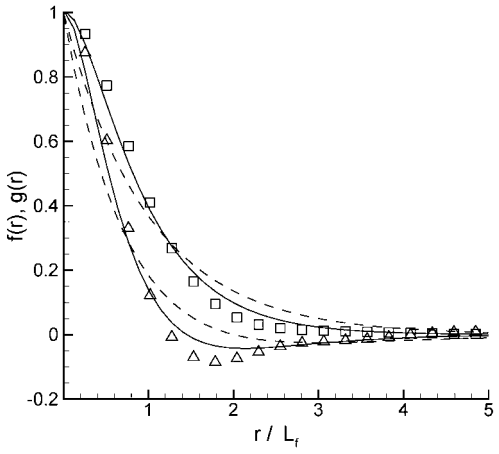

Figure 5.10: Eulerian auto-correlation functions in longitudinal □ and transversal △ direction of the fluid velocity measured in simulation case with $Re_\lambda = 18.1$. The dashed line − − − corresponds to the exponential form of the auto-correlation function and the solid line — to the model for the auto-correlation function proposed by Laviéville [73] based on the work of Sawford [112].

Table 5.3: Properties of initially monodisperse fluid-droplet flow fields. Fluid turbulence field $Re_\lambda = 60.5$.

Symbol	**Case 1**	**Case 2**	**Case 3**	**Case 4**	**Case 5**
N_p	100000	100000	100000	100000	100000
α_p	$8.311\ 10^{-5}$	$8.311\ 10^{-5}$	$8.311\ 10^{-5}$	$8.311\ 10^{-5}$	$8.311\ 10^{-5}$
$d_{p,ini}$	$1.493\ 10^{-4}$	$1.493\ 10^{-4}$	$1.493\ 10^{-4}$	$1.493\ 10^{-4}$	$1.493\ 10^{-4}$
ρ_p	68	272	680	1360	2040
q_p^2/q_f^2	1.010	0.770	0.560	0.380	0.298
$0.5\ q_{fp}/q_p^2$	1.00	1.00	1.00	1.01	1.00
$q_{f@p}^2/q_f^2$	1.05	0.98	1.00	0.98	0.99
τ_{fp}^F	$4.465\ 10^{-3}$	$1.659\ 10^{-2}$	$3.956\ 10^{-2}$	$7.730\ 10^{-2}$	$1.146\ 10^{-1}$
Re_p	0.55	1.37	2.03	2.40	2.59
$\tau_{f@p}^t$	$5.200\ 10^{-2}$	$5.267\ 10^{-2}$	$4.710\ 10^{-2}$	$4.728\ 10^{-2}$	$4.712\ 10^{-2}$
$St = \frac{\tau_{fp}^F}{\tau_{f@p}^t}$	0.11	0.42	1.06	1.63	2.43
$St_K = \frac{\tau_{fp}^F}{\tau_K}$	0.73	2.72	6.49	12.67	18.79

and transversal $\triangle$ direction of the fluid velocity measured in simulation with $Re_\lambda = 32.9$, $Re_\lambda = 18.1$ respectively. The model based on the Taylor micro-scales in (5.3) performs better in both cases than the exponential model in (5.1). However, the best fit is found for the highest Reynolds number in the simulations on the 256^3 point grid.

5.1.2 Initially monodisperse fluid-droplet flow fields before coalescence

After the fluid flow reached the state of a homogeneous isotropic turbulence, the droplet phase is added to the system. In the the third step of the fluid-droplet flow field initialization, the droplets may collide, but do not coalesce. Five different droplet classes are defined, such that the Stokes number $St = \frac{\tau_{fp}^F}{\tau_{f@p}^t}$ for each droplet case is the same in the three above introduced flow fields. The droplet fields are parameterized by changing the droplet density ρ_p only. Thus, it is possible to keep parameters such as the droplet number N_p, initial droplet diameter $d_{p,ini}$, droplet volume fraction α_p constant and at the same time vary the Stokes number St constant. Tables 5.3 to 5.5 show the statistics of the all the initially monodisperse droplet phases realized.

Tables 5.3 to 5.5 show, in particular, how the droplet inertia, expressed by means of the

Table 5.4: Properties of initially monodisperse fluid-droplet flow fields. Fluid turbulence field $Re_\lambda = 32.9$.

Symbol	**Case 1**	**Case 2**	**Case 3**	**Case 4**	**Case 5**
N_p	100000	100000	100000	100000	100000
α_p	$8.311\ 10^{-5}$	$8.311\ 10^{-5}$	$8.311\ 10^{-5}$	$8.311\ 10^{-5}$	$8.311\ 10^{-5}$
$d_{p,ini}$	$1.493\ 10^{-4}$	$1.493\ 10^{-4}$	$1.493\ 10^{-4}$	$1.493\ 10^{-4}$	$1.493\ 10^{-4}$
ρ_p	226.3	905	2263	4526	6790
q_p^2/q_f^2	1.006	0.764	0.535	0.402	0.310
$0.5\ q_{fp}/q_p^2$	1.00	1.00	1.01	1.01	1.02
$q_{f@p}^2/q_f^2$	1.036	0.961	0.962	1.054	1.065
τ_{fp}^F	$1.563\ 10^{-2}$	$6.022\ 10^{-2}$	$1.469\ 10^{-1}$	$2.889\ 10^{-1}$	$4.305\ 10^{-1}$
Re_p	0.168	0.438	0.657	0.825	0.892
$\tau_{f@p}^t$	$1.639\ 10^{-1}$	$1.664\ 10^{-1}$	$1.545\ 10^{-1}$	$1.752\ 10^{-1}$	$1.792\ 10^{-1}$
$St = \frac{\tau_{fp}^F}{\tau_{f@p}^t}$	0.10	0.36	0.95	1.65	2.43
$St_K = \frac{\tau_{fp}^F}{\tau_K}$	0.55	2.11	5.15	10.13	15.09

Table 5.5: Properties of initially monodisperse fluid-droplet flow fields. Fluid turbulence field $Re_\lambda = 18.1$.

Symbol	**Case 1**	**Case 2**	**Case 3**	**Case 4**	**Case 5**
N_p	100000	100000	100000	100000	100000
α_p	$8.311\ 10^{-5}$	$8.311\ 10^{-5}$	$8.311\ 10^{-5}$	$8.311\ 10^{-5}$	$8.311\ 10^{-5}$
$d_{p,ini}$	$1.493\ 10^{-4}$	$1.493\ 10^{-4}$	$1.493\ 10^{-4}$	$1.493\ 10^{-4}$	$1.493\ 10^{-4}$
ρ_p	500	2000	5000	10000	15000
q_p^2/q_f^2	0.999	0.757	0.529	0.361	0.277
$0.5\ q_{fp}/q_p^2$	1.00	1.00	1.00	1.01	1.02
$q_{f@p}^2/q_f^2$	1.031	0.960	0.965	0.980	0.987
τ_{fp}^F	$3.506\ 10^{-2}$	$1.369\ 10^{-1}$	$3.370\ 10^{-1}$	$6.681\ 10^{-1}$	$9.984\ 10^{-1}$
Re_p	0.086	0.223	0.331	0.380	0.427
$\tau_{f@p}^t$	$3.738\ 10^{-1}$	$4.135\ 10^{-1}$	$3.737\ 10^{-1}$	$3.573\ 10^{-1}$	$3.757\ 10^{-1}$
$St = \frac{\tau_{fp}^F}{\tau_{f@p}^t}$	0.09	0.33	0.90	1.87	2.66
$St_K = \frac{\tau_{fp}^F}{\tau_K}$	0.48	1.88	4.62	9.17	13.70

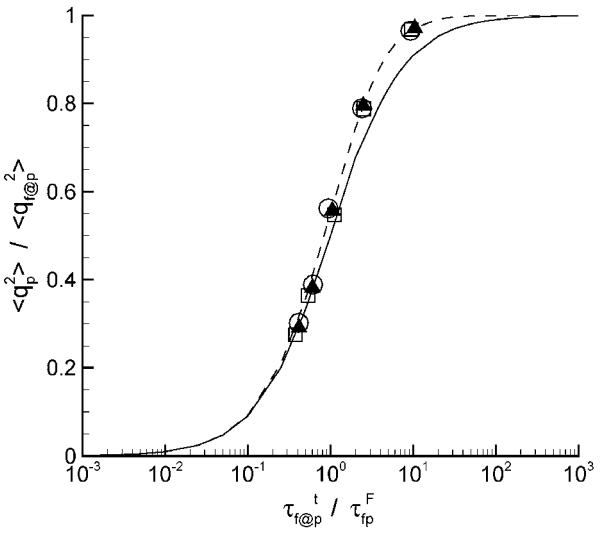

Figure 5.11: Ratio of $\frac{q_p^2}{q_{f@p}^2}$ plotted over the inverse of the Stokes number on a logarithmic abscissa. High-inertia droplets are found on the left and low-inertia droplets on the right side of the figure. The symbols stand for the three different fluid flows (□ for $Re_\lambda = 18.1$, ▲ for $Re_\lambda = 32.9$, ◯ for $Re_\lambda = 60.5$). The solid line — represents the relation based on the exponential auto-correlation function in (5.5). The dashed line − − − represents the relation based on the form for the auto-correlation function proposed by Sawford [112] and the work of Deutsch [28] and given in (5.11).

Stokes number St, is controlled by the dispersed phase density ρ_p. An increasing dispersed phase density ρ_p leads to a higher St. It is seen, that the Stokes numbers are in good accordance for the five different droplet flow cases over the three different fluid flow fields with its respective value. **Case 4** and **Case 5** on the 80^3 fluid flow only in tab. 5.5, show a slightly higher deviation from the corresponding values on the 128^3 and 256^3 fluid flows.

The ratio $\frac{q_{fp}}{2q_p^2}$ in tables 5.3 to 5.5 is based on the theory of Tchen and Hinze [129] [56] and indicates an equilibrium between the fluid and droplet phase. Deutsch [28] derives the following relations for the droplet- and fluid-droplet covariances in the case of a homogeneous isotropic turbulence, based on the analysis of Tchen and Hinze, by making use of the exponential form for the auto-correlation function of the fluid "seen" by the droplet, which can be written in terms of energy as

$$q_{fp} = 2q_p^2 = 2q_{f@p}^2 \frac{\eta_p}{1+\eta_p} \qquad \text{with} \qquad \eta_p = \frac{\tau_{f@p}^t}{\tau_{fp}^F} \quad . \tag{5.5}$$

The relation in (5.5) is plotted in fig. 5.11 (solid line —). The symbols in fig. 5.11 stand for the three different fluid flows (□ for $Re_\lambda = 18.1$, ▲ for $Re_\lambda = 32.9$, ◯ for $Re_\lambda = 60.5$). The inverse of the Stokes number is plotted on the logarithmic abscissa, thus high-inertia droplets are found on the left and low-inertia droplets on the right side of the fig. 5.11. The deviations in the Stokes numbers in **Case 4** and **Case 5** on the 80^3 fluid flow are also represented in fig. 5.11. Nevertheless, the values seem to be reasonable. It is clearly seen that the measured values do not coincide with the predictions of the relation of Tchen and Hinze (solid line —) for smaller droplet inertia. This is explained by the exponential form of the auto-correlation function, used for the relation in (5.5). The deviation is due to coarse sensitivity of the exponential form of the auto-correlation function to the scales low-inertia droplets are controlled by. Sawford [112] introduces an auto-correlation function, which takes the Taylor micro-scales into account. This auto-correlation function is written as

$$\mathcal{R}_f^t(\tau) = \frac{\exp\left(-\frac{\sqrt{Re^*}}{\tau_f^\infty}\tau\right) - \sqrt{Re^*}\exp\left(-\frac{\tau}{\tau_f^\infty}\right)}{1-\sqrt{Re^*}} \quad , \tag{5.6}$$

where τ_f^∞ corresponds to the integral Lagrangian time scale of the fluid. With a Lagrangian Reynolds number Re^* defined by Sawford it writes

$$\tau_f^\infty = \frac{\tau_f^t}{1+\frac{1}{\sqrt{Re^*}}} \qquad \text{and} \qquad Re^* = \left(\frac{\tau_f^\infty}{\tau_\lambda}\right)^2 \quad . \tag{5.7}$$

Sawford [112] writes Re^* in function of the Reynolds number on the Taylor micro-scales Re_λ as

$$Re^* = \frac{16a_0^2}{C_0^4}\frac{Re_\lambda^2}{15} \qquad \text{with} \qquad a_0 = 0.13\ Re_\lambda^{0.64} \quad . \tag{5.8}$$

The factor C_0 is determined as

$$\frac{\tau_f^t}{\tau_K} = \frac{2}{C_0}\frac{Re_\lambda}{\sqrt{15}}\left(1+\frac{C_0^2}{4a_0}\frac{\sqrt{15}}{Re_\lambda}\right) \tag{5.9}$$

Using a similar approach as Sawford [112], Boivin [17] defines a relation for the energies, making use of the work of Deutsch [28], as

$$q_{fp} = 2q_p^2 = 2q_{f@p}^2\eta_p^\infty\frac{1+\sqrt{Re^*}+\eta_p^\infty}{\sqrt{Re^*}+\left(1+\sqrt{Re^*}\right)\eta_p^\infty+\eta_p^{\infty 2}} \quad , \tag{5.10}$$

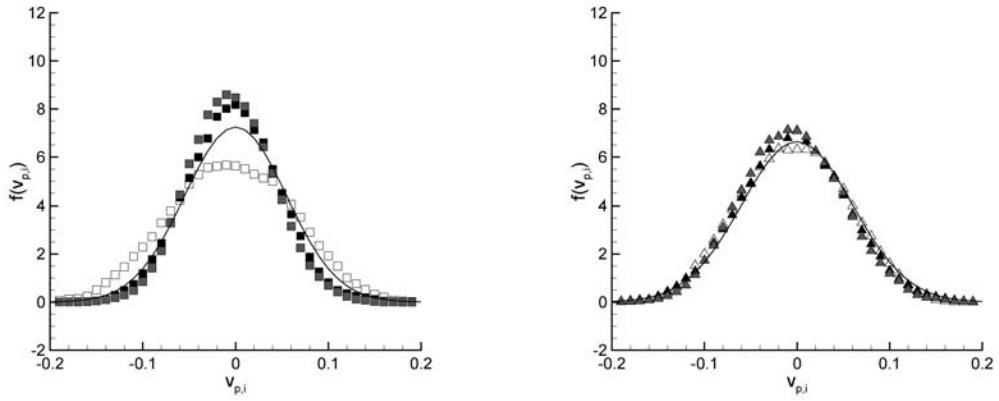

Figure 5.12: (Left) Droplet velocities for Case 1. (Right) Droplet velocities for Case 2. The symbols represent the droplet velocities in x-direction (Case 1 □, Case 2 △), y-direction (Case 1 ■, Case 2 ▲) and z-direction (Case 1 ■, Case 2 ▲) measured in DNS/DPS. The solid lines — are Gaussian distributions with mean $\mu = 0$ and variance $\sigma = 0.055$ for Case 1 and mean $\mu = 0$ and variance $\sigma = 0.06$ for Case 2.

where η_p^∞ is defined as

$$\eta_p^\infty = \frac{\tau_{f@p}^\infty}{\tau_{fp}^F} \qquad \text{with} \qquad \tau_{f@p}^\infty = \frac{\tau_{f@p}^t}{1 + \frac{1}{\sqrt{Re^*}}} \quad . \tag{5.11}$$

The relation in (5.11) is plotted in fig. 5.11 (dashed line − − −). It is clearly seen that this form for the auto-correlation function interprets the measured values better, for low droplet inertia, than the relation based on the exponential form of the auto-correlation function (solid line —).

Droplet velocity distribution

The droplet velocity distribution takes a Gaussian shape, if the droplets are in the state of local equilibrium, for droplets suspended in homogeneous isotropic turbulence. The more inertial the droplets are, the lower is the variance of the velocity distribution. Figures 5.12 to fig. 5.14 show the velocity distribution of the five different droplet classes suspended in homogeneous isotropic turbulence (flow field with $Re_\lambda = 32.9$). It is verified in fig. 5.12 to fig. 5.14 that this is the case. The same can be shown for the fluid-droplet simulations with $Re_\lambda = 18.1$ and $Re_\lambda = 60.5$, but the figures are spared here.

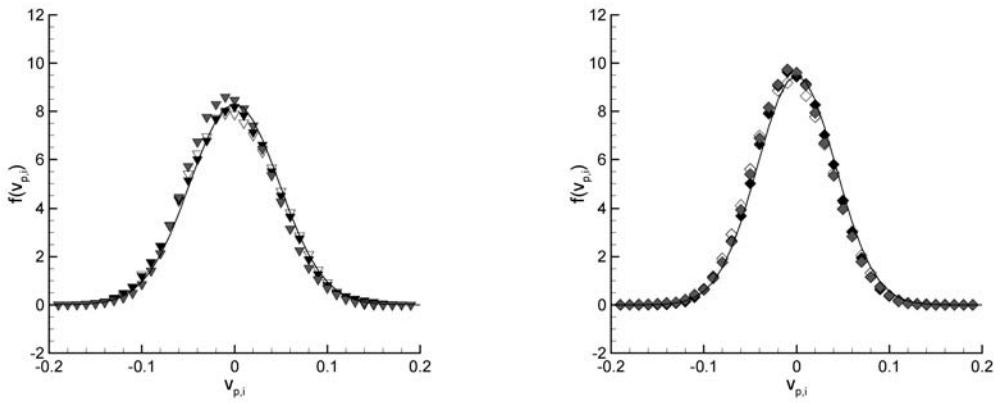

Figure 5.13: (Left) Droplet velocities for Case 3. (Right) Droplet velocities for Case 4. The symbols represent the droplet velocities in x-direction (Case 3 ∇, Case 4 $\Diamond$), y-direction (Case 3 $\blacktriangledown$, Case 4 $\blacklozenge$) and z-direction (Case 3 $\blacktriangledown$, Case 4 $\blacklozenge$) measured in DNS/DPS. The solid lines — are Gaussian distributions with mean $\mu = 0$ and variance $\sigma = 0.048$ for Case 3 and mean $\mu = 0$ and variance $\sigma = 0.042$ for Case 4.

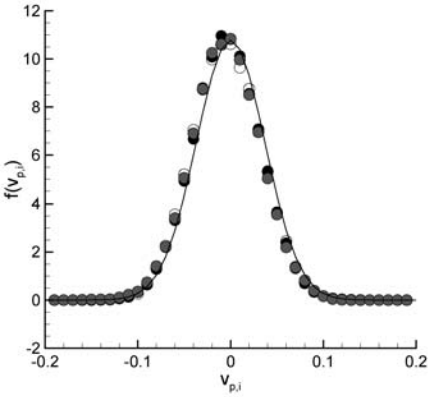

Figure 5.14: Droplet velocities for Case 5. The symbols represent the droplet velocities in x-direction (Case 5 $\bigcirc$), y-direction (Case 5 $\bullet$) and z-direction (Case 5 $\bullet$) measured in DNS/DPS. The solid lines — are Gaussian distributions with mean $\mu = 0$ and variance $\sigma = 0.037$ for Case 5.

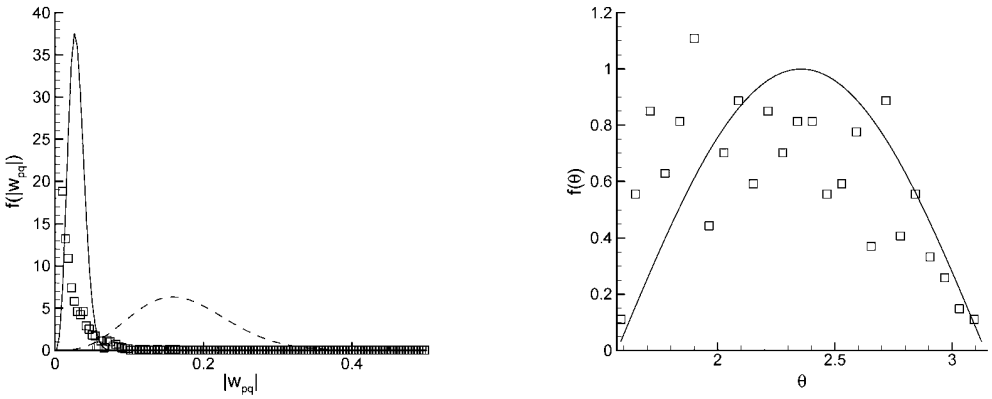

Figure 5.15: Norm of the droplet relative velocity at collision $|\mathbf{w}_{pq}|$ measured in fluid flow with $Re_\lambda = 32.9$, for droplet **Case 1** with $St = 0.11$ (left) represented by □ and collision angle θ (right). The dashed line − − − represents the distribution given in (3.53) based on the kinetic theory of rarefied gases. The solid line — represents the model given in (5.12) (left). (Right) The solid line — represents the distribution given in (3.52) based on the kinetic theory of rarefied gases.

Relative velocity at collision and collision angle

The norm of the droplet relative velocity at collision $|\mathbf{w}_{pq}|$ and the collision angle θ are used in section 3.4.4 for the validation of the collision angle in dry granular flows and section 3.4.4 for the validation of models in bi-dispersed granular flows. In turbulent two-phase flows the fluid turbulence influences the dispersed phase and by plotting these properties, the norm of the droplet relative velocity at collision $|\mathbf{w}_{pq}|$ and the collision angle θ, in turbulent two-phase flows, a measure for the influence of the fluid turbulence on the dispersed phase and on the droplet collisions is obtained.

Figure 5.15 (right) shows that the collision angle distribution given in (3.52) (solid line —) is not well represented for the smallest droplet Stokes number investigated within this work of $St = 0.11$. Already for a Stokes number $St = 0.42$ the collision angle distribution is well represented, as seen in fig. 5.16. Especially, lower collision angles are underestimated by the model in (3.52), based on the the kinetic theory of rarefied gases. These lower collision angles stand for grazing collisions. Figure 5.15 (left) exhibits very low relative velocities (□) of the droplets at the moment of collision. Combining these two measures, it can be concluded that the influence of the fluid turbulence on these low-inertia droplets ($St = 0.11$) is rather strong, such that the velocities of colliding droplets are similar in magnitude and direction. A similar velocity magnitude of the colliding droplets explains

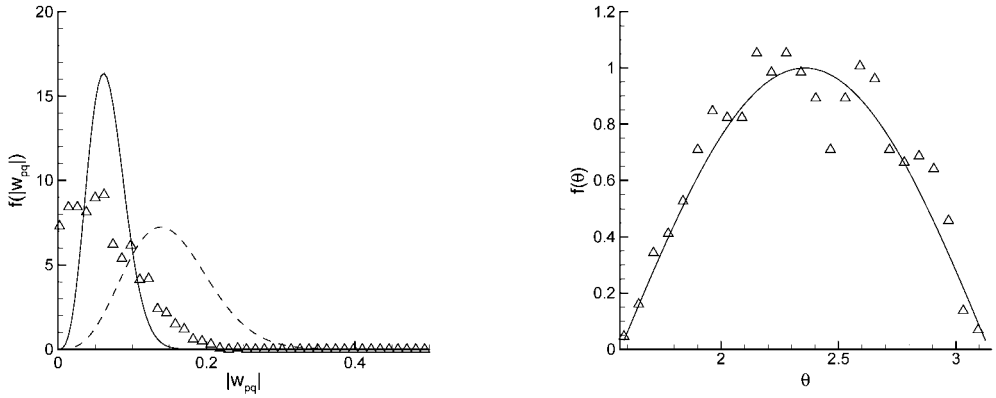

Figure 5.16: Norm of the droplet relative velocity at collision $|\mathbf{w}_{pq}|$ measured in fluid flow with $Re_\lambda = 32.9$, for droplet **Case 2** with $St = 0.42$ (left) represented by □ and collision angle θ (right). The dashed line − − − represents the distribution given in (3.53) based on the kinetic theory of rarefied gases. The solid line — represents the model given in (5.12) (left). (Right) The solid line — represents the distribution given in (3.52) based on the kinetic theory of rarefied gases.

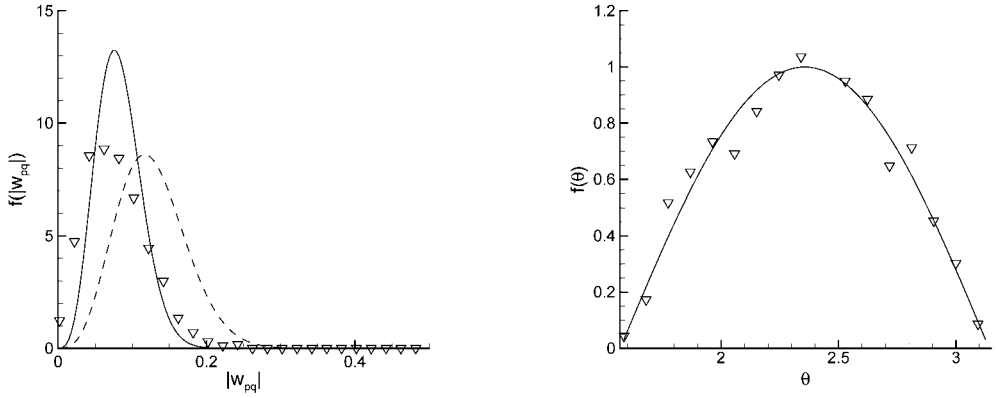

Figure 5.17: Norm of the droplet relative velocity at collision $|\mathbf{w}_{pq}|$ measured in fluid flow with $Re_\lambda = 32.9$, for droplet **Case 3** with $St = 1.03$ (left) represented by □ and collision angle θ (right). The dashed line − − − represents the distribution given in (3.53) based on the kinetic theory of rarefied gases. The solid line — represents the model given in (5.12) (left). (Right) The solid line — represents the distribution given in (3.52) based on the kinetic theory of rarefied gases.

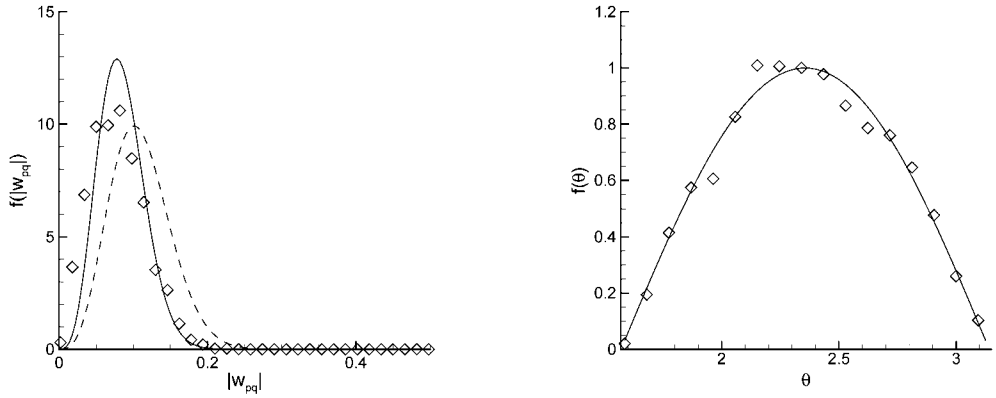

Figure 5.18: Norm of the droplet relative velocity at collision $|\mathbf{w}_{pq}|$ measured in fluid flow with $Re_\lambda = 32.9$, for droplet **Case 4** with $St = 1.83$ (left) represented by $\square$ and collision angle θ (right). The dashed line $- - -$ represents the distribution given in (3.53) based on the kinetic theory of rarefied gases. The solid line — represents the model given in (5.12) (left). (Right) The solid line — represents the distribution given in (3.52) based on the kinetic theory of rarefied gases.

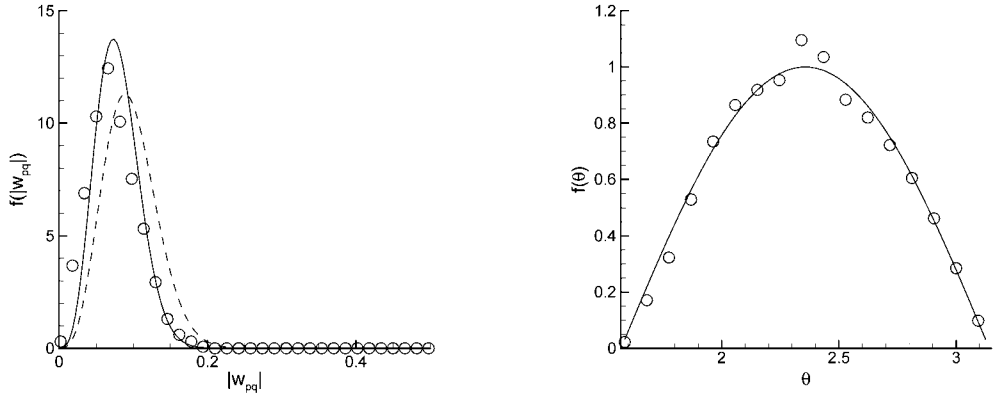

Figure 5.19: Norm of the droplet relative velocity at collision $|\mathbf{w}_{pq}|$ measured in fluid flow with $Re_\lambda = 32.9$, for droplet **Case 5** with $St = 2.72$ (left) represented by $\square$ and collision angle θ (right). The dashed line $- - -$ represents the distribution given in (3.53) based on the kinetic theory of rarefied gases. The solid line — represents the model given in (5.12) (left). (Right) The solid line — represents the distribution given in (3.52) based on the kinetic theory of rarefied gases.

the low relative velocities at collision and a similar direction leads to a higher number of grazing collision compared to the case of molecular chaos. Figure 5.15 (left) shows besides the measures in DNS/DPS (□) also two lines. The dashed line − − − corresponds to the distribution given in (3.53), based on the kinetic theory of rarefied gases. In order to account for the correlation of the droplet velocities by the fluid turbulence, the droplet agitation in (3.53) can be written, similar to the mean relative velocity in the collision source terms (see (4.141)), as

$$f_{\mathbf{w}_{pq}}\left(\mathbf{w}_{pq}\right) = 4n_p^2 d_p^2 \sqrt{\pi T_p} \frac{1}{8T_p^2} \mathbf{w}_{pq}^3 \exp\left(-\frac{\mathbf{w}_{pq}^2}{4T_p}\right) \quad , \tag{5.12}$$

with T_p as

$$T_p = \frac{2}{3} q_p^2 \left(1 - \xi_{fp}^2\right) \quad . \tag{5.13}$$

The distribution that corresponds to (5.12) is shown in fig. 5.15 (left) by the solid line —. The measured values (symbol □) do not really coincide with the distribution given in (5.12), but this model still performs much better than the model for the relative velocity based on the kinetic theory of rarefied gases not accounting for correlations (dashed line − − −).

Comparing fig. 5.15 to fig. 5.19 for the respective droplet inertia, it can be seen that collision angle θ is well represented by the model from (3.52), with exception of the case of $St = 0.11$. The norm of the droplet relative velocity at collision is always better interpreted by the model from (5.12), accounting for the correlation of the droplet velocities by the fluid turbulence. It is seen in fig. 5.15 to fig. 5.19 that the two models (dashed line − − − for the model based on the molecular-chaos assumption and solid line — for the model accounting for the correlation of droplet velocities) approach each other with increasing droplet inertia, which is logical, since the correlation coefficient tends to 0 for increasing droplet inertia (increasing Stokes number) in the model accounting for the correlation of droplet velocities and thus (3.53) and (5.12) are identical.

Figure 5.20 shows the influence of fluid turbulence on the collision angle for the least inertial droplets investigated at $St \approx 0.1$. Figure 5.20 (top left) exhibits the collision angle θ measured in the fluid flow with $Re_\lambda = 18.1$. It is seen that grazing collisions (for low values of collision angle) are overestimated in comparison to predictions based on the kinetic theory of rarefied gases. The same behavior is shown in fig. 5.20 (top right) for the fluid flow with $Re_\lambda = 32.9$, but to a lesser extent. For the fluid flow with the highest degree of turbulence with $Re_\lambda = 60.5$, the overestimation of grazing collisions almost vanishes. As the droplet Stokes number is comparable for the three investigated fluid turbulence fields, this

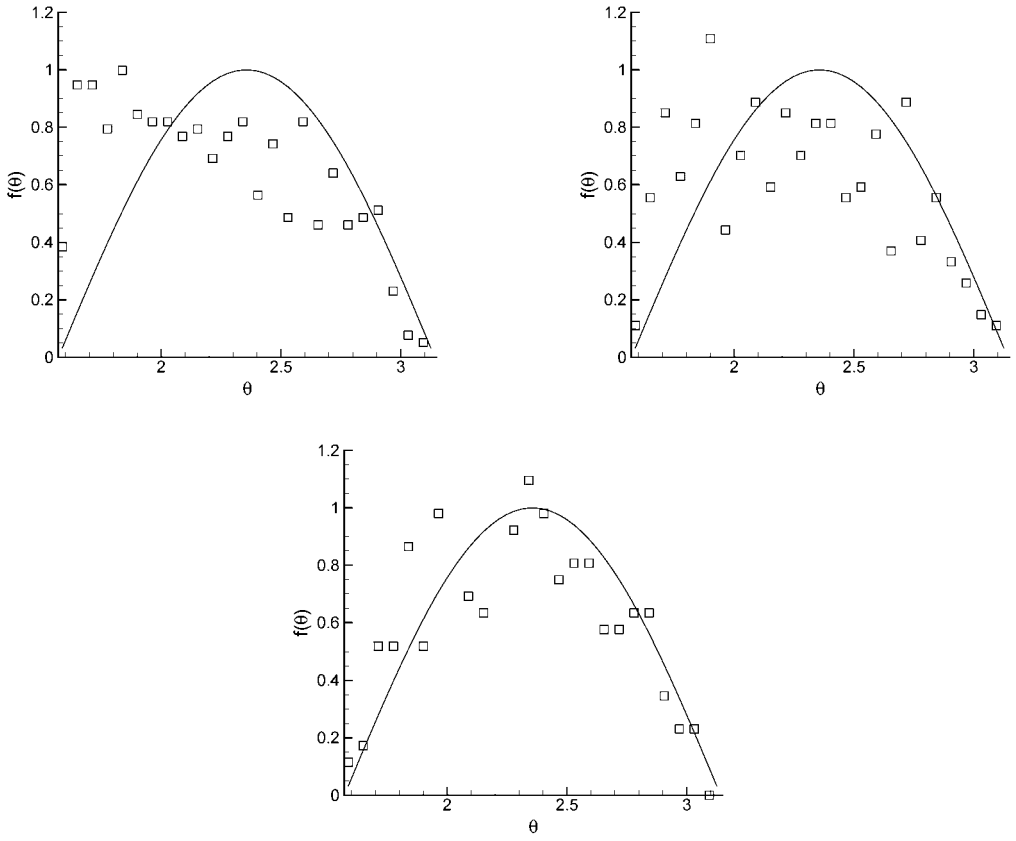

Figure 5.20: The solid line — represents the collision angle distribution given in (3.52) based on the kinetic theory of rarefied gases. Droplet **Case 1** with $St = 0.11$ represented by □ with fluid flow with $Re_\lambda = 18.1$ (top left), $Re_\lambda = 32.9$ (top right) and $Re_\lambda = 60.5$ (bottom).

Table 5.6: Properties of initially log-normal distributed droplet phase in fluid turbulence field $Re_\lambda = 32.9$.

Symbol	**Case LN-1**	**Case LN-2**	**Case LN-3**
N_p	100000	100000	100000
α_p	$4.388\ 10^{-4}$	$4.388\ 10^{-4}$	$4.388\ 10^{-4}$
$d_{p,mean,ini}$	$2.600\ 10^{-4}$	$2.600\ 10^{-4}$	$2.600\ 10^{-4}$
σ	0.12	0.12	0.12
ρ_p	226.3	905.3	2263.3
q_p^2/q_f^2	0.890	0.529	0.314
$0.5\ q_{fp}/q_p^2$	1.00	1.01	1.01
$q_{f@p}^2/q_f^2$	1.057	1.044	1.069
τ_p	$4.282\ 10^{-2}$	$1.625\ 10^{-1}$	$3.968\ 10^{-1}$
Re_p	0.670	1.250	1.551
$\tau_{f@p}^t$	$1.922\ 10^{-1}$	$1.631\ 10^{-1}$	$1.631\ 10^{-1}$
$St = \frac{\tau_p}{\tau_{f@p}^t}$	0.25	1.00	2.43
$St_K = \frac{\tau_p}{\tau_K}$	1.69	5.70	13.92

behavior is due to the influence of fluid turbulence. The higher the Reynolds number the smaller are the characteristic length and time scales that control the droplet behavior and consequently the absolute degree of correlation of the droplet velocities decreases, showing a collision angle distribution closer to the theoretic predictions.

5.1.3 Log-normal distributed droplet phase

In order to evaluate the influence of the droplet initial distribution on the coalescence rate, simulations are conducted with an initially log-normal distributed droplet phases. An overview of the properties is given in table 5.6. Three different droplet densities are used in order to achieve three droplet phases with different droplet inertia. Another strong interest of simulations with initially log-normal distributed droplets is the comparison to the DQMOM approach, as it allows to discretize the diameter distribution using the Gauss-Quadrature approximation. A comparison to a continuous distribution is thus possible, while using an initially monodisperse droplet phase the Dirac functions in DQMOM are compared to a Dirac distribution from DNS/DPS.

Figure 5.21 shows the log-normal distribution used. The symbols represent the measured

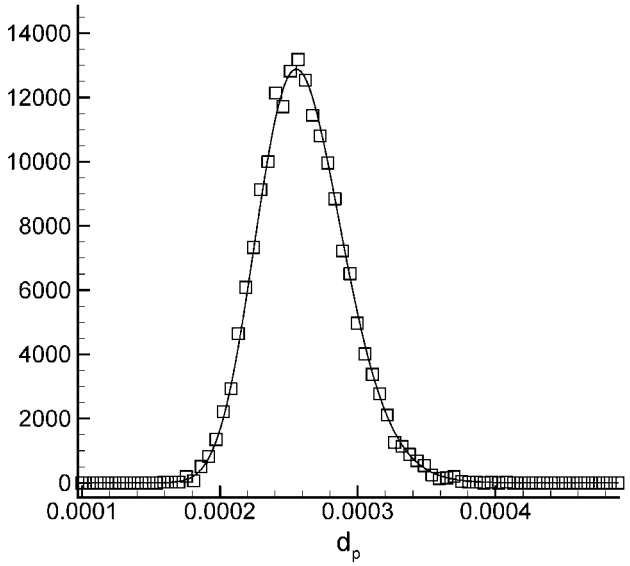

Figure 5.21: Initial mutual log-normal droplet diameter distribution for all three cases $LN-1$, $LN-2$ and $LN-3$ given in table 5.6. The solid line — represents the log-normal distribution with $d_{10} = 2.6\ 10^{-4}$ and $\sigma = 0.12$.

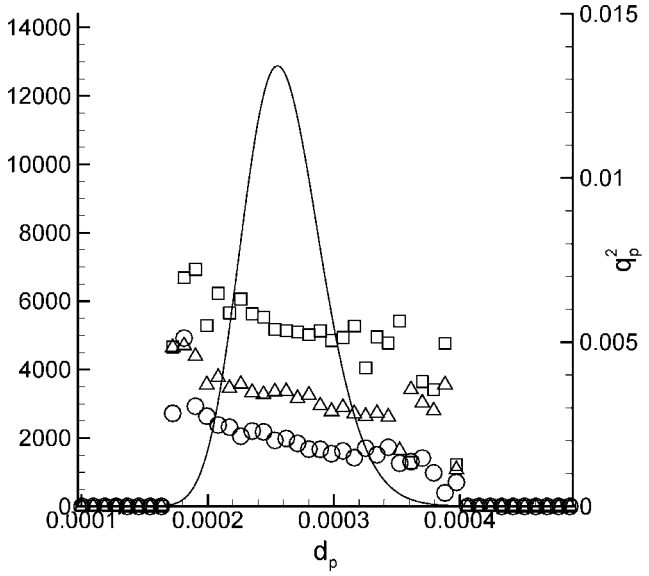

Figure 5.22: Droplet kinetic energy q_p^2 for all three cases $LN-1$ □, $LN-2$ △ and $LN-3$ ◯ given in table 5.6. The solid line represents the initial log-normal distribution from fig. 5.21.

diameter distribution function and the solid line — represents the log-normal distribution with $d_{10} = 2.6\ 10^{-4}$ and $\sigma = 0.12$. It is shown in section 3.4.4 that droplets with different masses exhibit different values for the droplet kinetic energy in the equilibrium state. Figure 5.22 shows the distribution of droplet kinetic energy over the droplet diameter for all three cases from table 5.6. Cases $LN-1$ □, $LN-2$ △ and $LN-3$ ◯ all show a decreasing droplet kinetic energy with increasing droplet diameter. The symbols are to be read on the right axis of fig. 5.22. The statistics of the droplet kinetic energy are not very clean on the left and right extremity of the log-normal droplet diameter distribution as seen in fig. 5.22. It will be seen in chapter 6 that this situation creates some difficulties in some of the simulations performed comparing DQMOM to DNS/DPS. The solid line — in fig. 5.22 represents the initial log-normal distribution from fig. 5.21.

5.2 Results from DNS/DPS

Once the fluid-droplet flow reached a local equilibrium after initialization, as shown in fig. 5.1, coalescence is activated and all droplet collisions lead, in a first step, to permanent coalescence. From this point on, it is not possible anymore to average over time, since the droplet phase keeps constantly changing its properties. The results shown in the following are mean values over all droplets in function of time or instantaneous distributions, like the droplet diameter distribution at a given time. In the simulations performed within this work, the influence of the fluid turbulence and the influence of the droplet inertia are assessed. In order to investigate the influence of the fluid turbulence, time is normalized by the Eulerian integral time scale of the fluid, whereas time is normalized by the initial droplet response time in order to account for the influence of the droplet inertia.

5.2.1 Initially mono-disperse distributed droplet phase

Droplet number

The first and most evident quantity, which changes accounting for coalescence of colliding droplets, is the number of droplets in the flow. The maximal droplet number $N_{p,ini}$ is given at the start of the coalescence phase in the simulations performed here and no continuous injection of additional droplets exists. Droplet break-up is neither considered. Figure 5.23 (top) shows the number of droplets normalized by initial droplet number $N_{p,ini}$ over time normalized by the integral Eulerian time scale of the fluid for the fluid flow with $Re_\lambda = 18.1$. Figure 5.23 (bottom) shows the number of droplets normalized by initial droplet number $N_{p,ini}$ over time normalized by the droplet response time τ_p of the corre-

sponding droplet class. Figures 5.24 and 5.25 show the same statistics as fig. 5.23, but for fluid flow fields with $Re_\lambda = 32.9$ (fig. 5.24) and with $Re_\lambda = 60.5$ (fig. 5.25) respectively. Basically two mechanisms can be identified in gas-solid flows, which are contributing to the collision rates of inertial droplets [141]. First, the correlation or de-correlation of the droplet relative velocity of neighboring droplets due to the fluid turbulence, and second, an accumulation of droplets in regions of low vorticity as a consequence of the centrifugal force. This accumulation effect is also referred to as preferential concentration and can lead to an increase of the collision frequency in homogenous turbulence [106], [133]. For both low-inertia droplets and high-inertia droplets two distinct solutions are well known. The solution of Saffman and Turner [110] for zero-inertia droplets with finite volume and the works of Abrahamson [1] for high-inertia droplets, which is based on the kinetic theory of rarefied gases. If the droplet response time τ_p is smaller than the Kolmogorov time scale τ_K, and consequently the Stokes number based on the Kolmogorov time scale St_K is smaller than 1, the solution of Saffman and Turner [110] is applicable and the collision frequency is small in gas-solid flows. Accounting for coalescence, a low coalescence rate should therefore be expected if the droplet Stokes number on the Kolmogorov time scale is smaller than 1, with an initially monodisperse diameter distribution of the dispersed phase.

The initial monodisperse droplet class with the lowest droplet inertia is denoted by $\square$ for all fluid flows in fig. 5.23 to 5.25. The droplet Stokes number on the Lagrangian time scale is $St = 0.11$, while the droplet Stokes number on the Kolmogorov time scale is equal to $St_K = 0.55$ for the fluid turbulence with $Re_\lambda = 32.9$. These droplets are thus strongly following the fluid flow and are entrained by the small vortical structures of fluid turbulence, which are responsible for the dissipation of fluid energy. Figures 5.23 to 5.25 show clearly that these low-inertia droplets exhibit the lowest coalescence rate of all computed droplet classes. With a droplet Stokes numbers based on the Kolmogorov time scale smaller than 1, this first class of droplets lies in the regime of Saffman and Turner [110]. Figures 5.24 to 5.25 (bottom) show the normalized number of droplets over time, which is normalized by the corresponding droplet response time. It is seen that a given reduction in droplet number is achieved the faster, in terms of time/τ_p, the higher the droplet inertia is. The limiting case for the highest droplet inertia corresponds to the molecular-chaos assumption and thus to a complete de-correlation of the droplet velocities before collision.

A major difficulty lies in a correct prediction of collision terms in the intermediate Stokes regime. The DNS/DPS simulations performed here constitute a reference for a pure coalescing regime. Figures 5.23 (top) to fig. 5.25 (top) demonstrate that the droplet class with the highest inertia, denoted by $\bigcirc$, does not show the most important coalescence rate over time/T_E, where time is normalized in fig. 5.23 (top) to fig. 5.25 (top) with the

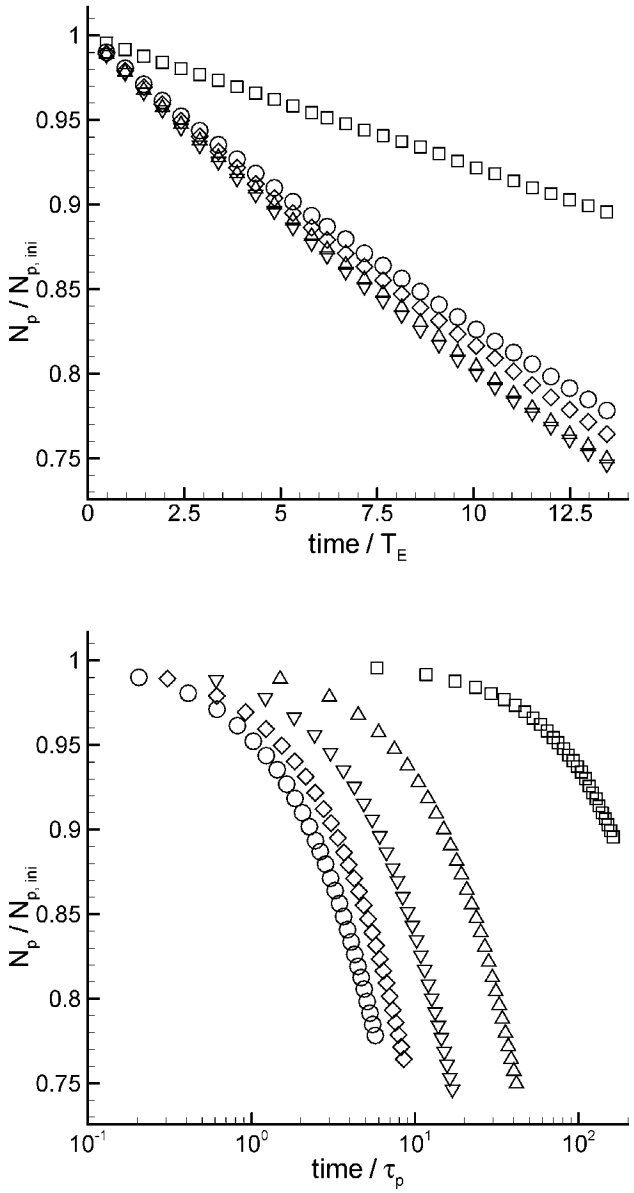

Figure 5.23: (Top) Fluid flow field $Re_\lambda = 18.1$. Number of droplets normalized by initial droplet number $N_{p,ini}$ over time normalized by the integral Eulerian time scale of the fluid (top) and time normalized by the droplet response time of the corresponding droplet class (bottom). The symbols stand for the following initial droplet Stokes numbers: $St = 0.11$ $\square$, $St = 0.44$ $\triangle$, $St = 1.09$ ∇, $St = 2.15$ $\Diamond$, $St = 3.22$ $\bigcirc$.

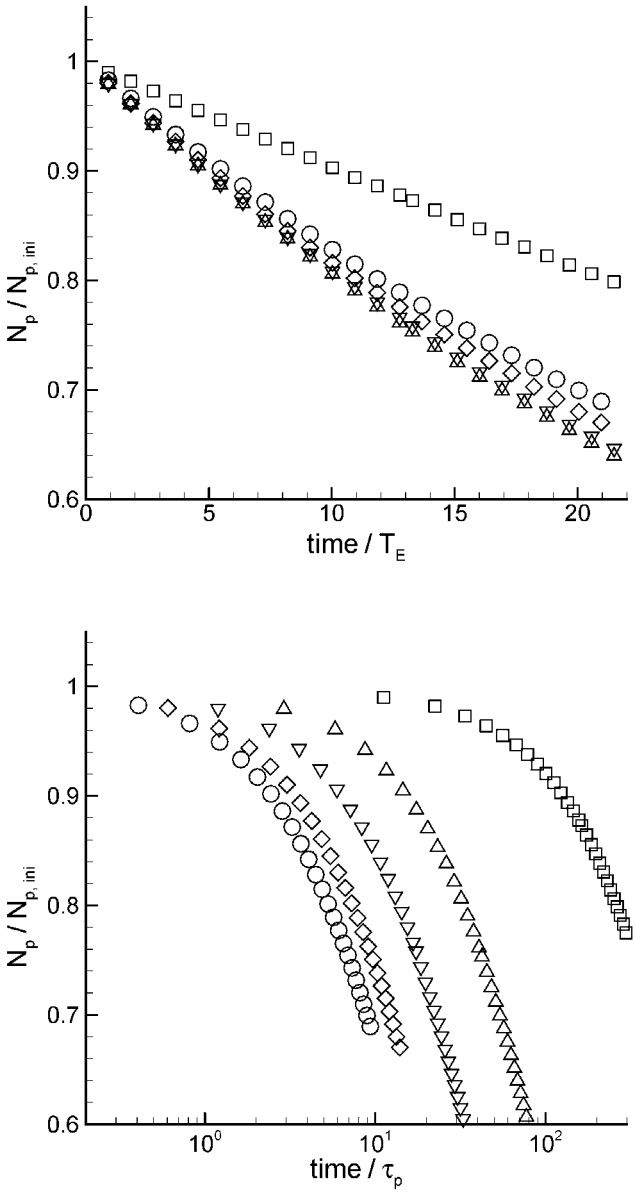

Figure 5.24: (Top) Fluid flow field $Re_\lambda = 32.9$. Number of droplets normalized by initial droplet number $N_{p,ini}$ over time normalized by the integral Eulerian time scale of the fluid (top) and time normalized by the droplet response time of the corresponding droplet class (bottom). The symbols stand for the following initial droplet Stokes numbers: $St = 0.11$ $\square$, $St = 0.42$ $\triangle$, $St = 1.03$ ∇, $St = 1.83$ $\Diamond$, $St = 2.72$ $\bigcirc$.

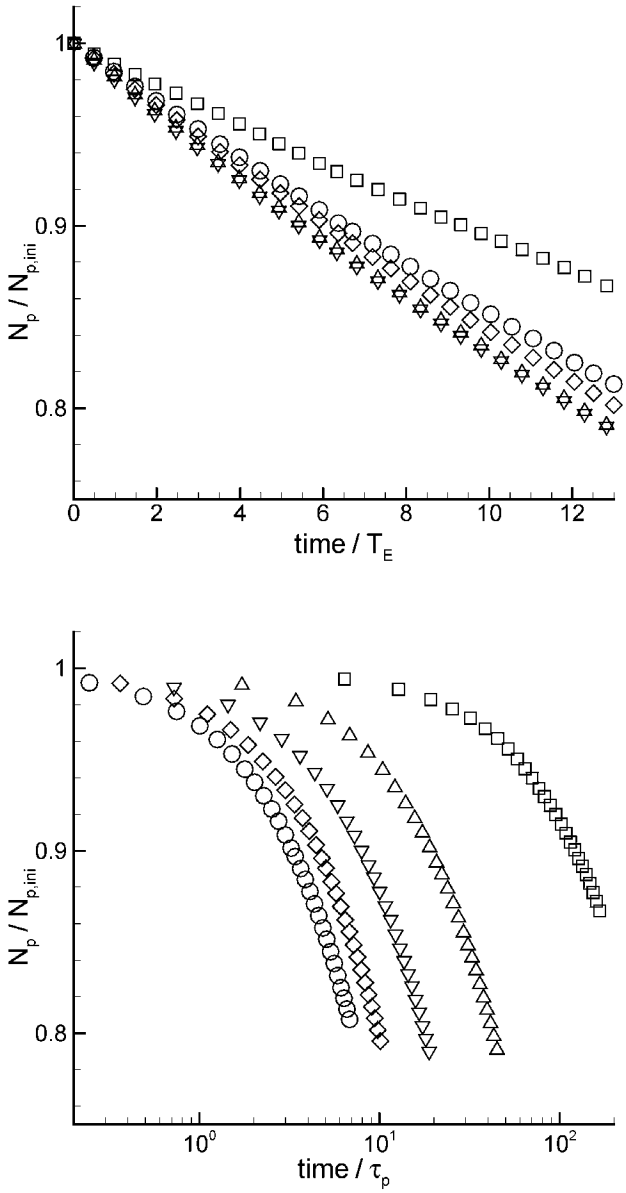

Figure 5.25: (Top) Fluid flow field $Re_\lambda = 60.5$. Number of droplets normalized by initial droplet number $N_{p,ini}$ over time normalized by the integral Eulerian time scale of the fluid (top) and time normalized by the droplet response time of the corresponding droplet class (bottom). The symbols stand for the following initial droplet Stokes numbers: $St = 0.12$ □, $St = 0.46$ △, $St = 1.10$ ▽, $St = 1.78$ ◊, $St = 2.63$ ◯.

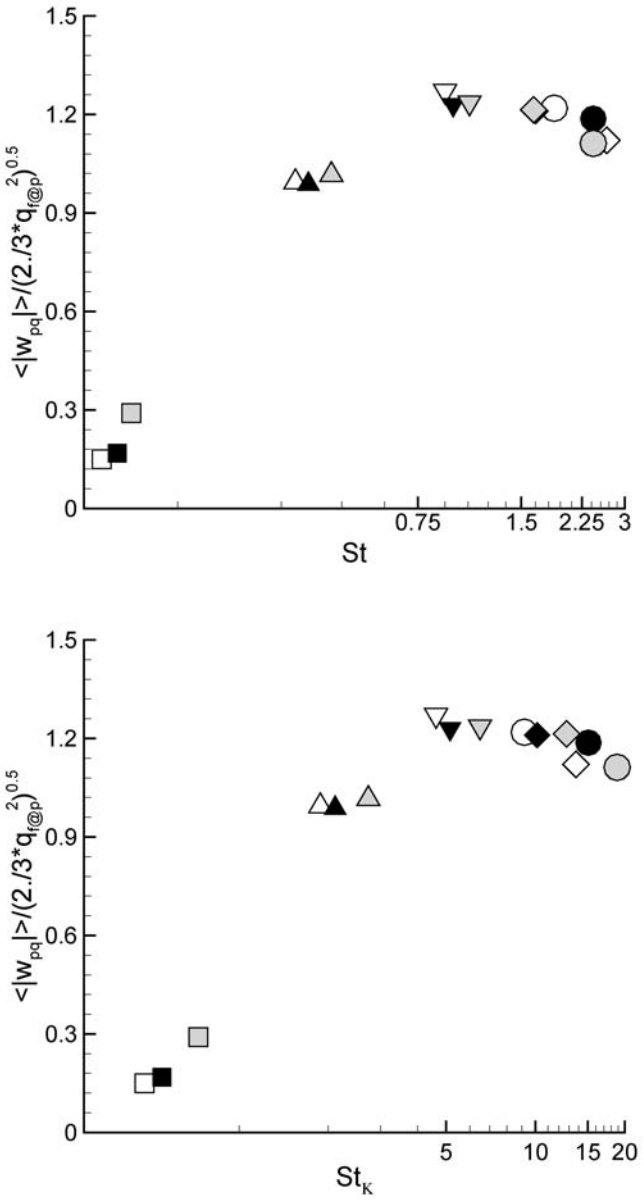

Figure 5.26: Average norm of relative velocity $\langle |\mathbf{w}_{pq}| \rangle / \sqrt{\frac{2}{3} q^2_{f@p}}$ at collision in non-coalescing regime over droplet Stokes number on the integral Lagrangian time scale (top) and over droplet Stokes number on Kolmogorov time scale (bottom) for, fluid flow with $Re_\lambda = 18.1$ (clear symbols) , $Re_\lambda = 32.9$ (black symbols) and $Re_\lambda = 60.5$ (grey symbols).

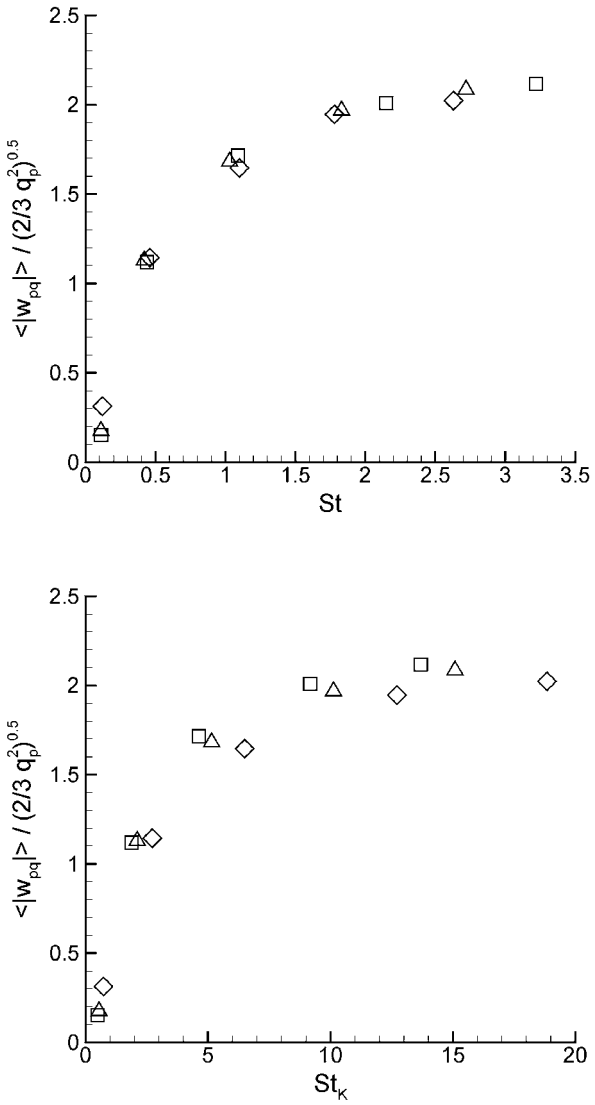

Figure 5.27: Average norm of relative velocity normalized by $\sqrt{\frac{2}{3}q_p^2}$, $\langle|\mathbf{w}_{pq}|\rangle / \sqrt{\frac{2}{3}q_p^2}$ at collision in non-coalescing regime over droplet Stokes number on the integral Lagrangian time scale (top) and over droplet Stokes number on Kolmogorov time scale (bottom) for, fluid flow with $Re_\lambda = 18.1$ $\square$, $Re_\lambda = 32.9$ $\triangle$ and $Re_\lambda = 60.5$ $\Diamond$.

integral Eulerian time scale of the fluid T_E. The most important statistical quantity, for the modeling of the coalescence rate, is the droplet relative velocity at the moment of collision, for an approach based on the kinetic theory of rarefied gases. Figure 5.26 shows the mean of the norm of relative velocity $\langle|\mathbf{w}_{pq}|\rangle$ at the moment of collision over the droplet Stokes number based on the integral Lagrangian time scale in the top of fig. 5.26, and based on the Kolmogorov time scale in the bottom of fig. 5.26. Whereas fig. 5.27 shows the average norm of relative velocity normalized by $2q_p^2$, $\langle|\mathbf{w}_{pq}|\rangle/2q_p^2$ over the droplet Stokes number based on the integral Lagrangian time scale (top) and the droplet Stokes number based on the Kolmogorov time scale (bottom). These values are measured in a pure collision regime, after a local equilibrium state is reached and where coalescence is not accounted for. While fig. 5.27 exhibits a maximum for the highest droplet Stokes numbers and indicates a asymptotic behavior for the largest Stokes numbers, fig. 5.26 shows, for all three turbulent flow fields, on the top that a maximum value for the norm of the relative velocity is obtained for a droplet Stokes number based on the integral Lagrangian time scale of about $St = 1$. Figure 5.26 (top) shows a maximum in the relative velocity at the moment of collision for the droplet class denoted by ∇. As mentioned before, these values are measured in a pure collision regime without coalescence, but just before coalescence is started. Figure 5.23 (top) and fig. 5.25 (top) show that the highest coalescence rate is obtained for these droplet classes, which possess the highest relative velocity at the moment of collision, just before coalescence is started. Figure 5.26 (black symbols) shows a maximum for the relative velocity at the moment of collision for the droplet class denoted by $\Diamond$, but not the most important coalescence rate as seen in fig. 5.24 (top). This indicates that the relative velocity at the moment of collision is not the only determining parameter for the coalescence rate of droplets with an intermediate Stokes number. This is in coherence with findings from gas-solid flows [141], where preferential concentration plays an important role. Fessler *et al.* [44], Février [47] or Wang and Squires [134] show that a maximum of accumulation of droplets is reached in homogeneous isotropic turbulence of gas-solid flows for droplet Stokes numbers based on the integral Lagrangian time scale in the order of $[0.1, 1.0]$.

Several authors [47], [124] attribute the effects of preferential concentration to large structures, which create centrifugal forces on the droplets, leading to zones of droplet accumulation. Fede [41] reproduces findings of Février [47], in which the intensity of accumulations diminishes with an increasing turbulent Reynolds number, which is explained by an increasing number of small structures disturbing the effects of accumulation. It should be mentioned here, that a second interpretation of droplet accumulation exists, which refers the droplet concentration to a regime in which the droplet response time is of the same order as the Kolmogorov time scale (see works of Wang and Maxey [132], Wang *et al.* [133])

and thus controlled by the dissipative scales of turbulence.

The droplet classes exhibiting the highest coalescence rates (see fig. 5.23 (top) to fig. 5.25 (top)) possess initial droplet Stokes numbers based on the integral Lagrangian time scale in the range in the order of $[0.1, 1.0]$ for which accumulation reaches a maximum, as shown by Fede [41]. This might indicate that, besides the droplet relative velocity at the moment of collision, the accumulation effect has an augmenting influence on the coalescence rate for droplets in this regime.

Figures 5.23 to fig. 5.25 compare different droplet Stokes numbers for the same turbulent Reynolds number. For the coalescence rates shown in fig. 5.28 to fig. 5.30 the droplet Stokes number is kept constant and the turbulent Reynolds number is altered. These results are shown for droplet inertia from **Case** 1 $\square$, **Case** 3 ∇ and **Case** 5 $\bigcirc$ only. The empty symbols $\square, \nabla, \bigcirc$ stand for the for fluid flows with $Re_\lambda = 18.1$, the black symbols $\blacksquare, \blacktriangledown, \bullet$ stand for the for fluid flows with $Re_\lambda = 32.9$ and the gray symbols $\blacksquare, \blacktriangledown, \bullet$ stand for the for fluid flows with $Re_\lambda = 60.5$. Figures 5.28 to fig. 5.30 show that the coalescence rate increases with an increasing turbulent Reynolds number. Here, it is not of importance, whether the time is normalized by the Eulerian integral time scales of the fluid as seen in fig. 5.28 (top) or by the droplet response time as given in fig. 5.28 (bottom), the coalescence rate increases for the lowest droplet Stokes number investigated with an increasing Reynolds number. Figure 5.26 shows the relative velocity of droplets at the moment of collision as discussed above. The lowest turbulent Reynolds number investigated $Re_\lambda = 18.1$ is given in fig 5.26 (top) and the highest turbulent Reynolds number investigated $Re_\lambda = 60.5$ is given in fig 5.26 (bottom). Comparing these to figures, an increase in magnitude of relative velocity can be read on the ordinates from $Re_\lambda = 18.1$ in fig 5.26 (top) to $Re_\lambda = 60.5$ in fig 5.26 (bottom). As a consequence, a higher coalescence rate is to be expected for a higher turbulent Reynolds number with the same time interval for the lowest-inertia droplets.

The degree of correlation of the droplet velocities by the fluid turbulence is expressed in terms of the droplet Stokes number. Throughout fig. 5.28 to fig. 5.30 the degree of correlation is therefore similar for the different investigated turbulent Reynolds numbers and can be regarded as a constant parameter, evaluating the coalescence rate. For **Case 1** in fig. 5.28 the droplet inertia is very low, and with a droplet Stokes number based on the Kolmogorov time scale smaller than 1, this class of droplets is partially controlled by the dissipative scales of fluid turbulence, as explained above. Figure 5.29 and fig. 5.30, for droplet **Case 3** and **Case 5** respectively, show an important difference in comparison with droplet **Case 1** for the lowest-inertia droplets in fig. 5.28. The coalescence rate does not increase with the turbulent Reynolds number for droplet Stokes numbers based on the integral Lagrangian time scales of the order or larger than 1, but it decreases. The degree

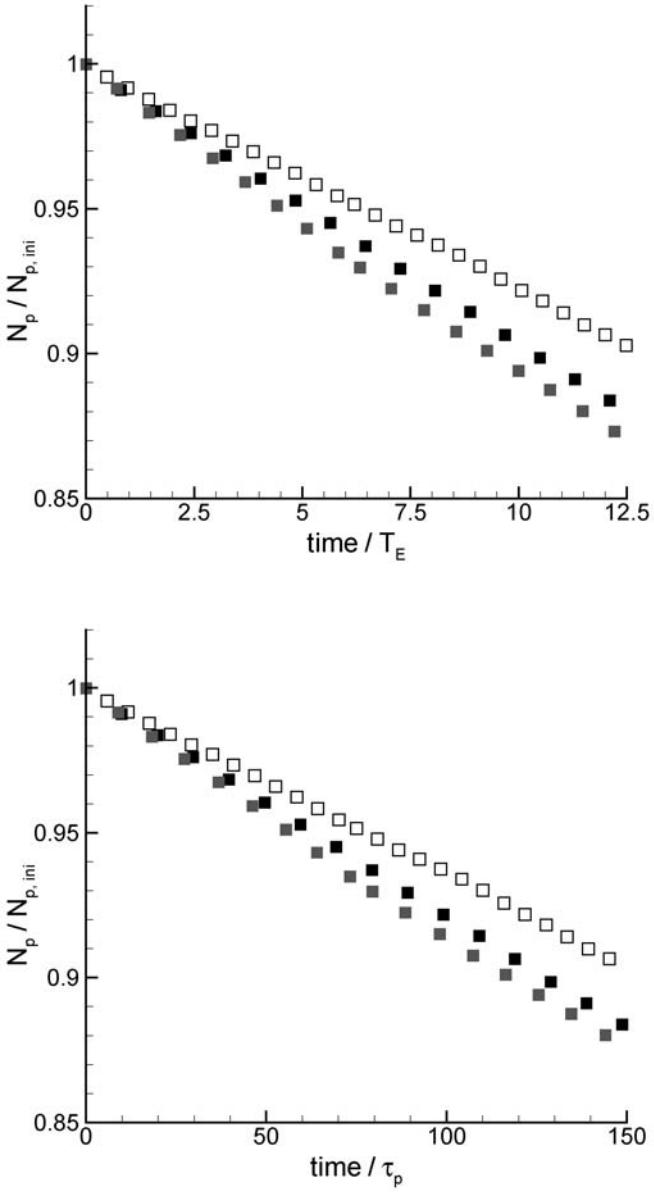

Figure 5.28: Number of droplets normalized by initial droplet number $N_{p,ini}$ over time normalized by the integral Eulerian time scale of the fluid (top) and over time normalized by the droplet response time of the corresponding droplet class (bottom). The symbols stand for droplet **Case 1** for all three turbulent flow fields $Re_\lambda = 18.1$ □, $Re_\lambda = 32.9$ ■ and $Re_\lambda = 60.5$ ■.

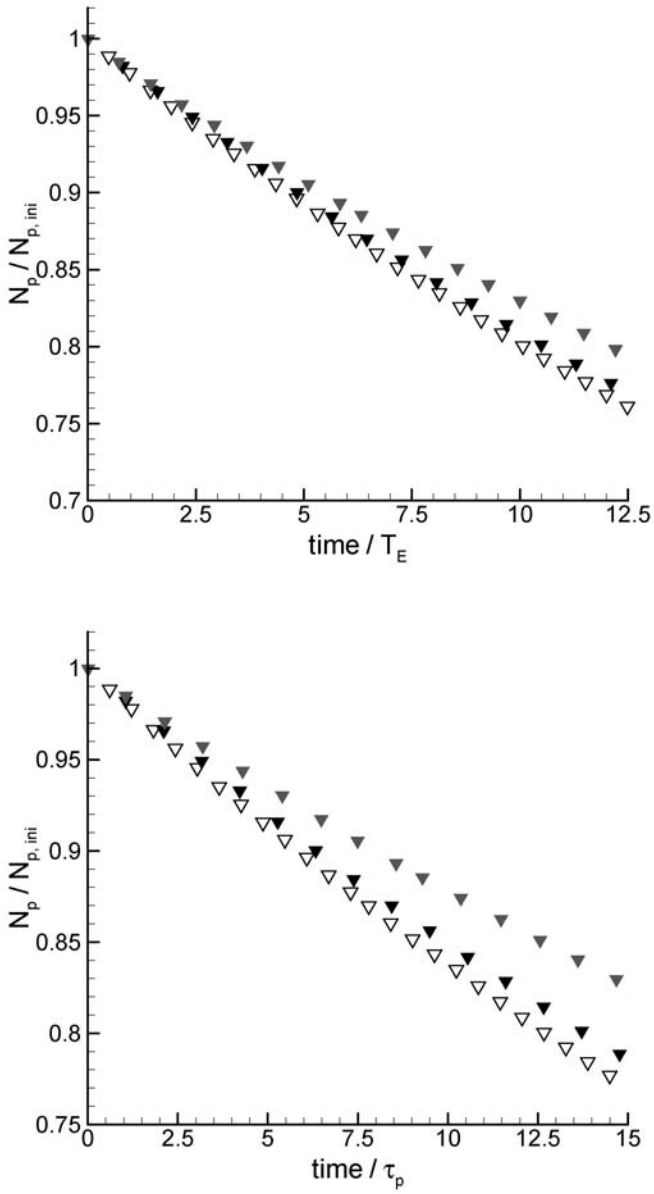

Figure 5.29: Number of droplets normalized by initial droplet number $N_{p,ini}$ over time normalized by the integral Eulerian time scale of the fluid (top) and over time normalized by the droplet response time of the corresponding droplet class (bottom). The symbols stand for droplet **Case 3** for all three turbulent flow fields $Re_\lambda = 18.1$ ∇, $Re_\lambda = 32.9$ $\blacktriangledown$ and $Re_\lambda = 60.5$ $\blacktriangledown$.

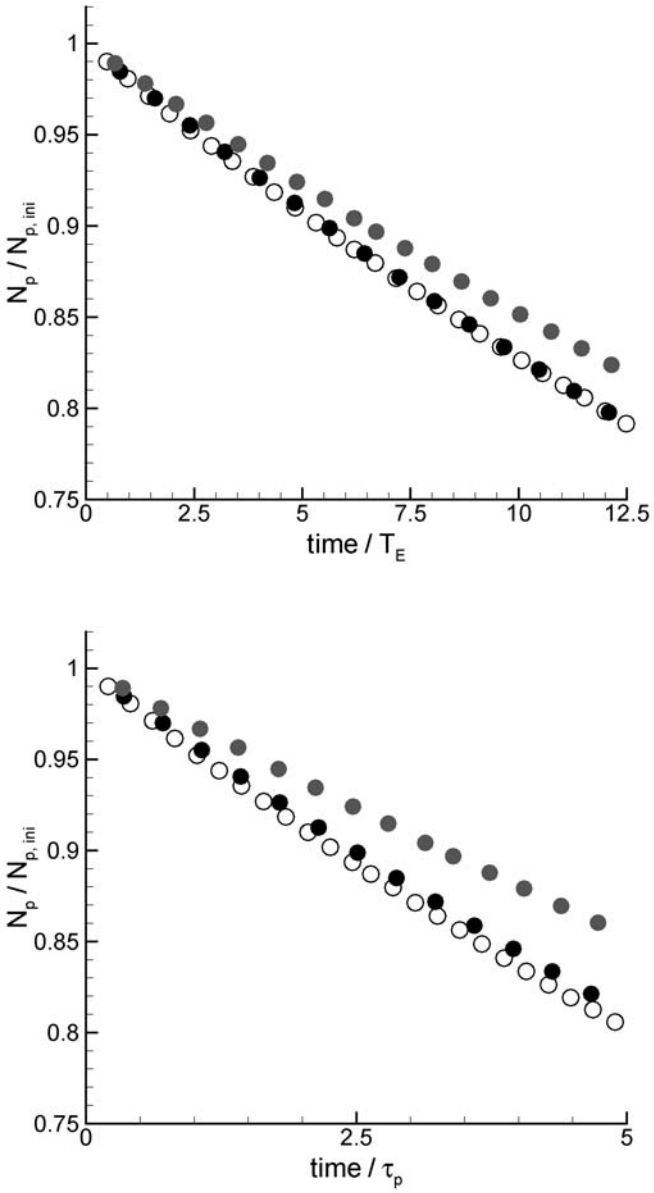

Figure 5.30: Number of droplets normalized by initial droplet number $N_{p,ini}$ over time normalized by the integral Eulerian time scale of the fluid (top) and over time normalized by the droplet response time of the corresponding droplet class (bottom). The symbols stand for droplet **Case 5** for all three turbulent flow fields $Re_\lambda = 18.1$ ◯, $Re_\lambda = 32.9$ ● and $Re_\lambda = 60.5$ ●.

of correlation of the droplet velocities by the fluid turbulence is the same for all three turbulent flow fields investigated. As explained above these droplets with droplet Stokes numbers based on the integral Lagrangian time scales of the order or larger than 1 do not fall into the regime of Saffman and Turner [110] and are thus not entirely controlled by the fluid turbulence. Two mechanisms contributing to the collision rate in gas-solid flows were identified [133], [135], [67]. The turbulent transport effect, based on the relative velocity of neighboring droplets and the accumulation effect, as already mentioned above. As fig. 5.26 shows an increase in the relative velocity of droplets with an increasing turbulent Reynolds number, but the DNS/DPS simulations performed here exhibit a decrease of the coalescence rate with increasing turbulent Reynolds number, this decrease in coalescence rate cannot be explained by the turbulent transport effect for droplet Stokes number of the order or larger than 1. The accumulation effect, however, can explain the measured behavior. Fede [41] shows that the degree of accumulation decreases with an increasing turbulent Reynolds number. This behavior is already discussed above. The degree of correlation of the droplet velocities is the same for the three investigated flow fields, and with a decreasing degree of accumulation for an increasing turbulent Reynolds number, the coalescence rate has to decrease, since a higher accumulation increases locally the droplet volume fraction, which has as a consequence an increase in collision frequency in gas-solid flow or coalescence rate.

Mean diameter and diameter distributions

Coalescence leads to the creation of larger droplets. Even an initially monodisperse droplet diameter distribution becomes very fast poly-disperse in diameter. If, as it is done in this work, droplet break-up is neglected and each collision leads to permanent coalescence, the droplet size distribution becomes wider continuously. If droplet break-up is accounted for, an even wider range of droplet diameters exists. These droplets with very different diameters (and thus different mass) exhibit a strongly inhomogeneous inertial behavior, as it is shown above for coalescence rates of droplet classes with different droplet inertia. The dispersion of droplets is therefore strongly influenced by the diameter distributions. The size of droplets is equally of great importance, if droplet evaporation is accounted for, since larger droplets take more time to evaporate than smaller ones.

In fig. 5.31 to fig. 5.33 (top) the Sauter mean diameter d_{32} normalized by initial Sauter diameter $d_{32,ini}$ over time normalized by the integral Eulerian time scale of the fluid is shown, and in fig. 5.31 to fig. 5.33 (bottom) the Sauter mean diameter d_{32} normalized by initial Sauter diameter $d_{32,ini}$ over time normalized by the droplet response time of the

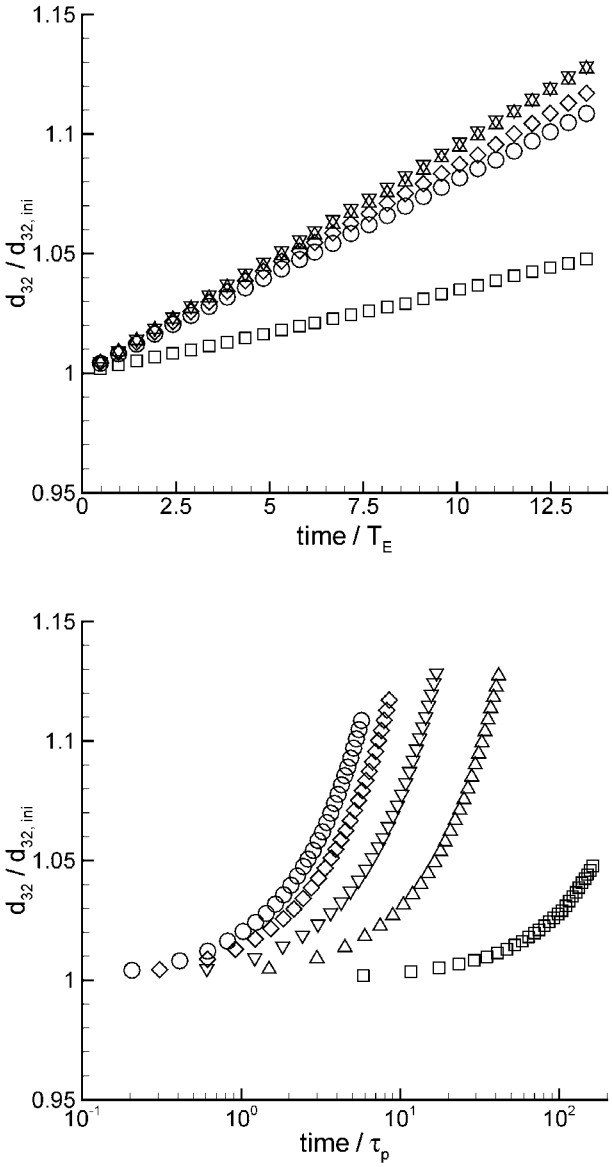

Figure 5.31: Fluid flow field $Re_\lambda = 18.1$. Sauter mean diameter d_{32} normalized by initial Sauter mean diameter $d_{32,ini}$ over time normalized by the integral Eulerian time scale of the fluid (top) and over time normalized by the droplet response time of the corresponding droplet class (bottom). The symbols stand for the following initial droplet Stokes numbers: $St = 0.11$ $\square$, $St = 0.44$ $\triangle$, $St = 1.09$ ∇, $St = 2.15$ $\Diamond$, $St = 3.22$ $\bigcirc$.

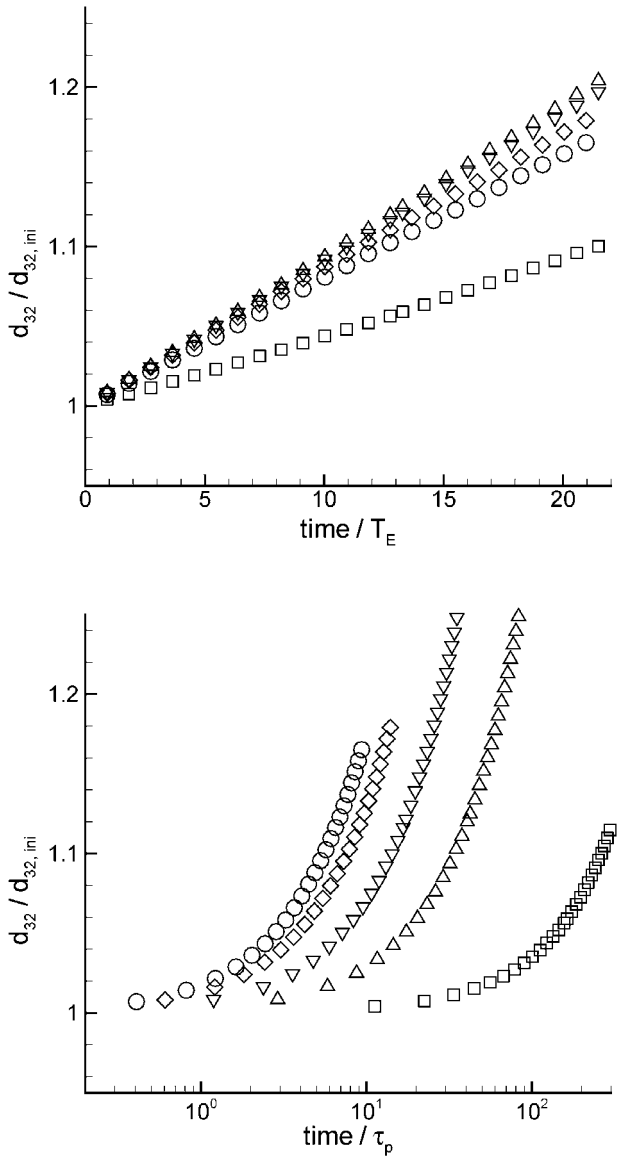

Figure 5.32: Fluid flow field $Re_\lambda = 32.9$. Sauter mean diameter d_{32} normalized by initial Sauter mean diameter $d_{32,ini}$ over time normalized by the integral Eulerian time scale of the fluid (top) and over time normalized by the droplet response time of the corresponding droplet class (bottom). The symbols stand for the following initial droplet Stokes numbers: $St = 0.11$ $\square$, $St = 0.42$ $\triangle$, $St = 1.03$ ∇, $St = 1.83$ $\Diamond$, $St = 2.72$ $\bigcirc$.

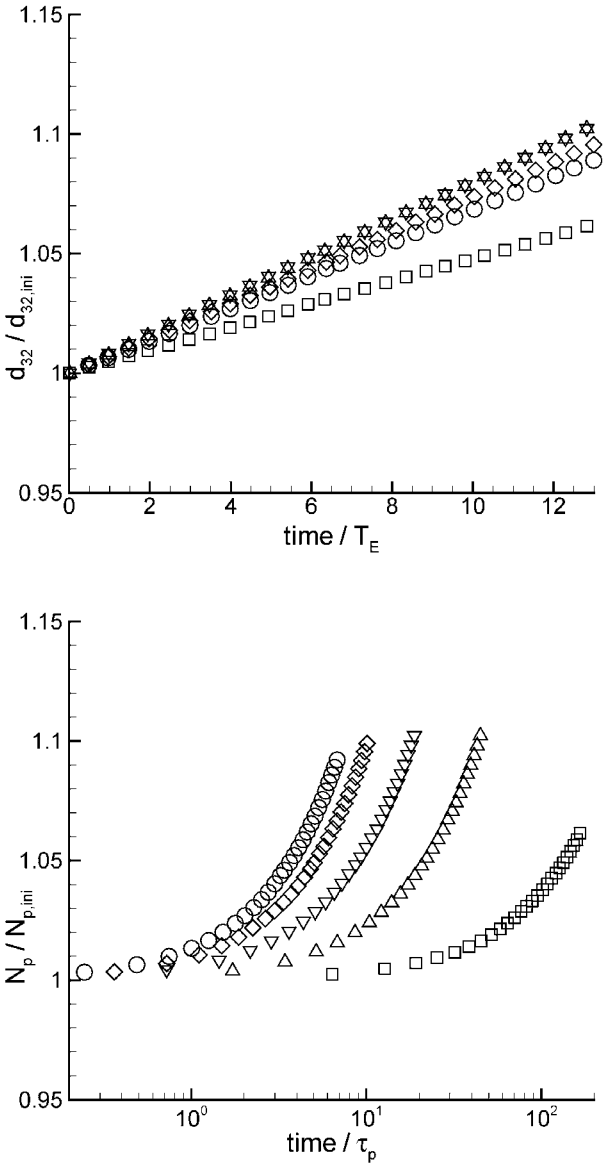

Figure 5.33: Fluid flow field $Re_\lambda = 60.5$. Sauter mean diameter d_{32} normalized by initial Sauter mean diameter $d_{32,ini}$ over time normalized by the integral Eulerian time scale of the fluid (top) and over time normalized by the droplet response time of the corresponding droplet class (bottom). The symbols stand for the following initial droplet Stokes numbers: $St = 0.12$ $\square$, $St = 0.46$ $\triangle$, $St = 1.10$ ∇, $St = 1.78$ $\Diamond$, $St = 2.63$ $\bigcirc$.

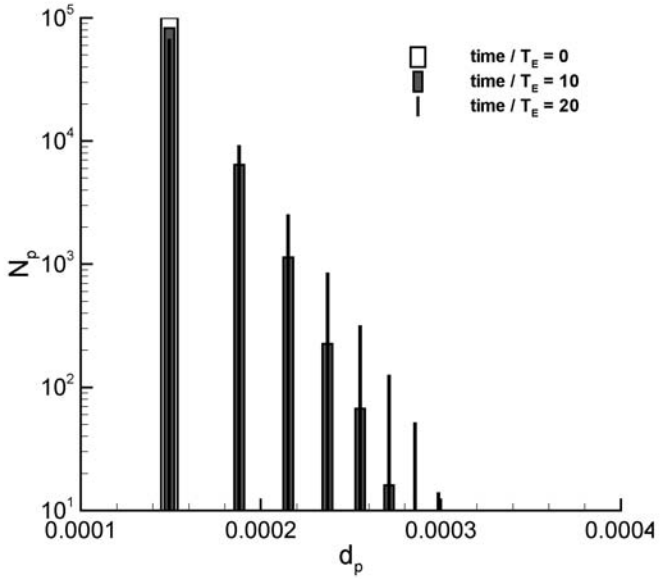

Figure 5.34: Fluid flow field with $Re_\lambda = 32.9$. Instantaneous diameter distribution for droplet **Case 1** with $St = 0.11$ at times $\frac{t}{T_E} = 0$ □, $\frac{t}{T_E} = 10$ ■ and $\frac{t}{T_E} = 20$ ■.

corresponding droplet class is shown. The Sauter mean diameter d_{32} is calculated as

$$d_{32} = \frac{\langle d_p^3 \rangle}{\langle d_p^2 \rangle} \quad . \tag{5.14}$$

Figures 5.31 to fig. 5.33 for the Sauter mean diameter over time show the inverse behavior of fig. 5.23 to fig. 5.25 for the droplet number over time. The higher the coalescence rate, the higher the resulting mean diameter of the droplet mixture, since more coalescence leads, in a pure coalescing regime, to larger droplets. The argumentation for the influence of the droplet inertia on the coalescence rate holds also for the Sauter mean diameter, as coalescence rate and mean diameter are directly linked.

Besides the mean diameter, also the diameter distribution is of great interest, especially because droplets of different diameter (and thus different mass) exhibit very different inertial behavior, as it is shown above. Figures 5.34 to fig. 5.36 show the diameter distribution of initially monodisperse droplet diameters for three different droplet inertia $St = 0.11$ (in fig 5.34), $St = 1.03$ (in fig 5.35) and $St = 2.72$ (in fig 5.36) for the fluid turbulence case with turbulent Reynolds number $Re_\lambda = 32.9$. The droplet diameter distribution is shown for this fluid turbulence case only. The white bar □ in fig. 5.34 to fig. 5.36 shows the

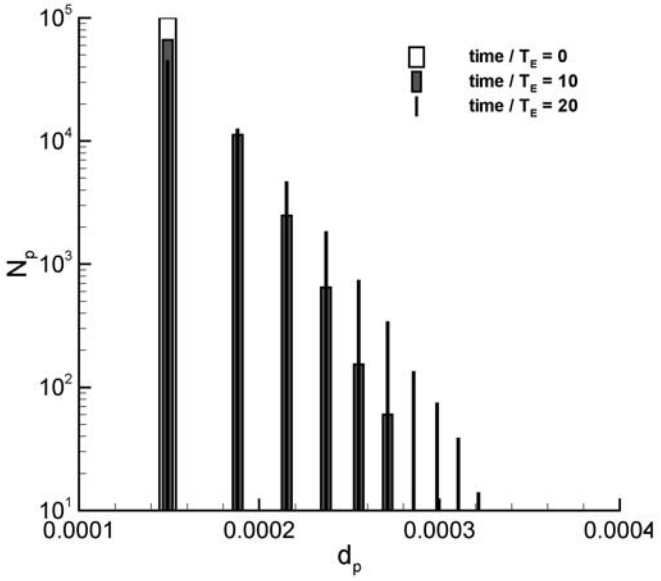

Figure 5.35: Fluid flow field with $Re_\lambda = 32.9$. Instantaneous diameter distribution for droplet **Case 3** with $St = 1.03$ at times $\frac{t}{T_E} = 0$ □, $\frac{t}{T_E} = 10$ ■ and $\frac{t}{T_E} = 20$ ■.

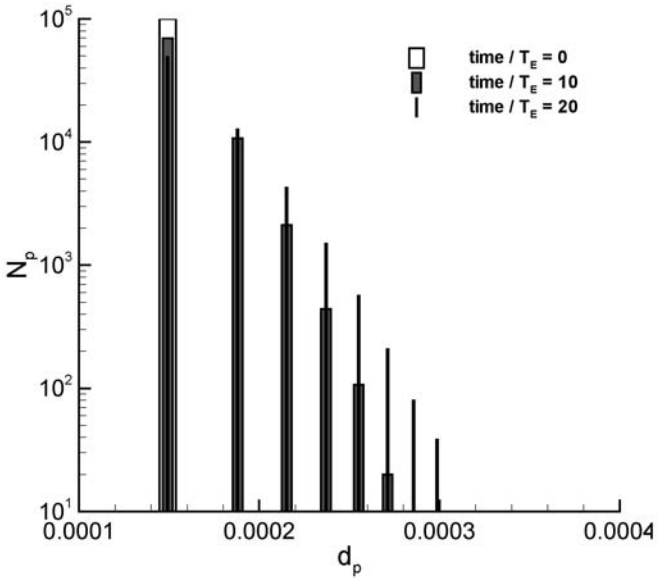

Figure 5.36: Fluid flow field with $Re_\lambda = 32.9$. Instantaneous diameter distribution for droplet **Case 5** with $St = 2.72$ at times $\frac{t}{T_E} = 0$ □, $\frac{t}{T_E} = 10$ ■ and $\frac{t}{T_E} = 20$ ■.

initial monodisperse diameter distribution at time/$T_E = 0$, the gray bars ■ the diameter distribution at time/$T_E = 10$ and finally the black bars ■ at time/$T_E = 20$. The largest diameters are reached at time/$T_E = 20$ for the droplet **Case 3** in fig. 5.35 with about 3.2 10^{-4}, which is not surprising since this intermediate droplet class in terms of inertia shows the highest coalescence rate among the cases presented here. It is seen, comparing fig. 5.34 to fig. 5.36, that the more larger diameters exist, the higher the coalescence rate is, which seems to be logic. The newly originating droplet diameters from coalescence shown in fig. 5.34 to fig. 5.36 are all the same, independently of the droplet inertia, as they are directly related to the initial diameter which is the same for all droplet cases.

Droplet kinetic energy

In chapter 2 the mechanisms of coalescence are detailed. The deformation of the droplets at collision dissipates droplet kinetic energy. In the simulations performed within this work, this aspect is neglected as explained in chapter 3. (3.81) shows the mass-and momentum conservation equations for droplet coalescence. In a homogeneous isotropic turbulence this leads to a decrease in droplet kinetic energy each time two droplets coalesce. The droplet kinetic energy should therefore diminish the stronger, the higher the coalescence rate is. Figure 5.37 to fig. 5.39 show the droplet kinetic energy q_p^2 over time normalized by the integral Eulerian time scale of the fluid flow with turbulent Reynolds number $Re_\lambda = 32.9$. The droplet kinetic energy in fig. 5.37 to fig. 5.39 is fluctuating with the kinetic energy of the fluid flow, the stronger the smaller the droplet inertia. The droplet inertia is the second influencing parameter next to the coalescence rate. The higher inertia a droplet possesses, the slower it responses to the flow and the clearer is the effect of coalescence in the decrease of the droplet kinetic energy in fig. 5.37 to fig. 5.39. The highest decrease in droplet kinetic energy is observed for the highest coalescence rate.

5.2.2 Initially lognormal distributed droplet phase

The results from simulations with initial lognormal distributed diameters are presented in the following. First, the evolution of the droplet number in a pure coalescing regime is shown, second the evolution of the Sauter mean diameter is shown. Third, the droplet diameter distribution in function of the droplet inertia is shown and finally, the evolution of the lognormal diameter distribution is presented. As presented in section 5.1.3, three different cases are computed (see table 5.6) with initial lognormal distributed diameters. For computational reasons, the minimum diameter of the initial lognormal distribution is the same as the initial diameter in the case of initially monodisperse diameters. The

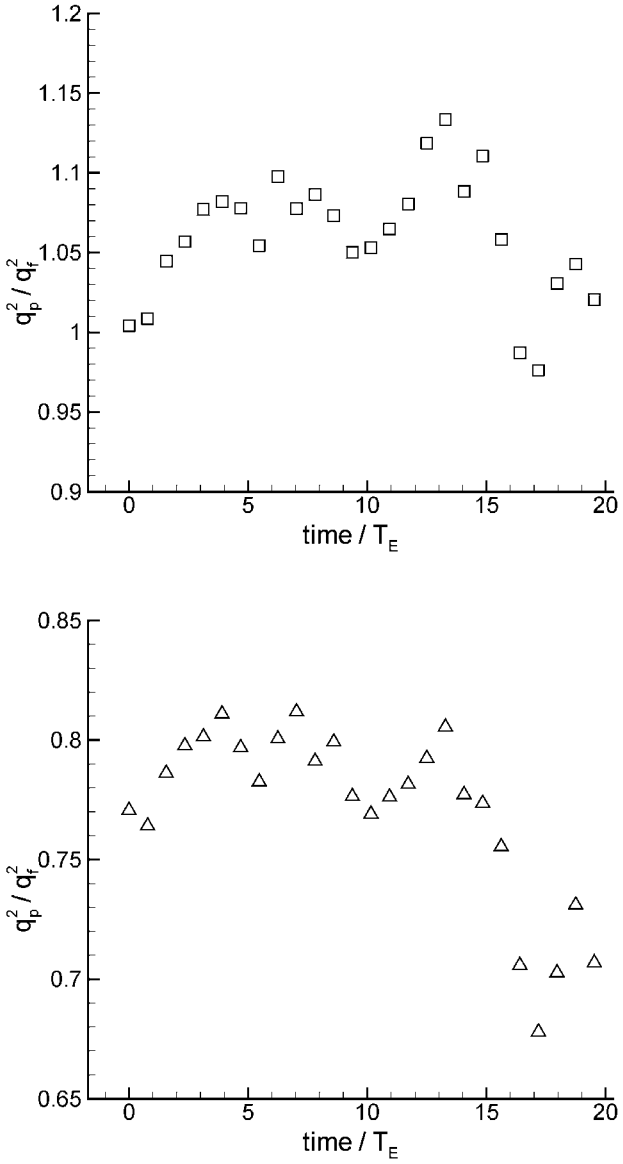

Figure 5.37: Fluid flow field $Re_\lambda = 32.9$. Droplet kinetic energy q_p^2 over time normalized by the integral Eulerian time scale of the fluid. The symbols □ stand for the initial droplet Stokes number $St = 0.11$ (top) and the symbols △ stand for the initial droplet Stokes number $St = 0.42$ (bottom).

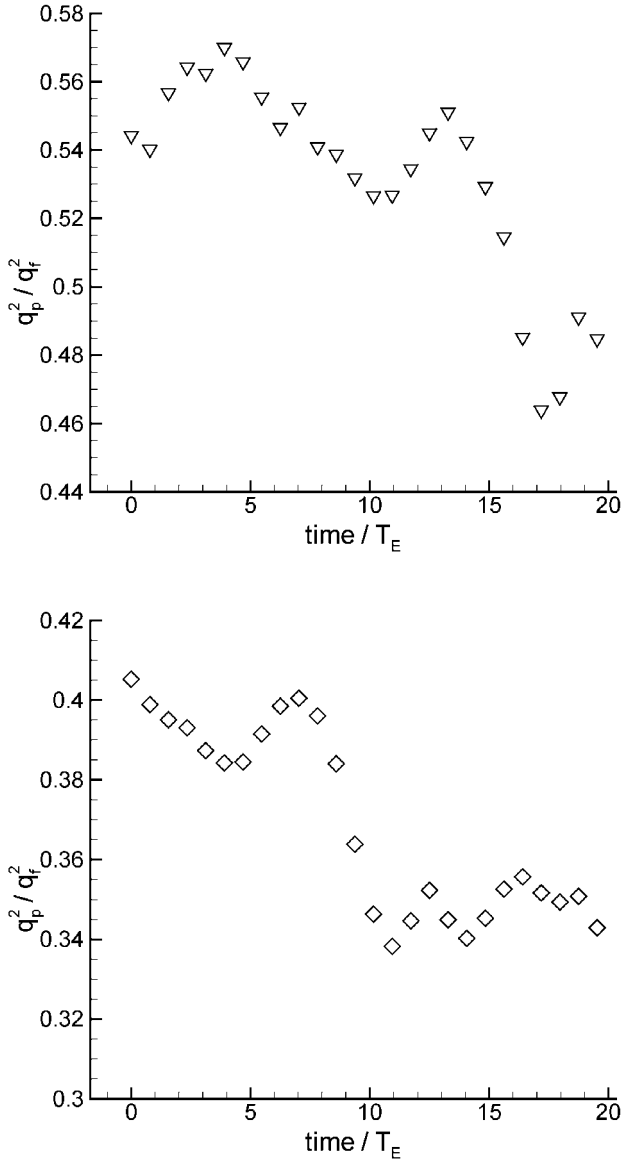

Figure 5.38: Fluid flow field $Re_\lambda = 32.9$. Droplet kinetic energy q_p^2 over time normalized by the integral Eulerian time scale of the fluid. The symbols ∇ stand for the initial droplet Stokes number $St = 1.03$ (top) and the symbols $\diamond$ stand for the initial droplet Stokes number $St = 1.83$ (bottom).

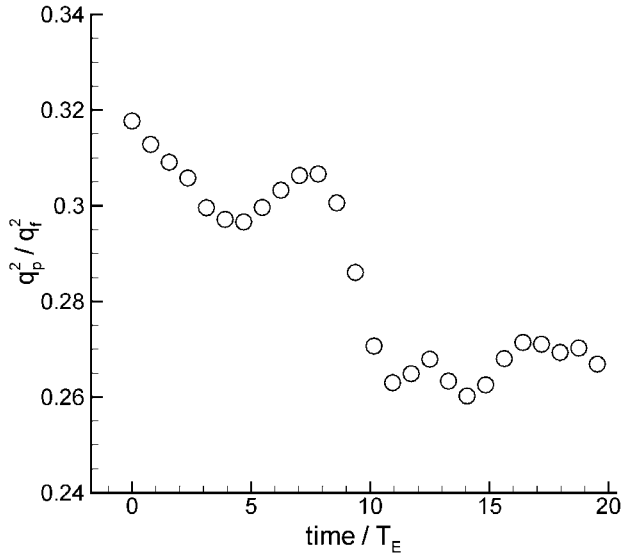

Figure 5.39: Fluid flow field $Re_\lambda = 32.9$. Droplet kinetic energy q_p^2 over time normalized by the integral Eulerian time scale of the fluid. The symbols ◯ stand for the initial droplet Stokes number $St = 2.72$.

simulations performed with a lognormal distribution show consequently much larger diameters. Therefore, it is difficult to compare these simulations to the ones done with an initial monodisperse diameter distribution. Figure 5.40 (top) shows the number of droplets normalized by the initial droplet number $N_{p,ini}$ over time normalized by the integral Eulerian time scale of the fluid for fluid flow case 128^3. It is seen that the decrease in droplet number follows an exponential law and is not linear, as it might be supposed for the simulations with an initial monodisperse distribution, because of its lesser reduction in droplet number of up to 20% only, compared with up to 60% for the results presented in fig. 5.40 (top). Figure 5.40 (bottom) shows the number of droplets normalized by initial droplet number $N_{p,ini}$ over time normalized by the droplet response time of the corresponding droplet class. Again, over an abscissa time/τ_p, the droplet class with the highest inertia exhibits the most important coalescence rate, as it is already seen for the case of an initial monodisperse diameter distributions. The Sauter mean diameter d_{32}, shown in fig. 5.41, develops with respect to the corresponding coalescence rates. The droplet class with the highest coalescence rate, denoted by □, shows the highest Sauter mean diameter evolution.

Besides the mean diameter, the evolution of the diameter distribution is of importance, since one single diameter might not be sufficient to represent correctly a distribution

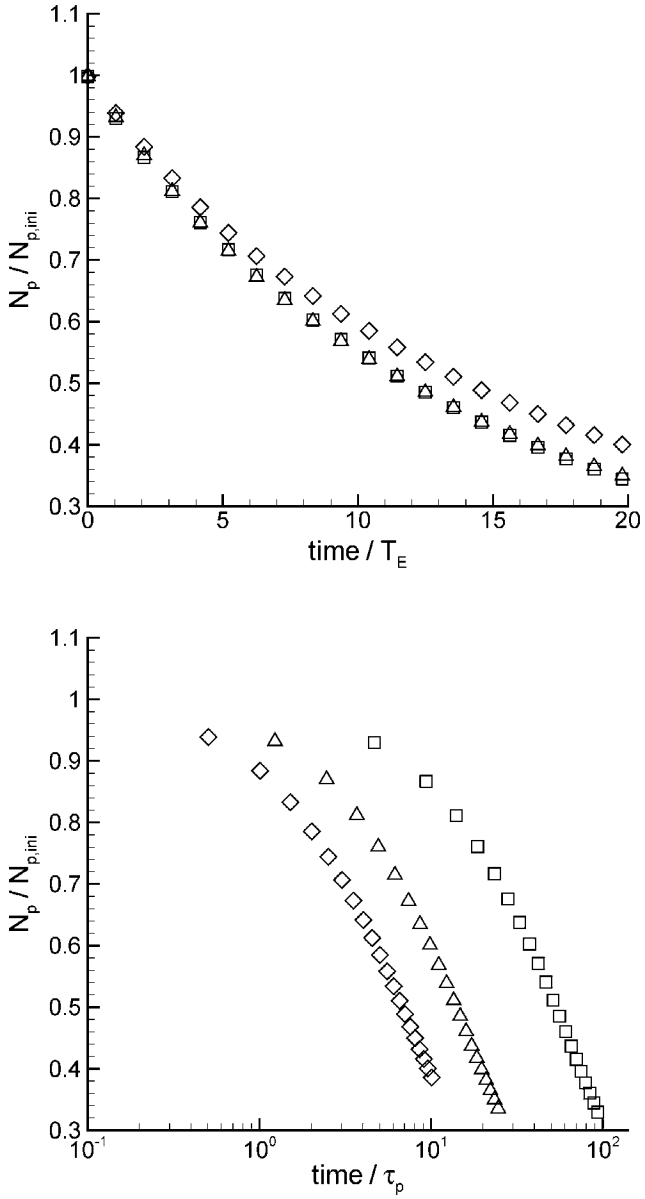

Figure 5.40: (Top) Number of droplets normalized by initial droplet number $N_{p,ini}$ over time normalized by the integral Eulerian time scale of the fluid (top) and over time normalized by the droplet response time of the corresponding droplet class (bottom). The symbols stand for droplet **Case LN-1** $\square$, **Case LN-2** $\triangle$ and **Case LN-3** $\Diamond$ for turbulent flow field with $Re_\lambda = 32.9$.

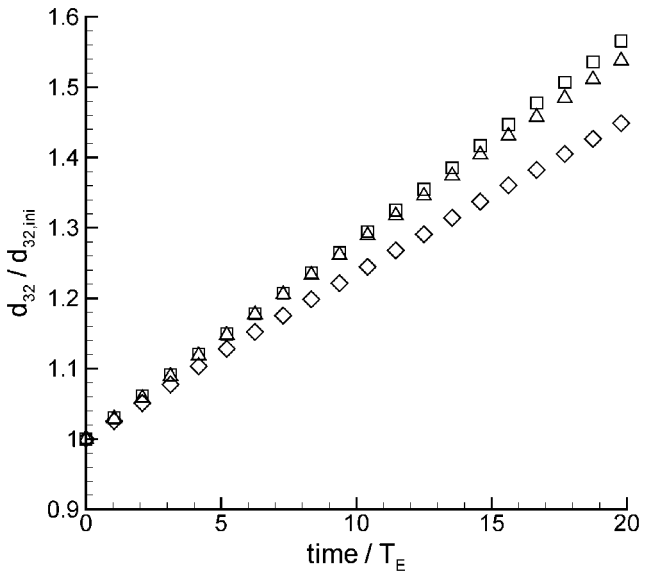

Figure 5.41: Sauter mean diameter d_{32} over time normalized by the integral Eulerian time scale of the fluid. The symbols stand for droplet **Case LN-1** $\square$, **Case LN-2** $\triangle$ and **Case LN-3** $\Diamond$ for turbulent flow field with 128^3 grid points and $Re_\lambda = 32.9$.

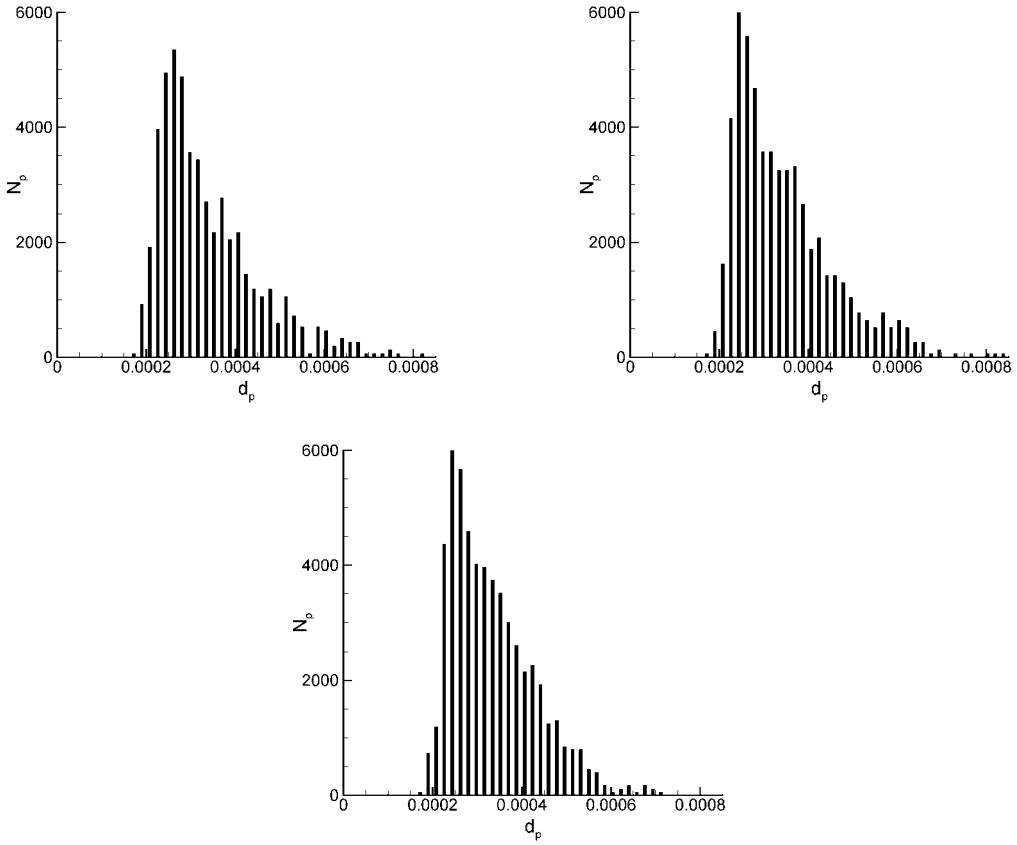

Figure 5.42: (Top left) Droplet diameter distribution at time $\frac{\text{time}}{T_E} = 20$ for initially lognormal droplet diameter distribution **Case LN-1**. (Top right) Droplet diameter distribution at time $\frac{\text{time}}{T_E} = 20$ for initially lognormal droplet diameter distribution **Case LN-2**. (Bottom) Droplet diameter distribution at time $\frac{\text{time}}{T_E} = 20$ for initially lognormal droplet diameter distribution **Case LN-3**.

and thus its inertial behavior. Both the study of the fundamental physics of turbulence-coalescence interaction and the comparison with statistical model predictions are subject of this work. To know the diameter distribution is of importance as reference for the validation of certain statistical models, as seen in chapter 6. Likewise, it serves a correct interpretation of the underlying physics. Figure 5.42 shows the droplet diameter distributions at time $\frac{\text{time}}{T_E} = 20$ for initially lognormal droplet diameter distributions. Figure 5.42 (top left) corresponds to the case with the highest coalescence rate. Whereas it is difficult to interpret the different evolution for larger diameters in comparison of the three distributions in fig. 5.42, it is seen that fig. 5.42 (top left) shows the highest reduction in droplet number for droplets around the initial mean diameter, which corresponds to the highest coalescence rate as mentioned. The distributions in fig. 5.42 will serve especially in chapter 6 for the comparison with predictions from DQMOM.

Figure 5.43 shows the time evolution of the initially lognormal distributed droplet diameters. As expected, the droplet number decreases, while new larger droplet diameters emerge from coalescence. From fig. 5.43 (middle left) on in time, it is seen that the tail of the distribution for large droplet diameters does not follow a pure exponential form, as it might have been expected. Authors often report on an exponential tail of the diameter distributions for either raindrop formation [58] or for fuel sprays [84]. This might be explained by the fact that, in the simulations performed here, the maximum number of droplets is given at the beginning and decreases constantly by coalescence at the same time as break-up or creation of satellite droplet are absent. In sprays new droplets are constantly created, which respect the initial diameter distribution characteristic to the injector. In other words, in the reported works a source for smaller diameters exists, while in this work no source exists. The only mechanism that acts on the droplet diameter distribution is permanent coalescence.

5.2.3 Different droplet collision outcomes

In a last study the influence of different droplet collision outcomes (permanent coalescence, stretching separation and reflexive separation) is investigated. The boundaries used in order to do so are introduced in chapter 2 and the droplet collision handling is described in section 3.4.5.

The strong dependence of the coalescence rate using different droplet collision outcomes, as it is seen in fig. 5.44 (top) must be underlined. While the lowest inertia droplets with a droplet Stokes number of $St = 0.11$ □ do not show any sensitivity, and in fact they show exact the same result, droplets with higher inertia are very sensitive to the different droplet

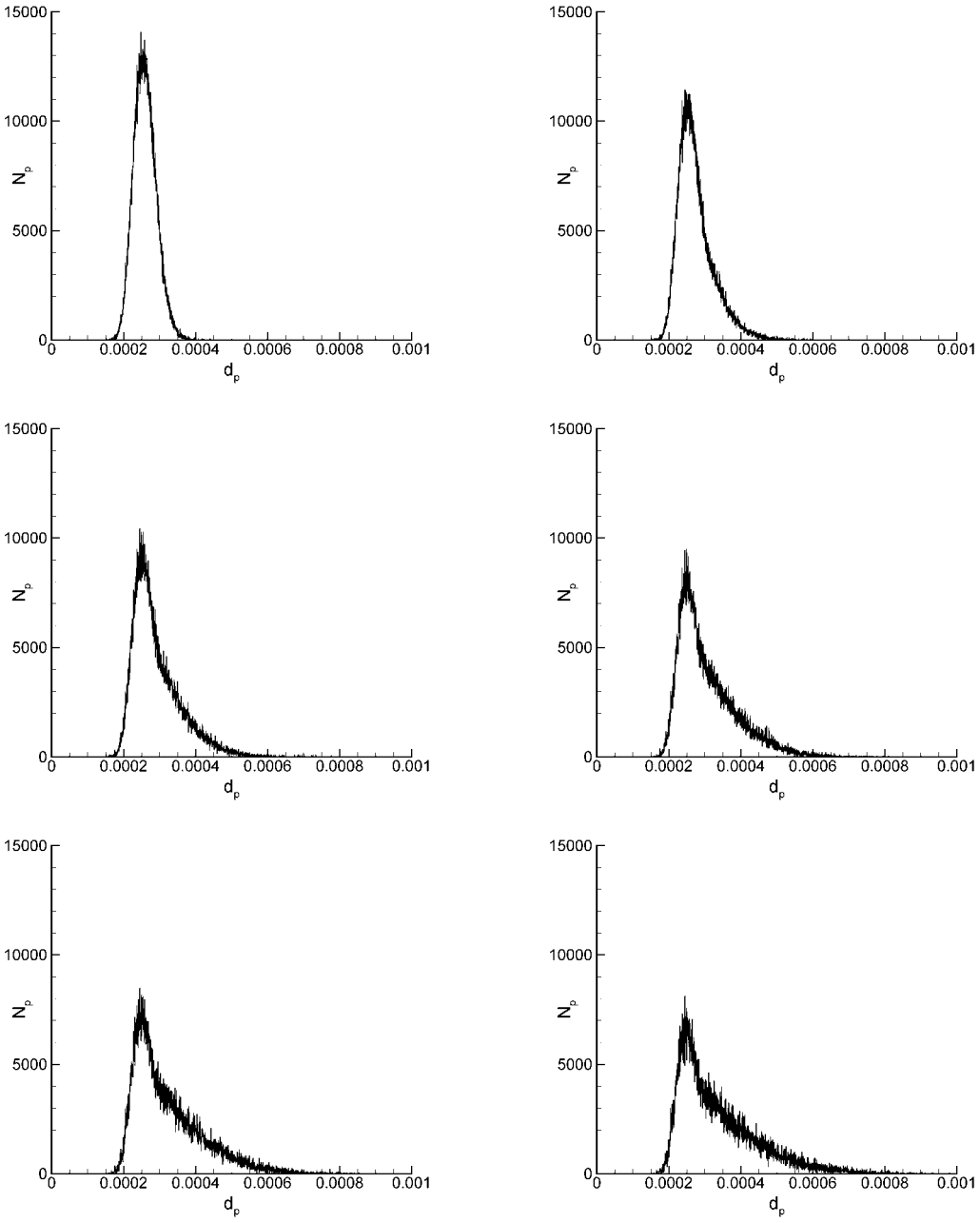

Figure 5.43: Droplet diameter evolution in time for **Case LN-1**: (Top left) $\frac{\text{time}}{T_E} = 0$, (Top right) $\frac{\text{time}}{T_E} = 3.5$, (Middle left) $\frac{\text{time}}{T_E} = 7.4$, (Middle right) $\frac{\text{time}}{T_E} = 11.3$, (Bottom left) $\frac{\text{time}}{T_E} = 15.2$, (Bottom right) $\frac{\text{time}}{T_E} = 19.1$.

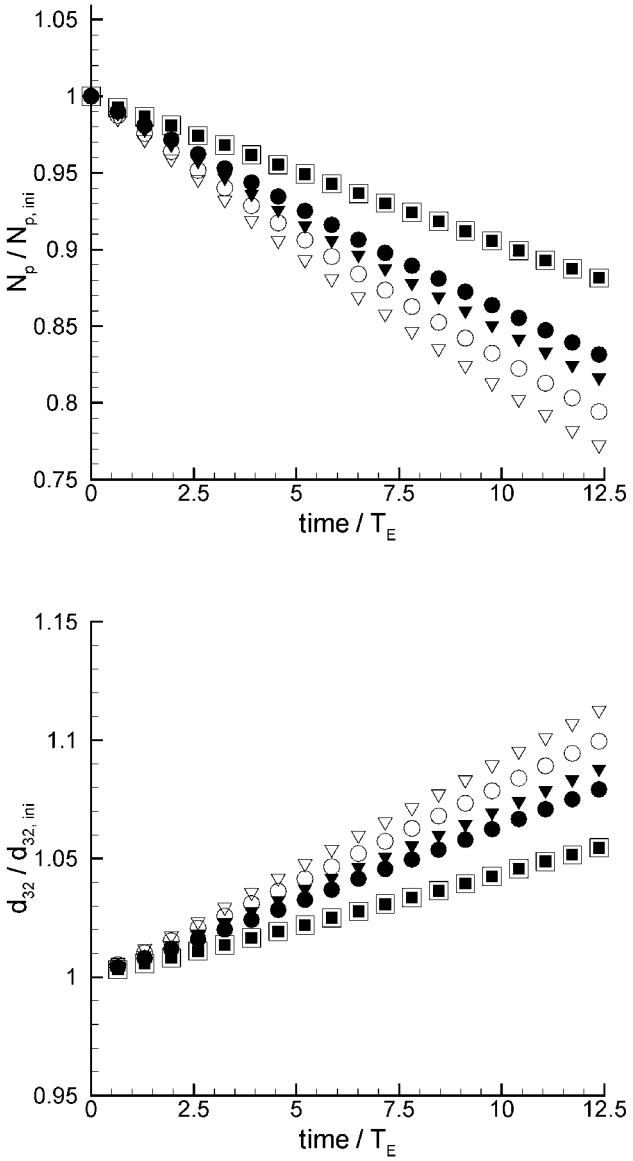

Figure 5.44: Number of droplets normalized by initial droplet number (top) and Sauter mean diameter normalized by initial Sauter diameter (bottom) over time normalized by the integral Eulerian time scale of the fluid for fluid turbulence with $Re_\lambda = 32.9$. The clear symbols stand for the results obtained in a pure coalescing regime and are the same as presented in fig. 5.24. The black symbols stand for the results obtained with different droplet collision outcomes. The droplet Stokes numbers for clear and black symbols are: $St = 0.11$ □, $St = 1.03$ ∇, $St = 2.72$ ◯.

collision outcomes. This behavior is explainable by the physics of coalescence as presented in chapter 2. Figure 2.2 (left) shows the partitioning of the permanent coalescence, stretching and reflexive separation regimes. It is seen, that in the case of low Weber numbers the permanent coalescence regime is predominant, even for very high impact parameters. The Weber number depends on the relative velocity of the droplets at collision and as it is shown in fig. 5.26 and fig. 5.27, the droplets with the lowest inertia, exhibit the weakest relative velocity at the moment of collision and therefore, the Weber numbers are small. Looking at a plot of the transition limits from permanent coalescence to stretching separation used, as shown in fig. 3.17, it is seen that for low Weber numbers, always permanent coalescence occurs, even for an impact parameter of 1. With increasing droplet Stokes numbers, the Weber number increases and thus other collision outcomes as permanent coalescence are possible. It is clearly seen in fig. 5.44 (top) that a pure permanent coalescence regime, does not predict the same coalescence rate for medium or high inertia droplets. Thus it seems necessary to include these effects into modeling approaches in order achieve a more realistic representation of droplet coalescence phenomena. Figure 5.44 (bottom) show the Sauter mean diameter evolution for the corresponding droplet Stokes numbers. The evolution of the Sauter mean diameter follows the droplet number evolution; the highest coalescence rate leads to the highest Sauter mean diameter and the dependence on the droplet Stokes of the Sauter mean diameter evolution is equally strong. No difference is seen for the lowest droplet inertia investigated in both a pure coalescence regime and accounting for different droplet collision outcomes, whereas the influence is not negligible for the medium and high droplet Stokes numbers investigated.

Chapter 6

Statistical modeling approaches compared to DNS/DPS

DNS/DPS simulations, as performed within this work, are feasible only in academic studies, due to the high computational effort they demand. For a more complex flow configuration other simulation strategies need to be followed. The results obtained in DNS/DPS simulations, and presented in chapter 5, are used in order to validate two different modeling approaches, which are considering the correlation of droplet velocities by the fluid turbulence and take coalescence phenomena into account. First, DNS/DPS results are compared to Euler-Lagrange Monte-Carlo predictions. The second approach is the Direct Quadrature Method of Moments presented in section 4.4.

6.1 Comparison with Lagrangian stochastic simulations

It is possible, as outlined in section 4.2, to solve directly the PDF transport equation (4.14) or (4.23). This is the so-called Direct Simulation Monte-Carlo (DSMC). Again in this approach, it is interesting to model the correlation of droplet velocities by the fluid turbulence, as a collision model based on the molecular-chaos assumption does not predict in a satisfying manner the coalescence rate of inertial droplets suspended in a turbulent flow. The results presented within this section correspond to simulations with an initially monodisperse droplet diameter distribution suspended in the turbulent flow field with turbulent Reynolds number $Re_\lambda = 32.9$ (see table 5.2 and table 5.4). The collision models are explained in section 4.2.2 and comparisons of predictions using the Euler-Lagrange stochastic approach to DNS/DPS results are presented in fig. 6.1 to 6.3, for both, molecular-chaos assumption and accounting for correlation of the droplet velocities. Figure 6.1 shows the

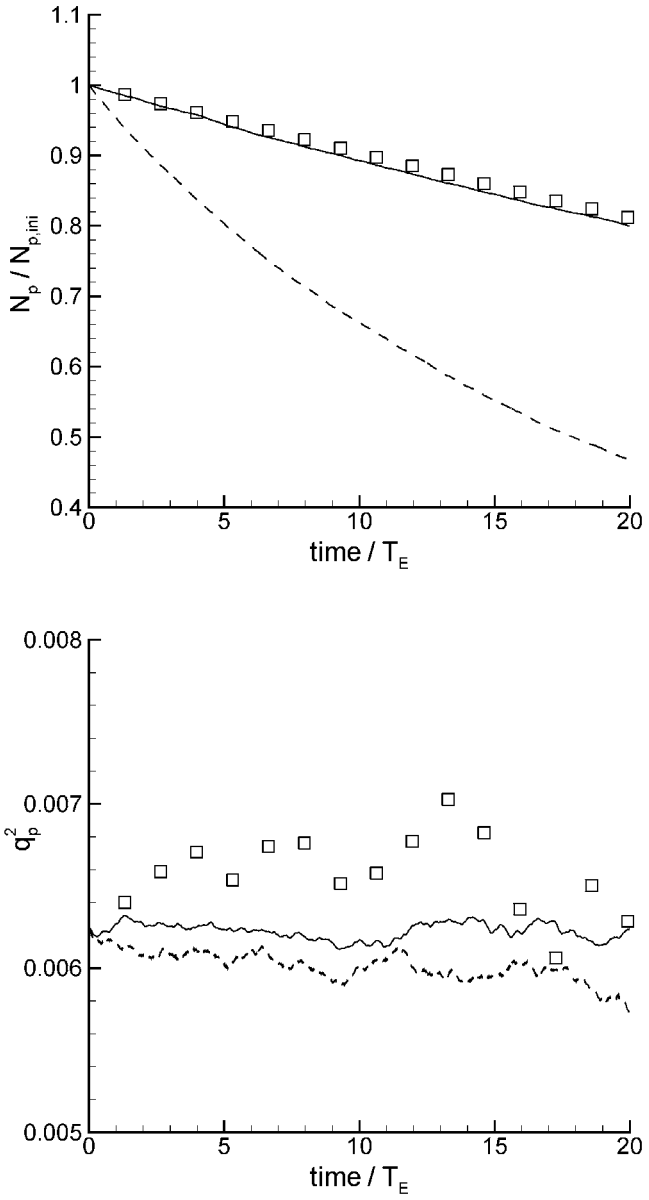

Figure 6.1: Number of droplets normalized by initial droplet number $N_{p,ini}$ (top) and droplet kinetic energy (bottom) over time normalized by the integral Eulerian time scale of the fluid, for fluid flow with $Re_\lambda = 32.9$. The symbols stand for the initial droplet Stokes numbers $St = 0.11$ □ measured in DNS/DPS. Monte-Carlo predictions based on the theory of molecular chaos (dashed line − − −) and accounting for the correlation in the droplet velocities by the fluid turbulence (solid line —) are shown.

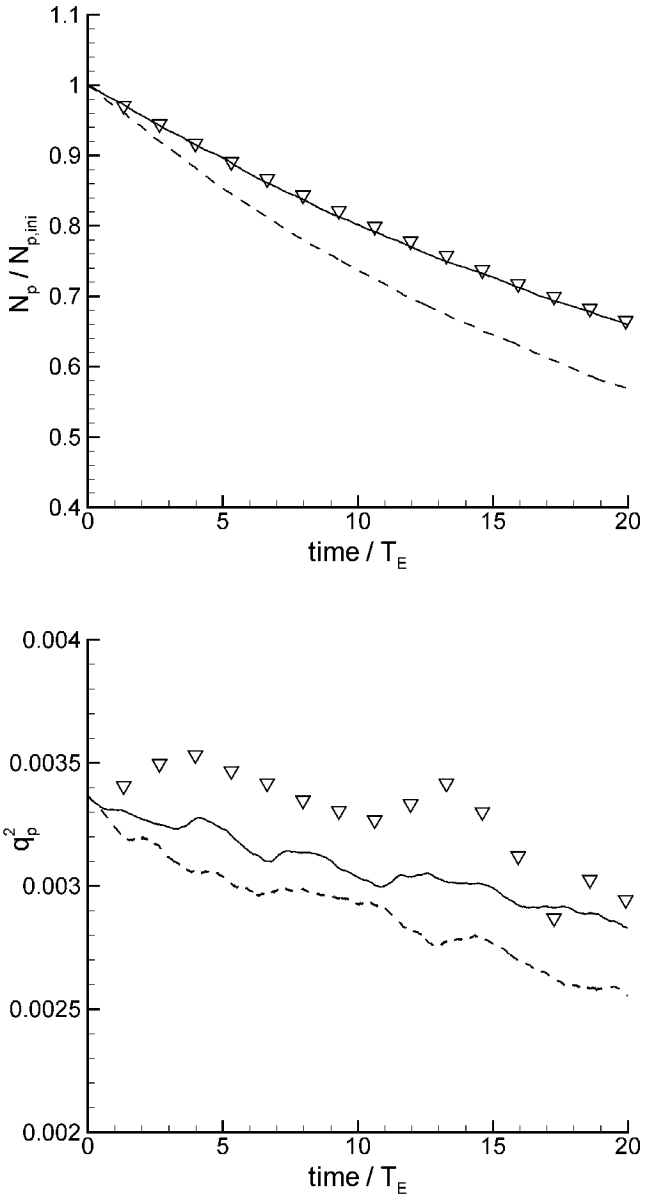

Figure 6.2: Number of droplets normalized by initial droplet number $N_{p,ini}$ (top) and droplet kinetic energy (bottom) over time normalized by the integral Eulerian time scale of the fluid, for fluid flow with $Re_\lambda = 32.9$. The symbols stand for the initial droplet Stokes numbers $St = 1.03$ ∇ measured in DNS/DPS. Monte-Carlo predictions based on the theory of molecular chaos (dashed line $- - -$) and accounting for the correlation in the droplet velocities by the fluid turbulence (solid line —) are shown.

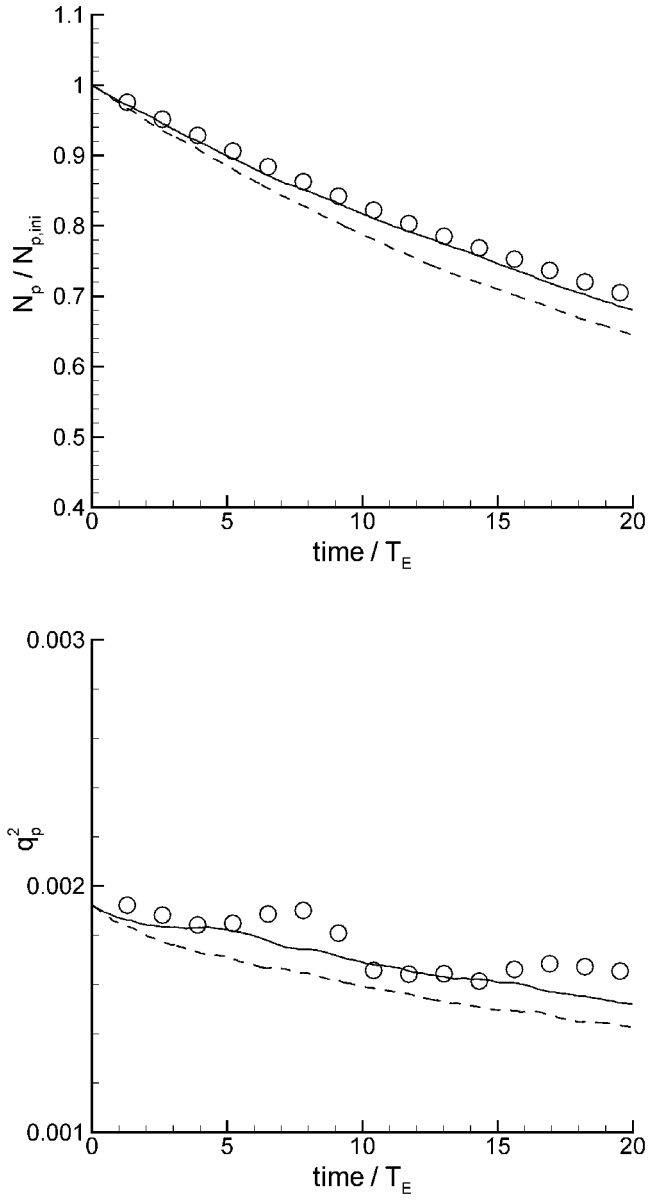

Figure 6.3: Number of droplets normalized by initial droplet number $N_{p,ini}$ (top) and droplet kinetic energy (bottom) over time normalized by the integral Eulerian time scale of the fluid, for fluid flow with $Re_\lambda = 32.9$. The symbols stand for the initial droplet Stokes numbers $St = 2.72$ ◯ measured in DNS/DPS. Monte-Carlo predictions based on the theory of molecular chaos (dashed line − − −) and accounting for the correlation in the droplet velocities by the fluid turbulence (solid line —) are shown.

number of droplets normalized by initial droplet number $N_{p,ini}$ (top) and the droplet kinetic energy (bottom) over time normalized by the integral Eulerian time scale of the fluid, for fluid flow with $Re_\lambda = 32.9$. The symbols stand for the initial droplet Stokes numbers $St = 0.11$ □ measured in DNS/DPS. The Monte-Carlo predictions based on the molecular-chaos assumption (dashed line − − −) and accounting for the correlation in the droplet velocities by the fluid turbulence (solid line —) are also shown. It is seen very clear, that the collision model based on the molecular-chaos assumption does not at all predict a correct value for the droplet number in a coalescing regime in comparison with measurements in DNS/DPS. On the other hand, the collision model accounting for the correlation of droplet velocities by the fluid turbulence predicts the correct coalescence rate very well. In the algorithm used, and as already explained in section 4.2.2, the droplets are sorted by their fluid velocity "seen" and it is assured that only droplets with a similar fluid velocity "seen" collide. Thus, this model imitates the correlation of spatially nearby droplets. Figure 6.1 (bottom) shows the droplet kinetic energy. It is seen that the model accounting for the correlation of droplet velocities is closer to the measured values in DNS/DPS, which is directly linked to the coalescence rate. The fluctuations in time measured in DNS/DPS are, however, larger in amplitude than those predicted by the Euler-Lagrange stochastic approach. Figure 6.2 and fig. 6.3 show the the number of droplets normalized by initial droplet number $N_{p,ini}$ (top) and the droplet kinetic energy (bottom) over time normalized by the integral Eulerian time scale of the fluid, for fluid flow with $Re_\lambda = 32.9$. The symbols stand for the initial droplet Stokes numbers $St = 1.03$ □ (fig. 6.2) and $St = 2.72$ ◯ (fig. 6.3) measured in DNS/DPS respectively. The Monte-Carlo predictions based on the molecular-chaos assumption (dashed line − − −) and accounting for the correlation in the droplet velocities by the fluid turbulence (solid line —) are shown in both figures. Figure 6.2 and fig. 6.3 both show, that the collision model accounting for the correlation of droplet velocities performs better than the collision model based on the molecular-chaos assumption. The difference between the two collision models diminishes with increasing droplet Stokes number, which is a behavior absolutely expected. The droplet kinetic energy is also better predicted for both droplet Stokes numbers $St = 1.03$ and $St = 2.72$ as shown in fig. 6.2 and fig. 6.3 (bottom) respectively.

Figure 6.4 and fig. 6.5 show the Sauter mean diameter d_{32} over time normalized by the integral Eulerian time scale of the fluid, for fluid flow with $Re_\lambda = 32.9$. The symbols stand for the initial droplet Stokes numbers $St = 0.11$ □ 6.4, $St = 1.03$ □ 6.5 (top) and $St = 2.72$ □ (fig. 6.5 (bottom)) measured in DNS/DPS. Monte-Carlo predictions based on the theory of molecular-chaos (dashed line − − −) and accounting for the correlation in the droplet velocities by the fluid turbulence (solid line —) are shown. The performance of the

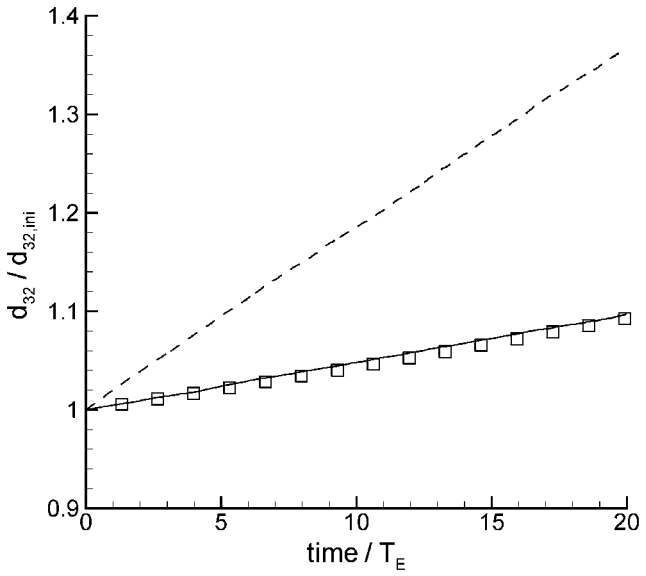

Figure 6.4: Normalized Sauter mean diameter $d_{32}/d_{32,ini}$ over time normalized by the integral Eulerian time scale of the fluid, for fluid flow with $Re_\lambda = 32.9$. The symbols stand for the initial droplet Stokes numbers $St = 0.11$ □ measured in DNS/DPS. Monte-Carlo predictions based on the theory of molecular-chaos (dashed line − − −) and accounting for the correlation in the droplet velocities by the fluid turbulence (solid line —) are shown.

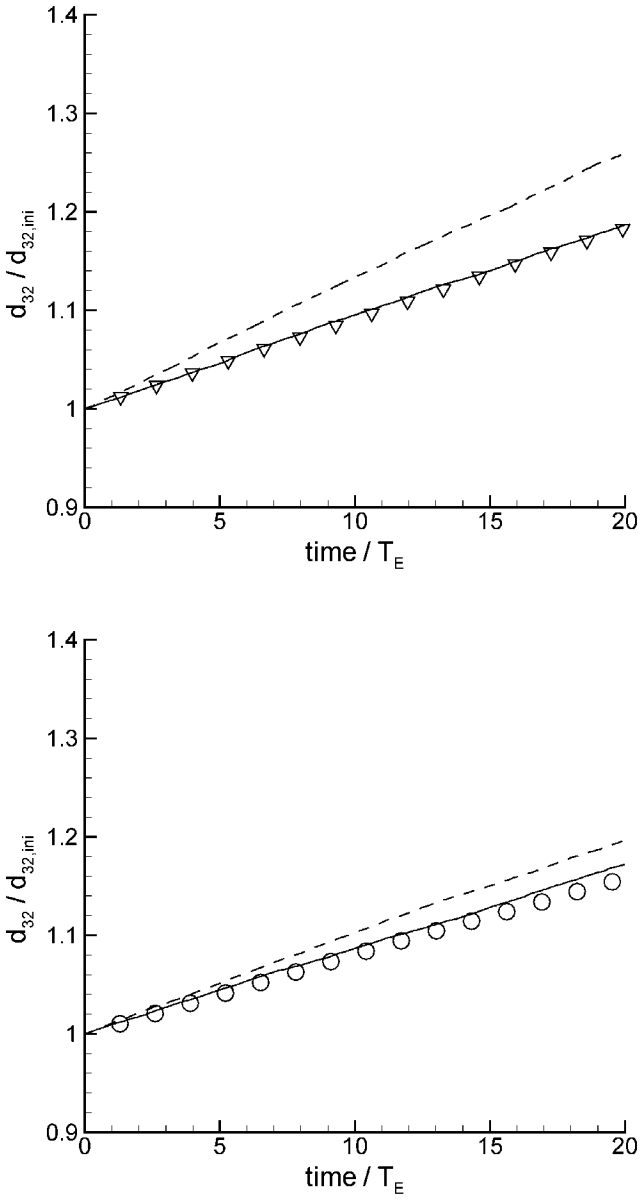

Figure 6.5: Normalized Sauter mean diameter $d_{32}/d_{32,ini}$ over time normalized by the integral Eulerian time scale of the fluid, for fluid flow with $Re_\lambda = 32.9$. The symbols stand for the initial droplet Stokes numbers $St = 0.95$ ∇ (top) and $St = 2.43$ $\bigcirc$ (bottom) measured in DNS/DPS. Monte-Carlo predictions based on the theory of molecular-chaos (dashed line $- - -$) and accounting for the correlation in the droplet velocities by the fluid turbulence (solid line —) are shown.

two collision models investigated is in analogy to the performance predicting the coalescence rate. The collision model accounting for the correlation of droplet velocities predicts better than the model based on the molecular-chaos assumption for all droplet Stokes numbers investigated. The higher the droplet Stokes number the closer the predictions of the models.

6.2 Comparison DNS/DPS with DQMOM

Within the section dealing with the comparison of DNS/DPS simulations with DQMOM predictions, three different configurations are treated. First, an initially monodisperse droplet phase applying the molecular-chaos assumption in the collision terms, and such not accounting for the correlation of the droplet velocities by the fluid turbulence. Second, an initially monodisperse dispersed phase applying a closure of the collision terms, accounting for the correlation of the droplet velocities by the fluid turbulence. And third, a lognormal diameter distribution applying both collision models, the molecular-chaos assumption and the model accounting for the correlation of the colliding droplet velocities by the fluid turbulence.

The DQMOM simulations performed are 0-dimensional, as the statistics of the DNS/DPS simulations of the homogeneous isotropic turbulence are obtained over the entire computation domain. The DQMOM equations given in section 4.4.2 simplify significantly in a homogeneous isotropic turbulence. Thus, all variations of the droplet quantities with respect to x_j are equal to 0.

6.2.1 Initial monodisperse particulate phase

A first study, with an initially monodisperse droplet phase applying the molecular-chaos assumption in the collision terms, aims at the evaluation and validation of the DQMOM approach, under the form proposed by Belt and Simonin [11]. Five different test cases are regarded here, as given below.

Case i) The droplet number and mass balance equations with a collision term based on the molecular-chaos assumption $\mathcal{C}\left(m_p^k\right)$ are solved only. For the collision term, the droplet kinetic energy is needed. These values are extracted for the corresponding diameters from the DNS/DPS simulations.

Case ii) The second test case solves the same equations as Case i), but additionally the droplet kinetic-energy equation. Now, the mean droplet response time and the fluid droplet covariance are needed. The mean droplet response time is obtained from

the DNS/DPS simulations, while the fluid droplet covariance is modeled following the theory of Tchen and Hinze [129].

Case iii) In the third test case the same equations as in Case ii) are solved, while the fluid-droplet covariance is now obtained from an additional transport equation.

Case iv) In this test case the same equations as in Case iii) are solved, but a collision source term is accounted for in the droplet kinetic stress equation $\mathcal{C}\left(m_p^k v'_{p,i} v'_{p,j}\right)$.

Case v) The last test case is performed in a dry granular flow, this means that no fluid turbulence is present. The goal of the test case is to evaluate the influence of the collision source term in the droplet kinetic stress equation, without the 'disturbing' influence of fluid turbulence.

It is important to give a brief explanation on the initialization of the 0-dimensional DQMOM simulations. A given number of Dirac functions (droplet classes) is used in the DQMOM simulations. In this work typically 3, unless otherwise stated. The initial droplet diameter distribution is monodisperse. The choice of an initially monodisperse diameter distribution is not optimal with regard to DQMOM simulations. It is not possible to initialize three droplet classes in DQMOM with a monodisperse distribution. All three classes would be at the same abscissa, which would turn the matrices $\boldsymbol{M}_1$ and $\boldsymbol{M}_2$ in (4.142) singular, and thus the system (4.142) can not be solved. A similar problem is reported by Fan *et al.* [40], where the matrices $\boldsymbol{M}_1$ and $\boldsymbol{M}_2$ become nearly singular, if two abscissas are too close to each other, leading to large round-off errors, while the matrices remain invertible. As a consequence the DQMOM simulations performed here are initialized after the droplet phase has been coalescing already for a while and two new droplet diameters have been formed in DNS/DPS simulations, the DQMOM simulations being thus initialiable. The figures which are presented in the following therefore do not exhibit a droplet number to initial droplet number ratio of 1 at the beginning of the simulations (see for example fig. 6.6 to fig. 6.8).

The equations solved and the terms used in the corresponding test cases are given below, followed by a discussion of the results.

Case i): Droplet number and mass balance equations with $\mathcal{C}\left(m_p^k\right)$

If the droplet number and mass balance equations are solved only and, in order to account for coalescence, a collision source term in these equations is considered, (4.125) and (4.126)

Table 6.1: Ratio of DNS/DPS results to DQMOM predictions for the $0th$ to $5th$ order mass moment. The droplet inertias are $St = 0.11$, $St = 1.03$ and $St = 2.72$ at $Re_\lambda = 32.9$ for simulation **Case i)** at $time/T_E = 20$. Molecular chaos assumption for collision source term $\mathcal{C}\left(\mu_p^k\right)$.

moment (order)	$St = 0.11$	$St = 1.03$	$St = 2.72$
N_p (0)	2.004	1.238	1.102
m_p (1)	0.9994	1.0000	0.9995
d_p $(\frac{1}{3})$	1.669	1.168	1.073
d_p^2 $(\frac{2}{3})$	1.323	1.087	1.039
(2)	0.353	0.750	0.877
(3)	0.138	0.620	0.920
(4)	0.113	0.789	2.191
(5)	0.212	1.857	11.114

simplify, in the case of a homogeneous isotropic turbulence, to

$$\frac{\partial}{\partial t}\left(n_\alpha\right) = a_\alpha^{(1)} \tag{6.1}$$

$$\frac{\partial}{\partial t}\left(n_\alpha m_{p,\alpha}\right) = b_\alpha^{(1)} \quad , \tag{6.2}$$

with a_α and b_α the source terms per droplet class. The system which is solved writes then, with k ranging from 0 to $2N-1$,

$$(1-k)\sum_{\alpha=1}^{N} m_{p,\alpha}^k a_\alpha^{(1)} + k\sum_{\alpha=1}^{N} m_{p,\alpha}^{k-1} b_\alpha^{(1)} \;=\; \mathcal{C}\left(m_p^k\right) \quad , \tag{6.3}$$

where $\mathcal{C}\left(m_p^k\right)$ represents the collision source term as defined in (4.134), using (4.138) and (4.139).

Table 6.1 shows the ratio of DNS/DPS results to DQMOM predictions for the $0th$ to $5th$ order mass moment, for droplet inertia $St = 0.11$, $St = 1.03$ and $St = 2.72$ at $time/T_E = 20$. The molecular-chaos assumption is used for the collision source term $\mathcal{C}\left(\mu_p^k\right)$. It is seen that the droplet mass m_p is conserved, the deviations from 1 which appear in table 6.1 being due to the initialization of the DQMOM simulations as described above. Further it is seen that the droplet number is the better predicted, the higher the droplet Stokes number is. The same is true for the mean droplet diameter.

It is stated above that 3 Dirac functions are used in DQMOM. This choice is, on the

Table 6.2: Ratio of DNS/DPS results to DQMOM predictions for the $0th$ to $5th$ order mass moment. The droplet inertia is $St = 2.72$ at $Re_\lambda = 32.9$ for simulation **Case i)** at $time/T_E = 20$. Molecular chaos assumption for collision source term $\mathcal{C}\left(\mu_p^k\right)$. Comparison of with 3 and 4 Dirac functions in DQMOM.

moment (order)	$St = 2.4$ 3 Dirac	$St = 2.4$ 4 Dirac
N_p (0)	1.102	1.101
m_p (1)	0.9995	0.9994
d_p $(\frac{1}{3})$	1.073	1.072
d_p^2 $(\frac{2}{3})$	1.039	1.038
(2)	0.877	0.878
(3)	0.920	0.917
(4)	2.191	2.101
(5)	11.114	9.515

one hand, driven by the issue of initialization for DQMOM in comparison with an initial monodisperse diameter distribution in DNS/DPS, on the other hand, the choice of 3 Dirac functions is sufficient. Table 6.2 shows the moments for the case of 3 and 4 Dirac functions. It is clearly seen in table 6.2, that the results for 3 or for 4 Dirac functions are practically identical and the choice of 3 Dirac functions is therefore justified. Marchisio and Fox [82] report that the choice of 3 or for 4 Dirac functions is sufficient using their approach.

Case ii): Droplet number and mass balance equations with additionally droplet kinetic-energy equation solved

The droplet kinetic stress equation (4.128) can be simplified in homogeneous isotropic turbulence as given in (6.4). As the droplet number and mass are known from (6.3), (6.4) contains the same information as (6.5), since it is only weighted by a different factor. The source terms are therefore related and $a_\alpha^{(3)}$ can be expressed in terms of $a_\alpha^{(1)}$, $b_\alpha^{(1)}$ and $d_\alpha^{(3)}$. The source terms of the droplet kinetic stress equation write as

$$\frac{\partial}{\partial t}\left(n_\alpha \langle v'_{p,i} v'_{p,j}\rangle_\alpha\right) - n_\alpha \langle v'_{p,j} \frac{F_{r,i}}{m}\rangle_\alpha - n_\alpha \langle v'_{p,i} \frac{F_{r,j}}{m}\rangle_\alpha = a_\alpha^{(3)} \tag{6.4}$$

$$\frac{\partial}{\partial t}\left(n_\alpha m_{p,\alpha} \langle v'_{p,i} v'_{p,j}\rangle_\alpha\right) - n_\alpha m_{p,\alpha} \langle v'_{p,j} \frac{F_{r,i}}{m}\rangle_\alpha - n_\alpha m_{p,\alpha} \langle v'_{p,i} \frac{F_{r,j}}{m}\rangle_\alpha = b_\alpha^{(3)} \quad . \tag{6.5}$$

Table 6.3: Ratio of DNS/DPS results to DQMOM predictions for the $0th$ to $5th$ order mass moment. The droplet inertia are $St = 0.11$, $St = 1.03$ and $St = 2.72$ at $Re_\lambda = 32.9$ for simulation **Case ii)** at $time/T_E = 20$. Molecular chaos assumption for collision source term $\mathcal{C}\left(m_p^k\right)$.

moment (order)	$St = 0.11$	$St = 1.03$	$St = 2.72$
N_p (0)	1.876	1.220	1.121
m_p (1)	0.9994	1.0004	0.9995
d_p $(\frac{1}{3})$	1.589	1.155	1.086
d_p^2 $(\frac{2}{3})$	1.289	1.081	1.045
(2)	0.388	0.770	0.862
(3)	0.166	0.655	0.897
(4)	0.147	0.857	2.136
(5)	0.297	2.071	10.868

The droplet kinetic stress equation (4.128) can then be written as shown in (6.6), if the influence of coalescence is not accounted for in the droplet kinetic stress equation and the collision source terms equals 0:

$$(1-k)\sum_{\alpha=1}^{N} m_{p,\alpha}^k a_\alpha^{(3)} + k\sum_{\alpha=1}^{N} m_{p,\alpha}^{k-1} b_\alpha^{(3)} = \mathcal{C}\left(m_p^k v_{p,i}' v_{p,j}'\right) = 0 \quad . \tag{6.6}$$

The system which needs to be solved in Case ii) consists of (6.3) and (6.6). The assumption of no influence of coalescence on the droplet kinetic energy is valid only if the effect of collisions on droplet kinetic stress is less important than the interaction with the fluid. If the collision source term is neglected, the source terms c_α and d_α equal 0.

The interaction with fluid turbulent motion is expressed by the force terms $F_{r,i}$ and $F_{r,j}$, which are given in (6.5). These terms are given following Simonin [117] as

$$n_\alpha m_{p,\alpha}\langle v_{p,j}'\frac{F_{r,i}}{m}\rangle_\alpha - n_\alpha m_{p,\alpha}\langle v_{p,i}'\frac{F_{r,j}}{m}\rangle_\alpha \approx -n_\alpha m_{p,\alpha}\frac{2}{\tau_{fp,\alpha}^F}\left[\langle v_{p,i}' v_{p,j}'\rangle_\alpha - R_{fp,ij}\right] \quad , \tag{6.7}$$

where the fluid-droplet covariance tensor $R_{fp,ij}$ is modeled using $q_{fp} = \frac{2q_f}{1+St}$. The mean droplet response time $\tau_{fp,\alpha}^F$ is extracted from the DNS/DPS simulations.

Table 6.3 shows basically the same behavior as seen in Case i), the ratio of DNS/DPS results to DQMOM predictions is closer to 1 for higher Stokes numbers for the droplet number N_p and the mean diameter d_p. The ratio of DNS/DPS results to DQMOM pre-

dictions for the droplet number or diameter is closer to 1 for the two lower droplet Stokes numbers investigated and larger in the case of the highest droplet Stokes number. No final conclusion can be drawn on a comparison of the performance of Case i) to Case ii).

Case iii): Droplet number and mass balance equations, droplet kinetic-energy equation solved additionally fluid-droplet covariance equation solved

The fluid-droplet covariance equation is given in the case of a homogeneous isotropic turbulence as seen in (6.9).

$$\frac{\partial}{\partial t}\left(n_\alpha \langle u'_{f,j} v'_{p,i}\rangle_\alpha\right) - n_\alpha \langle u'_{f,j}\frac{F_{r,i}}{m_p}\rangle_\alpha - n_\alpha \langle v'_{p,i} A_j\rangle_\alpha = a_\alpha^{(4)} \tag{6.8}$$

$$\frac{\partial}{\partial t}\left(n_\alpha m_{p,\alpha} \langle u'_{f,j} v'_{p,i}\rangle_\alpha\right) - n_\alpha m_{p,\alpha} \langle u'_{f,j}\frac{F_{r,i}}{m_p}\rangle_\alpha - n_\alpha m_{p,\alpha} \langle v'_{p,i} A_j\rangle_\alpha = b_\alpha^{(4)} \tag{6.9}$$

The force terms $F_{r,i}$ and $F_{r,j}$ are given by

$$\begin{aligned} n_\alpha m_{p,\alpha} \langle u'_{f,j}\frac{F_{r,i}}{m_p}\rangle_\alpha &- n_\alpha m_{p,\alpha} \langle v'_{p,i} A_j\rangle_\alpha \\ \approx &- n_\alpha m_{p,\alpha}\frac{2}{\tau^F_{fp,\alpha}}\left[\langle u'_{f,i} v'_{p,j}\rangle_\alpha - \langle u'_{f,i} u'_{f,j}\rangle_\alpha\right] \\ &- n_\alpha m_{p,\alpha}\frac{1}{T_L}\langle u'_{f,i} v'_{p,j}\rangle_\alpha \quad . \end{aligned} \tag{6.10}$$

The fluid-droplet covariance equation (6.9) can then be written as shown in (6.11), if the influence of coalescence is not accounted for in the fluid-droplet covariance equation and the collision source terms equals 0.

$$(1-k)\sum_{\alpha=1}^{N} m_{p,\alpha}^k a_\alpha^{(4)} + k\sum_{\alpha=1}^{N} m_{p,\alpha}^{k-1} b_\alpha^{(4)} = \mathcal{C}\left(m_p^k u'_{f,i} v'_{p,j}\right) = 0 \quad . \tag{6.11}$$

The results shown in table 6.4 show similar results as the simulations in Case i) and Case ii), which is positive, since more and more quantities are transported or modeled and not taken from DNS/DPS simulations.

Table 6.4: Ratio of DNS/DPS results to DQMOM predictions for the $0th$ to $5th$ order mass moment. The droplet inertia are $St = 0.11$, $St = 1.03$ and $St = 2.72$ at $Re_\lambda = 32.9$ for simulation **Case iii)** at $time/T_E = 20$. Molecular chaos assumption for collision source term $\mathcal{C}\left(m_p^k\right)$.

moment (order)	$St = 0.11$	$St = 1.03$	$St = 2.72$
N_p (0)	2.150	1.294	1.136
m_p (1)	0.9994	1.0004	0.9995
d_p $(\frac{1}{3})$	1.683	1.186	1.089
d_p^2 $(\frac{2}{3})$	1.300	1.086	1.043
(2)	0.489	0.862	0.927
(3)	0.345	0.965	1.162
(4)	0.552	1.760	3.595
(5)	1.990	5.925	24.306

Case iv): Droplet number and mass balance equations, droplet kinetic-energy equation solved additionally fluid-droplet covariance equation solved with collision source term in droplet kinetic stress equation $\mathcal{C}\left(m_p^k v'_{p,i} v'_{p,j}\right)$

In general it is difficult to write the collision term $\int c_p c_p \mu_p^k \left(\frac{\partial f_{fp}}{\partial t}\right)_{coll} d\mathbf{c}_p d\mathbf{c}_f d\mu_p$ in the droplet kinetic stress equation (6.6). In a homogeneous isotropic turbulence, the coalescence term can be written making use of the mass and moment conservation at the moment of collision (see (3.81)) in a first approximation as given in (6.13) with $\Lambda = 1$. The quantity ψ is chosen to $\psi = m_p^k q_p^2$.

$$\mathcal{B}(m_p^k q_p^2) = \Lambda \, \frac{1}{2} \sum_\alpha \sum_\kappa \, \beta_{\alpha,\kappa} \, m_p^{k,*} \tag{6.12}$$
$$\frac{3}{2} \left(\frac{m_{p,\alpha} \left(\frac{2}{3} q_{p,\alpha}^2\right)^{\frac{1}{2}} + m_{p,\kappa} \left(\frac{2}{3} q_{p,\kappa}^2\right)^{\frac{1}{2}}}{m_{p,\alpha} + m_{p,\kappa}} \right)^2$$

$$\mathcal{D}(m_p^k q_p^2) = \Lambda \, \sum_\alpha \sum_\kappa \, \beta_{\alpha,\kappa} \, m_{p,\alpha}^k \, \frac{2}{3} \, q_{p,\alpha}^2 \tag{6.13}$$

The equations to be solved are then (6.3), (6.11) and (6.14):

$$(1-k) \sum_{\alpha=1}^{N} m_{p,\alpha}^k a_\alpha^{(3)} + k \sum_{\alpha=1}^{N} m_{p,\alpha}^{k-1} b_\alpha^{(3)} = \mathcal{C}\left(m_p^k q_p^2\right) \quad . \tag{6.14}$$

Table 6.5: Ratio of DNS/DPS results to DQMOM predictions for the $0th$ to $5th$ order mass moment. The droplet inertia are $St = 0.11$, $St = 1.03$ and $St = 2.72$ at $Re_\lambda = 32.9$ for simulation **Case iv)** at $time/T_E = 20$. Molecular chaos assumption for collision source term $\mathcal{C}\left(m_p^k\right)$ and $\mathcal{C}\left(m_p^k q_p^2\right)$.

moment (order)	$St = 0.11$	$St = 1.03$	$St = 2.72$
N_p (0)	2.173	1.310	1.148
m_p (1)	0.9994	1.0004	0.9995
d_p $(\frac{1}{3})$	1.700	1.202	1.103
d_p^2 $(\frac{2}{3})$	1.308	1.098	1.054
(2)	0.471	0.794	0.843
(3)	0.312	0.763	0.855
(4)	0.462	1.151	1.974
(5)	1.534	3.184	9.668

Table 6.5 shows again similar results as seen in table 6.1 to table 6.4. Only looking at table 6.4 and table 6.5 it is difficult to evaluate the influence of the collision source term in the droplet kinetic stress equation. Figures 6.6 to fig. 6.8 show the number of droplets normalized by initial droplet number $N_{p,ini}$ over time normalized by the integral Eulerian time scale of the fluid, for fluid flow with $Re_\lambda = 32.9$. The symbols stand for results measured in DNS/DPS for initial droplet Stokes numbers $St = 0.11$ $\square$, $St = 1.03$ ∇ and $St = 2.72$ $\bigcirc$. The dashed line $- - -$ stands for a collision source term in the droplet number and mass balance equations $\mathcal{C}\left(m_p^k\right)$ only. The dotted line $\cdots$ stands for collision source terms in the droplet number and mass balance equations $\mathcal{C}\left(m_p^k\right)$ as well as in the droplet kinetic stress equation $\mathcal{C}\left(m_p^k q_p^2\right)$. Figures 6.6 to fig. 6.8 show that the collision models based on the molecular-chaos assumption predict the number of droplets the better, the higher the droplet Stokes number is. However, it has to be stated that, in both cases, a collision source term in the droplet number and mass balance equations only, and in the droplet number and mass balance equations and additionally in the droplet kinetic stress equation, the DQMOM predictions of the droplet number in the system is not satisfying. The higher the droplet Stokes, the better the DQMOM predictions using a collision source term based on the molecular-chaos assumption. Which is consequent, as higher-inertia droplets correspond more closely to the regime valid in the kinetic theory of rarefied gases.

Further it has to be stated, comparing fig. 6.6 to fig. 6.8, that the influence of the collision source in the droplet kinetic stress equation is negligible on the prediction of the

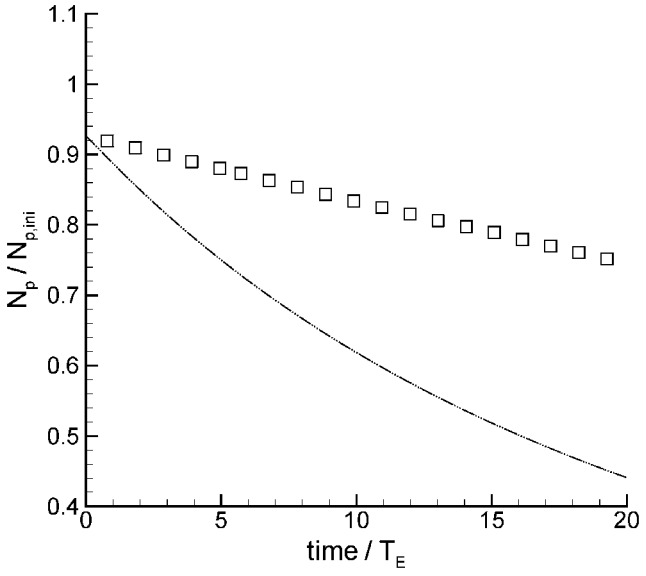

Figure 6.6: Number of droplets normalized by initial droplet number $N_{p,ini}$ over time normalized by the integral Eulerian time scale of the fluid, for fluid flow with $Re_\lambda = 32.9$. The symbols stand for the initial droplet Stokes numbers $St = 0.11$ □ measured in DNS/DPS. The dashed line $- - -$ stands for a collision source term in the droplet number and mass balance equation $\mathcal{C}\left(m_p^k\right)$ only. The dotted line $\cdots$ stands for collision source terms in the droplet number and mass balance equations $\mathcal{C}\left(m_p^k\right)$ as well as in the droplet kinetic stress equation $\mathcal{C}\left(m_p^k q_p^2\right)$.

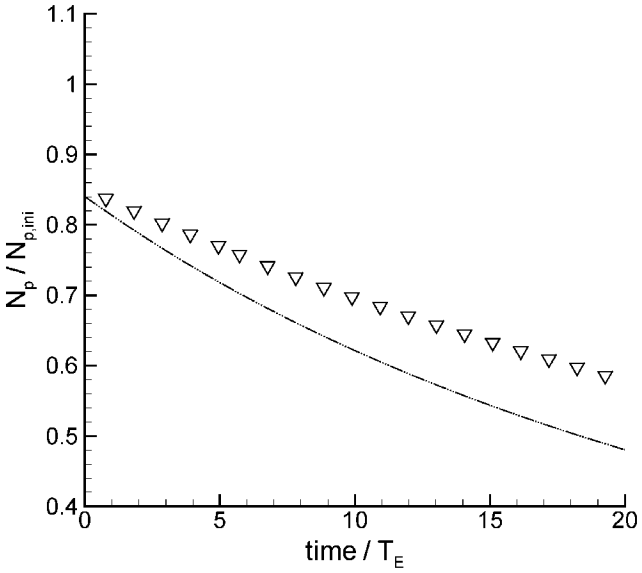

Figure 6.7: Number of droplets normalized by initial droplet number $N_{p,ini}$ over time normalized by the integral Eulerian time scale of the fluid, for fluid flow with $Re_\lambda = 32.9$. The symbols stand for the initial droplet Stokes numbers $St = 1.03$ ∇ measured in DNS/DPS. The dashed line $- - -$ stands for a collision source term in the droplet number and mass balance equation $\mathcal{C}\left(m_p^k\right)$ only. The dotted line $\cdots$ stands for collision source terms in the droplet number and mass balance equations $\mathcal{C}\left(m_p^k\right)$ as well as in the droplet kinetic stress equation $\mathcal{C}\left(m_p^k q_p^2\right)$.

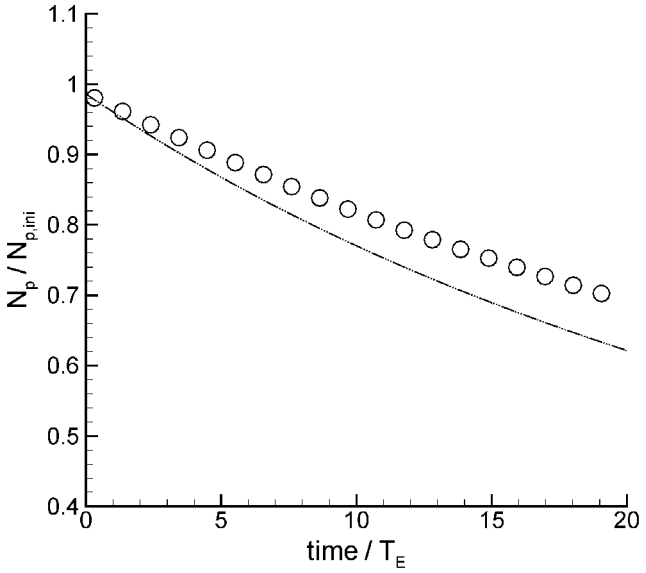

Figure 6.8: Number of droplets normalized by initial droplet number $N_{p,ini}$ over time normalized by the integral Eulerian time scale of the fluid, for fluid flow with $Re_\lambda = 32.9$. The symbols stand for the initial droplet Stokes numbers $St = 2.72$ ◯ measured in DNS/DPS. The dashed line $- - -$ stands for a collision source term in the droplet number and mass balance equation $\mathcal{C}\left(m_p^k\right)$ only. The dotted line $\cdots$ stands for collision source terms in the droplet number and mass balance equations $\mathcal{C}\left(m_p^k\right)$ as well as in the droplet kinetic stress equation $\mathcal{C}\left(m_p^k q_p^2\right)$.

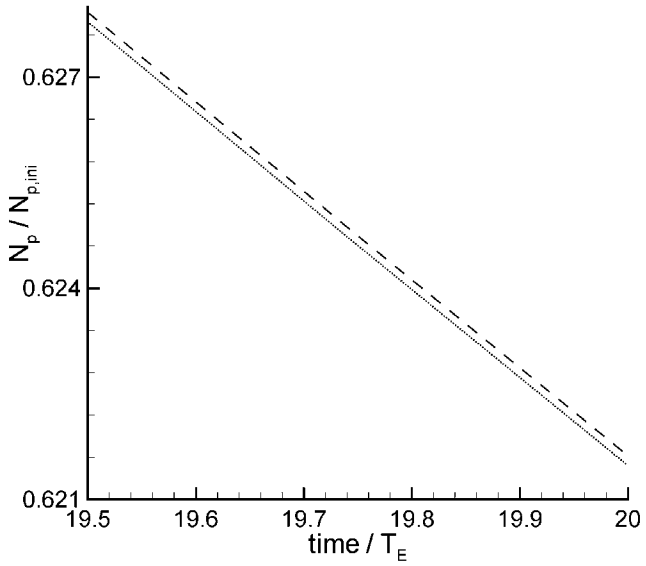

Figure 6.9: Zoom on DQMOM predictions for droplet Stokes number $St = 2.72$. The dashed line $- - -$ stands for a collision source term in the droplet number and mass balance equation $\mathcal{C}\left(m_p^k\right)$ only. The dotted line $\cdots$ stands for collision source terms in the droplet number and mass balance equations $\mathcal{C}\left(m_p^k\right)$ as well as in the droplet kinetic stress equation $\mathcal{C}\left(m_p^k q_p^2\right)$.

droplet number in the system. The dotted line $\cdots$, which represents the collision source term in the droplet kinetic-energy equation, is virtually identical to the dashed line $- - -$, which stands for a collision source term in the droplet number and mass balance equations only. If the results given in table 6.4 and table 6.5 are compared for the droplet number, it is seen that the values are not exactly the same. On the other hand, fig. 6.6 to fig. 6.8 seem to show exactly the same characteristics, which appears contradictory. Figure 6.9 emphasizes that the results are consistent and that it is only a problem of scale using the example of a droplet Stokes number of $St = 2.72$.

Case v): Dry granular case

The last test case is a configuration with a dry granular flow, which means that no fluid phase is present. The goal of this test case is to evaluate the influence of the collision source term in the droplet kinetic stress equation, without the 'disturbing' influence of the fluid turbulence. Where almost no influence of the collision source term in the droplet

Table 6.6: Ratio of DNS/DPS results to DQMOM predictions for the $0th$ to $5th$ order mass moment, for the dry granular **Case v)**. Comparison of different collision source terms.

moment (order)	$\frac{\mathcal{C}(\mu^k_{p,\alpha})}{q_p^2 \text{ DNS}}$	$\mathcal{C}(\mu^k_{p,\alpha})$	$\frac{\mathcal{C}(\mu^k_{p,\alpha})}{\mathcal{C}(c_{p,\beta}c_{p,\gamma}\mu^k_{p,\alpha})}$
N_p (0)	1.050	1.063	1.042
m_p (1)	1.0004	1.007	1.007
d_p $(\frac{1}{3})$	1.035	1.043	1.014
d_p^2 $(\frac{2}{3})$	1.019	1.023	1.013
(2)	0.947	1.001	0.955
(3)	0.972	1.036	0.867
(4)	1.475	1.144	0.806
(5)	4.320	1.396	0.824

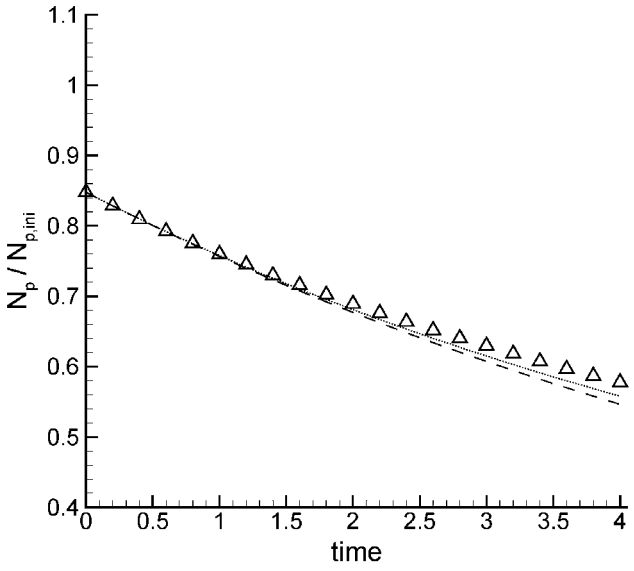

Figure 6.10: Number of droplets normalized by initial droplet number $N_{p,ini}$ over time for dry granular flow. The symbols stand for values measured in DPS. The dashed line $- - -$ stands for a collision source term in the droplet number and mass balance equations $\mathcal{C}\left(m_p^k\right)$ only. The dotted line $\cdots$ stands for collision source terms in the droplet number and mass balance equations $\mathcal{C}\left(m_p^k\right)$ as well as in the droplet kinetic stress equation $\mathcal{C}\left(m_p^k q_p^2\right)$.

kinetic stress equation is found in turbulent two-phase flows, as shown above, the collision source term in droplet kinetic stress equation has a small influence on the droplet number predictions in dry granular flows. Table 6.6 and fig. 6.10 summarize the results. Table 6.6 compares dry granular simulation results for three different simulations. First, resolving only the number and mass balance equations, while obtaining the droplet kinetic energy from DNS/DPS simulations. Second, two simulations solving the droplet kinetic stress equation with and without collision term, respectively. The only force terms in the droplet kinetic stress equation, in dry granular flows, result from droplet coalescence and thus allow to evaluate the influence of the collision source term.

6.2.2 Droplet velocity correlation closure

It is shown in section 6.2.1 that the predictions from DQMOM simulations agree rather poorly to measurements in DNS/DPS simulations of turbulent two-phase flows, if the molecular-chaos assumption is applied in the collision source terms. It seems crucial, to the predictions of the moments of the dispersed phase, that the correlations in the droplet velocities induced by the fluid turbulence are accounted for. How to account for these correlations is shown in section 4.1.3. If the mean droplet velocity is used as defined in (4.141), it is possible to account for the correlations in the droplet velocities by the fluid turbulence.

Figure 6.11 (top) shows a prominent improvement of the DQMOM predictions in comparison to DNS/DPS results accounting for the correlation of droplet velocities by the fluid turbulence. Figure 6.11 (bottom) and fig. 6.12 show equally satisfying results, if the correlation is accounted for. Droplet preferential concentration does not enter into the model accounting for droplet velocity correlations shown in fig. 6.11 (bottom) to fig. 6.12. However, as detailed in chapter 5, droplet preferential concentration has an influence on the collision frequency for intermediate droplet Stokes numbers. The results of the model accounting for droplet velocity correlations are nevertheless satisfying.

Figures 6.13 to fig. 6.14 show the droplet diameter distributions for droplets with initial Stokes number $St = 0.11$, $St = 1.03$ and $St = 2.72$ respectively, at time $time/T_E = 20$. As the initial distribution in DNS/DPS is chosen to be monodisperse, all future emerging droplet diameters are pre-defined and the distribution remains discrete. Therefore, the three Dirac functions from DQMOM are compared to a Dirac distribution. Figures 6.13 to fig. 6.14 show that the DQMOM Dirac distribution, which represents the model accounting for the correlations, is much closer to the real distribution than the DQMOM Dirac distribution, which is based on the molecular-chaos assumption. For increasing droplet Stokes numbers the two DQMOM Dirac distributions become more similar, which is explainable

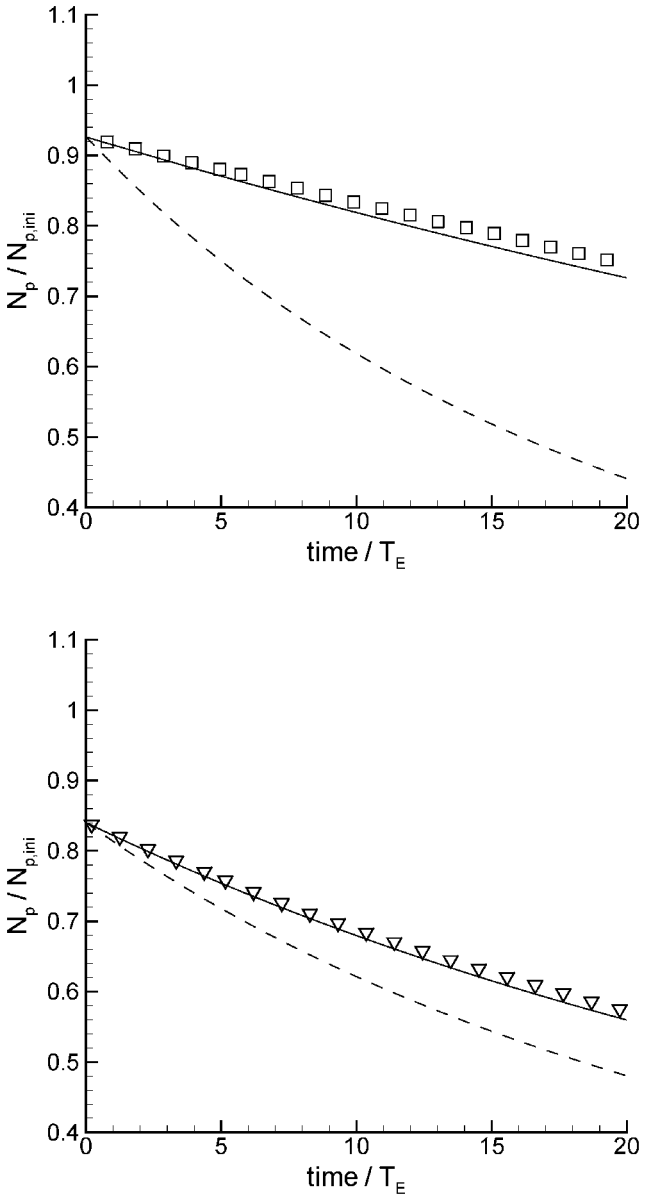

Figure 6.11: Number of droplets normalized by initial droplet number $N_{p,ini}$ over time normalized by the integral Eulerian time scale of the fluid, for fluid flow with $Re_\lambda = 32.9$. The symbols stand for the initial droplet Stokes numbers $St = 0.11$ $\square$ (top) and $St = 1.03$ ∇ (bottom) measured in DNS/DPS. The collision source term in the droplet number and mass balance equation based on the theory of molecular-chaos (dashed line $---$) and accounting for the correlation in the droplet velocities by the fluid turbulence (solid line —) are shown.

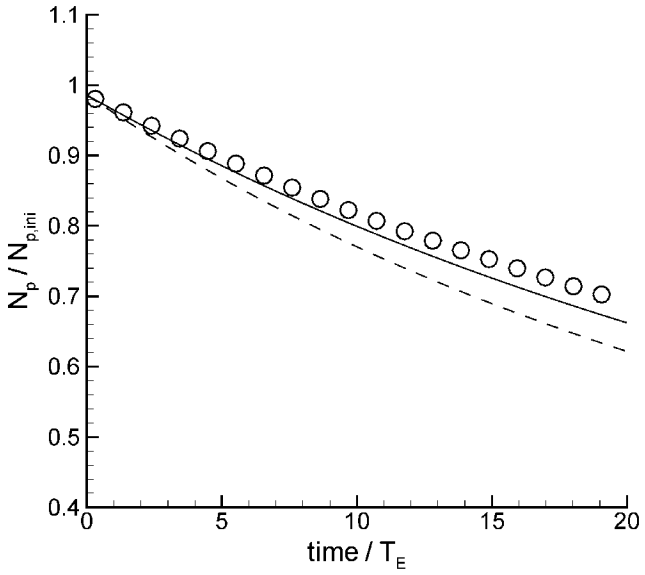

Figure 6.12: Number of droplets normalized by initial droplet number $N_{p,ini}$ over time normalized by the integral Eulerian time scale of the fluid, for fluid flow with $Re_\lambda = 32.9$. The symbols stand for the initial droplet Stokes numbers $St = 2.72$ ◯ measured in DNS/DPS. The collision source term in the droplet number and mass balance equation based on the theory of molecular-chaos (dashed line − − −) and accounting for the correlation in the droplet velocities by the fluid turbulence (solid line —) are shown.

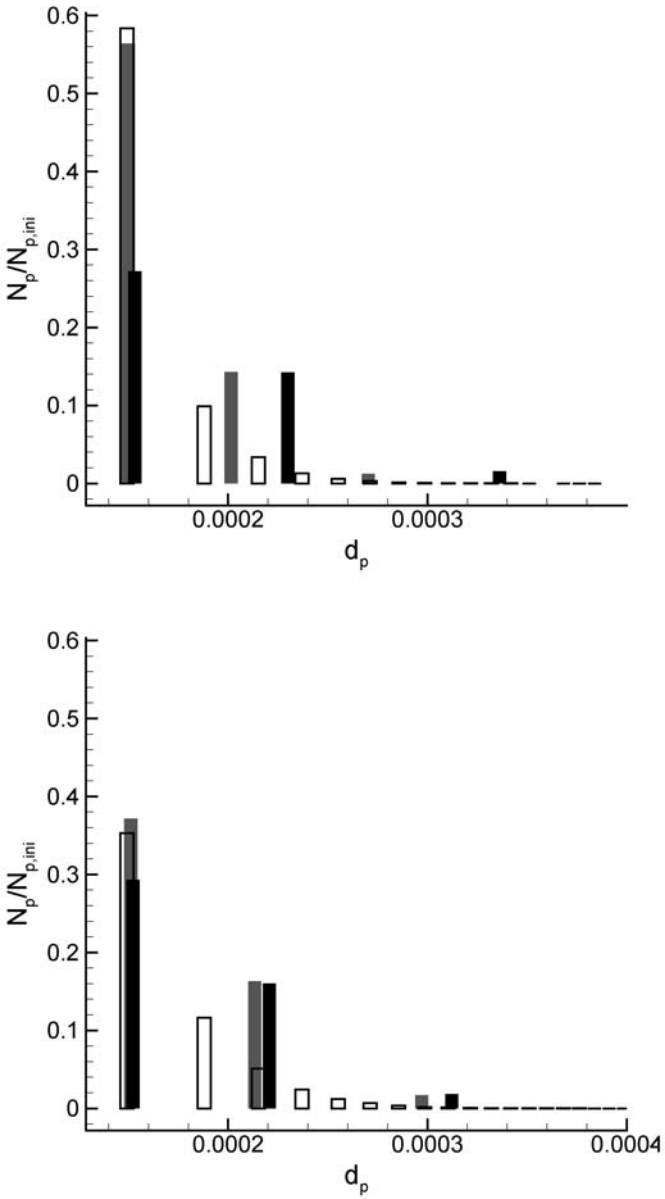

Figure 6.13: Droplet diameter distribution for droplet with Stokes number $St = 0.11$ (top) and $St = 1.03$ (bottom) at time $time/T_E = 20$. The white bars □ represent the measured values from DNS/DPS, the gray bars ■ stand for the three DQMOM Dirac functions using the collision model accounting for the correlation of droplet velocities by the fluid turbulence and the black bars ■ stand for the three DQMOM Dirac functions applying the molecular-chaos assumption.

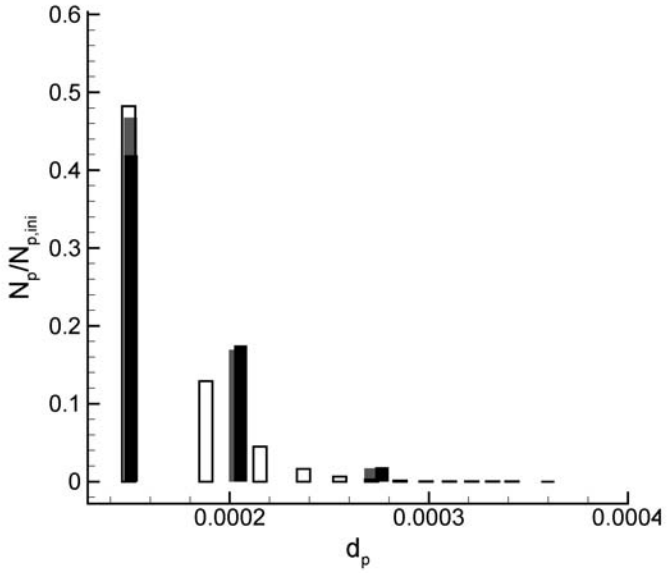

Figure 6.14: Droplet diameter distribution for droplet with Stokes number $St = 2.72$ at time $time/T_E = 20$. The white bars □ represent the measured values from DNS/DPS, the gray bars ■ stand for the three DQMOM Dirac functions using the collision model accounting for the correlation of droplet velocities by the fluid turbulence and the black bars ■ stand for the three DQMOM Dirac functions applying the molecular-chaos assumption.

by the fact, as already stated above, that droplets approach conditions that correspond to the kinetic theory of rarefied gases with increasing inertia.

6.2.3 Initial log-normal particulate phase

In order to test the DQMOM approach with a continuous diameter distribution, simulations are performed with a lognormal droplet diameter distribution, as presented in chapter 5. The initialization is done using the Gauss-Quadrature on the distribution given by DNS/DPS. The evolution of the lognormal droplet diameter distribution is shown in chapter 5. Figure 6.15 shows the initial and final droplet diameter distribution measured in DNS/DPS simulations (top) and from the DQMOM simulations (bottom). The dotted line $\cdots$ in fig. 6.15 (top) shows the initial droplet diameter distribution. Application of the Gauss-Quadrature approximation, if 3 Dirac functions are chosen, results in the Dirac distribution represented by the white bars $\square$ in fig. 6.15 (bottom). The solid line — in fig. 6.15 (top) shows the final distribution measured from DNS/DPS simulations. The Gauss-Quadrature approximation is applied on this final distribution and the resulting Dirac distribution is given by the gray bars ■ in fig. 6.15 (bottom). The sum of the weights of these three Dirac functions sums to 1 as it does by application of the Gauss-Quadrature approximation on the initial distribution. The number of droplets represented, however, has diminished and is not the same as at the beginning of the simulations due to droplet coalescence.

The droplet diameter distribution that is determined by DQMOM can always be compared to the final droplet diameter distribution measured from DNS/DPS simulations, accounting for different collision models. But, it is also possible to compare the Dirac distribution from the Gauss-Quadrature approximation applied on the final DNS/DPS diameter distribution as explained above and shown in fig. 6.15. As mentioned above, the sum of the weights of the Dirac functions sums to 1, the sum of the weights obtained at the end of the simulations from DQMOM also sums to 1, but the number of droplets has diminished due to coalescence. If the Gauss-Quadrature approximation is applied on the final DNS/DPS distribution, the results from DQMOM can be compared not only to this DNS/DPS final distribution, but also to the corresponding Dirac distribution. Figure 6.16 shows a comparison of the Dirac distribution obtained from the final DNS/DPS diameter distribution by the described procedure (gray bars ■) to the results obtained by DQMOM at $time/T_E = 20$ using two different collision models. First, the final distribution obtained applying the molecular-chaos assumption (black bars ■), and second, the collision model accounting for the correlation of the droplet velocities by the fluid turbulence (white

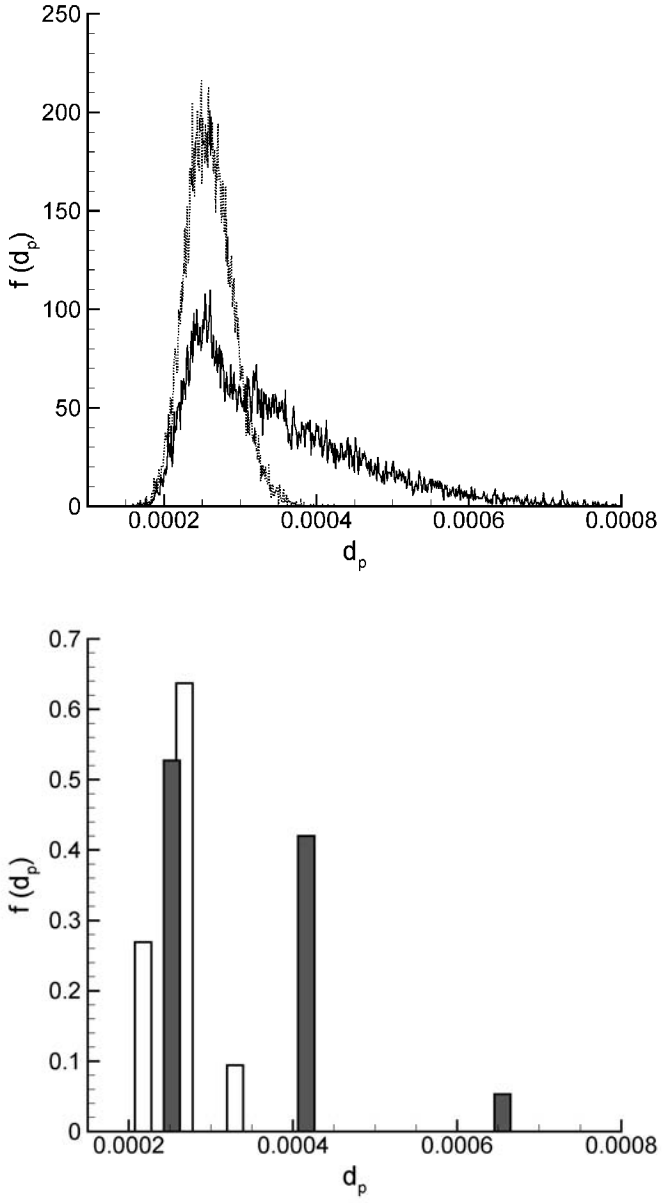

Figure 6.15: Initial and final droplet diameter distribution in DNS/DPS simulations (top) and DQMOM (bottom). The dotted line $\cdots$ and the white bars $\square$ stand for the initial distribution, the solid line — and the gray bars $\blacksquare$ for the final distribution.

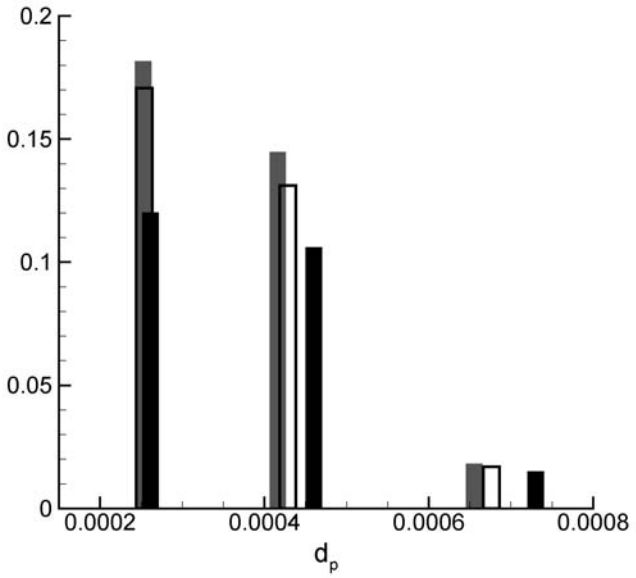

Figure 6.16: Comparison of final distributions. Droplet number per class normalized by initial total droplet number over droplet diameter. DQMOM using collision model accounting for correlation of droplet velocities □ and molecular-chaos assumption ■. The gray bars ■ stand for the Gauss-Quadrature on the final DNS/DPS distribution.

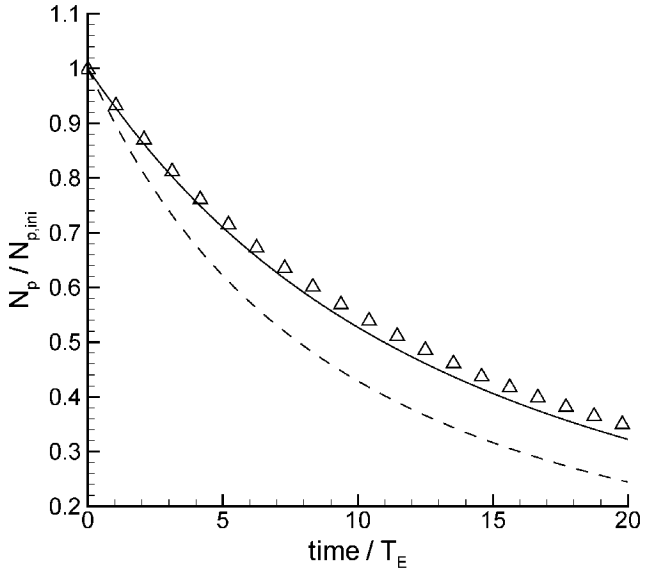

Figure 6.17: Number of droplets normalized by initial droplet number $N_{p,ini}$ over time normalized by the integral Eulerian time scale of the fluid, for fluid flow with $Re_\lambda = 32.9$. The symbols stand for the results measured in DNS/DPS. The collision source term in the droplet number and mass balance equation based on the theory of molecular-chaos (dashed line $- - -$) and accounting for the correlation in the droplet velocities by the fluid turbulence (solid line —) are shown.

bars □). It is clearly seen, that the collision model accounting for the correlation of the droplet velocities predicts better both, the abscissas and the weights of the Dirac functions, in comparison with the Dirac distribution obtained from the final DNS/DPS distribution. Figure 6.17, which shows the number of droplets normalized by initial droplet number $N_{p,ini}$ over time normalized by the integral Eulerian time scale of the fluid. Figure 6.17 shows clearly that the collision model accounting for the correlation of droplet velocities performs better than the collision model based on the molecular-chaos assumption. It should be noted that the coalescence rate is much higher in the simulations performed with an initial lognormal diameter distribution, compared to the initial monodisperse diameter distribution, even for the highest droplet Stokes numbers. The mean droplet diameter using a lognormal distribution is much higher than in the monodisperse diameter case, and thus the collision frequency of the droplets is increased.

Chapter 7

Conclusion

How can statistical models be validated, which account correctly for the influence of fluid turbulence on droplet coalescence? How can the development of these models be supported? What is the influence of fluid turbulence on droplet coalescence? This work focuses on the answers to these questions. A first element, to the challenges described by the preceding questions, is the creation of a reference solution, to which model predictions can be compared and which serves to understand the fundamental physics of turbulence-coalescence interaction. Direct Numerical Simulations of the fluid turbulence, solving all scales of turbulence and coupled with a deterministic particle/droplet tracking are performed, in order to create this reference solution, which can be regarded as exact.

The first element of this work consists in the development of a collision detection algorithm, which can account for poly-dispersion of the droplet diameters. If droplet coalescence is accounted for, even an initially monodisperse droplet diameter distribution turns polydisperse very quickly. The collision detection algorithm and all parts of the code, treating the dispersed phase implemented in the DNS solver used, cannot account for poly-dispersion in the version at the beginning of this work. Therefore, the development of a collision detection algorithm constitutes a first step within this work. This new collision detection algorithm is validated in dry granular flows of solid colliding particles, as dry granular flows allow to focus on the particle collision without the "disturbing" influence of a fluid phase. A solution, for many statistics gained in dry granular flows, is known from the kinetic theory of rarefied gases. The measured values can thus be compared to analytical solutions. The validation for binary collisions of mono- and bidisperse particle phases as well as of dry granular coalescence is shown in chapter 3. It is shown, that the algorithm correctly reproduces various statistics such as the particle collision angle, the particle relative velocity at the moment of collision and the collision frequency. It is also shown that the particle sys-

tem returns to an isotropic state, if turned anisotropic before, and coincides very well with model predictions. In order to handle the collision of poly-disperse particles or droplets, a second particle collision detection criterion is introduced next to the standard overlap criterion. This additional criterion compares the sign of the scalar product of particle relative velocity and droplet center connecting vector at two consecutive time steps. If the sign changes the droplets changed their relative position with each other and it is possible that the droplets collided, but are not detected by an overlap. It is shown that this second detection criterion increases the precision of the algorithm for grazing collision at the same time as it is possible to increase the time step by a factor of 10. Knowing that the time step criterion on the dispersed phase is more stringent than the stability criterion on the fluid phase in DNS, this improvement in time step represents a significant advantage. The reader may also refer to Wunsch *et al.* [138]. The code finally needed to be adapted to the vectorial structure of the super-computer used and revalidated, which is also shown for dry granular coalescence.

In a second part of this work, direct numerical simulations of the fluid turbulence coupled with a deterministic simulation of droplet trajectories are performed. These simulations assess the influence of droplet inertia and fluid turbulence on the coalescence rate of inertial droplets. Five different droplet inertias are investigated, suspended in three different turbulent flow fields. The turbulent fluid flow field configuration is a homogeneous isotropic turbulence and the droplets are in a local equilibrium before coalescence is studied. An initially monodisperse droplet diameter distribution and a lognormal droplet diameter distribution are investigated in order to study the influence of fluid turbulence on droplet coalescence. These simulations allow to obtain the time evolution of the coalescence rate, mean diameters, droplet kinetic energy and others as well as the droplet diameter distributions over time (see chapter 5). These simulations serve, besides their interest for the fundamental understanding of turbulence-coalescence interaction, as reference data base for statistical model predictions. For example the influence of fluid turbulence on the coalescence rate of different inertia droplets is studied and it is shown that the coalescence rate increases with fluid turbulence for low-inertia droplets but decreases for high-inertia droplets. It is shown that droplets with a Stokes number on the integral scale of the fluid of about 1, exhibit the highest coalescence rate for a given turbulent flow field. These simulations are performed in a pure coalescing regime, which means that each collision of droplets leads to permanent coalescence. A last study performed gives a series of collision outcomes and not only pure coalescence. The physical fundamentals therefore are shown in chapter 2. The collision treatment in the deterministic algorithm is modified in such a way, that it accounts for pure coalescence, stretching and reflexive separation. The droplet

phase properties need to be adjusted in this case, in order to create Weber numbers that cover the entire spectrum of potential collision outcomes. The reflexive separation regime is treated as a collision of droplets. The case of stretching separation is handle by ignoring the collision. In a first step it seems justifiable to ignore the collision of two droplets in the stretching separation regime, as the two droplets continue after such a collision almost on their initial trajectories as detailed in chapter 2. The creation of satellite droplets is neglected, likewise the induced rotation of the droplets. Accounting for the creation of satellite droplets is computationally demanding in DNS/DPS, as the time step criterion needs to be applied to the smallest of the droplets, in order to ensure a correct collision treatment. The satellite droplets are typically much smaller than the original droplets. The droplet diameter distribution would, however, be significantly modified if the creation of satellite droplets is considered. Some authors also report on a bouncing regime for certain liquids. The bouncing regime is not treated in this work. The coalescence regime shows a strong dependency on the droplet Stokes number in the performed simulations.

As many industrial applications are not accessible by direct numerical simulations today, and will not be in the near future, different strategies exist to access these flow configurations. Two different approaches are compared to results from DNS/DPS simulations in this work, which are based on the joint fluid-particle velocity PDF approach [117]. A first approach, Euler-Lagrange stochastic simulations [60], which resolve the PDF transport equation directly; and a second one, a moment method approach accounting for poly-dispersion and droplet coalescence, which is an extension of the DQMOM approach by Marchisio and Fox [82] to the equations of Simonin [117] for a monodisperse dispersed phase [11]. The equations found in this extension are the same as the equations of Simonin [117], if one single Dirac function is chosen. The different droplet classes conditioned on a droplet mass are coupled by coalescence source terms. The fundamentals of these two approaches, Euler-Lagrange stochastic and DQMOM, are given and the collision handling or the collision source terms respectively are given for the case of a pure coalescence regime. The standard approach accounting for droplet coalescence is based on the assumption of molecular chaos originating from the kinetic theory of rarefied gases. It is shown, in comparison with results obtained from DNS/DPS simulations, that in both cases, Euler-Lagrange stochastic and DQMOM, the models based on the assumption of molecular chaos do not predict the coalescence rate in a satisfying manner. Especially for low droplet inertia the deviations of model predictions to measured results from DNS/DPS are significant. These models based on the molecular chaos assumption perform the better, the higher the droplet inertia is. Within the droplet inertia investigated within this work, however, these predictions do not reach a satisfying performance. On the other hand, it is shown that collision models, which

account for the correlation of droplet velocities by the fluid turbulence, perform very well in comparison with results obtained from DNS/DPS simulations. These models exhibit a significant improvement for all droplet inertia investigated and the most prominent for the lowest droplet inertia studied. The coalescence rate, droplet mean diameter or droplet kinetic energy are well reproduced. The reader may also refer to Wunsch *et al.* [137] and Wunsch *et al.* [139]. The work done, using the DQMOM approach, allowed in addition to validate the influence of different collisional source terms. It is shown that, in the flow configuration of a homogeneous isotropic turbulence, the collision source term in the droplet number and mass balance equation is predominant and that the influence of a collision source term in the droplet kinetic energy equation can be neglected.

A future study using DNS/DPS could focus on the influence of a mean velocity of the droplets, created by gravity for example: a configuration which is relevant for the formation of rain droplets in clouds. Equally, it is of interest to investigate the influence of a fluid velocity gradient on the coalescence rates. Statistical model predictions could then be validated against these results, testing their performance in a more complicated flow configuration.

It is of interest to investigate the droplet break-up or the formation of satellite droplets. These are all configurations that can be investigated with the existing codes. Simulations with different droplet collision outcomes (coalescence, stretching separation, reflexive separation and bouncing) can be investigated in more details. These results may give relevant information for the development of statistical modeling approaches, which account not only for permanent coalescence, but also for break-up, satellite droplets or droplet bouncing, as first results obtained within this work indicate, that the droplet diameter distribution is strongly influenced for high droplet inertia, but not for low inertia. Also the agglomeration of solid particles or the break-up of these agglomerates could be investigated, accounting for the evolution of the form of agglomerates.

A sound description of droplet coalescence collisional source terms in DQMOM for droplet momentum or fluid-droplet variance is of interest, in order to account for these effects in configurations, like the before mentioned. These can be validated against DNS/DPS results by means of the here used solvers. A next step is then the implementation of this DQMOM approach and its source terms into a multi-fluid code and its validation against a more complex test case [121].

Finally, it is possible to use the results here obtained for the development of coalescence models in the frame of the Eulerian mesoscopic approach and for validation of Euler-Euler or Euler-Lagrange LES simulations accounting for coalescence.

Bibliography

[1] J. Abrahamson. Collision rates of small particles in a vigorously turbulent fluid. *Chemical Engineering Science*, 30:1371–1379, 1975.

[2] B. J. Alder and T. E. Wainwright. Studies in molecular dynamics. i. general method. *The Journal of Chemical Physics*, 31(2):459–466, August 1959.

[3] V.A. Arkhipov, G.S. Ratanov, and V.F. Trofimov. Experimental investigation of the interaction of colliding droplets. *Journal of Applied Mechanics and Technical Physics, Translated from Zhurnal Prikladnoi Mekhaniki i Teknnicheskoi Fiziki No. 2, pp.73-77, 1978*, 19 (2), 1978.

[4] N. Ashgriz and J.Y. Poo. Coalescence and separation in binary collisions of liquid drops. *J. Fluid Mech.*, 221:183–204, 1990.

[5] E. Aulissa, S. Manservisi, R. Scardovelli, and S. Zaleski. A geometrical area-preserving volume-of-fluid method. *J. Comput. Phys.*, 192:355–364, 2003.

[6] T. Auton, J.C.R. Hunt, and M Prud'homme. The force exerted on a body in inviscid unsteady non-uniform rotational flow. *Journal of Fluid Mechanics*, 197:241–257, 1988.

[7] H. Babovsky. On a simulation scheme for the boltzmann equation. *Math. Meth. Appl. Sci.*, 8:223–233, 1986.

[8] S. Balachandar and M.R. Maxey. Methods for evaluating fluid velocities in spectral simulations of turbulence. *J. Comptutational Physics*, 83:96–125, 1989.

[9] A.B. Basset. Treatise on hydrodynamics. *Bell, London*, 2, 1888.

[10] L. Bayvel and Z. Orzechowski. *Liquid Atomization*. Taylor and Francis, 1993.

[11] R.J. Belt and O. Simonin. Quadrature method of moments for the pdf modeling of droplet coalescence in turbulent two-phase flows. *Proc. of FEDSM2009, ASME 2009, FEDSM2009-78095*, 2009.

[12] A. Berlemont, P. Achim, and Z. Chang. Lagrangian approaches for particle collisions: The colliding particle velocity correlation in the multiple particles tracking method and in the stochastic approach. *Phys. of Fluids*, 13 (10):2946–2956, 2001.

[13] A. Berlemont, P. Desjonquères, and G. Gouesbet. Particle lagrangian simulation in turbulent flows. *Int. J. Multiphase Flow*, 16:19–34, 1990.

[14] A. Berlemont, O. Simonin, and M. Sommerfeld. Validation of inter-particle collision models based on large eddy simulation. *6th Int. Symp. on gas-solid flows, ASME FEDSM*, pages 359–369, 1995.

[15] G.A. Bird. Direct simulation and the boltzmann equation. *Phys. of Fluids*, 13:2676–2681, 1970.

[16] A. Boëlle, G. Balzer, and O. Simonin. Second-order prediction of the particle-phase stress tensor of inelastic spheres in simple shear dense suspensions. *Proc. 6th Int. Symp. on gas-solid flows, ASME FED*, 228:9–18, 1995.

[17] M. Boivin. *Etude de l'influence des particules sur la turbulence à partir des simulations directes et de simulations des grandes échelles d'écoulements diphasiques gaz-solides homogènes isotropes stationnaires.* PhD thesis, EDF-DRD, 1996.

[18] J. Boussinesq. Sur la résistance qu'oppose un liquide indeéfini en repos... *Comptes Rendus, Acad. Sci., Paris*, 100:935–937, 1885.

[19] P. R. Brazier-Smith, S. G. Jennings, and J. Latham. The interaction of falling water drops: coalescence. *Proceedings of the Royal Society London Series A, Mathematical and Physical sciences*, 326(1566):393–408, January 1972.

[20] C.F. Carnahan and K.E. Starling. Equation of state of non-attracting rigid spheres. *J. Chem. Phys.*, 51:635–636, 1969.

[21] S. Chapman and T.G. Cowling. *The mathematical theory of non-uniform gases.* Cambridge Mathematical Library, 1970.

[22] R. Clift, J.R. Grace, and M.E. Weber. *Bubbles, drops and particles.* Academic Press, 1978.

[23] G. Comte-Bellot and S. Corrsin. Simple eulerian time correlation of full- and narrow-band velocity signals in grid-generated 'isotropic' turbulence. *J. Fluid Mech.*, 48:273–337, 1971.

[24] T.H. Cormen, C.E. Leiserson, and R.L. Rivest. *Introduction to Algorithms*. The MIT Press, Cambridge, MA, 1990.

[25] S. Corrsin and J.L. Lumley. On the equation of motion of a particle in a turbulent fluid. *Appl. Sci. Res.*, sect. A. 6:114–116, 1957.

[26] I.V. Derevich. Coagulation of particles suspended in a turbulent flow. *Russian Academy of Sciences - Institute for High Temperature, Moscow*, 1995.

[27] I.V. Derevich and L.I. Zaichik. Precipitation of particles from a turbulent flow. *Izvestiyia Akademii Nauk SSSR, Mekhanika Zhidkosti i Gaza*, 5:96–104, 1988.

[28] E. Deutsch. *Dispersion de particules dans une trubulence homogène isotrope calculée par simulation numérique directe des grandes échelles*. PhD thesis, Ecole Centrale de Lyon, collection des notes internes de la DER, Electricité de France, Clamart, France, 1992.

[29] E. Deutsch and O. Simonin. Large eddy simulation applied to the motion of particles in stationary homogeneous fluid turbulence. *Turbulence Modification in Multiphase Flow, ASME-FED*, 110:35–42, 1991.

[30] A. Donev, S. Torquato, and F.H. Stillinger. Neighbor list collision-driven molecular dynamics simulation for nonspherical hard particles. i. algorithmic details. *J. Comput. Phys.*, 202:737–764, 2005.

[31] A. Donev, S. Torquato, and F.H. Stillinger. Neighbor list collision-driven molecular dynamics simulation for nonspherical hard particles. ii. applications to ellipses and ellipsoids. *J. Comput. Phys.*, 202:765–793, 2005.

[32] A. Donev, S. Torquato, F.H. Stillinger, and R. Connelly. A linear programming algorithm to test for jamming in hard-sphere packings. *J. Comput. Phys.*, 197:139–166, 2004.

[33] C. Dumouchel. On the experimental investigation on primary atomization of liquid streams. *Exp. Fluids*, 45:371–422, 2008.

[34] S. Elghobashi and G. C. Truesdell. On the two-way interaction between homogeneous turbulence and dispersed solid particles. i: Turbulence modification. *Phys. Fluids A*, 5 (7):1790–1801, 1993.

[35] S.E. Elghobashi and G.C. Truesdell. On the two-way interaction between homogeneous turbulence and dispersed solid particles: I. turbulence modification. *Phys. of Fluids A*, 5:1790, 1993.

[36] J.J. Erpenbeck and W.W. Wood. *Molecular dynamics for hard-core systems; in Statistical Mechanics B.* Plenum Press New York, 1977.

[37] J.-P. Estrade, H. Carentz, G. Lavergne, and Y. Biscos. Experimental investigation of dynamic binary collision of ethanol droplets - a model for droplet coalescence and bouncing. *International Journal of Heat and Fluid Flow*, 20:486–491, 1999.

[38] Jean-Philippe Estrade. *Etude Experimental et Numérique de la collision de gouttelettes.* PhD thesis, Ecole National Superieure de l'aeronautique et de l'espace, 1998.

[39] V. Eswaran and S.B. Pope. An examination of forcing in direct numerical simulations of turbulence. *Computers & Fluids*, 16 (3):257–278, 1988.

[40] R. Fan, D.L. Marchisio, and R.O. Fox. Application of the direct quadrature method of moments to poly-disperse gas-solid fluidized beds. *Powder Techn.*, 139:7–20, 2004.

[41] P. Fede. *Modélisation et simulation de l'influence de la turbulence sur les collisions dans les écoulements mono- et bi-solides.* PhD thesis, Institut National Polytechnique de Toulouse, 2004.

[42] P. Fede and O. Simonin. Application of a perturbated two-maxwellian approach for the modelling of kinetic stress transfer by collision in non-equilibrium binary mixture of inelastic particles. *Proceedings of FEDSM2005*, FEDSM2005-77127, 2005.

[43] P. Fede, O. Simonin, and P. Villedieu. Monte carlo simulation of colliding particles in gas-solid turbulent flows from a joint fluid-particle pdf equation. *ASME FEDSM 2002, FEDSM2002-31226*, 2002.

[44] J. Fessler, J. Kulick, and J. Eaton. Preferential concentration of heavy particles in a turbulent channel flow. *Phys. Fluids*, 6:3742–3749, 1994.

[45] R.O. Fox, F. Laurant, and M. Massot. Numerical simulation of spray coalescence in an eulerian framework: Direct quadrature method of moments and multi-fluid method. *Journal of Computational Physics*, 227:3058–3088, 2008.

[46] A. Frohn. *Einführung in die Kinetische Gastheorie.* AULA-Verlag Wiesbaden, 1988.

[47] P. Février. *Etude Numerique des effets de concentration preferentielle et de correlation spatiale entre vitesses de particules solides en turbulence homogène isotrope stationnaire*. PhD thesis, Institut National Polytechnique de Toulouse, 2000.

[48] P. Février, O. Simonin, and K.D. Squires. Partitioning of particle velocities in gas-solid turbulent flows into a continuous field and a spatially uncorrelated random distribution: theoretical formalism and numerical study. *Journal of Fluid Mechanics*, 533:1–46, 2005.

[49] R. Gatingol. The faxen formulas for a rigid particle in an unsteady non-uniform stokes flow. *J. Mec. Theor. Appl.*, 1:143–154, 1983.

[50] E. Goldman and L. Sirovich. Equations for gas mixtures. *Phys. of Fluids*, 10:1928–1840, 1967.

[51] A.D. Gosman and E. Ioannides. Aspects of computer simulation of liquid-fuelled combustions. *AIAA, 19th Aerospace Sciences Meeting, St. Louis, Missouri*, 1981.

[52] C. Gourdel. *Modélisation et Simulations de Mélange Binaires de Particules en Interaction avec un Champ Fluid Turbulent pour l'application aux lits fluidisés circulants.* PhD thesis, Université de Technologie de Compiègne, 1999.

[53] H. Grad. On the kinetic theory of rarefied gases. *Communications on Pure and Applied Mathematics*, 2 (4):331–407, 1949.

[54] J. B. Greenberg, I. Silvermann, and Y. Tambour. On the origin of spray sectional conservation equations. *Combust. Flame*, 93:90–96, 1993.

[55] M. Hermann. A eulerian level set/vortex sheet method for two-phase interface dynamics. *J. Comput. Phys.*, 203:539–571, 2005.

[56] J.O. Hinze. *Turbulence*. McGraw-Hill, 1975.

[57] M.A. Hopkins and M.Y. Louge. Inelastic microstructue in rapid granular flows of smooth disks. *Phys. of Fluids A*, (3) 1, 1990.

[58] Z. Hu and R. C. Srivastava. Evolution of raindrop size distribution by coalescence, break-up, and evaporation: Theory and observations. *Journal of the Atmospheric Sciences*, 52 (10):1761–1783, 1995.

[59] J. J. Hylkema. *Modélisation cinétique et simulation numérique d'un brouillard dense de gouttelettes. Application aux propulseurs à poudre.* PhD thesis, École National supérieure de l'aéronautique et de l'espace, 1999.

[60] J. J. Hylkema and P. Villedieu. A random particle method to simulate coalescence phenomena in dense liquid sprays. *Proc. 16th Int. Conf. on Num. Meth. in Fluid Dynamics, Lecture Notes in physics 515; Springer Verlag*, 1999.

[61] F. James. Ranlux: A fortran implementation of the high-quality pseudorandom number generator by lüscher. *Computer Physics Communications*, 79:111–114, 1994.

[62] J.T. Jenkins and M.W. Richman. Grad's 13-moment system for a dense gas of inelastic spheres. *Arch. Ration. Mech. Anal.*, 87:355–377, 1985.

[63] Y.J. Jiang, A. Umemura, and C.K. Law. An experimental investigation on the collision behaviour of hydrocarbon droplets. *Journal of Fluid Mechanics*, 234:171–190, 1992.

[64] C. Josserand, L. Lemoyne, R. Troeger, and S. Zaleski. Droplet impact on a dry surface: triggering the splash with a small obstacle. *J. Fluid Mech.*, 524:47–56, 2005.

[65] A.N. Kolmogorov. The local structure of trubulence in incompressible viscous fluid for very large reynolds numbers. *Dokl. Akad. Nauk SSSR (in Russian)*, 30:19–21, 1941.

[66] R.H. Kraichnan. Inertial-range spectrum of hydromagnetic turbulence. *Phys. of Fluids*, 8:doi:10.1063/1.1761412, 1965.

[67] F. Kruis and K. Kuster. The collision rate of particle in turbulent flow. *Chem. Eng. Comn.*, 158:201–230, 1997.

[68] D. Lathouwers and J. Bellan. Modeling of dense gas-solid reactive mixture applied to biomass pyrolysis in a fluidized bed. *Int. J. Multiphase Flow*, 27:2155–2187, 2001.

[69] F. Laurent. *Modélisation mathématique et numérique de la combustion de brouillards de gouttes polydispersés.* PhD thesis, Université Claude Bernard, Lyon 1, France, 2002.

[70] F. Laurent and M. Massot. Multi-fluid modeling of laminar poly-dispersed spray flames: origin, assumption and comparison of sectional and sampling methods. *Comb. Theory and Modelling*, 5:537–572, 2001.

[71] F. Laurent, M. Massot, and P. Villedieu. Eulerian multi-fluid modeling for the numerical simulation of coalescence in polydisperse dense liquid sprays. *J. Comput. Phys.*, 194:505–543, 2004.

[72] J. Lavieville, E. Deutsch, and O. Simonin. Large eddy simulation of interaction between colliding particles and a homogeneous isotropic turbulence field. *6th Int. Symp. on gas-solid flows, FEDSM*, 228:347–257, 1995.

[73] J. Laviéville. *Numerical simulations and modelling of interactions between turbulence dragging and interparticle collisions applied to gas-solid two-phase flows.* PhD thesis, Département Laboratoire National d'Hydraulique, 1997.

[74] A. H. Lefebvre. *Atomization and sprays.* Taylor and Francis, 1989.

[75] M. Lüscher. A portable high-quality random number generator for lattice field theory calculations. *Computer Physics Communications*, 79:100–110, 1994.

[76] B.D. Lubachevsky. How to simulate billiards and similar systems. *J. Comput. Phys.*, 94:255–283, 1991.

[77] F. H. Ludlam. The production of showers by the coalescence of cloud droplets. *Quart. J. Roy. Meteor. Sco.*, 77 (333):402–417, 1951.

[78] C.K.K Lun and S.B. Savage. The effects of an impact velocity dependent coefficient of restitution on stresses developed by sheared granular materials. *Acta Mechanica*, 63:539–559, 1986.

[79] J. Magnaudet, M. Rivero, and J. Fabre. Accelerated flows past a rigid sphere or a spherical bubble. part 1: steady straining flow. *Journal of Fluid Mechanics*, 284:97–135, 1995.

[80] G.A. Mansoori, N.F. Carnahan, K.E. Starling, and T.W. Leland. Equilibrium thermodynamic properties of the mixture of hard sphere. *J. Chem. Phys.*, 54:1523–1525, 1971.

[81] D. L. Marchisio, R. D. Virgil, and R.O. Fox. Quadrature method of moments for aggregation-breackage processes. *J. Colloid Interface Sci.*, 258 (2):322–334, 2003.

[82] D.L. Marchisio and R.O. Fox. Solution of population balance equations using the direct quadrature method of moments. *Aerosol Sci.*, 36:43–95, 2005.

[83] M. Marin, D. Risso, and P. Cordero. Efficient algorithms for many-body hard particle molecular dynamics. *J. Comput. Phys.*, 109:306–317, 1993.

[84] P. Marmottant and E. Villermaux. On spray formation. *J. of Fluid Mech.*, 498:73–111, 2004.

[85] G. Marsaglia and A. Zaman. A new class of random number generators. *Ann. Appl. Prob.*, 1:462–480, 1991.

[86] G. K. Mather. Coalescence enhancement in large multicell storms caused by the emissions from a kraft paper mill. *J. of Appl. Meteor.*, 30 (8):1134–1146, 1991.

[87] M.R. Maxey and J.J. Riley. Eauqtion of motion for a small rigid sphere in a nonuniform flow. *Phys. of Fluids*, 26(4):2883–2889, 1983.

[88] R. McGraw. Description of aerosol dynamics by the quadrature method of moments. *Aerosol Sci. Technol.*, 27:255–265, 1997.

[89] E.E. Michaelides and Z.G. Feng. The equation of motion of a small viscous sphere in an unsteady flow with interface slip. *Int. J. Multiphase Flow*, 21(2):315–321, 1995.

[90] J.P. Minier and J. Pozorski. Analysis of existing lagrangian models and new propositions for particle dispersion in homogeneous stationary turbulence. Technical report, Rapport EDF HE-44/92.29, 1992.

[91] S. Morioka and T. Nakajima. Modeling of gas and solid particles in two-phase flow and application to fluidized bed. *Journal of Theoretical and Applied Mechanics*, 6:77–88, 1987.

[92] K. Nanbu. Stochastic solution method of the master equation and the boltzmann equation. *J. Phys. Soc. Japan*, 52:2654–2658, 1983.

[93] B. Oesterlé and P. Petitjean. Simulation of particle-to-particle interactions in gas-solid flows. *Int. J. Multiphase Flow*, 19:199–211, 1993.

[94] A. Ormancey. *Simulation du Comportement de Particules dans des Ecoulements Turbulents*. PhD thesis, Ecole National Supérieure des Mines de Paris, 1984.

[95] C.W. Oseen. *Hydrodynamik*. Leipzig, 1927, p. 132.

[96] M.R. Overholt and S.B. Pope. A deterministic forcing scheme for direct numerical simulations of turbulence. *Computers & Fluids*, 27(1):11–28, 1998.

[97] R.W. Park. *Behavior of water drops colliding in humid nitrogen.* PhD thesis, University of Wisconsin, july 1970.

[98] G. Patino-Palacios and O. Simonin. General derivation of eulerian-eulerian equations for mutliphase flows. Technical report, IMFT, 2003.

[99] R.J. Perkins, S. Gosh, and J.C. Phillips. *The Interaction between Particles and Coherent Structures in a Plane Turbulent Jet.* Springer Verlag, Berlin, 1991.

[100] F. Pigeonneau. *Modélisation numérique des collisions de gouttes en écoulements laminaires et turbulents.* PhD thesis, Université Paris VI, 1998.

[101] S.B. Pope. On the relationship between stochastic lagrangian models of turbulence and second-moment closures. *Phys. of Fluids*, 6:973–985, 1994.

[102] Stephen B. Pope. *Turbulent Flows.* Cambridge University Press, 2000.

[103] J. Qian and C.K. Law. Regimes of coalescence and separation in droplet collision. *J. Fluid Mechanics*, 331:59–80, 1997.

[104] C. Rabe. *Etude de la coalescence dans les rampes de spray: application au système d'aspersion des Réacteurs à Eau Pressurisée.* PhD thesis, Université Pierre et Marie Curie, 2009.

[105] D.C. Rapaport. A note on algorithms for billiard-ball dynamics. *J. Comput. Phys.*, 105:367–368, 1993.

[106] W. C. Reade and L. R. Collins. Effect of preferential concentration on turbulent collision rates. *Phys. of Fluids*, 12:2530, 2000.

[107] M.W. Reeks. On a kinetic equation for the transport of particles in turbulent flows. *Phys. of Fluids A*, 3:446–456, 1991.

[108] M.W. Reeks. On the continuum equations for dispersed particles in nonuniform flows. *Phys. of Fluids A*, 4:1290–1303, 1992.

[109] M.W. Reeks. On the constitutive relations for dispersed particles in nonuniform flows. 1: Dispersion in a simple shear flow. *Phys. of Fluids A*, 5:750–761, 1993.

[110] P.G. Saffman and J.S. Turner. On the collision of drops in turbulent clouds. *Journal of Fluid Mechanics*, 1:16–30, 1956.

[111] M. Sakiz. *Simulation numérique lagrangienne et modélisation eulérienne d'écoulement diphasiques gaz-particules en canal vertical*. PhD thesis, Ecole National des Ponts et Chaussés, 1999.

[112] B. L. Sawford. Reynolds number effects in lagrangian stochastic models of turbulent dispersion. *Phys. of Fluids*, 3(6):1577–1586, 1991.

[113] L. Schiller and A. Naumann. A drag coefficient correlation. *VDI Zeitung*, 77:318–320, 1935.

[114] B. Selma, R. Bannari, and P. Proulx. Simulation of bubbly flows: Comparison between direct quadrature method of moments (dqmom) and method of classes (cm). *To appear in: Chemical Engineering Science*, doi:10.1016/j.ces.2009.11.018, 2009.

[115] Hersir Sigurgeirsson, Andrew Stuart, and Wing-Lok Wan. Algorithms for particle-field simulations with collisions. *Journal of Computational Physics*, 172(2):766–807, September 2001.

[116] O. Simonin. Second-moment prediction of dispersed phase turbulence in particle-laden flows. annex 3: Third-moment closure. Technical report, EDF HE 44/91.24, 1991.

[117] O. Simonin. *Combustion and Turbulence in Two-Phase Flows*. von Karman Institute for Fluid Dynamics, Lecture Series 1996-02, 1996.

[118] O. Simonin, E. Deutsch, and J.P. Minier. Eulerian prediction of the fluid/particle correlated motion in turbulent two-phase flows. *Applied Scientific Research*, 51:275–283, 1993.

[119] O. Simonin, P. Fevrier, and J. Lavieville. On the spatial distribution of heavy-particle velocities in turbulent flow: from continuous field to particulate chaos. *Journal of Turbulence*, 3 (040), 2002.

[120] M. Sommerfeld. The importance of inter-particle collisions in horizontal gas-solid channel flows. *Gas-Particle Flows, ASME Fluids Engineering Conference, Hilton Head*, FED 228:335, 1995.

[121] M. Sommerfeld. Analysis of isothermal and evaporating turbulent sprays by phase-doppler anemometry and numerical calculations. *Int. Journal of Heat and Fluid Flow*, 19 (2):173–186, 1998.

[122] M. Sommerfeld. Inter-particle collisions in turbulent flows: A stochastic lagrangian model. *Proc. Turbulence and Shear Flow Phenomena*, 1:265–270, 1999.

[123] M. Sommerfeld. Validation of a stochastic lagrangian modelling approach for inter-particle collisions in homogeneous isotropic turbulence. *Int. J. Multiphase Flow*, 27:1829–1858, 2001.

[124] K. D. Squires and J. K. Eaton. Preferential concentration of particles by turbulence. *Phys. of Fluids*, 5:1169–1178, 1991.

[125] K.D. Squires and J.K. Eaton. Particle response and turbulence modification in isotropic turbulence. *Phys. of Fluids*, 2:1191–1203, 1990.

[126] G.G. Stokes. On the effect of the internal friction of fluids on the motion of pendulums. *Trans. Cambridge Phil. Soc.*, 9:8–23, 1850.

[127] S. Sundaram and L.R. Collins. Collision statistics in an isotropic particle-laden turbulent suspension. part 1: Direct numerical simulations. *Journal of Fluid Mechanics*, 335:75–109, 1997.

[128] S. Tanguy and A. Berlemont. Development of a level set method for interface tracking: application to droplet collisions. *Int. J. Multiphase Flows*, 31 (9):1015–1035, 2005.

[129] C.M. Tchen. *Mean value and correlation problems connected with the motion of small particles suspended in a turbulent fluid*. PhD thesis, Delft, Martinus Nijhoff, The Hague, 1947.

[130] P. Villedieu and O. Simonin. Modelling of coalescence in turbulent gas-droplet flows. *COMM. MATH. SCI., Supplemetal Issue*, 1:13–33, 2004.

[131] T. von Karman and L. Howarth. On the statistical theory of isotropic turbulence. *Proc. R. Soc. London Ser. A*, 164:192–215, 1938.

[132] L. P. Wang and M. R. Maxey. Settling velocity and concentration distribution of heavy particles in homogeneous isotropic turbulence. *J. Fluid Mech.*, 256:27–68, 1993.

[133] L.P. Wang, A.S. Wexler, and Y. Zhou. Statistical mechanical descriptions and modelling of turbulent collision of inertial particles. *Journal of Fluid Mechanics*, 415:117–153, 2000.

[134] Q. Wang and K. D. Squires. Large eddy simulation of particle-laden turbulent channel flow. *Phys. Fluids*, 8 (5):1207–1223, 1996.

[135] J.J.E. Williams and R.I. Crane. Particles collision rate in turbulent flow. *Int. J. Multiphase Flow*, 9 (4):421–435, 1983.

[136] J. D. Woods, J. C. Drake, and P. Goldsmith. Coalescence in a turbulent cloud. *Quart. J. Roy. Meteor. Sco.*, 98 (415):135–149, 2006.

[137] D. Wunsch, R. J. Belt, P. Fede, and O. Simonin. Dns/dps of inertial droplet coalescence in homogeneous isotropic turbulence and comparison with pdf model predictions using the direct quadrature method of moments. *Proc. of ASME FEDSM 2009*, FEDSM2009-78091, 2009.

[138] D. Wunsch, P. Fede, and O. Simonin. Development and validation of a binary collision detection algorithm for a polydispersed particle mixture. *Proc. of ASME FEDSM 2008*, FEDSM2008-55159, 2008.

[139] D. Wunsch, P. Fede, O. Simonin, and P. Villedieu. Numerical simulation and statistical modeling of inertial droplet coalescence in homogeneous isotropic turbulence. *Notes on Numercial Fluid Mechanics and Multidisciplinary Design*, 2009.

[140] Y. Yamamoto, M. Potthoff, T. Tanaka, T. Kajishima, and Y. Tsuji. Large-eddy simulation of turbulent gas-particle flow in a vertical channel: effect of considering inter-particle collisions. *J. Fluid Mech.*, 442:303–334, 2001.

[141] L. I. Zaichik, O. Simonin, and V. M. Alipchenkov. Two statistical models for predicting collision rates of inertial particles in homogeneous isotropic turbulence. *Phys. of Fluids*, 15 (10):2995–3005, 2003.

[142] L. I. Zaichik, O. Simonin, and V. M. Alipchenkov. Collision rates of bidisperse inertial particles in isotropic turbulence. *Phys. Fluids*, 18:035110, 2006.

[143] L.I. Zaichik, V.A. Pershukov, M.V. Koselev, and A.A. Vinberg. Modelling of dynamics, heat transfer and combustion in two-phase turbulent flows: 1. isothermal flows. *Experimental Thermal and Fluid Science*, 15:291–310, 1997.

[144] L.I. Zaichik and A.A. Vinberg. Modelling of particle dynamics and heat transfer in turbulent flows using equations for first and second moments of velocity and temperature fluctuations. *Proc. 8th Int. Symp. on Turbulent Shear Flows, Munich*, 1:1021–1026, 1991.

[145] Y. Zhou, A.S. Wexler, and L.P. Wang. On the collision rate of small particles in isotropic turbulence. ii. finite inertia case. *Phys. of Fluids*, 10:1206–1216, 1998.

Appendix A

Collision model for particle kinetic stress

The collision model for particle kinetic stress is given in details in Fede [41] and in Fede and Simonin [42]. The equations used in this work, are given here.

The simulations are performed in dry granular flows, with no particle mean velocity. The particle velocity fluctuating components are altered to anisotropy at the beginning of the simulation in order to account for the transfer of anisotropy between the velocity components of the different particle classes. Under these conditions the particle kinetic stress transport equation for particle p can be written

$$\frac{\partial}{\partial t} m_p n_p \left\langle v'_{p,i} v'_{p,j} \right\rangle = \sum_{\beta=p,q} \chi_{p\beta} \left(m_p v'_{p,i} v'_{p,j} \right) \quad , \tag{A.1}$$

where $\chi_{p\beta}\left(m_p v'_{p,i} v'_{p,j}\right)$ is given by

$$\begin{aligned}
\chi_{p\beta}\left(m_p v'_{p,i} v'_{p,j}\right) = \; & - \; m_p \left[\frac{2m_\beta}{m_p+m_\beta}\right]^2 \frac{1-e_c^2}{4} f_{p\beta}^K \; \frac{2}{3}\left(\frac{2}{3}q_p^2 + \frac{2}{3}q_\beta^2\right)\delta_{ij} \\
& - \; m_p \frac{2m_\beta}{m_p+m_\beta} \frac{1+e_c}{2} f_{p\beta}^K \; \frac{4}{3} \frac{m_p \frac{2}{3} q_p^2 - m_\beta \frac{2}{3} q_\beta^2}{m_p+m_\beta} \delta_{ij} \\
& - \; m_p \frac{2m_\beta}{m_p+m_\beta} \frac{1+e_c}{2} f_{p\beta}^K \; \frac{2}{3} \left[\frac{2m_p}{m_p+m_\beta} \widehat{R}_{p,ij} - \frac{2m_\beta}{m_p+m_\beta} \widehat{R}_{\beta,ij}\right] \\
& - \; m_p \left[\frac{2m_\beta}{m_p+m_\beta}\right]^2 f_{p\beta}^K \; \frac{(1+e_c)(3-e_c)}{5} \frac{1}{2} \left(\widehat{R}_{p,ij} + \widehat{R}_{\beta,ij}\right)
\end{aligned}$$

$$- \quad m_p \frac{2m_\beta}{m_p + m_\beta} \frac{1 + e_c}{2} f_{p\beta}^K \; \frac{4}{15} \frac{1}{T_p + T_\beta} \frac{m_p \frac{2}{3} q_p^2 - m_\beta \frac{2}{3} q_\beta^2}{m_p + m_\beta} \left(\widehat{R}_{p,ij} + \widehat{R}_{\beta,ij} \right) \quad . \tag{A.2}$$

It is reminded that $\widehat{R}_{p,ij}$ is given by

$$\widehat{R}_{p,ij} = \left\langle v'_{p,i} v'_{p,j} \right\rangle_p - \frac{2}{3} q_p^2 \tag{A.3}$$

Appendix B

Publications

D.Wunsch, P. Fede, and O. Simonin. Validation procedure for Discret Particle Simulation of turbulent two-phase flows with droplet coalescence. *ERCOFTAC Bulletin*, 2010

D. Wunsch, R. J. Belt, P. Fede, and O. Simonin. DNS/DPS of inertial droplet coalescence in homogeneous isotropic turbulence and comparison with pdf model predictions using the direct quadrature method of moments. *Proc. of ASME FEDSM 2009*, FEDSM2009-78091, 2009.

D. Wunsch, P. Fede, O. Simonin, and P. Villedieu. Numerical simulation and statistical modeling of inertial droplet coalescence in homogeneous isotropic turbulence. *Notes on Numercial Fluid Mechanics and Multidisciplinary Design*, 2009.

D.Wunsch, P. Fede, and O. Simonin. Development and validation of a binary collision detection algorithm for a polydispersed particle mixture. *Proc. of ASME FEDSM 2008*, FEDSM2008-55159, 2008.

Validation procedure for Discrete Particle Simulation of turbulent two-phase flows with droplet coalescence

D. Wunsch[1, 2], P. Fede[1, 2] & O. Simonin[1, 2]

[1]*Université de Toulouse; INPT, UPS; IMFT; 31400 Toulouse, France*
[2]*CNRS; Institut de Mécanique des Fluides de Toulouse; 31400 Toulouse, France*

ABSTRACT Discrete Particle Simulation (DPS) can be used in order to understand the physical mechanisms fluid turbulence exerts on particle dispersion or on particle-particle collisions and at the same time to provide a reliable reference data base for the development of statistical modelling approaches. A correct prediction of these deterministic simulations is therefore fundamental for the understanding and modelling of these complex phenomena. In this work a validation procedure for DPS is proposed focusing on both the correct prediction of fluid properties at the particle position and a correct prediction of collision handling. The strategy to validate the collision algorithm is based on dry granular flows, which allow testing the algorithm performance without the disturbing influence of the fluid phase. Finally it is shown how a correct handling of droplet coalescence can be assured.

1. INTRODUCTION

Particle laden turbulent flows are found in many industrial and practical applications like pneumatic conveying, circulating fluidized bed, liquid-fuel injection in internal combustion engines or rain drop formation. These flows involve a variety of complex phenomena, such as turbulent dispersion, particle-particle collisions, droplet coalescence, particle-wall interactions, turbulence modulation by the particles or heat and mass transfer.

The numerical simulation of turbulent two-phase flows has been extensively improved for the last decades. Nowadays the development of numerical methods and the parallel computing allow performing a Direct Numerical Simulation (DNS) of the interstitial fluid between moving particles [*Prosperetti & Oguz 2001*]. This approach is the most physical as it requires a minimum of closure models. However, even for the simulation of low-scale particle-liquid fluidized beds [*Corre et al. 2009*], the computational cost restricts this method to a quite low number of particles (roughly 5000 particles). Hence, this method is usually employed to investigate the momentum or heat transfer at the particle diameter scale [*Massol 2004*], but it is impossible to investigate collective phenomena taking place, such as particle accumulation.

An alternative approach considers each particle as a material point and the trajectory of each individual particle is computed in a Lagrangian frame. This approach, called Discrete Particle Simulation (DPS), can be applied for several millions of particles and can be coupled either with DNS or Large Eddy Simulation (LES) of the carrier phase. The DPS needs models for the momentum or heat transfer from the fluid to the particles. The turbulence modulation by the particles (the so-called two-way coupling) is questionable especially when the DPS is coupled with a LES.

The DPS can be used in order to understand the physical mechanisms fluid turbulence exerts on particle dispersion or on particle-particle collisions and at the same time to provide a reliable reference data base for the development of statistical modelling approaches. A correct prediction of these deterministic simulations is therefore fundamental for the understanding and modelling of these complex phenomena.

In this paper we propose a step-by-step validation procedure for DPS of inertial droplets suspended in turbulent flows and undergoing droplet coalescence. This work proposes a methodology that ensures an accurate treatment of particle dispersion (section 3) and particle-particle collisions or droplet coalescence handling (section 4). As particles transported by a turbulent flow a considered, section 2 briefly introduces the numerical predictions of turbulent flows, while focusing on the problems related to the coupling of DPS with the numerical simulation of single-phase turbulent flows.

2. PARTICLE PATH COMPUTATION AND VALIDATION

2.1. Particle trajectory

A dispersed phase of N_p spherical particles with diameter d_p and density ρ_p is considered in this work. Turbulence modulation by the dispersed phase (two-way coupling) is neglected, as the solid mass loading is small. Assuming that the particle to fluid density ratio ($\rho_p >> \rho_f$) is large, the forces acting on a single particle are reduced to the drag force and gravity only. Thus, the governing equations of a single particle is written as [*Maxey & Riley 1983*, *Gatignol 1983*]

$$\frac{d\mathbf{x}_p}{dt} = \mathbf{v}_p, \tag{1}$$

$$\frac{d\mathbf{v}_p}{dt} = -\frac{\mathbf{v}_p - \mathbf{u}_{f@p}}{\tau_p} + \mathbf{g} \quad , \tag{2}$$

where $\mathbf{x}_p$ and $\mathbf{v}_p$ are the position and velocity vector of the *p*-particles. The particle response time τ_p is given by

$$\tau_p = \frac{4}{3}\frac{\rho_p}{\rho_f}\frac{d_p}{C_D}\frac{1}{\left|\mathbf{v}_p - \mathbf{u}_{f@p}\right|} \quad . \tag{3}$$

According to [*Schiller & Naumann 1935*], for particle Reynolds number smaller than 1000 the drag coefficient C_D is written as

$$C_D = \frac{24}{\mathrm{Re}_p}\left(1 + 0.15\,\mathrm{Re}_p^{0.687}\right) \quad , \tag{4}$$

with $\mathrm{Re}=d_p|\mathbf{v}_p-\mathbf{u}_{f@p}|/\nu_f$ and ν_f the kinematic viscosity of the fluid.

2.2. Fluid flow prediction

The computation of particle paths in a turbulent flow needs the knowledge of the exact instantaneous fluid velocity. From a theoretical point of view, Direct Numerical Simulation (DNS) of the Navier-Stokes equations is the most accurate approach. It is well known that the DNS is restricted by the Reynolds number and the consequently required grid. However, the development of the parallel computing permits to perform DNS of quite large Reynolds number by using with a huge number of grid points [*Kaneda 1996*].

The Large Eddy Simulation (LES) consists in solving the large scales of turbulence and in modelling the small scales (subgrid scales). The coupling of DPS with a LES is questionable, as in order to compute the particle trajectory the instantaneous fluid velocity is required, but LES gives the instantaneous filtered fluid velocity only. In the literature many papers are found analyzing the effects of the subgrid fluid velocity [*Armenio et al. 1996,*

Yamamoto et al. 2001, Kuerten 2006, Fede & Simonin 2006] and proposing stochastic or deconvolution models [*Fede et al. 2006, Pozorski & Apte 2009, Mashayek & Randya 2003*].

For a very large number of particles, more than 10 millions, the coupling of DPS with an evolving DNS becomes unrealizable due to the computational cost. However, it is possible to couple the DPS with a frozen turbulent velocity field extracted from an evolving DNS [*Wang et al. 2000*]. In such a numerical simulation some spurious effect may appear leading to unphysical phenomena. Figure 1 shows the particle kinetic energy with respect to the inverse of the Stokes number with

$$q_p^2 = \frac{1}{2}\left\langle v'_{p,i} v'_{p,i} \right\rangle \qquad q_{f@p}^2 = \frac{1}{2}\left\langle u'_{f@p,i} u'_{f@p,i} \right\rangle \qquad \frac{\tau_{f@p}^t}{\tau_{fp}^F} = \frac{1}{St} \quad ,$$

where $1/\tau_{fp}^F = \left\langle 1/\tau_p \right\rangle$ and $\tau_{f@p}^t$ is the Lagrangian integral time scale given by

$$\tau_{f@p}^t = \int_0^{+\infty} R_{f@p}(\tau) d\tau \quad , \tag{5}$$

with

$$R_{f@p}(\tau) = \frac{\left\langle u'_{f@p,i}(t) u'_{f@p,i}(t+\tau) \right\rangle}{2/3 q_{f@p}^2} \quad . \tag{6}$$

Figure 1 shows that the particle kinetic energy measured in DPS coupled with evolving DNS is the same as the one in DPS coupled with a frozen flow for a wide range of Stokes numbers.

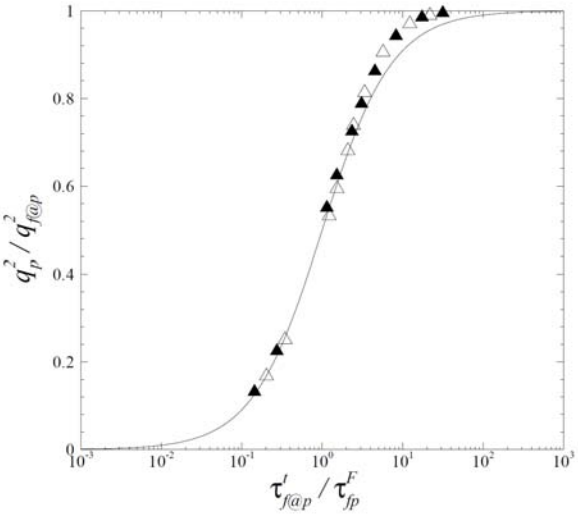

Figure 1: Particle kinetic energy normalized by the fluid kinetic energy measured at the particle position with respect to the inverse of Stokes number measured along inertial particle suspended in Homogeneous Isotropic Turbulent flows. The black filled symbols are the evolving DNS, the empty symbols the frozen flow and the solid line the relations based on the theory of Tchen & Hinze.

In contrast, fig. 2 shows that the Lagrangian fluid integral time scale seen by the particle measured in a frozen flow deviates from the one in evolving DNS for large Stokes number. The particles with a large Stokes number experience the turbulent field as a motionless observer. Then the time scale seen by the particles goes to the Eulerian time scale which is nearly identical to the eddy-life time that is infinite in frozen flows. This effect is clearly shown in fig. 2 and it is seen that frozen flow simulation (empty symbols) clearly overestimates the Lagrangian fluid integral time scale seen by large Stokes number particles.

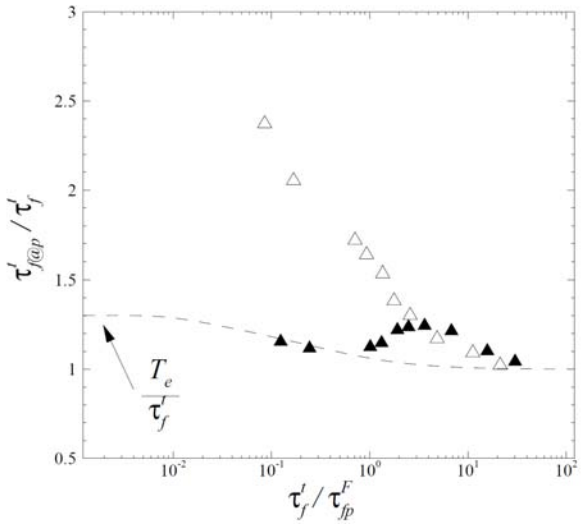

Figure 2: Lagrangian fluid integral time scale seen by the particle with respect to the inverse of Stokes number measured along the path of inertial particles suspended in Homogeneous Isotropic Turbulent flows. The black filled symbols are the evolving DNS and the empty symbols the frozen flow.

Therefore, frozen flows can be coupled with DPS, if particle dispersion is investigated. However, care should be taken for particles with larger Stokes numbers, as the particle distribution could be modified and consequently have an effect on the collision kernels or coalescence rates.

2.3. Validation of particle trajectory computation

The key element for solving system (1) is the computation of the undisturbed fluid velocity at the particle position $\mathbf{u}_{f@p}$. As two-way coupling is neglected the fluid velocity at the position of the particle is computed by interpolating the turbulent fluid flow predictions obtained by means of DNS [*Balachandar & Maxey 1989*]. As an interpolation scheme is a filter, an inaccurate interpolation scheme may change the physics of the two-phase flow. The validation of the interpolation scheme is done using a staggered grid. Therefore, the fluid flow is predicted by DNS (or LES) on a given uniform grid with N^3 grid points. Then the interpolation scheme is used to compute the velocity field on a second uniform grid staggered from the first one. For illustration, three interpolation schemes are used here: linear, Shape Function Method (SFM) and cubic splines.
Two turbulent velocity fields are considered: first, a flow field predicted by means of DNS on a grid with 128^3 grid points and a turbulent Reynolds number *Re=60*. Second, a flow field predicted by LES with 96^3 grid points and turbulent Reynolds number *Re=819*. The first-order evaluation of the interpolation scheme consists of comparing the moments of the fluid velocity computed for both grids, the original and staggered one. The error of the interpolation scheme is quantified by

$$\frac{\Delta q_f^2}{q_f^2} = 100 \frac{\left[q_f^2\right]_{DNS} - \left[q_f^2\right]_{Stag}}{\left[q_f^2\right]_{DNS}} \quad . \tag{7}$$

The error produced by the linear scheme is much more important than the error given using by the SFM or cubic spline scheme, as expected and seen in Tab. 1. Following the results given in tab. 1, the question about the real value of a cubic spline scheme instead of SFM might arise, as SFM already gives an error of the order of 0.05% and is much more computational cost efficient compared to the cubic spline scheme. To answer this question,

fig. 3 compares the energy spectrum computed on the DNS grid and on the staggered grid. It is observed that all interpolation schemes modify the turbulent spectrum as a filter. However the cubic spline gives a better representation of the small scales of turbulence. Fig. 4 shows the difference between the spectra normalized by the integral of the DNS spectrum given as

$$\frac{\left[\kappa\Delta E(\kappa)\right]_{DNS} - \left[\kappa\Delta E(\kappa)\right]_{Stag}}{\left[\int \kappa\Delta E(\kappa) d\kappa\right]_{DNS}} = \frac{\kappa\Delta E(\kappa)}{q_f^2} \quad . \tag{8}$$

Figure 4 clearly shows that the cubic splines interpolation scheme predicts better for the small scales of fluid turbulence. This is a very important point. If only particle dispersion is studied, the SFM interpolation scheme is probably sufficiently accurate. However, if particle-particle collisions in homogeneous isotropic turbulence are studied, the collision frequency in the limit case of zero inertia but finite volume particles is controlled by the local fluid velocity gradients (see Saffman & Turner). In this case an inaccurate interpolation scheme may lead to erroneous collision rates.

Tab 1: Error of the interpolation scheme on turbulent kinetic energy.

		Linear	SFM	Cubic splines
$\Delta q_f^2 / q_f^2$ (%)	*Re*=60	1.60	0.053	0.007
	Re=819	2.90	0.24	0.05

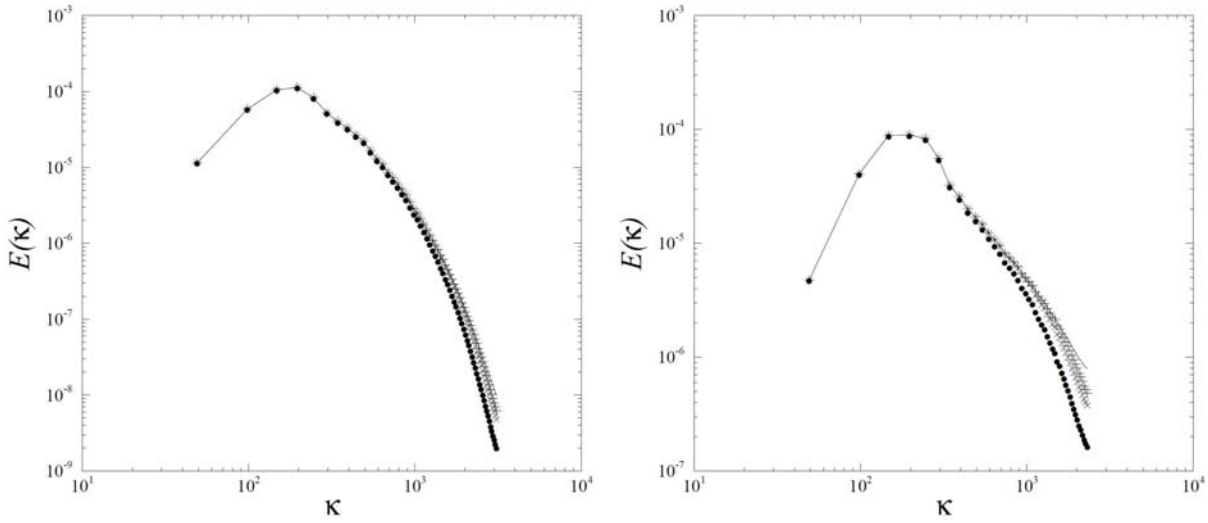

Figure 3: Turbulent spectrum computed on staggered grid. Left: DNS with Re=60 (128^3 grid points) and right: LES with $Re = 819$ (96^3 grid points). Solid lines are the spectrum computed on fluid grid, •: linear scheme, ×: SFM and +: cubic splines.

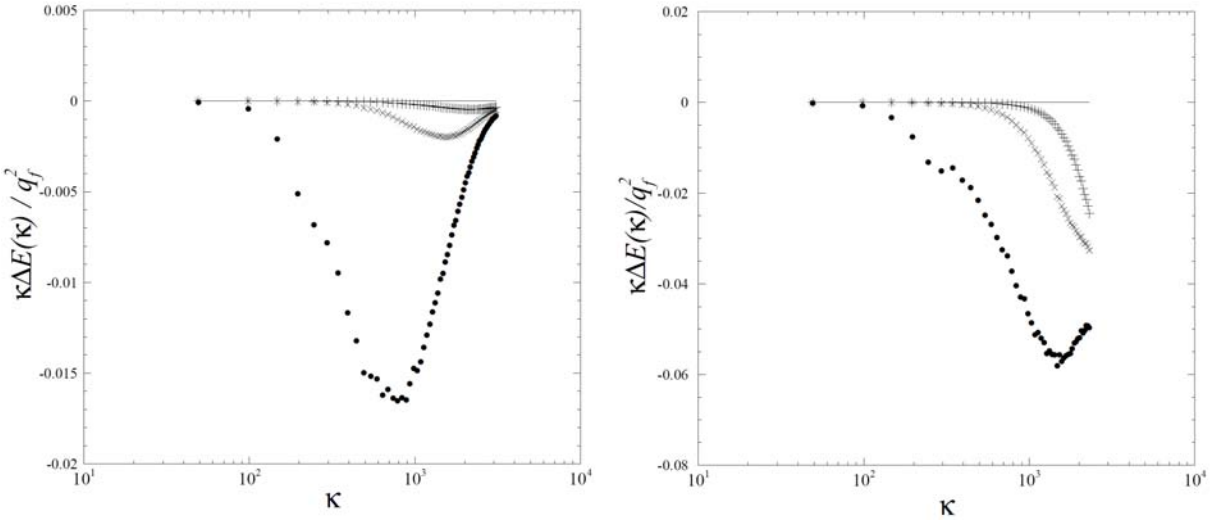

Figure 4: Error evaluation of the interpolation scheme. Left: DNS with Re=60 (128^3 grid points) and right: LES with Re = 819 (96^3 grid points). Solid lines are the spectrum computed on fluid grid, •: linear scheme, ×: SFM and +: cubic splines.

2.4. Particle dispersion with mean slip (as for example induced by gravity)

The settling of particles in a turbulent field is an important complex phenomenon in multiphase flows. DPS is a powerful tool to bring some answers about the physical mechanisms acting in particle-turbulence interaction [*Fessler et al. 1994, Février et al. 2005*] or preferential concentration [*Squires & Eaton 1991*]. However, [*Fede et al. 2007*] show that the periodical boundary conditions may cause a statistical bias in DPS of inertial particles falling in a homogeneous turbulence. Indeed, in such a numerical simulation a particle that crosses an edge of the computational domain is re-injected at the opposite side.
[*Fede et al. 2007*] show that when the particle residence time in the box is smaller than the turbulent eddy-life time the particles may interact with nearly the same fluid velocity field. Consequently the fluid velocities seen by the particles are correlated with themselves inducing a statistical bias. To illustrate this phenomenon fig. 5 shows the Lagrangian fluid velocity correlation function measured along the solid particle path.

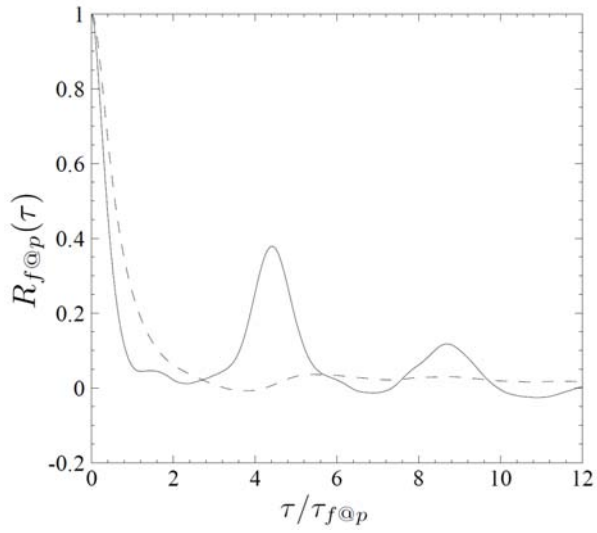

Figure 5: Fluid velocity correlation seen by settling particles for τ_{inbox}/τ_E = 0.91 (solid line) and τ_{inbox}/τ_E = 4.34 (dashed line). The fluid integral time scale $\tau_{f@p}$ is computed by integration of $R_{f@p}$ (Eq. 6)

Figure 5 shows the fluid velocity correlation function measured for two kinds of particles differing by the residence time to Eddy-Life time ratio. The particle residence time is defined as

$$\tau_{inbox} = \frac{L_b}{|V_{set}|} = \frac{L_b}{g\tau_p} \quad , \tag{9}$$

where L_b is the computational box length and V_{set} is the settling velocity $V_{set} = \tau_p g$. As seen in fig. 5 peaks appear in the Lagrangian correlation function for a small value of τ_{inbox}/τ_E. It corresponds to a re-correlation effect due to periodical boundary conditions. Fede *et al.* proposed the limiting value of $\tau_{inbox}/\tau_E < 4$ to ensure that this statistical bias does not change the particles behaviour.

3. COLLISION/COALESCENCE VALIDATION

If collisions or coalescence are taken into account in DPS validation needs to be performed at two levels: first for the collision or coalescence model (in terms of momentum transfer) and second for the detection algorithm as both are independent.

The collision algorithm is validated performing dry granular flow simulations of mono- and bi-disperse particle mixtures. The results on a bi-disperse mixture, which are comparing the statistics obtained in dry granular flows with predictions originating from the kinetic theory of rarefied gases, can equally be considered as a validation of the collision detection algorithm in a poly-disperse particle mixture. As usually only binary collisions are treated, a bi-disperse simulation validates the case of a poly-disperse mixture. The validation is conducted in dry granular flows as the statistical properties that should represent the particulate system are known from the theory of rarefied gases. It is therefore possible to conduct simulation without the 'disturbing influence' of a fluid phase. All changes in the particle trajectories are exclusively related to particle-particle collisions. This configuration of dry granular flows offers therefore ideal conditions for the validation of the collision detection algorithm.

In this section we first introduce a detection algorithm and a collision model. Second we present criteria in order to validate the collision model and third the detection algorithm. The last part is dedicated to the validation of coalescence. It is emphasized that the validation criteria do not dependent on the collision model or detection algorithm.

3.1. Particle detection and collision model

Several algorithms for the treatment of the dispersed phase are found in literature [*Hopkins & Louge 1990, Sigurgeirsson et al. 2001, Sundaram & Collins 1997*]. The simplest, but also an extremely inefficient way to detect particle-particle collisions is checking for collision between all possible particle pairs in the computation domain. This way the cost of checking for collision is $N_p(N_p\text{-}1)/2$ and hence in the order of $O(N_p^2)$. The computation cost can be reduced by using a detection grid. In [*Wunsch et al. 2008*] a collision detection algorithm for a polydisperse particulate phase is proposed. This algorithm has two collision detection criteria, the first is the standard overlap criterion, i.e. a collision between two particles is found by overlap of the particles at a given time step. This kind of algorithm demands a small time step in order to accurately predict the collision frequency. [*Wunsch et al. 2008*] show that the introduction of a second criterion that compares the relative position of the colliding particles in two consecutive time steps increases the time step significantly.

The detection algorithm provides a list of colliding particles for which a collision, or coalescence, model has to be applied. Assuming an instantaneous pure slip collision of spherical solid particles, the particle velocities after a collision are given by

$$\mathbf{v}_p^{\bullet} = \mathbf{v}_p + \frac{m_q}{m_p + m_q}(1+e_c)(\mathbf{w}.\mathbf{k})\mathbf{k} \quad ; \quad \mathbf{v}_q^{\bullet} = \mathbf{v}_q - \frac{m_p}{m_p + m_q}(1+e_c)(\mathbf{w}.\mathbf{k})\mathbf{k} \quad , \qquad (10)$$

where **w** is the particle-particle relative velocity, **k** the normalized unit vector connecting both particle centres and m_p the *p*-particle mass. The particle restitution coefficient e_c represents the loss of particle energy during the collision.

3.2. Collision model validation

The validation of the collision model is handled by performing DPS of homogeneous granular flows. The particles are initially randomly distributed and the particle velocity distribution becomes Gaussian due to the redistribution effects of collisions as seen in fig. 6. In case of monodisperse elastic particles ($e_c=1$) the particle kinetic energy is perfectly conserved. So the particle kinetic energy must be constant.

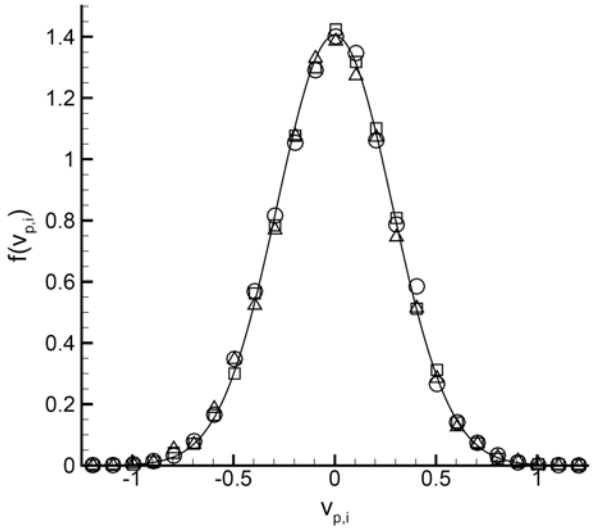

Figure 6: Particle velocity distribution. Gaussian distribution with mean μ=0 and σ=0.284 (Solid line), □: x-component, Δ: y-component, ○: z-component.

One of the main differences with a system of a mono-disperse mixture is the fact that in a bi-disperse particle mixture the energy levels for each particle class are not the same in the thermal equilibrium state. Heavier particles do not show the same particle agitation in the equilibrium state as lighter particles. This equilibrium state of the particle agitation can be expressed by the following relation

$$m_p q_p^2 = m_q q_q^2 \qquad . \qquad (11)$$

If the particle collisions are elastic, the particle agitation of the bi-disperse mixture q_m^2 can be written as

$$q_m^2 = \frac{n_p m_p q_p^2 + n_q m_q q_q^2}{n_p m_p + n_q m_q} \qquad (12)$$

The relations (11) and (12) allow writing the particle agitation for each class in function of the particle agitation of the mixture

$$q_p^2 = \frac{n_p m_p + n_q m_q}{m_p\left(n_p + n_q\right)} q_m^2 \qquad \text{and} \qquad q_q^2 = \frac{n_p m_p + n_q m_q}{m_q\left(n_p + n_q\right)} q_m^2 \qquad (13)$$

Now, it is possible to find an expression for the ratio of $q_p{}^2/q_m{}^2$ and $q_q{}^2/q_m{}^2$, which only depends on the mass of the particle classes m_p and m_q as well as on their number densities n_q and n_q. The same values can be measured in the DPS simulations. A comparison of the measured values to the predictions of the equilibrium theory is given in fig.7. Figure 7 shows

that the particle kinetic energies converge around their respective theoretical values. This is due to the transfer of particle kinetic energy by collisions.

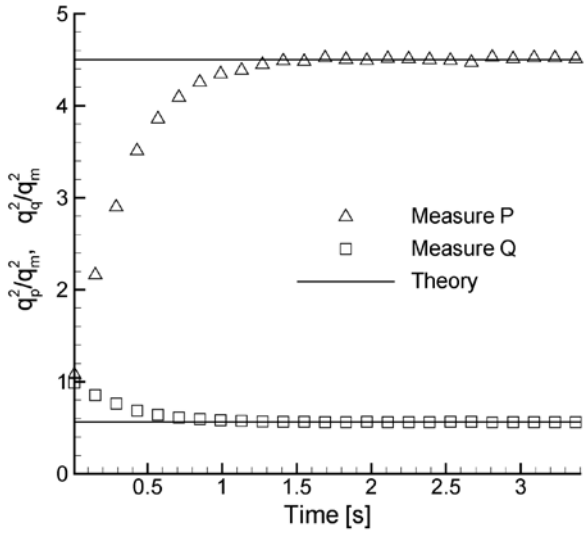

Figure 7: Comparison of particle kinetic energy ratios measured in DPS to predictions from the equilibrium theory (13).

Note that the proposed validation of the collision model is independent of the collision detection algorithm. Indeed the detection algorithm gives the number of collision, in other word the collision frequency. Then even if the collision frequency is wrong the relation (13) is remains correct. The difference is the time needed to reach the equilibrium (11).

3.3. Collision detection algorithm

The validation of the detection algorithm is mainly related to the collision frequency and consequently with the time step of the simulation. To evaluate the collision detection algorithm the relevant parameter is the mean particle displacement during a time step δl. For a mean displacement larger than the particle diameter collision missing is expected. In the frame of the kinetic theory of rarefied gases applied to granular media, the mean particle displacement during a time step normalized by the particle diameter is expressed as

$$\frac{\delta l}{d_p} = \frac{3}{2}\sqrt{\frac{2\pi}{3}q_p^2}\,\frac{\Delta t}{d_p} \quad . \tag{10}$$

Distributions of collision angle N_θ and relative velocity at the moment of collision $N_{\mathbf{w}_{pq}}$ are used to quantify the efficiency of the collision algorithm. The kinetic theory provides the following theoretical relations

$$f(\theta) = -4n_p^2 d_p^2 \sqrt{\frac{2\pi}{3}q_p^2}\,\sin(2\theta) \tag{11}$$

and

$$f(\mathbf{w}_{pq}) = n_p^2 d_p^2 \sqrt{\frac{2\pi}{3}q_p^2}\,\frac{9}{8q_p^2}\mathbf{w}_{pq}^3 \exp\left(-\frac{3\mathbf{w}_{pq}^2}{8q_p^2}\right), \tag{12}$$

The accuracy of the predictions with respect to the time step criterion $\delta l/d_p$ is shown in fig.8 and fig.9.

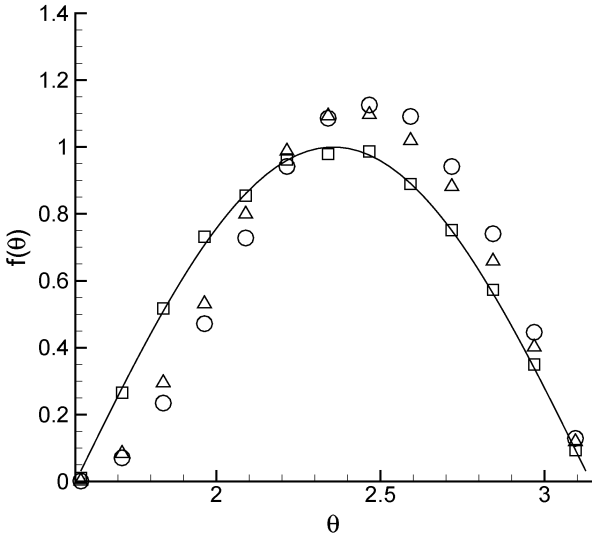

Figure 8: Collision angle PDF in dependence on ratio dl/d_p using a pure overlap detection algorithm. Thy symbols stand for □:0.13, Δ:1.3, ○:1.9 and the solid line the prediction given by (11).

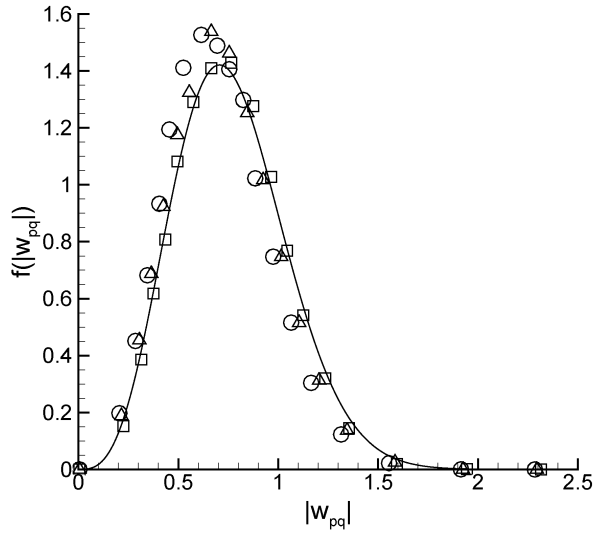

Figure 9: Impact relative velocity PDF dependence on ratio dl/d_p using a pure overlap detection algorithm. Thy symbols stand for □:0.13, Δ:1.3, ○:1.9 and the solid line the prediction given by (11).

As clearly seen in fig.8 and fig.9 a sufficient algorithm performance is achieved when the particle propagation is limited to about 13% of a particle diameter, thus for a ratio $\delta l/d_p$=0.13. Similar results are obtained by [*Sakiz 1999*]. For ratios $\delta l/d_p$ larger than this value the simulation results deviate from the prediction based on the kinetic theory of rarefied gases and especially grazing collision are missed. In dependence of the flow configuration in DNS/DPS simulations of turbulent two-phase flows the criterion $\delta l/d_p$ can be more stringent than the CFL number of the DNS, which is disadvantageous as the DNS of the continuous phase then needs to be solved applying a time step which is not optimal. In fig.9 it is seen that with an increasing ratio of $\delta l/d_p$ more and more particle-particle collisions are missed between particles with a high relative velocity. This appears logic as faster particles cover a larger distance during a fixed time step than slower ones. Consequently fig.8 shows that the grazing collisions are more sensitive to a higher ratio of $\delta l/d_p$. To remedy this restriction in the time step criterion a second particle pair detection criterion is introduced in the algorithm developed in [*Wunsch et al. 2008*]. In practice, this criterion is a significant advantage as the

time step criterion on the dispersed phase is still more stringent than the one on the fluid phase and therefore corresponds to a net increase of the time step by a factor of ten.

Representing correctly the relative velocity and collision angle distributions is not sufficient for the validation of the detection algorithm. If for example a systematic error in the detection algorithm persists that affects random particles, the distribution PDF's exhibit a correct behaviour, but the collision frequency is not correctly represented. A correct prediction of the collision frequency is crucial. It is the most important statistic of the dispersed phase. The influence of collisions on any quantity is written as the change in the quantity by the collision multiplied with the collision frequency. Therefore, the collision frequency measured is compared to the predictions of the theoretical collision frequency. For a binary mixture of particles the kinetic theory gives the following relation for the collision frequency

$$f_{pq}^{\kappa} = g_0 n_p n_q \pi \left(\frac{d_p + d_q}{2} \right)^2 \sqrt{\frac{16}{3\pi} \left(q_p^2 + q_q^2 \right)} \quad , \tag{13}$$

where g_0 is radial distribution function introduced to take into account the increase of collision frequency due to particle packing. In diluted granular flows the radial distribution function is nearly equal to 1 but for dense flows g_0 depends on the particle volume fraction α_p *[Carnahan & Starling 1969, Lun & Savage 1986*].

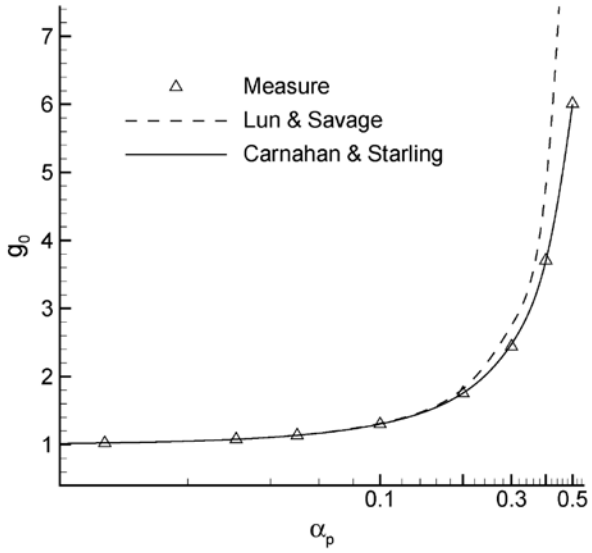

Figure 10: Comparison of radial distribution function g_0 measured in DPS to theoretical predictions with respect to the particle volume fraction α_p

As can be seen in fig.10 the DPS results correspond very well with the theoretical predictions for the collision frequency corrected by the model for the radial distribution function of [*Carnahan & Starling 1969*]. Thus, it is verified that the collision frequency is correctly predicted.

3.3. Coalescence

The droplet pair detection in case of other collision outcomes than rebounds, such as permanent coalescence, reflexive or stretching separation of remains the same in the case of gas-liquid flows. The droplet collision handling is altered only. The collision outcome for colliding droplets is basically described by two dimensionless quantities, the Weber number *We* and the impact parameter *X*.

Coalescence phenomena are modelled representing a pure coalescence regime only for the sake of distinctness. This means that each collision leads to permanent coalescence and no

other collision outcomes exist. Permanent coalescence is modelled applying mass and momentum conservation

$$m^* = m_p + m_q$$
$$m^* = m_p \mathbf{v}_p + m_q \mathbf{v}_q \tag{14}$$

with m_p and m_q the mass of the particles before coalescence and m^* after. Analogous for the particle velocities $\mathbf{v}_p$, $\mathbf{v}_q$ and $\mathbf{v}^*$. The corresponding particle diameter is directly deductible from the mass conservation equations as the particle density is constant and the particles are modelled as rigid spheres. The position of the new particle that arises from coalescence is given as

$$\mathbf{x}^* = \frac{d_p^3 \mathbf{x}_p + d_q^3 \mathbf{x}_q}{d^{*3}} \quad , \tag{15}$$

with $\mathbf{x}^*$ the position of the new particle and d_p, d_q and d^* the particle diameters.

The outcome of droplet collisions can be expressed in terms of the Weber number (We) and the impact parameter X. It is possible to determine a theoretical probability density function (PDF) for both the Weber number and the impact parameter. For the purposes of this article, only the PDF of the impact parameter is regarded. A distribution function is derived for the impact parameter X [*Wunsch 2009*], which is a purely geometrical quantity and can be calculated as a function of the collision angle PDF given in (11). It can be written as

$$N(X)dX = N_\theta(\theta)d\theta \tag{16}$$

This leads to

$$N_X(X) = \frac{N_\theta(\theta)}{\left|\frac{dX}{d\theta}\right|} \quad . \tag{17}$$

With some manipulations, respecting the relation between the collision angle and impact parameter, this equation can be transformed applying trigonometric rules in the interval $\theta \in \left[\frac{\pi}{2}; \pi\right]$, which is the interval of collision angles as it is defined here. It writes then

$$N_X(\theta) = 2\sin(\theta), \tag{20}$$

which, expressed in terms of the impact parameter and applying $\theta = \pi - \arcsin(X)$, gives the final form for the PDF of the impact parameter as

$$N_X(\theta) = 2X \, . \tag{21}$$

The PDF of the impact parameter therefore describes a straight line through the origin. A comparison with measurements from DPS on a dry permanent coalescence flow is given in fig.11. The statistics verify this theoretical prediction of the impact parameter, although the statistics are moderate, which is due to the lack of events that can be taken into consideration. The number of particles finds its maximum at the beginning of the simulation and decreases then with each single collision in the simulations performed here. Therefore, collisions are limited in number.

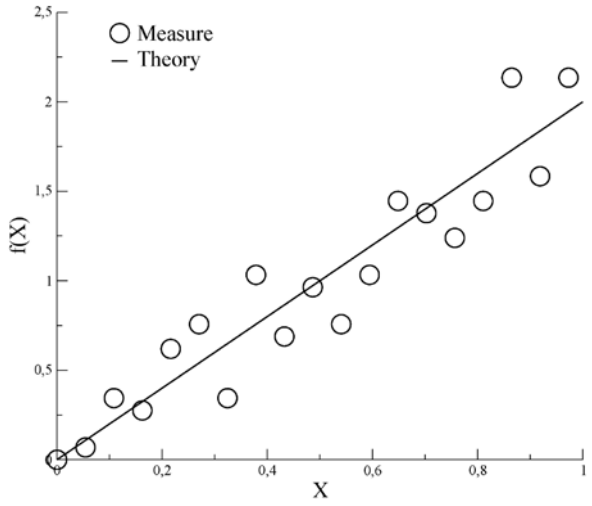

Figure 11: Comparison of measured impact parameter X in dry coalescence to predictions from theory.

Measures of the coalescence rate in DPS simulations of dry coalescence, where permanent coalescence is the only possible collision outcome, are compared to predictions of Monte-Carlo simulations. These simulations are considered to be exact in dry granular flows and a correct measure of the coalescence rate and particle kinetic energy in the system is qualified by agreement with the Monte-Carlo predictions. First, the coalescence rate is presented and second, these comparisons to predictions of Monte-Carlo simulations are used to validate the algorithm on different platforms.

The initialization of the Monte-Carlo simulations is done with an underlying fluid flow field which brings the particulate phase into a stationary state. At the moment coalescence is started the fluid flow is turned off and thus the configuration of dry granular flows is produced. Figure 12 shows that the particle number (and therefore the coalescence rate) is correctly represented.

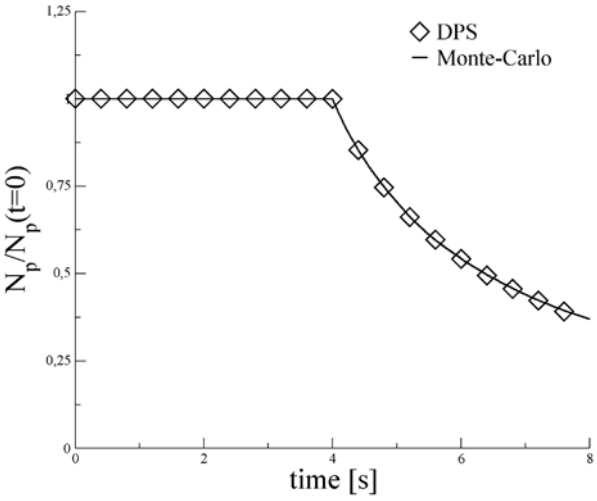

Figure 12: Particle number measured in DPS in comparison with Monte-Carlo simulations in dry coalescence.

The collision detection algorithm and collision treatment is integrated into the DNS solver and adapted to its structure. Then, the algorithm is vectorized due to the vectorial structure of the NEC-SX-8 on which the DNS/DPS simulations were performed. Obviously a re-validation is necessary in order to assure not to introduce errors by these modifications. Besides the validations presented above, while validating the collision algorithm, also the coalescence rate and particle kinetic energy on different platforms are compared. The results

are presented in fig.13. It is seen that the particle number as well as the particle kinetic energy are well represented and coincide with predictions on other platforms.

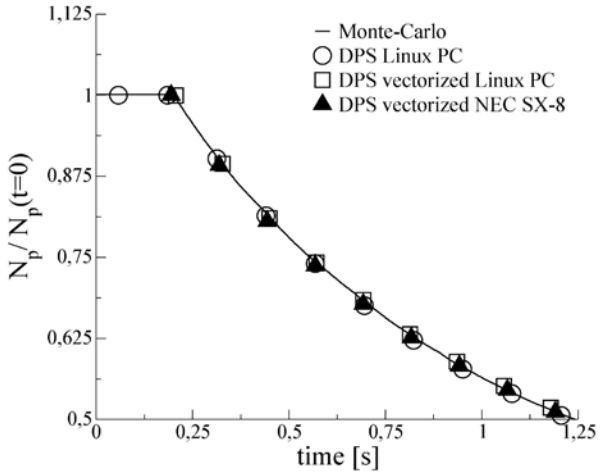

Figure 13: Droplet number N_p measured in DPS in comparison with predictions from Monte-Carlo simulations comparing vectorized and non-vectorized versions of the code on different platforms.

4. CONCLUSIONS

Several validation procedures for Discrete Particle Simulation of turbulent two-phase flows with droplet coalescence are proposed. First, restrictions of the coupling of DPS with DNS or LES are discussed, showing first limits for turbulent Reynolds number, in respect of computational cost for DNS and in terms of accuracy for LES and second for the high number of droplets for which a frozen DNS needs to be applied. Then a validation procedure for particle-particle collisions or droplet coalescence is presented. First discussing the correct prediction of fluid properties at the particle position and then validating the collision handling. The collision handling consists of first, validating the collision model and second the collision detection algorithm. The particle energies and PDFs of collision statistics are used to verify a correct collision handling. Finally, the modelling of droplet coalescence is validated in comparison with Monte-Carlo type simulations which are considered as accurate in dry granular flows.

5. ACKNOWLEDGMENTS

This work was granted access to the HPC resources of [CCRT/CINES/IDRIS] under the allocation 2009- i2009021066 made by GENCI (Grand Equipement National de Calcul Intensif).

This research project has been supported by a Marie Curie Early Stage Research Training Fellowship of the European Community's Sixth Framework Programme under contract number 'MEST-CT-2005-020426'.

6. REFERENCES

V. Armenio, U. Piomelli, V. Fiorotto, 1999, Effect of the subgrid scales on particle motion, Phys. Fluids 11, 3030

S. Balachandar & M.R. Maxey, 1989, Methods for evaluating fluid velocities in spectral simulations of turbulence, J. Comput. Physics 83:96-125

C.F. Carnahan & K.E. Starling, 1969, Equation of state of non-attracting rigid spheres, J. Chem. Phys., 51:635-636

C. Corre, J.-L. Estivalezes, S. Vincent, O. Simonin, S. Glockner, 2009, Simulation of a fluidized bed using a hybrid Eulerian-Lagrangian method for particle tracking, to appear in Notes on Numerical Fluid Mechanics and Multidisciplinary Design

P. Fede & O. Simonin, 2006, Numerical study of the subgrid fluid turbulence effects on the statistics of heavy colliding particles, Phys. Fluids 18, 045103

P. Fede, O. Simonin, P. Villedieu, K.D. Squires, 2006, Stochastic modelling of the turbulent subgrid fluid velocity along inertial particle trajectories, Proc. of the summer program, Center of Turbulence Research, Stanford University, pp.247-258

P. Fede, O. Simonin, P. Villedieu, 2007, Crossing trajectory effect on the subgrid fluid turbulence seen by solid inertial particles, Proc. of ICMF 2007

J. Fessler, J. Kulick and J. Eaton, 1994, Preferential concentration of heavy particles in a turbulent channel flow, Phys. Fluids, 6:3742-3749

P. Février, O. Simonin, K.D. Squires, 2005, Partitioning of particles velocities in gas-solid turbulent flows into a continuous field and a spatially uncorrelated random distribution: theoretical formalism and numerical study, J. of Fluid Mechanics, 533:1-46

R. Gatignol, 1983, The faxen formulas for a rigid particle in an unsteady non-uniform stokes flow, J. Mec. Theor. Appl., 1:143-154

M.A. Hopkins & M.Y. Louge, 1990, Inelastic microstructure in rapid granular flows of smooth disks, Phys. of Fluids A, (3) 1

Y. Kaneda & M. Yokokawa, 1996, DNS of Canonical turbulence with up to 4096^3 grid points, Parallel Comput. Fluid Dynamics 2004, pp. 23-32

J.G.M. Kuerten, 2006, Subgrid modelling in particle-laden channel flow, Phys. Fluids 18, 025108

C.K.K. Lun & S.B. Savage, 1986, The effects of an impact velocity dependent coefficient of restitution on stresses developed by sheared granular materials, Acta Mechanica, 63:539-559

F. Mashayek & R.V.R. Randya, 2003, Analytical description of particle/droplet-laden turbulent flows, Progress in Energy and Combustion Science, 29, 329-378

A. Massol, 2004, Simulation d'écoulement autour de réseaux de particules sphériques, Ph.D. thesis, INPT-CERFACS

M.R. Maxey & J.J. Riley, 1983, Equation of motion for a small rigid sphere in a non-uniform flow, Phys. Fluids, 26(4):2883-2889

J. Pozorski & S.V. Apte, 2009, Filtered particle tracking in isotropic turbulence and stochastic modelling of subgrid-scale dispersion, Int. J. Multiphase Flow, 35 (2), 118-128

A. Prosperetti and H.N. Oguz, 2001, Physalis: A new o(N) method for the numerical simulation of disperse systems: Potential Flow of Spheres, J. of Comp. Phys. 167, 196-216

P.G. Saffman and J.S. Turner, 1956, On the collision of drops in turbulent clouds, J. of Fluid Mechanics, 1:16-30

M. Sakiz, 1999, Simulation numérique lagrangienne et modélisation eulérienne d'écoulement diphasique gaz-particules en canal vertical, Ph.D. thesis, Ecole National des Ponts et Chaussés

H. Sigurgeirsson, A. Stewart, W.-L. Wan, 2001, Algorithms for particle-field simulations with collisions, J. of Comp. Physics, 172(2):766-807

K.D. Squires and J.K. Eaton, 1991, Preferential concentration of particles by turbulence, Phys. of Fluids, 5:1169-1178

S. Sundaram & L.R. Collins, 1997, Collision statistics in an isotropic particle-laden turbulent suspension. Part 1: Direct Numerical Simulations, J. of Fluid Mechanics, 335:75-109

L.P. Wang, A.S. Wexler & Y. Zhou, 2000, Statistical mechanical descriptions and modelling of turbulent collision of inertial particles, J. of Fluid Mechanics, 415:117-153

D. Wunsch, 2009, Theoretical and numerical study of collisions and coalescence – Statistical modelling approaches in gas-droplet turbulent flows, Ph.D. thesis, INPT

D. Wunsch, P. Fede, O. Simonin, 2008, Development and validation of a binary collision detection algorithm for a polydispersed particle mixture, Proc. of ASME FEDSM 2008, FEDSM2008-55159

Y. Yamamoto, M. Potthoff, T. Tanaka, T. Kajishima, Y. Tsuji, 2001, Large-eddy simulation of turbulent gas-particle flow in a vertical channel: effect of considering inter-particle collisions, J. Fluid Mech. 442, 303

Proceedings of FEDSM2009
ASME 2009 Fluids Engineering Division Summer Meeting
August 2-6, 2009, Vail, Colorado, USA

FEDSM2009-78091

DNS/DPS OF INERTIAL DROPLET COALESCENCE IN HOMOGENEOUS ISOTROPIC TURBULENCE AND COMPARISON WITH PDF MODEL PREDICTIONS USING THE DIRECT QUADRATURE METHOD OF MOMENTS

Dirk Wunsch[1,2], **Roel Belt**[1,2], **Pascal Fede**[1,2], **Olivier Simonin**[1,2*]
[1] Université de Toulouse; INPT, UPS; IMFT
31400 Toulouse, France

[2] CNRS, Institut de Mécanique des Fluides de Toulouse
31400 Toulouse, France
Email: simonin@imft.fr

ABSTRACT

To analyze in detail the coalescence mechanisms and validate modeling approaches, deterministic Lagrangian simulations of droplet trajectories (DPS) coupled with Direct Numerical Simulations (DNS) of a Homogeneous Isotropic Turbulence (HIT) are performed. The influence of the colliding particle velocity correlations induced by the fluid turbulence on the rate of droplet coalescence is investigated for different particle inertia. The results are compared to predictions using the Direct Quadrature Method of Moments (DQMOM) accounting for coalescence. The particle diameter distribution is written as a summation of Dirac functions. This allows to derive Eulerian transport equations for the dispersed phase statistics, which account for coalescence and conserve the low-order moments of the particle size distribution. The collision terms are modeled applying the molecular chaos assumption in order to account for coalescence. Particle size distributions and moments obtained from DQMOM are compared to those of the DNS/DPS simulations in function of particle inertia.

INTRODUCTION

The study of collisions between particles in turbulent dispersed multiphase flows is of interest for many engineering applications. Examples of flows where droplet coalescence is likely to play an important role include many topics such as solid-fuel rocket propulsion, internal combustion engines and electric power generation by liquid fuel turbines. The droplet size generally has a major influence on the global performance of the system and must be accurately taken into account in numerical simulations. As the carrier flow is often turbulent, droplets located in the vicinity of the same point may have different velocities, collide and perhaps coalesce leading to a strong modification of the droplet size distribution.

The statistical representation of the coalescence rates is gained based on a Lagrangian tracking of the dispersed phase, here referred to as Discrete Particle Simulation (DPS), in a physical study of coalescence in Homogeneous Isotropic Turbulence. This approach is coupled with Direct Numerical Simulations (DNS) in order to account for the influence of the turbulent motion of a fluid on the particle distribution. Coalescence is accounted for using an algorithm allowing to detect collision in a broad droplet size distribution. This algorithm was validated for dry granular test cases [1]. The results are compared to predictions using the Direct Quadrature Method of Moments (DQMOM) accounting for coalescence. The here applied DQMOM approach [2] is a recently developed extension of the approach by Marchisio and Fox [3] based on the formalism of the joint fluid-particle PDF approach by Simonin [4].

Coalescence phenomena are various and each collision between two droplets leads to the creation of one to several new droplets, depending on the relative properties of the colliding droplets. Several studies concerned with coalescence phenomena have been performed, pointing out the diversity of the collision outcome [5–7]. In this study, in order to better understand

*Address all correspondence to this author.

the physical mechanisms of turbulence-coalescence interaction, only the permanent coalescence regime is considered. Each collision leads to permanent coalescence.

The article is structured as follows. First, the DNS/DPS approach is explained. Second, the DQMOM approach is detailed by explaining the general formalism, the closure of the collision operator and then outlining the equations solved in the frame of this work. Then the fluid flow is described and finally results are presented for the comparison of DQMOM with DNS/DPS.

DNS/DPS APPROACH

Direct Numerical Simulations (DNS) coupled with a Lagrangian tracking of the particle phase (DPS) are performed here and have been extensively used to investigate gas-particle flows [8–11]. The flow configuration is a Homogeneous Isotropic Turbulence (HIT) forced by a scheme initially proposed by Eswaran and Pope [12], which assures a statistical steadiness. The particles are considered as rigid spheres with diameters smaller than the Kolmogorov turbulence length scale η_K. The turbulence modulation by the dispersed phase (two-way coupling) is not considered, as the particle mass fraction is small. Assuming that the particle fluid density ratio ($\rho_p \gg \rho_f$) is large, the forces acting on the particle are reduced to the drag force only. Thus, the governing equations of the N_p particle system in interaction with the surrounding flow field and undergoing particle-particle collisions are written as

$$\begin{aligned} \frac{d\mathbf{x}_p}{dt} &= \mathbf{v}_p \\ m_p \frac{d\mathbf{v}_p}{dt} &= m_p \frac{[\mathbf{v}_p - \mathbf{u}_{f@p}]}{\tau_p} + \sum_{i=1;j\neq i}^{N_p} \mathbf{F}_{p,ij} \end{aligned} \tag{1}$$

where $\mathbf{x}_p, \mathbf{u}_p$ are the position and velocity vectors of the particle p and m_p is the particle mass. $\mathbf{u}_{f@p}$ is the undisturbed fluid velocity at the position of the particle and $\mathbf{F}_{p,ij}$ represents the impulsive force resulting from particle-particle collisions. As two-way coupling is neglected, $\mathbf{u}_{f@p}$ is computed with an accurate interpolation scheme [13]. The particle response time τ_p is given using the relation of Schiller and Naumann [14] by

$$\begin{aligned} \tau_p &= \frac{4}{3}\frac{\rho_p}{\rho_f}\frac{d_p}{C_D}\frac{1}{|\mathbf{v}_p - \mathbf{u}_{f@p}|} \\ C_D &= \frac{24}{Re_p}\left(1 + 0.15 Re_p^{0.687}\right) \\ Re_p &= \frac{|\mathbf{v}_p - \mathbf{u}_{f@p}|\, d_p}{\nu_f} \end{aligned} \tag{2}$$

with d_p the particle diameter and ν_f the kinematic viscosity of the fluid. Coalescence is modeled assuming that each collision leads to permanent coalescence. Other collision outcomes as identified by several authors [5–7] are not regarded for the sake distinctness. The mass and momentum conservation equations of two particles undergoing coalescence are written as

$$\begin{aligned} m^* &= m_p + m_q \\ m^*\mathbf{v}^* &= m_p\mathbf{v}_p + m_q\mathbf{v}_q \end{aligned} \tag{3}$$

with m_p and m_q the mass of the particles before coalescence and m^* after. Analogous for the particle velocities $\mathbf{v}_p, \mathbf{v}_q$ and $\mathbf{v}^*$. The corresponding particle diameter is directly deductible from the mass conservation equations as the particle density is constant and the particles are modeled as rigid spheres, as mentioned above. The position of the new particle that arises from coalescence is given as

$$\mathbf{x}^* = \frac{d_p^3\mathbf{x}_p + d_q^3\mathbf{x}_q}{d^{*3}} \tag{4}$$

with $\mathbf{x}^*$ the position of the new particle and d_p, d_q and d^* the particle diameters. Coalescence is detected using a recently developed algorithm allowing detecting collisions in a poly-dispersed particle mixture [1].

DQMOM APPROACH

The here used DQMOM approach is an extension of the approach proposed by Marchisio and Fox [3] based on the formalism of the joint fluid-particle PDF approach by Simonin [4] recently developed by Belt and Simonin [2].

To account for droplet coalescence (particle aggregation) or poly-dispersion in the frame of the Euler-Euler modeling approach is challenging. Marchisio and Fox [3] proposed the DQMOM approach to tackle these difficulties. However, as the velocity distribution for a given diameter is represented by a Dirac, coalescence effects appear only in the mass balance equations. Consequently, as outlined by Belt and Simonin [2], particle momentum and particle kinetic stress transport equations cannot be written accounting for coalescence effects. Instead, in the approach of Marchisio and Fox [3], an ad-hoc formulation of the multi-class Eulerian approach without collision modeling is applied. In the novel approach, these equations can be derived accounting for particle coalescence. This new approach is briefly summarized in the following. The reader may refer to [2] for a more complete description of the formalism.

General DQMOM formalism

The dispersed phase statistics can be described in turbulent two-phase flows in terms of the joint fluid-particle probability

density function (pdf) $f_{fp}(\mathbf{x},t,\mathbf{c}_f,\mu_p,\mathbf{c}_p)$, which is defined such that $f_{fp}(\mathbf{x},t,\mathbf{c}_f,\mu_p,\mathbf{c}_p)d\mathbf{c}_f d\mu_p d\mathbf{c}_p d\mathbf{x}$ is the probable number of droplets at time t with the center of mass located in the volume $[\mathbf{x},\mathbf{x}+d\mathbf{x}]$, a translation velocity $\mathbf{u}_p$ in $[\mathbf{c}_p,\mathbf{c}_p+d\mathbf{c}_p]$ and a mass m_p in $[\mu_p,\mu_p+d\mu_p]$, seeing a locally undisturbed fluid velocity $\mathbf{u}_{f@p}$ in $[\mathbf{c}_f,\mathbf{c}_f+d\mathbf{c}_f]$. The evolution equation can be written as a Boltzmann-type equation [4]:

$$\begin{aligned}\frac{\partial f_{fp}}{\partial t}+\frac{\partial}{\partial x_j}\left(c_{p,j}f_{fp}\right)+\frac{\partial}{\partial c_{p,j}}\left(\langle\frac{\mathrm{d}u_{p,j}}{\mathrm{d}t}|\mu_p,\mathbf{c}_p,\mathbf{c}_f\rangle f_{fp}\right)\\+\frac{\partial}{\partial c_{f,j}}\left(\langle\frac{\mathrm{d}u_{f@p,j}}{\mathrm{d}t}|\mu_p,\mathbf{c}_p,\mathbf{c}_f\rangle f_{fp}\right)\\+\frac{\partial}{\partial \mu_p}\left(\langle\frac{\mathrm{d}m_p}{\mathrm{d}t}|\mu_p,\mathbf{c}_p,\mathbf{c}_f\rangle f_{fp}\right)\\=\left(\frac{\partial f_{fp}}{\partial t}\right)_{coll}\end{aligned}\tag{5}$$

where $\langle.\rangle$ represents an ensemble averaging operator and $\frac{d}{dt}$ the rate of change along the particle path of any particle property. The notation $\langle.|\mu_p,\mathbf{c}_p,\mathbf{c}_f\rangle$ is written for the conditional expectation $\langle.|m_p=\mu_p,\mathbf{u}_p=\mathbf{c}_p,\mathbf{u}_{f@p}=\mathbf{c}_f\rangle$. Exact expressions for the third to fifth term can be found in [4]. The collision operator $\left(\frac{\partial f_{fp}}{\partial t}\right)_{coll}$ will be detailed below.

Marchisio and Fox [3] wrote the particle pdf f_p as a summation of N Dirac functions in mass and velocity space:

$$\begin{aligned}f_p(\mathbf{x},t,\mu_p,\mathbf{c}_p)=\\\sum_{\alpha=1}^{N}\omega_\alpha(\mathbf{x},t)\delta(\mu_p-\tilde{\mu}_{p,\alpha}(\mathbf{x},t))\delta(\mathbf{c}_p-\tilde{\mathbf{c}}_{p,\alpha}(\mathbf{x},t))\end{aligned}\tag{6}$$

where $\mu_{p,\alpha}(\mathbf{x},t)$ and $\mathbf{c}_{p,\alpha}(\mathbf{x},t)$ are the mass and velocity of class α, respectively. As seen in (6), one single mean velocity is associated with each mass and as a consequence transport equations for the particle agitation cannot be derived. Belt and Simonin [2] define for each class one mass associated with a velocity distribution, which is written as:

$$f_{fp}(\mathbf{x},t,\mu_p,\mathbf{c}_p,\mathbf{c}_f)=n_p(\mathbf{x},t)h^*_{fp}(\mathbf{x},t,\mathbf{c}_p,\mathbf{c}_f|\mu_p)g^*(\mathbf{x},t,\mu_p)\tag{7}$$

with $n_p(\mathbf{x},t)$ the number of particles per unit volume at $\mathbf{x}$ and t. $h^*_{fp}(\mathbf{x},t,\mathbf{c}_p,\mathbf{c}_f|\mu_p)$ is the joint fluid-particle velocity probability density function at time t, conditioned by the mass m_p equal to μ_p, with the center of mass located in the volume $[\mathbf{x},\mathbf{x}+d\mathbf{x}]$ and a translation velocity $\mathbf{u}_p$ in $[\mathbf{c}_p,\mathbf{c}_p+d\mathbf{c}_p]$, seeing a locally undisturbed fluid velocity $\mathbf{u}_{f@p}$ in $[\mathbf{c}_f,\mathbf{c}_f+d\mathbf{c}_f]$. $g^*(\mathbf{x},t,\mu_p)$ is the mass probability density function at time t with the center of mass located in the volume $[\mathbf{x},\mathbf{x}+d\mathbf{x}]$ and a mass m_p in $[\mu_p,\mu_p+d\mu_p]$. The pdfs h^*_{fp} and g^* verify:

$$\int h^*_{fp}(\mathbf{x},t,\mathbf{c}_p,\mathbf{c}_f|\mu_p)\mathrm{d}\mathbf{c}_p\mathrm{d}\mathbf{c}_f=1\quad\forall\,\mu_p\tag{8}$$

$$\int g^*(\mathbf{x},t,\mu_p)\mathrm{d}\mu_p=1\tag{9}$$

Belt and Simonin [2] write the pdf g^*, similar to [3], as a summation of Dirac functions with the sum of the weights ω_α over all classes equal to one (10).

$$g^*(\mathbf{x},t,\mu_p)=\sum_{\alpha=1}^{N}\omega_\alpha(\mathbf{x},t)\delta(\mu_p-\tilde{\mu}_{p,\alpha}(\mathbf{x},t))\tag{10}$$

This presumed pdf g^* is equivalent to make the Gauss quadrature approximation for the moments of g^*:

$$\int\mu_p^k g^*(x,t,\mu_p)\mathrm{d}\mu_p=\sum_{\alpha=1}^{N}\tilde{\mu}^k_{p,\alpha}(\mathbf{x},t)\omega_\alpha(\mathbf{x},t)\tag{11}$$

The weights ω_α and the abscissas $\tilde{\mu}_{p,\alpha}$ in (10) are unknown, thus $2N$ unknowns must be determined. With the help of the Gauss quadrature approximation, the moments of g^* can be computed. Following the DQMOM approach $2N$ transport equations on the low-order mass-moments are derived by integration of the Boltzmann-type equation (5) multiplied with μ_p^k. After some manipulation the following system is obtained with k ranging from 0 to $2N-1$:

$$\begin{aligned}&\int\mu_p^k\left(\frac{\partial f_{fp}}{\partial t}\right)_{coll}\mathrm{d}\mathbf{c}_p\mathrm{d}\mathbf{c}_f\mathrm{d}\mu_p\\&=(1-k)\sum_{\alpha=1}^{N}\tilde{\mu}^k_{p,\alpha}\left[\frac{\partial}{\partial t}(n_\alpha)+\frac{\partial}{\partial x_j}\left(\langle c_{p,j}\rangle_\alpha n_\alpha\right)\right]\\&\quad+k\sum_{\alpha=1}^{N}\tilde{\mu}^{k-1}_{p,\alpha}\left[\frac{\partial}{\partial t}(n_\alpha\tilde{\mu}_{p,\alpha})+\frac{\partial}{\partial x_j}\left(\langle c_{p,j}\rangle_\alpha n_\alpha\tilde{\mu}_{p,\alpha}\right)-n_\alpha\langle\Gamma\rangle_\alpha\right]\end{aligned}\tag{12}$$

For the sake of clarity, the quantity dependencies with respect to $\mathbf{x}$ and t are not written out in (12). The mean number of particles per unit volume n_α with mass $\tilde{\mu}_{p,\alpha}$ is defined as $n_\alpha=\omega_\alpha n$. The physical meaning of the weight ω_α appears in this approach, as the ratio of number of droplets per class α to the total number of droplets at $\mathbf{x}$ and t. System (12) gives the values for the N abscissas $\tilde{\mu}_{p,\alpha}$ and N weights n_α, from which the droplet diameter distribution is reconstructed. This reconstructed distribution should show the correct moments up to the order $2N-1$. The operator $\langle\phi\rangle_\alpha$ represents the conditional average on a mass m_p

equal to $\tilde{\mu}_{p,\alpha}$: $\langle\phi\rangle_\alpha = \int \phi h^*_{fp}(\mathbf{x},t,\mathbf{c}_p,\mathbf{c}_f|\tilde{\mu}_{p,\alpha})\mathrm{d}\mathbf{c}_p\mathrm{d}\mathbf{c}_f$. The term $n_\alpha\langle\Gamma\rangle_\alpha$ represents the evaporation rate of droplets, which is zero throughout this work.

For $N=1$ the equation (12) is identical to the number $(k=0)$ and mass $(k=1)$ transport equations for monodisperse droplets derived by Simonin [4]. Also, (12) is equivalent to the system obtained by Marchisio and Fox [3] if written in terms of diameter. However, system (12) is not closed since it contains the velocity $\langle\mathbf{c}_p\rangle_\alpha$ conditioned by the mass of class α. Following a similar way as Simonin [4] to derive transport equations for momentum, particle kinetic stress and fluid-particle covariance, the velocity $\langle\mathbf{c}_p\rangle_\alpha$ can be obtained in the framework of the DQMOM approach. Those equations are in agreement with Simonin's [4] transport equations for a monodisperse droplet cloud. For more details, the reader may refer to [2] and [4], readers interested in the resolution of the equation system to [2] and [3].

In a Homogeneous Isotropic Turbulence, as in this study, all variations with respect to $\frac{\partial}{\partial x_j}$ are zero and thus equation (12) simplifies significantly. In particular the momentum balance equation does not need to be solved, since the mean velocity is equal to zero. As detailed below, the particle kinetic energy is required for the closure of the collision term. In a first step, within this work, the corresponding values of q_p^2 are directly obtained from the performed DNS/DPS simulations. In a second step, the particle kinetic stress tensor equation is solved in the DQMOM approach. In order to account for the interaction of the particle phase with the fluid turbulent motion, the mean particle response time $\tau^F_{fp} = \langle\tau_p\rangle_\alpha$ and the fluid-particle symmetrical velocity covariance tensor $R_{fp,\gamma\beta} = \frac{1}{2}\left(\langle u'_{f@p,\gamma}c'_{p,\beta}\rangle_\alpha + \langle c'_{p,\gamma}u'_{f@p,\beta}\rangle_\alpha\right)$ are then needed. The value for τ^F_{fp} is taken from the DNS/DPS simulations. A transport equation for R_{fp} can be derived in the DQMOM framework (14). The equilibrium state from the theory of Tchen and Hinze [15] is used to determine the fluid-particle covariance, which is given using the relation of Tchen [15] $q_{fp} = \frac{2q_f}{1+St}$ where the Stokes number is defined as $St = \frac{\tau^F_{fp}}{T_L}$, when the particle kinetic stress equation is solved only. The particle kinetic stress tensor equation is given in (13).

$$
\begin{aligned}
&\int c'_{p,\gamma}c'_{p,\beta}\mu_p^k\left(\frac{\partial f_{fp}}{\partial t}\right)_{coll}\mathrm{d}\mathbf{c}_p\mathrm{d}\mathbf{c}_f\mathrm{d}\mu_p + E \\
&= (1-k)\sum_{\alpha=1}^{N}\tilde{\mu}^k_{p,\alpha}\left[\frac{\partial}{\partial t}\left(n_\alpha\langle c'_{p,\gamma}c'_{p,\beta}\rangle_\alpha\right)\right. \\
&\quad + \frac{\partial}{\partial x_j}\left(n_\alpha\langle c'_{p,\gamma}c'_{p,\beta}\rangle_\alpha\langle c_{p,j}\rangle_\alpha\right) + \frac{\partial}{\partial x_j}\left(n_\alpha\langle c'_{p,\gamma}c'_{p,\beta}c'_{p,j}\rangle_\alpha\right) \\
&\quad + n_\alpha\langle c'_{p,\gamma}c'_{p,j}\rangle_\alpha\frac{\partial}{\partial x_j}\langle c_{p,\beta}\rangle_\alpha + n_\alpha\langle c'_{p,\beta}c'_{p,j}\rangle_\alpha\frac{\partial}{\partial x_j}\langle c_{p,\gamma}\rangle_\alpha \\
&\qquad\left. - n_\alpha\langle c'_{p,\beta}\frac{F'_\gamma}{m}\rangle_\alpha - n_\alpha\langle c'_{p,\gamma}\frac{F'_\beta}{m}\rangle_\alpha\right] \\
&+ k\sum_{\alpha=1}^{N}\tilde{\mu}^{k-1}_{p,\alpha}\left[\frac{\partial}{\partial t}\left(n_\alpha\tilde{\mu}_{p,\alpha}\langle c'_{p,\gamma}c'_{p,\beta}\rangle_\alpha\right)\right. \\
&\quad + \frac{\partial}{\partial x_j}\left(n_\alpha\tilde{\mu}_{p,\alpha}\langle c'_{p,\gamma}c'_{p,\beta}\rangle_\alpha\langle c_{p,j}\rangle_\alpha\right) + \frac{\partial}{\partial x_j}\left(n_\alpha\tilde{\mu}_{p,\alpha}\langle c'_{p,\gamma}c'_{p,\beta}c'_{p,j}\rangle_\alpha\right) \\
&\quad + n_\alpha\tilde{\mu}_{p,\alpha}\langle c'_{p,\gamma}c'_{p,j}\rangle_\alpha\frac{\partial}{\partial x_j}\langle c_{p,\beta}\rangle_\alpha + n_\alpha\tilde{\mu}_{p,\alpha}\langle c'_{p,\beta}c'_{p,j}\rangle_\alpha\frac{\partial}{\partial x_j}\langle c_{p,\gamma}\rangle_\alpha \\
&\quad - n_\alpha\tilde{\mu}_{p,\alpha}\langle c'_{p,\beta}\frac{F'_\gamma}{m}\rangle_\alpha - n_\alpha\tilde{\mu}_{p,\alpha}\langle c'_{p,\gamma}\frac{F'_\beta}{m}\rangle_\alpha \\
&\quad \left. - n_\alpha\langle\Gamma c'_{p,\gamma}c'_{p,\beta}\rangle_\alpha\right] \qquad (13)
\end{aligned}
$$

The only term of equation (13) that remains in the equation for a Homogeneous Isotropic Turbulence are detailed below.

Finally, the fluid-particle covariance equation (14) is solved. τ^F_{fp} is taken again from the DNS/DPS simulations and the fluid energy q_f^2 is also known. The fluid-particle covariance equation writes as:

$$
\begin{aligned}
&\mathcal{C}(c'_{f,\beta}c'_{p,\gamma}\mu_p^k) + E' = \\
&\qquad (1-k)\sum_{\alpha=1}^{N}\tilde{\mu}^k_{p,\alpha}e_\alpha + k\sum_{\alpha=1}^{N}\tilde{\mu}^{k-1}_{p,\alpha}f_\alpha \qquad (14)
\end{aligned}
$$

where e_α and f_α are the source terms of the following equations:

$$
\begin{aligned}
&\frac{\partial}{\partial t}\left(n_\alpha\langle c'_{f,\beta}c'_{p,\gamma}\rangle_\alpha\right) + \frac{\partial}{\partial x_j}\left(n_\alpha\langle c'_{f,\beta}c'_{p,\gamma}\rangle_\alpha\langle c_{p,j}\rangle_\alpha\right) \\
&\quad + \frac{\partial}{\partial x_j}\left(n_\alpha\langle c'_{f,\beta}c'_{p,\gamma}c'_{p,j}\rangle_\alpha\right) \\
&\quad - n_\alpha\langle c'_{f,\beta}\frac{F'_\gamma}{m_p}\rangle_\alpha - n_\alpha\langle c'_{p,\gamma}A_\beta\rangle_\alpha \quad = \quad e_\alpha \qquad (15) \\
&\frac{\partial}{\partial t}\left(n_\alpha\tilde{\mu}_{p,\alpha}\langle c'_{f,\beta}c'_{p,\gamma}\rangle_\alpha\right) + \frac{\partial}{\partial x_j}\left(n_\alpha\tilde{\mu}_{p,\alpha}\langle c'_{f,\beta}c'_{p,\gamma}\rangle_\alpha\langle c_{p,j}\rangle_\alpha\right) \\
&\quad + \frac{\partial}{\partial x_j}\left(n_\alpha\tilde{\mu}_{p,\alpha}\langle c'_{f,\beta}c'_{p,\gamma}c'_{p,j}\rangle_\alpha\right) \\
&\quad - n_\alpha\tilde{\mu}_{p,\alpha}\langle c'_{f,\beta}\frac{F'_\gamma}{m_p}\rangle_\alpha - n_\alpha\tilde{\mu}_{p,\alpha}\langle c'_{p,\gamma}A_\beta\rangle_\alpha \\
&\quad - n_\alpha\langle\Gamma c'_{f,\beta}c'_{p,\gamma}\rangle_\alpha \quad = \quad f_\alpha \qquad (16)
\end{aligned}
$$

The remaining terms in the equation are explained below when detailed for Homogeneous Isotropic Turbulence. The reader may note that the term E and E' on the left hand side of equations (13) and (14) is equal to zero in a Homogeneous Isotropic Turbulence. For its definition as well as an exhaustive explanation of the terms in (13) and (14) the reader may refer to [2].

Closure of collision operator

The coalescence operator $\mathcal{C}(\psi)$ is the integral of the change in a quantity ψ (for a distinct collision) multiplied with its probable collision frequency over all binary collisions. If ψ^* is the quantity after collision and ψ before collision, the change in ψ can be written as $\Delta\psi = \psi^* - \psi$ and thus the coalescence operator $\mathcal{C}(\psi)$ for two particles P and Q as:

$$\mathcal{C}(\Psi) = \frac{1}{2} d_{pq}^2 \int_{\mathbf{w}\cdot\mathbf{k}<0} (\Psi_{pq}^* - \Psi_{pq}) \, [\mathbf{w}\cdot\mathbf{k}] \\ f_{fp}^{(2)}(\mathbf{c}_{f@p}, \mu_p, \mathbf{c}_p, \mathbf{x}, \mathbf{c}_{f@q}, \mu_q, \mathbf{c}_q, \mathbf{x} + d_{pq}\mathbf{k}, t) \\ \mathrm{d}\mathbf{k}\mathrm{d}\mu_p\mathrm{d}\mu_q\mathrm{d}\mathbf{c}_{f@p}\mathrm{d}\mathbf{c}_p\mathrm{d}\mathbf{c}_{f@q}\mathrm{d}\mathbf{c}_q \tag{17}$$

where $d_{pq} = (d_p + d_q)/2$ is the collision diameter, $\mathbf{w} = \mathbf{c}_q - \mathbf{c}_p$ is the relative velocity between the two colliding droplets, $\mathbf{k}$ is the unit center connecting vector pointing from particle P to Q. $f_{fp}^{(2)}(\mathbf{c}_{f@p}, \mu_p, \mathbf{c}_p, \mathbf{x}_p, \mathbf{c}_{f@q}, \mathbf{c}_q, \mu_q, \mathbf{x}_q, t)$ is the joint fluid-particle-fluid-particle pair distribution function. The particle pair distribution function $f_p^{(2)}$ is per definition obtained by integration over the particle velocities as given in equation (18).

$$f_p^{(2)}(\mathbf{c}_p, \mu_p, \mathbf{x}, \mu_q, \mathbf{c}_q, \mathbf{x} + d_{pq}\mathbf{k}, t) \\ = \int\int f_{fp}^{(2)}(\mathbf{c}_{f@p}, \mu_p, \mathbf{c}_p, \mathbf{x}, \mathbf{c}_{f@q}, \mu_q, \mathbf{c}_q, \mathbf{x} + d_{pq}\mathbf{k}, t) \\ \mathrm{d}\mathbf{c}_{f@p}\mathrm{d}\mathbf{c}_{f@q} \tag{18}$$

According to the "molecular chaos" assumption the particle pair distribution function $f_p^{(2)}$ can be written as a product of to single one-particle distribution functions:

$$f_p^{(2)}(\mathbf{c}_p, \mu_p, \mathbf{x}, \mu_q, \mathbf{c}_q, \mathbf{x} + d_{pq}\mathbf{k}, t) \\ \approx f_p(\mathbf{c}_p, \mu_p, \mathbf{x}, t) \, f_p(\mathbf{c}_q, \mu_q, \mathbf{x} + d_{pq}\mathbf{k}, t), \tag{19}$$

It needs to be mentioned that according to [9] the "molecular chaos" assumption is valid only, if the particle response time is much larger than the fluid Lagrangian time scale. If the particle response time is of the same order or smaller than the fluid Lagrangian time scale, the particle velocities become correlated through the interaction with the fluid. This can be accounted for by a specific closure of $f_{fp}^{(2)}$ proposed by [9]. Nevertheless, the "molecular chaos" assumption is the simplest approach and is used here.

The coalescence operator is here written, similar to [3] as outlined in [2], as a function of the "birth" rate $\mathcal{B}$ and "death" rate $\mathcal{D}$ for a quantity $\psi = \mu_p^k$:

$$\mathcal{C}(\Psi) = \mathcal{B}(\Psi) - \mathcal{D}(\Psi) \tag{20}$$

$$\mathcal{B}(\Psi) = \frac{1}{2} \int \Psi_{pq}^* \, \beta(\mu_p, \mu_q) \\ g^*(\mathbf{x}, t, \mu_p) g^*(\mathbf{x}, t, \mu_q) \mathrm{d}\mu_p \mathrm{d}\mu_q \tag{21}$$

$$\mathcal{D}(\Psi) = \int \Psi_p \, \beta(\mu_p, \mathbf{c}_p, \mu_q, \mathbf{c}_q) \\ g^*(\mathbf{x}, t, \mu_p) g^*(\mathbf{x}, t, \mu_q) \mathrm{d}\mu_p \mathrm{d}\mu_q \tag{22}$$

with $\beta(\mu_p, \mu_q)$ the radial relative velocity. It can be written as:

$$\beta = \pi n_p^2 d_{pq}^2 \left(\frac{16}{\pi} \frac{1}{3} (q_p^2 + q_q^2) \right)^{1/2} \tag{23}$$

DQMOM in Homogeneous Isotropic Turbulence (HIT)

The DQMOM approach is here compared with a homogeneous isotropic turbulence coupled with a dispersed phase of spherical particles undergoing coalescence. As mentioned above, all variations with respect to $\frac{\partial}{\partial x_j}$ are zero and equation (12) and (13) simplify significantly. Five different cases are regarded here. In the first case i) only the number and mass balance equation are solved. The particle kinetic energy is extracted from the DNS/DPS simulations. Second, the particle kinetic stress equation is in case ii) solved making use of from DNS/DPS values for the mean particle response time, while the fluid particle covariance is modeled following the theory of Tchen and Hinze [15]. In case iii) additionally the fluid particle covariance equation is solved, with the fluid energy from the DNS/DPS simulations. In case iv) a collision term in the particle kinetic stress equation is added. And last in case v) dry granular simulations are performed in order to evaluate the influence of the collision term in the particle kinetic stress equation. The equations to solve are the following. For the number and mass balance equation (12) the source terms can be written per class α:

i) Number and mass balance equation HIT

$$\frac{\partial}{\partial t}(n_\alpha) = a_\alpha \tag{24}$$

$$\frac{\partial}{\partial t}(n_\alpha \tilde{\mu}_{p,\alpha}) = b_\alpha \tag{25}$$

Then, the system to solve becomes (12), with k ranging from 0 to $2N-1$:

$$(1-k) \sum_{\alpha=1}^{N} \tilde{\mu}_{p,\alpha}^k a_\alpha + k \sum_{\alpha=1}^{N} \tilde{\mu}_{p,\alpha}^{k-1} b_\alpha = \mathcal{C}(\mu_p^k) \tag{26}$$

where $\mathcal{C}(\mu_p^k)$ represents the collision term as defined in (20).

ii) Particle kinetic stress equation (HIT) The particle kinetic stress equation can be written as seen in (28). It can also be obtained from (27). As the particle number and mass are known from (26), (27) contains the same information as (28) as it is only weighted by a different factor. The source terms are related and c_α can be expressed in terms of a_α, b_α and d_α.

$$\frac{\partial}{\partial t}\left(n_\alpha\langle c'_{p,\gamma}c'_{p,\beta}\rangle_\alpha\right) - n_\alpha\langle c'_{p,\beta}\frac{F'_\gamma}{m}\rangle_\alpha - n_\alpha\langle c'_{p,\gamma}\frac{F'_\beta}{m}\rangle_\alpha = c_\alpha \quad (27)$$

$$\frac{\partial}{\partial t}\left(n_\alpha\tilde{\mu}_{p,\alpha}\langle c'_{p,\gamma}c'_{p,\beta}\rangle_\alpha\right) - n_\alpha\tilde{\mu}_{p,\alpha}\langle c'_{p,\beta}\frac{F'_\gamma}{m}\rangle_\alpha - n_\alpha\tilde{\mu}_{p,\alpha}\langle c'_{p,\gamma}\frac{F'_\beta}{m}\rangle_\alpha = d_\alpha \quad (28)$$

(13) can be written as shown in (29), if the influence of coalescence is not accounted for in the particle kinetic stress equation. In the case $ii)$ the system to solve consists thus of (26) and (29). This assumption is valid only, if the effect of collisions on particle kinetic stress is less important than the interaction with the fluid. In this case the source terms $c_\alpha = 0$ and $d_\alpha = 0$ equal zero.

$$(1-k)\sum_{\alpha=1}^{N}\tilde{\mu}^k_{p,\alpha}c_\alpha + k\sum_{\alpha=1}^{N}\tilde{\mu}^{k-1}_{p,\alpha}d_\alpha = \mathcal{C}\left(\mu^k_p c'_{p,\beta}c'_{p,\gamma}\right) = 0 \quad (29)$$

The interaction with the fluid turbulent motion is expressed by the force terms F' in (28). They are written following [4] as follows:

$$n_\alpha\tilde{\mu}_{p,\alpha}\langle c'_{p,\beta}\frac{F'_\gamma}{m}\rangle_\alpha - n_\alpha\tilde{\mu}_{p,\alpha}\langle c'_{p,\gamma}\frac{F'_\beta}{m}\rangle_\alpha \approx -n_\alpha\tilde{\mu}_{p,\alpha}\frac{2}{\tau^F_{fp,\alpha}}\left[\langle c'_{p,\gamma}c'_{p,\beta}\rangle_\alpha - R_{fp,\gamma\beta}\right] \quad (30)$$

Where the fluid-particle covariance tensor $R_{fp,\gamma\beta}$ is modeled using $q_{fp} = \frac{2q_f}{1+St}$. The mean particle response time $\tau^F_{fp,\alpha}$ is extracted from the DNS/DPS simulations.

iii) Fluid particle covariance equation (HIT) The fluid particle covariance equation is given in the case of a Homogeneous Isotropic Turbulence by (31).

$$\frac{\partial}{\partial t}\left(n_\alpha\tilde{\mu}_{p,\alpha}\langle c'_{f,\beta}c'_{p,\gamma}\rangle_\alpha\right) - n_\alpha\tilde{\mu}_{p,\alpha}\langle c'_{f,\beta}\frac{F'_\gamma}{m_p}\rangle_\alpha - n_\alpha\tilde{\mu}_{p,\alpha}\langle c'_{p,\gamma}A_\beta\rangle_\alpha = f_\alpha \quad (31)$$

The force terms can be written as:

$$n_\alpha\tilde{\mu}_{p,\alpha}\langle c'_{f,\beta}\frac{F'_\gamma}{m_p}\rangle_\alpha - n_\alpha\tilde{\mu}_{p,\alpha}\langle c'_{p,\gamma}A_\beta\rangle_\alpha \approx -n_\alpha\tilde{\mu}_{p,\alpha}\frac{2}{\tau^F_{fp,\alpha}}\left[\langle c'_{f,\gamma}c'_{p,\beta}\rangle_\alpha - \langle c'_{f,\gamma}c'_{f,\beta}\rangle_\alpha\right] - n_\alpha\tilde{\mu}_{p,\alpha}\frac{1}{T_L}\langle c'_{f,\gamma}c'_{p,\beta}\rangle_\alpha \quad (32)$$

iv) Collision term in particle kinetic stress equation In general it is difficult to write the collision term $\int q_p^2\mu_p^k\left(\frac{\partial f_{fp}}{\partial t}\right)_{coll}\mathrm{d}\mathbf{c}_p\mathrm{d}\mathbf{c}_f\mathrm{d}\mu_p$ in (13). In the here presented case, a Homogeneous Isotropic Turbulence, the particle mean velocity is zero, as already mentioned. This allows to write the coalescence term making use of (3) and applying (20) and with $\psi = \mu_p^k q_p^2$, if f_p is assumed Gaussian, as it is justified in this isotropic flow configuration. In a first attempt we can then write with $\Lambda = 1$:

$$\mathcal{B}\left(\mu_p^k q_p^2\right) = \Lambda\,\frac{1}{2}\sum_\alpha\sum_\kappa\beta_{\alpha,\kappa}\,\mu_p^{k,*}\,\frac{3}{2}\left(\frac{\mu_{p,\alpha}\left(\frac{2}{3}q^2_{p,\alpha}\right)^{\frac{1}{2}} + \mu_{p,\kappa}\left(\frac{2}{3}q^2_{p,\kappa}\right)^{\frac{1}{2}}}{\mu_{p,\alpha}+\mu_{p,\kappa}}\right)^2 \quad (33)$$

$$\mathcal{D}\left(\mu_p^k q_p^2\right) = \Lambda\sum_\alpha\sum_\kappa\beta_{\alpha,\kappa}\,\mu^k_{p,\alpha}\,\frac{2}{3}\,q^2_{p,\alpha} \quad (34)$$

The equations to solve are then (26) and (35):

$$(1-k)\sum_{\alpha=1}^{N}\tilde{\mu}^k_{p,\alpha}c_\alpha + k\sum_{\alpha=1}^{N}\tilde{\mu}^{k-1}_{p,\alpha}d_\alpha = \mathcal{C}\left(\mu^k_p q^2_p\right) \quad (35)$$

The term E in (13) equals zero in a Homogeneous Isotropic Turbulence, as mentioned above. For further information, the reader may refer to [2].

v) Influence of Collision terms in dry granular flows In this last case the influence of the collision term in the particle kinetic stress equation is evaluated. Dry granular simulations are therefore compared with DQMOM predictions for three different dry granular cases. In the first one, the number and mass balance equation only are solved and the particle kinetic energy is updated using results from DNS/DPS simulations. In the second dry granular case, the particle kinetic stress equation is solved, while the collision term is neglected and finally this collision term is taken into consideration in the last dry granular case. The collision term is shown under iv).

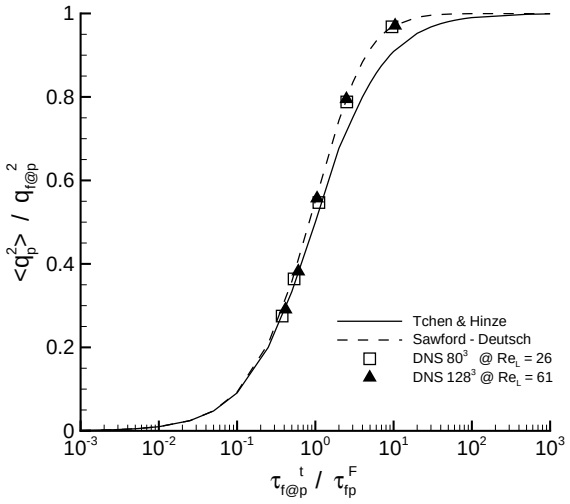

Figure 1. Simulated cases in comparison with the theory of Tchen & Hinze [15], [16] as well as its extension by Deutsch [17], [18]

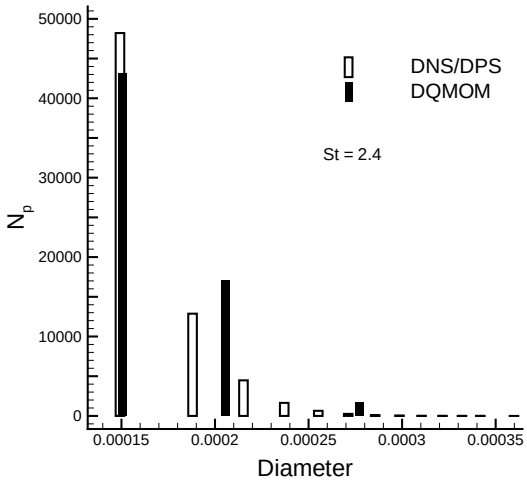

Figure 2. Particle number - diameter pdf for $St = 2.4$ at $Re_L = 61$

Table 1. Characteristics of fluid turbulence for turbulent Reynolds number $Re_L = 61.2$

Cube length	L_b	0.128
Grid points	N	128^3
Turbulent energy	q_f^2	$6.6616\,10^{-3}$
Integral longitudinal length scale	L_f/L_b	0.1056
Integral transversal length scale	L_g/L_f	0.4673
Reynolds number	Re_L	61.2
Kolmogorov length scale	η_k/L_b	0.0506
	$k_{max}\eta$	2.00

Table 2. DNS/DPS to DQMOM ratio of $0th$ to $5th$ order moment for particle inertia of $St = 0.1$, $St = 0.95$ and $St = 2.4$ at $Re_L = 61$ for simulation **case i**

moment (order)	$St = 0.1$	$St = 0.95$	$St = 2.4$
$N_p\ (0)$	2.004	1.238	1.102
$m_p\ (1)$	0.9994	1.0000	0.9995
$d_p\ (\frac{1}{3})$	1.669	1.168	1.073
$d_p^2\ (\frac{2}{3})$	1.323	1.087	1.039
(2)	0.353	0.750	0.877
(3)	0.138	0.620	0.920
(4)	0.113	0.789	2.191
(5)	0.212	1.857	11.114

Description of fluid-particle flow field

The fluid flow field is a homogeneous isotropic turbulence. Once the fluid flow field reaches a steady state the particulate phase is initiated and converges around an equilibrium with the fluid turbulence, as seen in figure 1. The particle Stokes numbers are chosen to be identical for different Reynolds numbers. The initial particle diameter d_p is the same in all simulations, only the particle density ρ_p is modified for different particle inertia. Table 1 summarizes the fluid field values for the turbulent Reynolds number $Re_L = 61$.

RESULTS

The results obtained from DNS/DPS simulations are compared with the DQMOM simulations described above under i) to v) in this section.

Case i)

DQMOM simulations are conducted for five different particle classes, as they are presented in figure 1. However, results are here only presented for the lowest, highest and the intermediate Stokes number. They are characterized by different particle inertia. As the DQMOM approach assumes 'molecular chaos' and thus independence of the coalescing particle velocities, it is supposed to perform best for high inertia particles, as this case is the closest to the 'molecular chaos' assumption. The DNS/DPS simulations are initialized with a monodisperse particle phase (all

particles have the same initial diameter), thus the particle size pdf is represented by one single Dirac function. As three Dirac functions are used in DQMOM to represent the particle diameter distribution, numerical problems could be caused by the initial monodisperse distribution. In order to avoid these problems, the DQMOM simulations are initialized with DNS/DPS data, in which three different particle sizes have occurred since the start of the coalescence simulation. As the DQMOM approach is written to conserve the first $2N-1$ moments of the particle diameter distribution, these moments are calculated for results obtained with the DNS/DPS as well as for results of the DQMOM (11). The ratio of the same moments of the corresponding distributions is used to evaluate the accuracy of the DQMOM in the here used configuration. Results are shown in table 2. Figure 2 compares distributions of inertial particles. The empty bars represent the Dirac distribution obtained from DNS/DPS simulations. As the initial distribution is monodisperse, all emerging droplet diameters are determined by the initial diameter. The black bars represent the Diracs from DQMOM.

Throughout this work, three Diracs are used in the DQMOM approach for two reasons. First, it appears the most feasible choice for comparison with the DNS/DPS data and second, the low-order moments give the same results for three or four Diracs as seen in table 3. Only the 4th-order and higher moments exhibit a significant change in magnitude. The choice of three Diracs seems to be justified. Naturally, if higher than 5th-order moments are of interest, an adequate number of Diracs needs to be chosen.

Under the impression of an increasing accuracy of the moments ratio DNS/DPS to DQMOM with increasing particle inertia, a dry granular test case was performed. Dry granular flows are performed for example in [1]. No fluid phase exists. The collision operator in DQMOM is based, as mentioned above, on the molecular chaos assumption. In dry granular flows this assumption leads to correct collisions frequencies, if the particles size distribution is correctly represented. If only binary collisions are treated and if the particle agitation per particle class is known and if one class exists for every different particle mass as well as for every emerging new particle mass, this approach should lead to correct collision frequencies for dry granular flows. In DQMOM, however, the number of particle classes (Diracs) is given and limited and thus compromises the results. Table 3 shows the moment ratios for this dry granular test case. In comparison with results for simulations with particle inertia of $St = 2.4$, the moment ratios of the dry granular test case exhibit an improvement of up to 50% error. Under the in case i) given conditions, the dry granular case can be considered as the most accurate result possible.

Table 3. DNS/DPS to DQMOM ratio of $0th$ to $5th$ order moment for particle inertia of $St = 2.4$ at $Re_L = 61$ with 3 respectively 4 Diracs and for the dry granular test case

moment (order)	dry granular q_p^2 DNS	$St = 2.4$ 3 Diracs	$St = 2.4$ 4 Diracs
N_p (0)	1.050	1.102	1.101
m_p (1)	1.0004	0.9995	0.9994
d_p ($\frac{1}{3}$)	1.035	1.073	1.072
d_p^2 ($\frac{2}{3}$)	1.019	1.039	1.038
(2)	0.947	0.877	0.878
(3)	0.972	0.920	0.917
(4)	1.475	2.191	2.101
(5)	4.320	11.114	9.515

Table 4. DNS/DPS to DQMOM ratio of $0th$ to $5th$ order moment for particle inertia of $St = 0.1$, $St = 0.95$ and $St = 2.4$ at $Re_L = 61$ for simulation **case ii**

moment (order)	$St = 0.1$	$St = 0.95$	$St = 2.4$
N_p (0)	1.876	1.220	1.121
m_p (1)	0.9994	1.0004	0.9995
d_p ($\frac{1}{3}$)	1.589	1.155	1.086
d_p^2 ($\frac{2}{3}$)	1.289	1.081	1.045
(2)	0.388	0.770	0.862
(3)	0.166	0.655	0.897
(4)	0.147	0.857	2.136
(5)	0.297	2.071	10.868

Case ii)

Results from additionally solving the particle kinetic stress equation using the theory of Tchen and Hinze [15] for the fluid particle covariance are presented in table 4. Results are similar for all particle inertia to those obtained under conditions given in i). Resolving the set of equations in ii) is applicable to less academic simulations as the here presented, in contrast to conditions under i).

Case iii)

Solving the fluid particle covariance equation in addition leads to results, presented in table 5, which show slightly worse

Table 5. DNS/DPS to DQMOM ratio of $0th$ to $5th$ order moment for particle inertia of $St = 0.1$, $St = 0.95$ and $St = 2.4$ at $Re_L = 61$ for simulation **case iii**

moment (order)	$St = 0.1$	$St = 0.95$	$St = 2.4$
N_p (0)	2.150	1.294	1.136
m_p (1)	0.9994	1.0004	0.9995
d_p $(\frac{1}{3})$	1.683	1.186	1.089
d_p^2 $(\frac{2}{3})$	1.300	1.086	1.043
(2)	0.489	0.862	0.927
(3)	0.345	0.965	1.162
(4)	0.552	1.760	3.595
(5)	1.990	5.925	24.306

Table 6. DNS/DPS to DQMOM ratio of $0th$ to $5th$ order moment for particle inertia of $St = 0.1$, $St = 0.95$ and $St = 2.4$ at $Re_L = 61$ for simulation **case iv**

moment (order)	$St = 0.1$	$St = 0.95$	$St = 2.4$
N_p (0)	2.173	1.310	1.148
m_p (1)	0.9994	1.0004	0.9995
d_p $(\frac{1}{3})$	1.700	1.202	1.103
d_p^2 $(\frac{2}{3})$	1.308	1.098	1.054
(2)	0.471	0.794	0.843
(3)	0.312	0.763	0.855
(4)	0.462	1.151	1.974
(5)	1.534	3.184	9.668

results as in the previous cases. Especially for the most interesting lowest order moments.

Case iv)

In this case, the collision term in the particle kinetic stress equation is added to the source terms. Results are shown in table 6. Comparison of results from case iii) and iv) shows a very similar performance. Only for the highest order moments results are better applying the collision term in the particle kinetic stress equation.

Case v)

Finally, in order to evaluate the influence of the collision term in the particle kinetic stress equation, simulations are done with and without this collision term in dry granular flows. The advantage of dry granular flows is the independence of the fluid properties and thus allows to evaluate the influence of this collision term in an isolated manner. It is the only remaining source term in the particle kinetic stress equation. Table 7 compares dry granular simulation results for three different simulations. First, resolving only the number and mass balance equation, while obtaining the particle kinetic energy in regular intervals from DNS/DPS simulations. Second, for two simulations solving the particle kinetic stress equation with and without collision term, respectively. In the first case, where the particle kinetic energy is obtained from the DNS/DPS data, an error of 5% remains for example for the particle number. This flow configuration is entirely controlled by the coalescence rate and thus the collision frequency, which requires a correct value for the particle kinetic energy per Dirac. As the update is done at fixed intervals, the collision frequency is calculated with not exact values for the particle kinetic energy.

Table 7. DNS/DPS to DQMOM ratio of $0th$ to $5th$ order moment for dry granular flows comparing results with different collision terms **case v**

moment (order)	$\mathcal{C}(\mu^k_{p,\alpha})$ q_p^2 DNS	$\mathcal{C}(\mu^k_{p,\alpha})$	$\mathcal{C}(\mu^k_{p,\alpha})$ $\mathcal{C}(c_{p,\beta}c_{p,\gamma}\mu^k_{p,\alpha})$
N_p (0)	1.050	1.063	1.009
m_p (1)	1.0004	1.005	1.005
d_p $(\frac{1}{3})$	1.035	1.043	1.014
d_p^2 $(\frac{2}{3})$	1.019	1.023	1.013
(2)	0.947	0.981	0.915
(3)	0.972	1.086	0.816
(4)	1.475	1.866	1.058
(5)	4.320	6.605	2.825

Introducing the particle kinetic stress equation provides an up-to-date value of the particle kinetic energy at each time increment. As can be seen in table 7 in the second column, results, however, did not improve. They exhibit even a slightly worse performance. Considering finally, as seen in the third column of table 7, a collision term in the particle kinetic stress equation, leads to a significant improvement of the results. For example, the particle number deviates less than 1% from the value obtained in dry DPS simulations. All other moments are in a good agreement either.

CONCLUSION

A recently developed extension of the DQMOM approach [2] based on the formalism of the joint fluid-particle PDF approach by Simonin [4] is evaluated. The great advantage of this extension is the possibility to write the particle momentum and particle kinetic stress transport equation accounting for coalescence effects. In particular a collision term in the particle kinetic stress transport equation can be written for the here presented case of Homogeneous Isotropic Turbulence. Several different cases, considering different sets of transports equations and collision terms (assuming molecular chaos) are compared to results obtained from DNS/DPS simulations. Their influence is evaluated and the overall performance of DQMOM is estimated. In dry granular flows an accuracy of less than 1% error in the particle number is obtained for DQMOM taking into account the collision term in the particle kinetic stress transport equation. As a correct prediction of the particle kinetic energy seems to be crucial to a good performance, other collision models will be tested in the future that take into account the fluid-particle interaction. In the here presented results the collision frequency in DQMOM is overestimated, thus the introduction of collision models that diminish the collision frequency like the correlated collision model in [9] could lead to an improved performance.

ACKNOWLEDGMENTS

Numerical simulations were performed on the NEC-SX8 supercomputer at the Institut de Développement et des Ressources en Informatique Scientifique (IDRIS). The CPU time has been provided by IDRIS in the frame of project 91066.

Financial support of Agence National de Recherche under project DYNAA is gratefully acknowledged.

This research project has been supported by a Marie Curie Early Stage Training Fellowship of the European Community's Sixth Framework Programme under contract number 'MEST-CT-2005-020429'.

REFERENCES

[1] Wunsch, D., Fede, P., and Simonin, O., 2008. "Development and validation of a binary collision detection algorithm for a polydispersed particle mixture". *Proceedings of the ASME FEDSM 2008,* **FEDSM2008-55159**.

[2] Belt, R. J., and Simonin, O., 2009. "Quadrature method of moments for the pdf modeling of droplet coalescence in turbulent two-phase flows". *Proceedings of the ASME FEDSM 2009,* **FEDSM2009-78095**.

[3] Marchisio, D. L., and Fox, R. O., 2005. "Solution of population balance equations using the direct quadrature method of moments". *Aerosol Sci.,* **36**, pp. 43–95.

[4] Simonin, O., 2000. "Statistical and continuum modeling of turbulent reactive particulate flows". *Von Karman Institute Lecture Notes*.

[5] Ashgriz, N., and Poo, J. Y., 1990. "Coalescence and separation in binary collisions of liquid drops". *J. Fluid Mech.,* **221**, pp. 183–204.

[6] Qian, J., and Law, C. K., 1997. "Regimes of coalescence and separation in droplet collision". *J. Fluid Mech.,* **331**, pp. 59–80.

[7] Estrade, J. P., 1998. "Etude expérimentale et numerique de la collision de gouttelettes". *Ecole nationale supérieure de l'aéronautique et de l'espace: Thèse*.

[8] Fevrier, P., Simonin, O., and Squires, K. D., 2005. "Partitioning of particle velocities in gas-solid turbulent flows into a continuous field and a spatially uncorrelated random distribution: theoretical formalism and numerical study". *J. Fluid Mech.,* **533**, pp. 1–46.

[9] Lavieville, J., Deutsch, E., and Simonin, O., 1995. "Large eddy simulation of interaction between colliding particles and a homogeneous isotropic turbulence field". *6^{th} Int. Symp. on Gas-Solid Flows, FEDSM 1995,* **228**, pp. 347–357.

[10] Fede, P., and Simonin, O., 2003. "Modelling of kinetic energy transfer by collision in a non-settling binary mixture of particles suspended in a turbulent homogeneous isotropic flow". *Proceedings of the ASME FEDSM 2003*.

[11] Simonin, O., Fevrier, P., and Lavieville, J., 2002. "On the spatial distribution of heavy-particle velocities in turbulent flow: from continious field to particulate chaos". *Journal of Turbulence,* **3, 040**.

[12] Eswaran, V., and Pope, S. B., 1988. "An examination of forcing in direct numerical simulations of turbulence". *Computers and Fluids,* **16 (3)**, pp. 257–278.

[13] Maxey, B. ., 1988. "Methods for evaluating fluid velocities in spectral simulations of turbulence". *Journal of Computational Physics,* **83**, pp. 96–125.

[14] Schiller, L., and Naumann, A., 1935. "A drag coefficient correlation". *VDI Zeitung,* **77**, pp. 318–320.

[15] Tchen, C. M., 1947. "Mean value and correlation problems connected with the motion of small particles suspended in a turbulent fluid". *Thesis: Delft, Martinus Nijhoff, The Hague*.

[16] Hinze, J. O., 1975. "Turbulence". *McGraw-Hill*.

[17] Deutsch, E., and Simonin, O., 1991. "Large eddy simulation applied to the motion of particles in stationary homogeneous fluid turbulence". *Turbulence Modification in Multiphase Flows,* **ASME FED, Vol. 110**, pp. 35–42.

[18] Sawford, B. L., 1991. "Reynolds number effects in lagrangian stochastic models of turbulent dispersion". *Phys. of Fluids,* **3 (6)**, pp. 1577–1586.

Numerical Simulation and Statistical Modeling of Inertial Droplet Coalescence in Homogeneous Isotropic Turbulence

Dirk Wunsch, Pascal Fede, Olivier Simonin and Philippe Villedieu

Abstract A comparative parameter study is performed in order to analyze the influence of turbulence on the rate of droplet coalescence. Therefore, Direct Numerical Simulations (DNS) of the fluid turbulence are coupled with a Lagrangian tracking of the particle phase (DPS) accounting for collisions leading to coalescence and to a broad droplet size distribution. In addition the accuracy of stochastic collision models is evaluated by comparison of Monte-Carlo predictions with the obtained results from the DNS/DPS simulations and statistical collision models are evaluated.

1 Introduction

The study of collisions between particles in turbulent dispersed multiphase flows is of interest in many engineering applications. In particular, flows in which droplet coalescence is likely to play an important role include many topics such as solid-fuel rocket propulsion, internal combustion engines and electric generation by a liquid fuel turbine. The droplet size generally has a major influence on the global performance of the system and must be accurately taken into account in numerical simulations. As the carrier flow is often turbulent, droplets located in the vicinity of the same point may have different velocities, collide and perhaps coalesce leading to a strong modification of the initial droplet size distribution. Several numerical approaches can be used to investigate the effect of the fluid turbulence on the coalescence rate in a cloud of inertial droplets (with a particle relaxation time appreciably

Dirk Wunsch, Pascal Fede, Olivier Simonin
Université de Toulouse, INPT, UPS, IMFT, 31400 Toulouse, France,
CNRS, Institut de Mécanique des Fluides de Toulouse, 31400 Toulouse, France
e-mail: wunsch@imft.fr, fede@imft.fr, simonin@imft.fr

Philippe Villedieu
ONERA; DMAE, 2 avenue Edouard Belin, 31055 Toulouse, France
e-mail: Philippe.Villedieu@onera.fr

larger than the Kolmogorov time scale). One possibility is the stochastic approach based on the Monte-Carlo method in order to solve the kinetic equation governing the probability density function of the droplet cloud. Villedieu and Simonin [15] proposed a kinetic approach for the calculation of the collision probability that takes into account the correlations between neighboring particles due to the interaction with the fluid turbulence [13]. Model evaluations for simplified test cases have shown that the correlation effect may modify appreciably the droplet growth rate prediction in comparison with results obtained assuming standard molecular chaos assumption. In order to analyze the influence of the colliding particle velocity correlations induced by the fluid turbulence on the rate of droplet coalescence, reveal coalescence mechanisms and to validate this new statistical modeling approach, deterministic Lagrangian simulations of inertial particles (DPS) coupled with Direct Numerical Simulations (DNS) of the fluid turbulence have been carried out.

2 DNS/DPS approach

Direct Numerical Simulations (DNS) coupled with a Lagrangian tracking of the particle phase (DPS) are performed here and have been extensively used to investigate gas-particle flows [6], [9]. The flow configuration is a Homogeneous Isotropic Turbulence (HIT) forced by a scheme initially proposed by Eswaran and Pope [5], which assures a statistical steadiness. The particles are considered as rigid spheres with diameters smaller than the Kolmogorov turbulence length scale η_K. The turbulence modulation by the dispersed phase (two-way coupling) is not considered, as the particle mass fraction is small. Assuming that the particle fluid density ratio ($\rho_p \gg \rho_f$) is large, the forces acting on the particle are reduced to the drag force only. Thus, the governing equations of the N_p particle system in interaction with the surrounding flow field and undergoing particle-particle collisions is written as

$$\begin{aligned} \frac{d\mathbf{x}_p}{dt} &= \mathbf{v}_p \\ m_p \frac{d\mathbf{v}_p}{dt} &= m_p \frac{\left[\mathbf{v}_p - \mathbf{u}_{f@p}\right]}{\tau_p} + \sum_{i=1;j\neq i}^{N_p} \mathbf{F}_{p,ij} \end{aligned} \tag{1}$$

where $\mathbf{x}_p, \mathbf{v}_p$ are the position and velocity vectors of the particle p and m_p is the particle mass. $\mathbf{u}_{f@p}$ is the fluid velocity at the position of the particle and $\mathbf{F}_{p,ij}$ represents the impulsive force resulting from particle-particle collisions. As two-way coupling is neglected, $\mathbf{u}_{f@p}$ is computed with an accurate interpolation scheme [3]. The particle response time τ_p is given using the relation of Schiller and Naumann [11] by

$$\tau_p = \frac{4}{3}\frac{\rho_p}{\rho_f}\frac{d_p}{C_D}\frac{1}{\left|\mathbf{v}_p - \mathbf{u}_{f@p}\right|}$$

$$C_D = \frac{24}{Re_p}\left(1 + 0.15 Re_p^{0.687}\right) \qquad Re_p = \frac{\left|\mathbf{v}_p - \mathbf{u}_{f@p}\right| d_p}{\nu_f} \tag{2}$$

with d_p the particle diameter and ν_f the kinematic viscosity of the fluid. Coalescence is modeled assuming that each collision leads to permanent coalescence. Other collision outcomes as identified by several authors [1],[4],[10] are not regarded for the sake distinctness. The mass and momentum conservation equations for two particles undergoing coalescence are written as

$$\begin{aligned} m^* &= m_p + m_q \\ m^*\mathbf{v}^* &= m_p\mathbf{v}_p + m_q\mathbf{v}_q \end{aligned} \tag{3}$$

with m_p and m_q the mass of the particles before coalescence and m^* after. Analogous for the particle velocities $\mathbf{v}_p, \mathbf{v}_q$ and $\mathbf{v}^*$. The corresponding particle diameter is directly deductible from the mass conservation equations as the particle density is constant and the particles are modeled as rigid spheres, as mentioned above. The position of the new particle that arises from coalescence is given as

$$\mathbf{x}^* = \frac{d_p^3\mathbf{x}_p + d_q^3\mathbf{x}_q}{d^{*3}} \tag{4}$$

with $\mathbf{x}^*$ the position of the new particle and d_p, d_q and d^* the particle diameters. Coalescence is detected using a recently developed algorithm allowing detecting collisions in a poly-dispersed particle mixture [16].

3 Monte-Carlo Approach

The Monte-Carlo method represents a stochastic approach to solve the kinetic equation governing the probability density function of the droplet cloud. The particle PDF transport equation is written by Simonin in [12] introducing the fluid-particle joint PDF. Villedieu and Simonin [15] proposed a new kinetic approach in order to account for correlations between neighboring particles in the collision probability due to their interaction with the fluid. The here applied method is of the Babovsky type [2] and described shortly in the following. The particles are sorted by their fluid velocity and grouped into pairs, the collision probability for each pair is then calculated. A rejection method is used to decide whether the collision takes place or not. This procedure is applied for all pairs of particles, then the system advances to the next time step. In order to account for the correlation of the particle velocities by the fluid, the particles fluid velocity is discretized into several classes. The Babovsky algorithm is applied within each of these classes. Therefore, only particles collide that show a similar fluid velocity.

4 Fluid-Particle flow fields

The fluid flow field is a Homogeneous Isotropic Turbulence. Three turbulent flow fields are compared in this study, in order to investigate the influence of the turbulent Reynolds number on particle statistics. Once the fluid flow field reaches a steady state the particulate phase is initiated and reaches an equilibrium defined by Tchen and Hinze [14] with the fluid turbulence. From this equilibrium state on the coalescence effect is started and collisions between particles lead now to coalescence. The particle Stokes numbers are chosen to be identical for different Reynolds numbers. The initial particle diameter d_p is the same in all simulations, only the particle density ρ_p is modified for different particle inertia.

5 Coalescence in DNS/DPS and model comparison

5.1 Influence of particle inertia

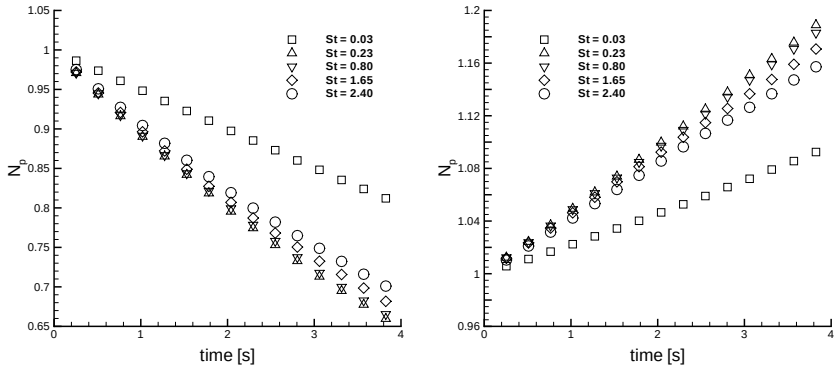

Fig. 1 Number of particles (left panel) and Sauter diameter (right panel) in coalescence with respect to Stokes number. Numerical simulation with $Re_L = 61$

Figure 1 (left) shows the reduction of particle number due to coalescence in a turbulent fluid flow at Reynolds number $Re_L = 61$ for different particle inertia. Figure 1 (right) shows the corresponding Sauter diameter $d_s = \frac{\langle d_p^3 \rangle}{\langle d_p^2 \rangle}$. The lowest coalescence rate is found for particles with a small Stokes number and increases with an increasing Stokes number. This means that higher particle inertia lead to more collisions, which is consequential. The highest coalescence rate, however, is not found for $St = 2.4$, which represents the highest particle inertia investigated here, but for intermediate Stokes numbers. This seems to be surprising but may be explained by

preferential particle concentration. Simonin *et al.* [13] showed in turbulent gas-solid flows that particles with a particle response time in the order of the Lagrangian time scale tend to accumulate in regions of low vorticity due to the interaction with fluid turbulence. This effect increases the particle volume fraction locally and may lead to a higher coalescence rate and consequently explain an elevated coalescence rate for these particle inertia. The behavior of the Sauter diameter, in figure 1 (right), corresponds to the coalescence rates and the effect of the Stokes number accords.

The initial particle size distribution is a monodisperse Dirac function. Figures 2 show the time development of the initial particle distribution for the smallest and largest Stokes number investigated here.

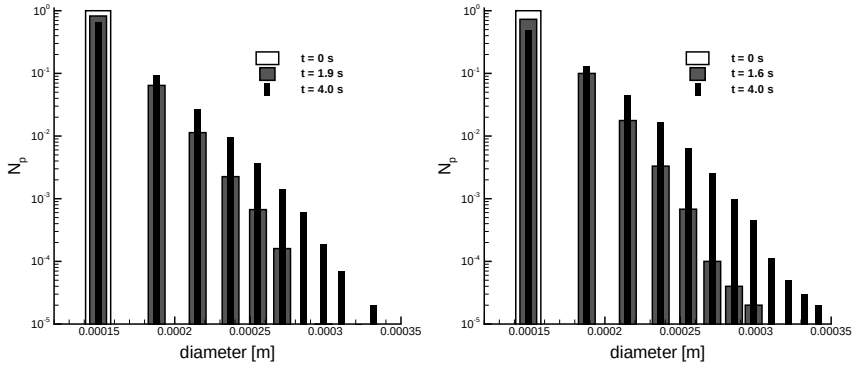

Fig. 2 Time-evolution of the particle diameter distribution measured from DPS / DNS for $St = 0.03$ (left) and $St = 2.4$ (right)

5.2 Comparison with Monte-Carlo predictions

The coalescence rates in figure 3 (left panels) and the particle kinetic energy in figure 3 (right panels) obtained from the DNS/DPS simulations are compared to predictions from Monte-Carlo simulations. First, applying the standard uncorrelated collision model based the 'molecular chaos' assumption (dashed lines) and second, applying a correlated model (solid lines), which takes fluid-particle correlations into consideration. This is done by applying the same collision algorithm as in the uncorrelated case to subsections of the particle vector, which is sorted by means of fluid velocity. This has a consequence that particles will collide with particles, which see a similar fluid velocity. In these simulations 10 sections are used.

It can be seen that the correlated collision model predicts a considerably better coalescence rate than the uncorrelated model for either small and large particle inertia, as seen in figure 3 (left). Also the particle kinetic energy is better predicted using the correlated model (figure 3 (right)).

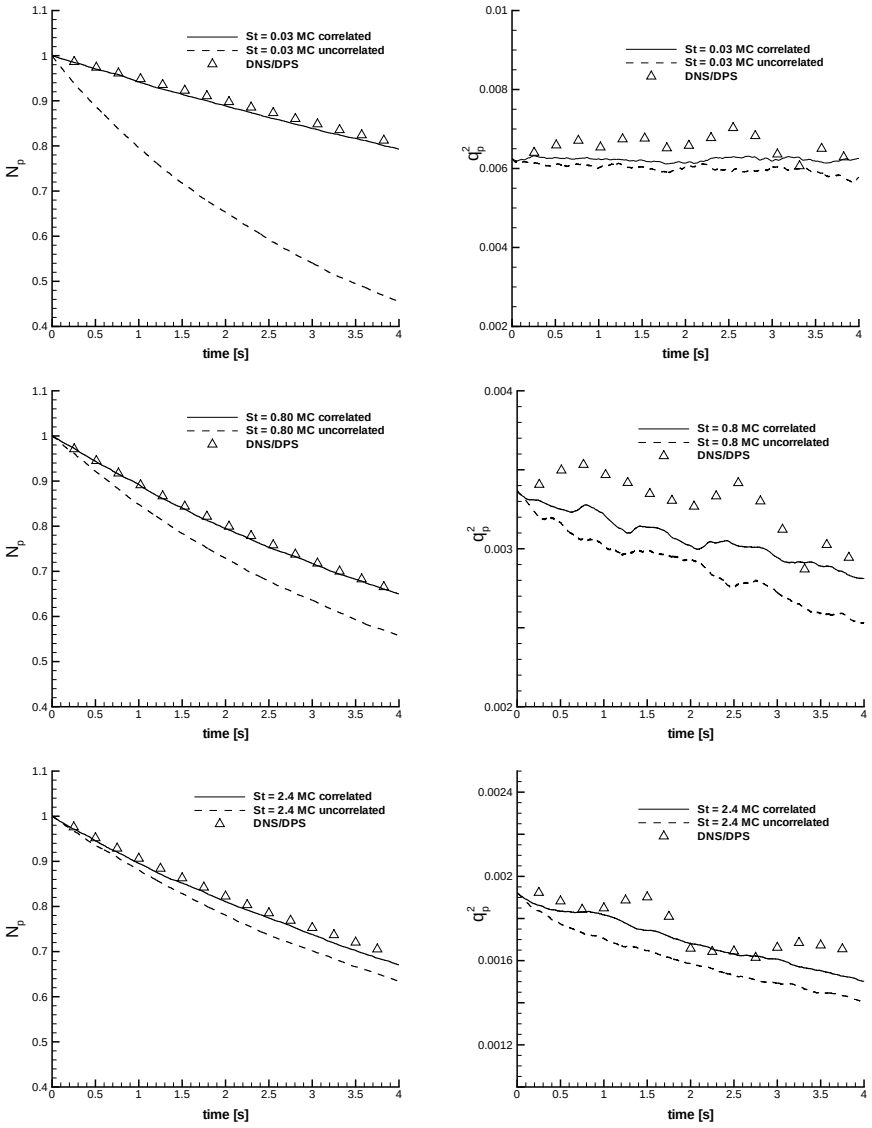

Fig. 3 Comparison of particle number (left panel) and of particle kinetic energy (right panel) in the coalescence regime for DNS/DPS and Monte-Carlo simulations with respect to Stokes number. White symbols represent the uncorrelated collision model and black symbols a correlated collision model. For $St = 0.03$ (top), $St = 0.8$ (middle) and Stokes $St = 2.4$ (bottom)

6 Acknowledgments

Numerical simulations were performed on NEC-SX8 supercomputer. The CPU time has been provided by the Institut de Développement et des Ressources en Informatique Scientifique (IDRIS) in the frame of the Project 91066. This research project has been supported by a Marie Curie Early Stage Training Fellowship of the European Community's Sixth Framework Programme under contract number 'MEST-CT-2005-020429'.

References

1. Ashgriz, N., Poo, J.Y.: Coalescence and separation in binary collisions of liquid drops, J. Fluid Mech., 221, pp. 183-204 (1990)
2. Babovsky, H.: On a simulation scheme for the Boltzmann equation, Mth. Meth. in Appl. Sc., 8, pp. 223-233 (1986)
3. Balachandar, S., Maxey, M.R.: Method for evaluating fluid velocities in spectral simulations of turbulence. Journal of Computational Physics, 83, pp. 96-125 (1988)
4. Estrade, J.-P.: Etude expérimentale et numérique de la collision de gouttelettes, Ecole national supérieure de l'aéronautique et de l'espace: Thèse (1998)
5. Eswaran, V., Pope, S.B.: An examination of forcing in direct numerical simulations of turbulence. Computers and Fluids, 16(3), pp.257-278 (1988)
6. Fede, P., Simonin, O.: Modelling of kinetic energy transfer by collision in a non-settling binary mixture of particles suspended in a turbulent homogeneous isotropic flow. Proceedings of the ASME FEDSM 2003, FEDSM2003-45735 (2003)
7. Fede, P., Simonin, O., Villedieu, P.: Monte-Carlo simulation of colliding particles in gas-solid turbulent flows from a joint fluid-particle PDF equation. ASME FEDSM2002, FEDSM2002-31226 (2002)
8. Hylkema, J.J., Villedieu, P.: A random particle method to simulate coalescence phenomena in dense liquid sprays. Proc. of 16th Int. Conf. on Numerical Methods in Fluid Dynamics, Lecture notes in physics 515, Springer-Verlag (1999)
9. Laviéville, J., Deutsch, E., Simonin, O.: Large Eddy Simulation of interaction between colliding particles and a homogeneous isotropic turbulence field. 6^{th} Int. Symp. on Gas-Solid Flows, FEDSM 2005, 228, pp. 347-357 (1995)
10. Qian, J., Law, C.K.: Regimes of coalescence and separation in droplet collision, J. Fluid Mech., 331, pp. 59-80 (1997)
11. Schiller, L., Naumann, A.: A drag coefficient correlation, VDI Zeitung, 77, pp. 318-320 (1935)
12. Simonin, O.: Combustion and turbulence in two-Phase-Flows, von Karman Institute for Fluid Dynamics, Lecture Series 1996-02 (1996)
13. Simonin, O., Février, P., Laviéville, J.: On the spatial distribution of heavy-particle velocities in turbulent flow: from continuous field to particulate chaos. Journal of Turbulence, Vol. 3, 040. (2002)
14. Tchen, C.M.: Mean value and correlation problems connected with the motion of small particles suspended in a turbulent fluid. Thesis: Delft, Martinus Nijhoff, The Hague (1947)
15. Villedieu, P., Simonin, O.: Modeling of coalescence in turbulent gas-droplet flows. Comm. Math. Sci., Suppl. Issue, No. 1, pp. 13-33 (2004)
16. Wunsch, D., Fede, P., Simonin, O.: Development and validation of a binary collision detection algorithm for a poly-dispersed particle mixture. Proceedings of ASME FEDSM2008, FEDSM2008-55159 (2008)

Proceedings of FEDSM2008
ASME Fluids Engineering Division Summer Conference
August 10-14, 2008, Jacksonville, Florida, USA

FEDSM2008-55159

DEVELOPMENT AND VALIDATION OF A BINARY COLLISION DETECTION ALGORITHM FOR A POLYDISPERSED PARTICLE MIXTURE

Dirk Wunsch, Pascal Fede, Olivier Simonin

Institut de Mécanique des Fluides de Toulouse
UMR CNRS-INPT-UPS 5502
Allée du Professeur Camille Soula
31400 Toulouse, France

wunsch@imft.fr fede@imft.fr simonin@imft.fr

ABSTRACT

A time driven Lagrangian particle detection algorithm for a poly-dispersed mixture of particles is developed and validated. The advantage of this algorithm is the possibility to treat a distribution of particle diameters. We are especially interested in the collision treatment of poly-dispersed particle mixtures and coalescence. Particle pairs are found by applying the overlap criteria and additionally another second criterion, which allows a substantial increase of the time step without limiting the algorithm's accuracy. The algorithm, which is developed here, is validated with test cases by comparison with predictions of the kinetic theory of rarefied gases. They are applied to dry granular flows. The algorithm accuracy is determined with respect to time step criteria, for both dilute and dense systems.

Keywords: particle detection algorithm, poly-dispersed particle mixture, binary collisions, granular flow

INTRODUCTION

Multiphase flows occur in many industrial applications, such as injection and combustion in engines, sprays or meteorology. These flows show a set of physical phenomena such as interaction between fluid and particles, particle segregation, loss of energy due to collisions or coalescence. Among others we are especially interested in the coalescence rate and the influence of turbulence on coalescence phenomena.

There are various coalescence phenomena and each collision between two droplets leads to the creation of one to several new droplets, depending on the relative properties of the colliding droplets. It is easily foreseeable that even a binary mixture of droplets fast leads to a wide distribution of particle diameters, even if the creation of satellite droplets in the regimes of separation is neglected. Several studies dealing with coalescence phenomena have been performed, pointing out the diversity of the collision outcome [1] - [3]. The collision and coalescence rates are determined based on a Lagrangian tracking of the dispersed phase; here referred to as Discrete Particle Simulation (DPS). This approach can be coupled with Direct Numerical Simulations (DNS) in order to account for the influence of the fluid turbulent motion on the particle distribution. The outcome of this numerical simulation (DNS + DPS) can then be compared to predictions of Euler – Lagrange stochastic or Euler – Euler models in order to develop and validate those models.

Several algorithms for the treatment of the dispersed phase exist. The simplest, but also an extremely inefficient way to detect particle-particle collisions is checking for collision between all possible particle pairs in the computation domain. With N_p particles in the system the cost of checking for collision is $N_p(N_p-1)/2$ and hence in the order of $O(N_p^2)$. To reduce computation cost Hopkins & Louge [5] proposed an algorithm based on a detection grid. This algorithm [5] however is limited to one particle diameter and thus not suitable to simulate a dispersed system with a particle diameter distribution. Therefore, in order to be able to adequately represent the particle diameter distribution, a particle detection algorithm is developed, which suits the demands. This algorithm, which is intended to be used in numerical

simulations including a turbulent flow field (DNS + DPS) is developed and validated in this paper. The validation is done by comparison with theoretical predictions of the kinetic theory of rarefied gases for mono- and bi-dispersed particle systems, using of the radial distribution function of particle pairs.

NOMENCLATURE

Latin symbols

$b_{p,ii}$	Normalized anisotropy tensor
d_p	Particle diameter
DNS	Direct Numerical Simulation
DPS	Direct Particle Simulation
ED	Event Driven
$f^{(1)}$	One particle distribution function
$f^{(2)}$	Two particle distribution function
$\vec{F}_{p,ij}$	Force vector of particle-particle collisions
g_0	Radial distribution function
m_p	Particle mass
N_p	Number of particles
n_p	Particle density
PDF	Probability Density Function
q_p^2	Particle kinetic energy
r_p	Radius of particle i
T	Granular particle agitation
t	Time
$\vec{u}_f$	Fluid velocity
$\vec{v}_p$	Particle velocity
$\vec{w}_{pq}$	Relative velocity of particles
$\vec{x}_p$	Particle position
TD	Time Driven

Greek symbols

α_p	Particle volume fraction
μ_f	Dynamic fluid viscosity
ρ_p	Particle density
τ_c	Mean particle collision time
τ_p	Particle response time
Δt	Time step

ALGORITHMIC DETAILS

Preliminary considerations

The governing equations to simulate a system of N_p particles moving along straight lines during one time step, interacting with the surrounding flow field and by collision with one another can be written as

$$\frac{d\vec{x}_p}{dt} = \vec{v}_p$$
$$m_p \frac{d\vec{v}_p}{dt} = m_p \frac{\left[\vec{v}_p - \vec{u}_f\left(\vec{x}_p\right)\right]}{\tau_p} + \sum_{\substack{i=1 \\ j\neq i}}^{N_p} \vec{F}_{p,ij} \qquad (1)$$

where $\vec{x}_p$, $\vec{v}_p$ and m_p are the position, velocity and particle mass. $\vec{u}_f\left(\vec{x}_p\right)$ is the velocity of the fluid, τ_p is the particle response time given by

$$\tau_p = \frac{\rho_p d_p^2}{18\mu_f} \qquad \text{for} \qquad \mathrm{Re}_p << 1 \qquad (2)$$

with ρ_p the particle density, d_p the particle diameter, μ_f the dynamic viscosity of the fluid and Re_p the particle Reynolds number. The last term $F_{p,ij}$ represents the impulsive force resulting from particle-particle collisions. Within this work numerical simulations are carried out for dry granular flows, not including any continuous phase. No interaction of fluid and particle phase exists and the particle velocities are only altered by particle-particle collisions. Hence, this configuration is suitable to validate the detection algorithm, as well as to check models of quantities altered by collision only, by comparison with the direct simulations conducted with the new algorithm.

Two basically different approaches to simulate a system like (1) exist. First, an event-driven (ED) approach in which the system is advancing event by event. Those events might be collisions or depending on the kind of detection used a transfer from detection cell to detection cell, as described by Sigurgeirsson *et al.* [4]. The ED approach leads to an asynchronous system in which the particles are not at the same point in time. Event-driven algorithms and the related event scheduling problem were investigated by [4],[8]-[9]. As soon as the particle phase is coupled with direct simulations of a continuous phase a time step is introduced, which forces a synchronization of the particle phase at the end of each time step. This makes the ED approach not feasible and its advantage in granular flows disappears. The second existing approach is the time-driven (TD) approach where the system is discretized in time and advanced by a time step. This approach is followed here. Possible collisions are detected at the end of each time step and appropriately processed. The TD approach keeps the system synchronous. Time-driven algorithms were developed and applied for example by [5]-[6],[10]. Both approaches hold advantages and drawbacks. The ED approach guarantees not to miss any collision as the system advances event by event. Such kind of algorithm may perform very efficiently and with the correct choice of parameters optimally as shown in [4]. Furthermore, a second detection criterion was introduced in this work, which allows a substantial increase of the time step compared to a TD algorithm which detects particle-particle collisions by overlap only.

It must be noticed that each particle in the system may collide only once per time step. Multiple collisions of the same

particle can create inaccurate collision frequencies. It is assumed that each collision between more than two particles can be expressed as consecutive collisions each between two particles. A schematic of the algorithm is given in Fig.1.

Detection of particle pairs

As mentioned above the simplest but also most inefficient algorithm compares all possible particle pairs in the computation domain. As the probability of collision between two sufficiently distant particles during one time step is very small if not zero, it is not necessary to check for a particle of reference with all other particles in the domain. It is sufficient to search for possible collision partners in adequately large vicinity around this reference particle. To search in the vicinity of a particle, the computation domain is subdivided into cells, which contain one or more particles. If the number of particles per cell is sufficiently low the cost of checking for collisions can be reduced to the order of O(N), as for each particle only a constant number of particle pairs need to be checked. Therefore, the computation domain is subdivided into cells in such a way that the least particles possible are found in one cell. A higher number of lagrangian particles per detection cell will increase the computation time. On the other hand the detection cell edge length must be superior to the largest particle diameter in order to ensure a correct detection of all colliding particle pairs. The vicinity to be searched for potential colliding pairs is composed of 27 cells. However, checking half of this neighborhood is sufficient, as it is searched for particle pairs. Searching in the entire neighborhood would lead to double check every particle pair. Hence, only 14 cells need to be checked per particle and computation time can be reduced by half for checking particle pairs.

Each particle pair within the vicinity is then checked by two criteria for collision. The first criterion is the so-called overlap criterion. This is the standard approach which has been implemented many times. Two particles are tested for an overlap at the end of each time step by comparing the distance of the two particle centers to the sum of their radii. The particles overlap if the distance is smaller than the sum of their radii and then their collision is handled as described below.

Checking for overlap only, introduces a time step criterion, which is intended for avoiding particles passing through one another during one time step and for consequently not overlapping at the end of the time step. Especially grazing collisions are subject to being missed if the time step is too large. In order to increase the time step and assure that grazing particle-particle collisions are reliably detected a second detection criterion is introduced. If a particle pair is found not to overlap at the end of a time step, the scalar product between the relative velocity of the particles $\vec{w}_{pq} = \vec{v}_q - \vec{v}_p$ and the normalized connecting vector of their centers, which points from P to Q, is determined at the beginning and the end of the time step. If the sign of this scalar product changes during the time step the particle centers changed their relative position one to another.

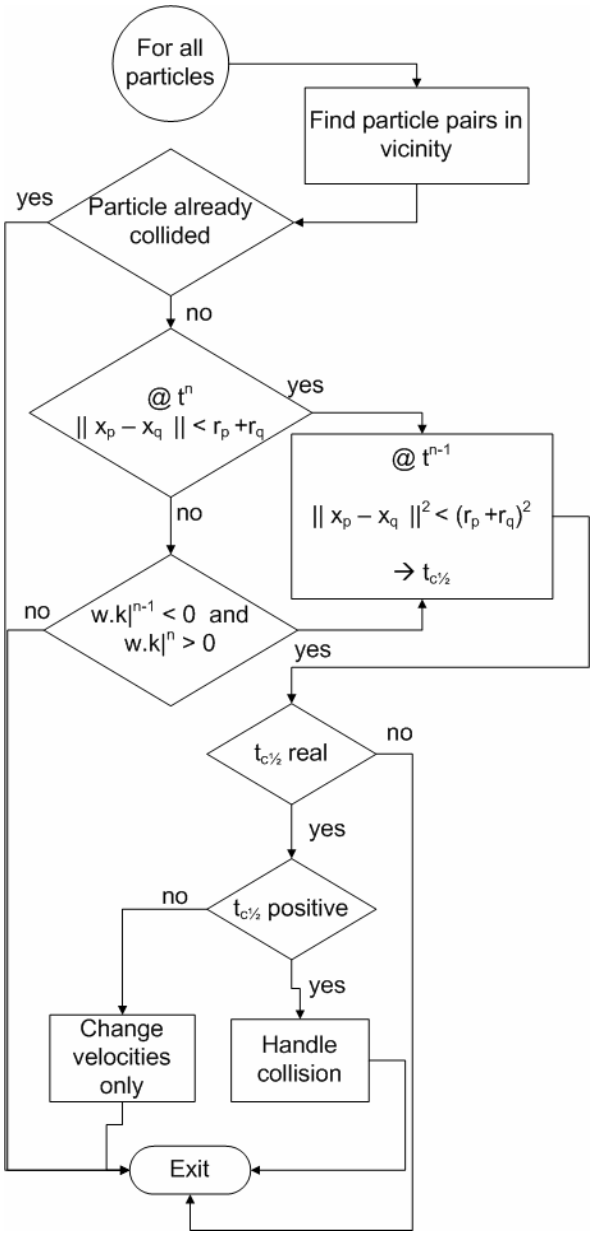

Fig.1: Schematic of algorithm

$$\vec{w}_{pq}.\vec{k}_{pq}\,|^{n-1} < 0 \qquad \text{and} \qquad \vec{w}_{pq}.\vec{k}_{pq}\,|^{n} > 0 \tag{3}$$

Even if they changed sides, they did not necessarily collide as it is possible that they passed each other in a distance greater than the sum of their radii. To decide whether the particles collided or not the following equation in time is solved for the exact time of collision based on the particle position and velocity of the previous time step

$$\left\| \vec{x}_q(t_c) - \vec{x}_p(t_c) \right\| = r_p + r_q \tag{4}$$

where t_c is the time of collision and r_p and r_q the particle radii. $\vec{x}_p$ and $\vec{x}_q$ are written as:

$$\vec{x}_p(t_c) = \vec{x}_p^{n-1} + \vec{v}_p \cdot t_c$$
$$\vec{x}_q(t_c) = \vec{x}_q^{n-1} + \vec{v}_q \cdot t_c \quad (5)$$

As can be seen from (3) particle positions and velocities are needed for two consecutive time steps. Thus, this particle information is stored in the particle vector. Squaring both sides of (4) leads to a quadratic equation in time.

$$\left\|\vec{v}_q - \vec{v}_p\right\|^2 t_c^{\,2} + 2\left(\vec{v}_q - \vec{v}_p\right)\left(\vec{x}_q^{n-1} - \vec{x}_p^{n-1}\right) t_c + \left\|\vec{x}_q^{n-1} - \vec{x}_p^{n-1}\right\|^2 - \left(r_p + r_q\right)^2 = 0 \quad (6)$$

Only if this quadratic equation has two solutions the not overlapping particles at t^{n-1} collide during the time step. The smaller solution is the moment of collision. If this solution is within the time step the particles collided and will be processed.

Collision treatment

Once particle-particle collisions are detected either by the overlap criterion or the second criterion they are handled equally as described below. The Hard Sphere Model is applied, which implies that the particles are perfectly spherical and not deformable. In our simulations either friction between the particles and particle rotation are disregarded. It is assumed that only binary collisions take place.

All detected particle pairs are found at their current state t^n. To determine the time of collision and handle it accurately, equation (6) is solved for all detected particle pairs at time step t^{n-1}. If (6) has only complex solutions – which is only possible if the particle pair was found by the second detection criterion – the particles did not collide during the time step but passed one another in a distance superior to the sum of their radii. If (6) has two real positive solutions, the smaller value is the time of collision t_c. In case (6) has only one real solution the particles touch but do not collide as the scalar product in (7) equals zero and the velocity components are not altered. If any negative real solution of (6) exists the particles are overlapping at t^{n-1}. Some thoughts are given to this case at the end of this section. Once the time of collision t_c is found the particles are moved forward in time until $(t^{n-1} + t_c)$. The particles touch now and the collision can be handled by

$$\dot{\vec{v}}_p = \vec{v}_p + \frac{m_q}{m_p + m_q}\left(1 + e_c\right)\left(\vec{w}_{pq}.\vec{k}_{pq}\right)\vec{k}_{pq}$$
$$\dot{\vec{v}}_q = \vec{v}_q - \frac{m_p}{m_p + m_q}\left(1 + e_c\right)\left(\vec{w}_{pq}.\vec{k}_{pq}\right)\vec{k}_{pq} \quad (7)$$

where the dot denotes the values after the collision and e_c is the coefficient of restitution. Now the particles are moved forward until the end of the time step following their trajectory determined by (7). The remaining time until the end of the time step is calculated as $(t^n - (t^{n-1} + t_c))$. The particles are marked in order to prevent that a second collision during the same time step is handled.

Displacing particles after the collisions could indeed lead to a new problem if by doing so an overlap with a third particle is created. This new overlapping particle pair could then be treated as another collision during the same time step if not inhibited. This collision might be one that takes place during the time step respecting the previous collision of the first particle. In this case the collision is missed. But it might also be a collision that never occurs as the third particle collided before with another particle, a collision which has not been treated yet or it might be a collision that occurs outside the current time step. The difficulties involved with allowing another collision are much more important than the disadvantage of missing a single collision. Note that one of the fundamental assumptions is that only binary collisions occur, which is justified if the time step is not too large. A time step criterion will be shown that guarantees an appropriate error control in the statistics measured as function of the mean particle collision time. Due to the particle displacement after collision or the initial distribution of particles especially in dense systems, an overlap of particles at t^{n-1} is possible. To be able to simulate rather dense systems, collisions are treated differently if the particles overlap at t^{n-1} and t^n while approaching one another at t^n. Here, only the velocity components are altered following equations (7), particles are not displaced to t_c. Keep in mind that the goal of this study is mainly coalescence and thus volume fractions superior to 10% will not be handled. However, there is an interest in an algorithm that performs well for collisions over a wide range of volume fractions. One drawback of not displacing particles after collisions could be some alteration of statistical results in non-homogeneous flow configurations. In strong shear flows or close to walls small differences in particle positions might lead to different results. In homogeneous flow configurations such statistical deviations are not expected.

ALGORITHM VALIDATION

The algorithm is validated performing dry granular flow simulations of mono- and bi-dispersed particle mixtures. First, a homogeneous system and second, a system where the initial particle velocity fluctuations are altered to anisotropy are analyzed. Statistics like the probability density functions (PDF) of the relative velocity at the moment of collisions or the collision angle, the collision frequency or particle energy levels are compared with predictions of the kinetic theory of rarefied gases, using the radial distribution function. The assumption of molecular chaos is made, which means that the particle velocities are uncorrelated. The particle pair distribution function can therewith be written as the product of one-particle distribution functions:

$$f^{(2)}\left(\vec{x}_p, \vec{x}_q, \vec{v}_p, \vec{v}_q; t\right) = g_0 \; f^{(1)}\left(\vec{x}_p, \vec{v}_p; t\right) f^{(1)}\left(\vec{x}_q, \vec{v}_q; t\right) \quad (8)$$

where g_0 is the radial distribution function accounting for the increase of the collision frequency when considering particle volume fractions initially not covered by the kinetic theory of rarified gases. $f^{(2)}$ and $f^{(1)}$ are the two-particle and the one-particle distribution functions respectively. Based on the particle pair distribution function (8) theoretical predictions for statistical quantities can be obtained, like collision angle or relative velocity at the time of collision.

Mono-dispersed simulations – homogeneous system

As mentioned above, a pure overlap detection algorithm requires a time step criterion that limits the forward motion of the particles during a time step in order not to miss particle-particle collisions, especially grazing ones. As for grazing collisions the penetration length of the two particles is smaller than for head on collisions, these are most likely to be missed. This limiting criterion is expressed as

$$\frac{\delta l}{d_p} = \frac{3}{2}\sqrt{\pi T}\,\frac{\Delta t}{d_p} \tag{9}$$

with T the granular particle agitation and Δt the time step. In a previous work [11] a pure overlap detection algorithm was used. Its accuracy in regard to missing grazing collisions was expressed by plotting the collision angle and relative velocity PDFs with respect to criterion (9) as seen in fig. 2. A ratio of one for the criterion (9) means that a particle moves exactly one particle diameter forward during one time step. As clearly seen in fig. 2 a sufficient algorithm performance is achieved when the particle propagation is limited to about 13% of a particle diameter. For ratios of (9) larger than this value the simulation results deviate from the prediction based on the kinetic theory. Depending on the flow configuration in DNS+DPS simulations criterion (9) can be more stringent than the CFL number of the DNS, which is disadvantageous as the DNS of the continuous phase then needs to be solved applying a time step which is not optimal.

In the top image of fig. 2 one can see that with an increasing ratio of (9) particle-particle collisions are missed between particles with a high relative velocity, which appears obvious as faster moving particles cover a more important distance during a fixed time step as slower ones. Consequently fig. 2 (bottom) shows that the grazing collisions are more sensitive to a higher ratio of (9). A correct prediction of the collision angle is even harder to achieve as a correct prediction of the relative velocity as it can be seen for a ratio of $\delta l/d_p$=0.13 in fig. 2, where a slight deviation appears even for this low ratio. To remedy this restriction the above described second particle pair detection criterion is introduced into our algorithm. Figure 3 shows results from comparable simulations to the ones from [11]. Also here the relative velocity of colliding particles and the collision angle are represented with respect to criterion (9). However, only the limit case from [11] $\delta l/d_p$=0.13 as well as the worst case scenario with $\delta l/d_p$=1.3 are shown. It is obvious that both the relative velocity and the collision angle are very well represented even with a ratio of (9) as large as $\delta l/d_p$=1.3. This corresponds to an increase of the time step by a factor of ten.

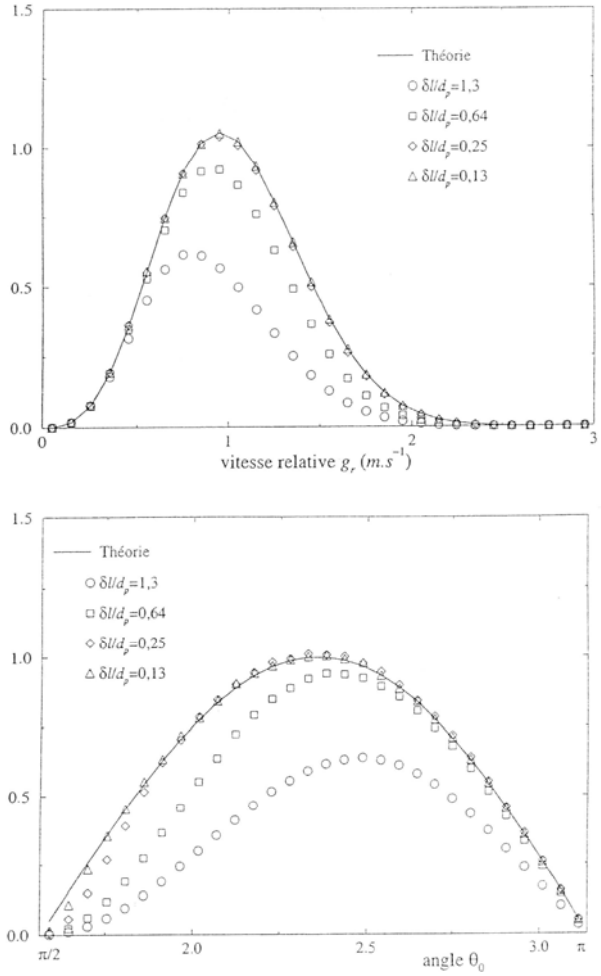

Fig. 2: Relative velocity (top) and collision angle (bottom) at time of collision in dependence of criterion $\delta l/d_p$, using a pure overlap algorithm. Source [11]

A comparison of fig. 2 (bottom) and fig. 3 (bottom) shows that grazing collisions are better represented when the new criterion is applied even for the smallest ratio of (9). Another criterion of validation is a correct prediction of the collision frequency. A correct prediction of the collision frequency is crucial. Using equation (8) a prediction of the collision frequency can be deduced, which is expressed as

$$f_{pq}^{\kappa} = g_0 n_p n_q \pi \left(\frac{d_p + d_q}{2}\right)^2 \sqrt{\frac{16}{\pi}\frac{1}{3}\left(q_p^2 + q_q^2\right)} \tag{10}$$

where n_p and n_q are the particle number densities and q_p^2 and q_q^2 the particle kinetic energies. The radial distribution function g_0 is expressed using the model of Carnahan and Starling [12], shown in (11). Furthermore, the simulation results are compared to another model by Lun and Savage [13] shown in (12).

$$g_0(\alpha_p) = \frac{1}{1-\alpha_p} + \frac{3}{2}\frac{\alpha_p}{(1-\alpha_p)^2} + \frac{1}{2}\frac{\alpha_p^2}{(1-\alpha_p)^3} \quad (11)$$

$$g_0(\alpha_p) = \left(1 - \frac{\alpha_p}{\alpha_{\max}}\right)^{-2.5\alpha_{\max}} \quad (12)$$

with α_p obeying $n_p m_p = \rho_p \alpha_p$ and $\alpha_{max}=0.64$, which corresponds to the maximum packing of uniform random distributed spheres.

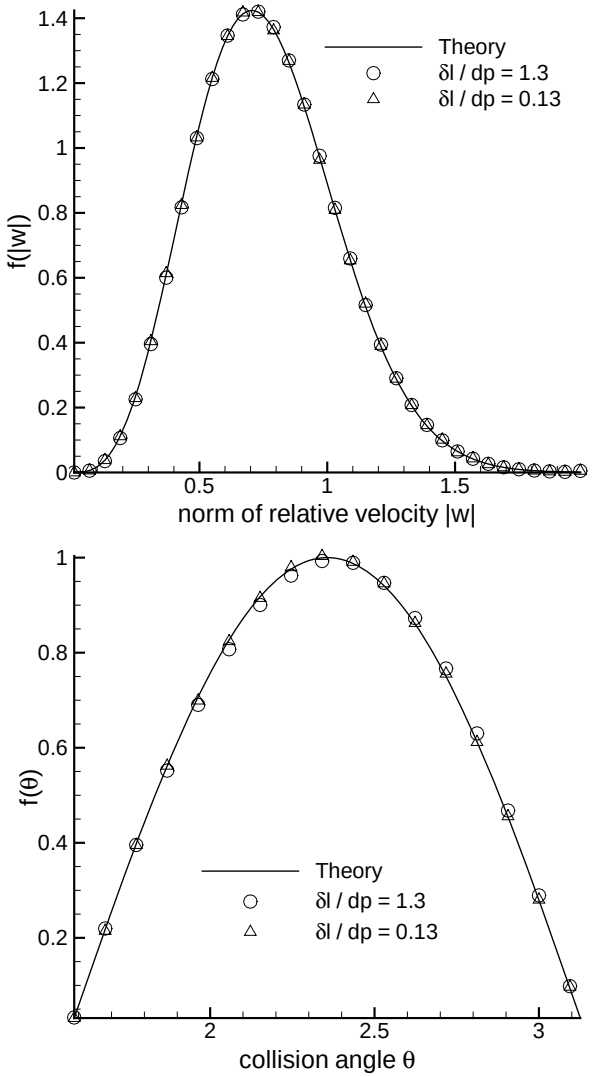

Fig.3: Relative velocity (top) and collision angle (bottom) at time of collision in dependence of criterion $\delta l/d_p$. Using overlap and the second here introduced detection criterion.

If the computed collision frequency is divided by the theoretical value from (10) without respecting g_0, the radial distribution function g_0 can be measured. The simulation results are compared in fig. 4 to the model predictions for particle volume fractions α_p varying from 0.001 to 0.5. The simulation results coincide very well with the theoretical predictions corrected by the model of Carnahan and Starling [12]. Finally, the mono-dispersed simulations pointed out another characteristic, which is intrinsic to the statistical nature of the mean particle collision time $\tau_c=n_p/f_{pq}$ and lead to a second time step criterion which needs to be respected for high particle volume fractions.

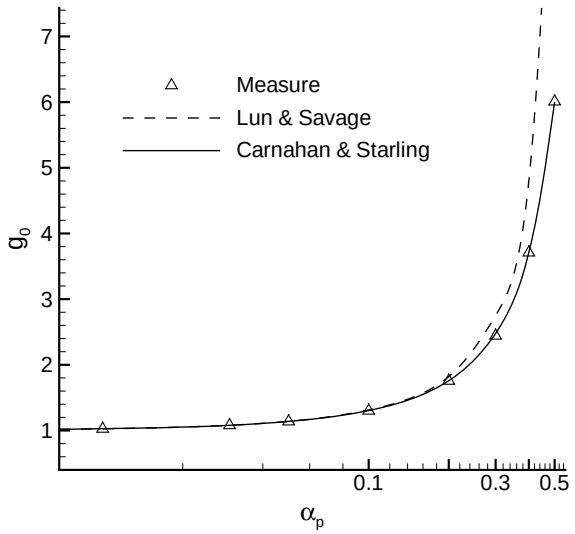

Fig. 4: Comparison of radial distribution function measured to theoretical predictions with respect to the particle volume fraction

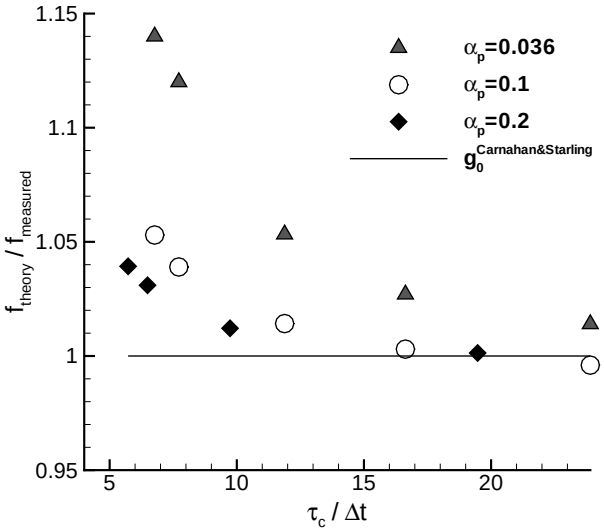

Fig. 5: Ratio of theoretical to measured collision frequency over time step criterion $\tau_c/\Delta t$.

With an increasing particle volume fraction α_p the collision frequency increases and thus the mean particle collision time decreases. First calculations were conducted only respecting $\delta l/d_p \approx 1$ as time step criterion, which led to significant deviations from the theoretical predictions for the collision frequency for particle volume fractions larger than $\alpha_p=0.2$ while agreeing very well for smaller particle volume fractions. As shown in fig. 5 the ratio between the mean particle collision

time and the time step must respect a certain value in order to predict correctly the collision frequency.

The continuous line in fig. 5 represents the ratio between the theoretical predictions of the collision frequency - applying the model of Carnahan & Starling (10) - and the measured collision frequency. The closer the symbols to the continuous line the lesser the error. Calculations were performed over a range of time steps and for several particle volume fractions α_p. It is clearly shown in fig. 5 that numerical predictions are getting better with a diminishing time step Δt (increasing ratio $\tau_c / \Delta t$). This might on first sight contradict the validity of the increase of the time step gained by introducing the second detection criterion (3) and challenge its validity. But as mentioned before, this behavior is explainable by the nature of the mean particle collision time, which is a statistical mean value of a Poisson-like distribution. This means that if the time step is in the order of the mean particle collision time, hence, the ratio $\tau_c / \Delta t=1$, too many particles exist in the system with a collision time much smaller than the mean value and thus have a high probability to collide more than once per time step. Keep in mind that only one single collision per particle is allowed by the fundamental work hypothesis. As a consequence collisions that physically occur are suppressed by the algorithm and thus the collision frequency is underestimated. The ratio of $\tau_c / \Delta t$ for which a certain deviation from the theoretical predictions is achieved varies with respect to the particle volume fractions α_p. It can be seen that the lesser α_p, the higher the necessary ratio of $\tau_c / \Delta t$. This becomes explainable if ones looks at the possible propagation of the particles during the time that corresponds to the mean particle collision time τ_c. The denser a system the lesser a particle moves forward relative to its particle diameter, as the mean particle collision time decreases.

Thus, two time step criteria exist now, the first $\delta l / d_p$ which could be amplified by a factor of ten and a second criterion, which becomes necessary when calculating with the first extended criterion. Those two criteria lead always to a larger time step as in the case of pure overlap algorithm or for very dense systems to the same time step obtaining the same accuracy.

BI-DISPERSE PARTICLE MIXTURE SIMULATIONS

Homogeneous system

Simulations of bi-dispersed particle mixtures are crucial on the way towards poly-dispersed mixture simulations as the bi-dispersed case offers a manageable amount of validation data and gives the chance to test models for different particle diameters. One of the main differences to the mono-dispersed case is that in a bi-dispersed mixture of particles the energy levels for each particle class are not the same in the thermal equilibrium. This equilibrium state is expressed by

$$m_p q_p^2 = m_q q_q^2 \tag{13}$$

The particle granular velocity of the mixture q_m^2 can be written as

$$q_m^2 = \frac{n_p m_p q_p^2 + n_q m_q q_q^2}{n_p m_p + n_q m_q} \tag{14}$$

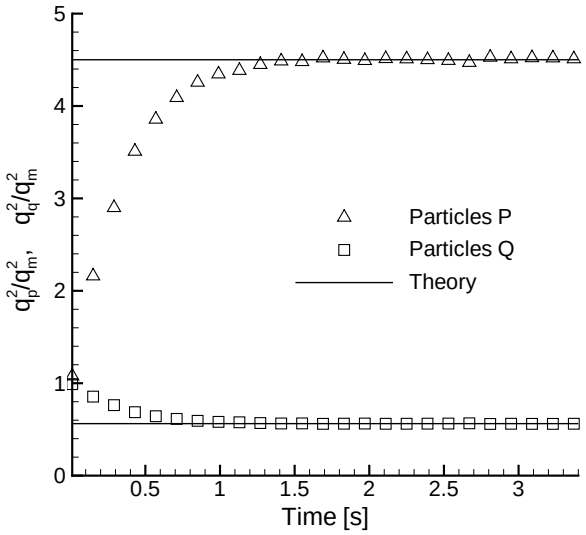

Fig. 6: Time evolution of particle kinetic energy in a binary mixture. The lines are the asymptotic values predicted by (13) and the symbols are numerical simulations

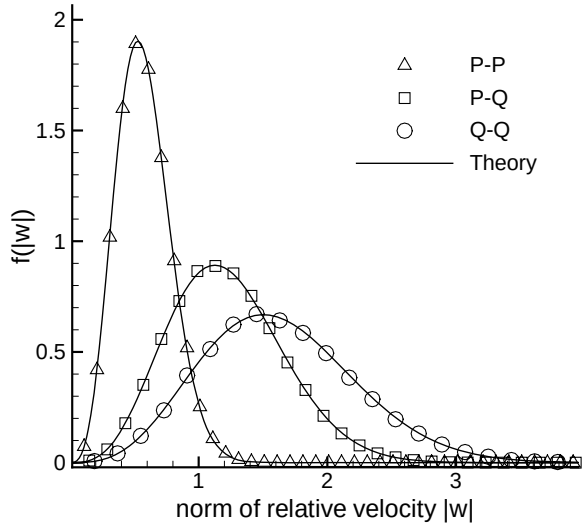

Fig. 7: Relative velocity of the colliding particles for a bi-disperse mixture of particles

Equations (13) and (14) allow us to test whether the particle system reaches an equilibrium state or not. Figure 6 shows that bi-disperse particle mixtures well converge around their theoretical predictions and thus reach a state of equilibrium. Statistics obtained for the mono-dispersed case can also be determined from the same theoretical formulations for bi-dispersed particle mixtures. However, in a bi-disperse mixture more than one distribution will be obtained, as collisions occur between particles of classes P-P, Q-Q but as well P-Q. Hence, three curves must be plotted for the relative velocity at the time of collision in a bi-dispersed particle

mixture. As seen in fig. 7, the simulation results coincide very well with the theoretical predictions.

A correct prediction of the collision frequency remains important also in the case of a bi-dispersed particle mixture. In this case, however, another model for the radial distribution function g_0 is necessary. Also three different values of g_0 will be obtained. The model used in this work, is the one from Mansoori *et al.* [14]. The radial distribution functions are given by

$$g_0^{pq}(\alpha_m) = \frac{1}{1-\alpha_m} + \frac{3}{2}\left(\frac{d_p d_q}{d_p + d_q}\right)\frac{\xi_{pq}}{(1-\alpha_m)^2} + \frac{1}{2}\left(\frac{d_p d_q}{d_p + d_q}\right)^2 \frac{\xi_{pq}^2}{(1-\alpha_p)^3} \tag{15}$$

with

$$\alpha_m = \sum_{i=p,q} \alpha_i \qquad \text{and} \qquad \xi_{pq} = 2\sum_{i=p,q}\frac{\alpha_i}{d_i} \tag{16}$$

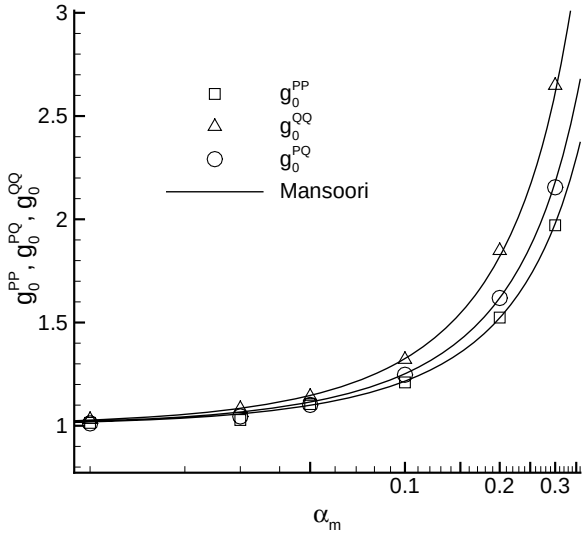

Fig. 8: Comparison of radial distribution function measured to theoretical predictions in bi-dispersed case

Figure 8 shows the comparison of the measured values of g_0 over a range of mixture particle volume fractions. The model of Mansoori e*t al.* [14] is found to coincide very well with the results from the numerical simulations. One of the inconveniences of this model from Mansoori *et al.* is that it does not tend towards infinity for a particle volume fraction tending towards the maximum particle volume fraction. A model suggested by Patino & Simonin [16] that remedies the extreme value problem by delivering good agreement for very high particle volume fractions is also compared to the simulations. However it appears to be more suitable for rather dense systems close to the maximum particle volume fraction.

Anisotropic simulations

The velocity components of a converged bi-dispersed homogenous particle mixture are altered to anisotropy at the beginning of the simulation in order to account for the transfer of anisotropy in the velocity components between the different particle classes. Additionally, it is possible to disturb the thermal equilibrium and wait for a return to the equilibrium state. The modification of the velocity components is done by

$$v_{p,i} = \alpha_i \cdot v_{p,i}^{\text{homogenous}}$$
$$v_{q,i} = \beta_i \cdot v_{q,i}^{\text{homogenous}} \tag{17}$$

where α_i and β_i obey the following relations in order to keep the thermal equilibrium

$$\alpha_1^2 + \alpha_2^2 + \alpha_3^2 = 3 \qquad \text{and} \qquad \beta_1^2 + \beta_2^2 + \beta_3^2 = 3 \tag{18}$$

$$q_p^2 = \frac{\alpha_1^2 + \alpha_2^2 + \alpha_3^2}{3} q_{p,\text{homogenous}}^2 \tag{19}$$

If the thermal equilibrium is disturbed the relations (18) do not equal three anymore and the system will converge around a new equilibrium state. The following three test cases are performed here:

$$\alpha_1 = 0.4; \alpha_2 = 1.0; \alpha_3 = \sqrt{3-\alpha_1^2-\alpha_2^2} \approx 1.3565$$
$$\beta_1 = 1.0; \beta_2 = 1.0; \beta_3 = \sqrt{3-\beta_1^2-\beta_2^2} = 1.0 \tag{20}$$

$$\alpha_1 = 0.4; \alpha_2 = 1.0; \alpha_3 = \sqrt{3-\alpha_1^2-\alpha_2^2} \approx 1.3565$$
$$\beta_1 = 0.6; \beta_2 = 1.0; \beta_3 = \sqrt{3-\beta_1^2-\beta_2^2} \approx 1.2806 \tag{21}$$

$$\alpha_1 = 0.4; \alpha_2 = 1.0; \alpha_3 = \sqrt{1.5-\alpha_1^2-\alpha_2^2} \approx 0.583$$
$$\beta_1 = 0.6; \beta_2 = 1.0; \beta_3 = \sqrt{2.5-\beta_1^2-\beta_2^2} \approx 1.06 \tag{22}$$

A collision model for particle kinetic stresses [15] is validated with the direct simulations performed here for a bi-dispersed mixture of particles. Configuration (20) is chosen with one class altered to anisotropy and the second class remains homogenous. Configuration (21) is intended to show the return to isotropy by collisions within the classes P or Q. For (20) and (21) the thermal equilibrium is conserved. Finally, configuration (22) represents a case, where the thermal equilibrium is disturbed. The model details can be found in [15]. The following specifications are used in the simulations: particle diameter ratio $d_p/d_q = 2$, particle volume fraction ratio $\alpha_p/\alpha_q = 1$ and a total particle mixture volume fraction of $\alpha_m = \alpha_p + \alpha_q = 0.1$. The normalized anisotropy tensor is written as

$$b_{p,ij} = \frac{\left\langle v'_{p,i} v'_{p,j} \right\rangle}{\frac{2}{3} q_p^2} - \delta_{ij} \tag{23}$$

Figure 9 shows that the model [15] is in good agreement with the numerical simulation. While the altered velocity

components in class P return to isotropy as expected and predicted by [15], the initially un-altered component remains zero. However, the second particle class Q, which was not altered either exhibits a creation of anisotropy in those velocity fluctuation components that were turned to anisotropy for the other class. This can mainly be explained by a transfer of anisotropy by collisions P-Q.

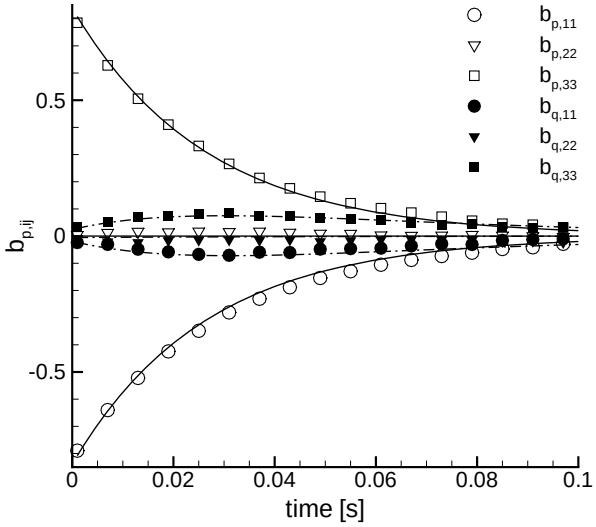

Fig. 9: Simulations with configuration (20). The solid (P) and dashed lines (Q) correspond to the model prediction for the transfer of anisotropy of the two particle classes with different diameters

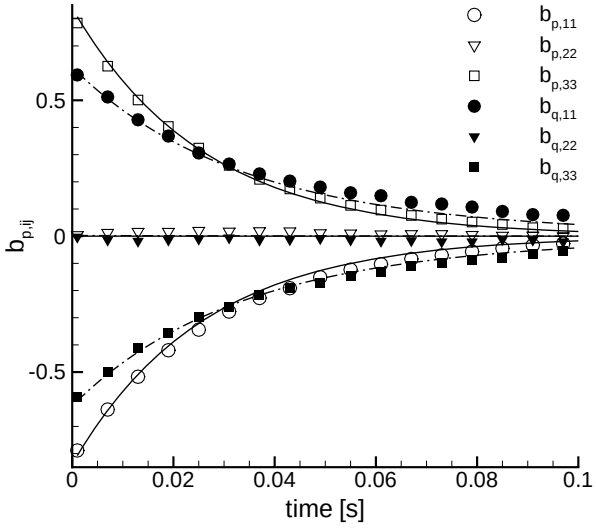

Fig. 10: Simulations with configuration (21). The solid (P) and dashed lines (Q) correspond to the model prediction for the transfer of anisotropy of the two particle classes with different diameters

Figure 10 shows the effect of redistribution of anisotropy within the same particle class. Both particle classes are altered to anisotropy following configuration (21). The return to isotropy here is mainly due to collisions P-P or Q-Q.

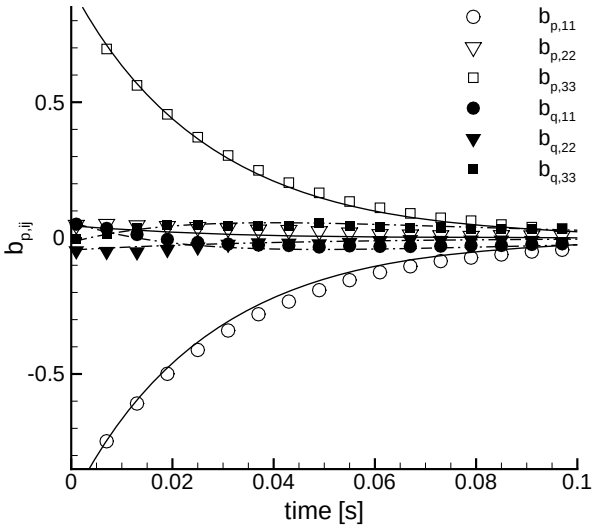

Fig. 11: Simulations with configuration (22). The solid (P) and dashed lines (Q) correspond to the model prediction for the transfer of anisotropy of the two particle classes with different diameters

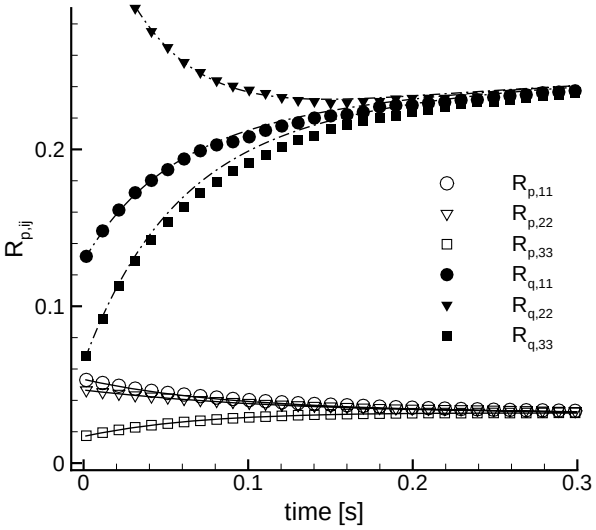

Fig. 13: Simulations with configuration (22). The solid (P) and dashed lines (Q) correspond to the model prediction for the transfer of anisotropy of the two particle classes with different diameters. Particle kinetic stresses $R_{p,ij} =< v'_{p,i} v'_{q,i} >$

Finally, the thermal equilibrium is disturbed by not respecting relations (18) and calculating with configuration (22). Figure 11 shows that the model predicts the correct return

to isotropy. It is interesting to see that the crossing courses for the components of class Q are well represented.

In order to amplify the effect of finding a new equilibrium state fig. 13 shows the simulations and model predictions for a case with the specifications (22). Figure 13 shows that the system converges around its new equilibrium state. However, the particle diameter ratio is $d_p/d_q = 0.5$ and the particle volume fraction ratio is $\alpha_p/\alpha_q = 0.125$. The model predictions are found to coincide well with the direct simulation results.

CONCLUSION

An algorithm for the treatment of particle-particle collisions in poly-dispersed particle mixtures is developed and validated in several different test cases for mono- and bi-disperse configurations. Besides the ability to treat particles with different diameters, several improvements are achieved. First, the time step criterion that limits the particle propagation during a time step in overlap detection algorithms could significantly be increased by introduction of a second detection criterion comparing the relative quantities of the colliding particles. Furthermore, by applying this second criterion grazing collisions are more reliably detected. It was shown that PDFs of the relative velocity of the colliding particles and of the collision angle are correctly represented and that the collision frequencies can properly be determined. It was shown for bi-dispersed particle mixtures that the model of Mansoori *et al.* coincides very well with the simulations, especially in the most interesting domain of volume fraction for the purpose of this work. Also it was shown that bi-dispersed mixtures converge around their thermal equilibrium and that the system returns into a state of isotropy after artificially disturbing its isotropy. Hereby, the model predictions from [15] were verified conducting bi-disperse simulations. The expected transfer of isotropy from one particle class to the other could be shown. In this work a suitable tool for the direct simulation of particle mixtures with different diameters is created. It will serve within direct simulations of two-phase flows (DNS+DPS) for the determination of the coalescence rate respecting fluid particle interactions in order to develop and validate Eulerian models.

ACKNOWLEDGMENTS

This research project has been supported by a Marie Curie Early Stage Research Training Fellowship of the European Community's Sixth Framework Programme under contract number 'MEST-CT-2005-020426'.

REFERENCES

[1] Ashgriz, N. and Poo, J.Y., 1990, Coalescence and separation in binary collisions of liquid drops, J. Fluid Mech., vol. 221, pp. 183-204

[2] Qian, J. and Law, C.K., 1997, Regimes of coalescence and separation in droplet collision, J. Fluid Mech., vol. 331, pp. 59-80

[3] Estrade, J.-P., 1998, Etude expérimentale et numérique de la collision de gouttelettes, Thèse de l'école national supérieure de l'aéronautique et de l'espace

[4] Sigurgeirsson, H., Stuart, A., Wan, W.-L., 2001, Algorithms for Particle-Field Simulations with Collisions, J. of Comp. Physics **172**, 766-807

[5] Hopkins, M.A. and Louge, M.Y., 1990, Inelastic microstructure in rapid granular flows of smooth disks, Phys. Fluids **A** 3 (1)

[6] Sundaram, S. and Collins, L.R., 1996, Numerical Considerations in Simulating a Turbulent Suspension of Finite-Volume Particles, J. of Comp. Physics **124**, 337-350

[7] Lubachevsky, B.D., 1990, How to simulate Billiards and Similar Systems, J. of Comp. Physics **94**, 255-283

[8] Rapaport, D.C., 1980, The event scheduling problem in molecular dynamic simulation, J. of Comp. Physics **34**, 184-201

[9] Donev, A., Torquato, S., Stillinger, F., 2005, Neighbor list event driven molecular dynamics simulation for non-spherical hard particles I. Algorithmic details, J. of Comp. Physics **202**, 737-764

[10] Fede, P., 2004, Modélisation et simulation de l'influence de la turbulence sur les collisions dans les écoulements mono- et bi-solides, Thèse de l'Institut National Polytechnique de Toulouse

[11] Sakiz, M., 1999, Simulation numérique lagrangienne et modélisation eulérienne d'écoulement diphasiques gaz-particules en canal vertical, Thèse de l'Ecole National des Ponts et Chaussées

[12] Carnahan, C.F. and Starling, K.E., 1969, Equation of state of non-attracting rigid sphere, J. Chem. Phys. 51, 635-636

[13] Lun, C.K.K. and Savage, S.B., 1986, The effects of an impact velocity dependent coefficient of restitution on stresses developed by sheared granular materials, Acta Mechanica 63, 539-559

[14] Mansoori, G.A., Carnahan, N.F., Starling, K.E., Leland, T.W., 1971, Equilibrium thermodynamic properties of the mixture of hard sphere, J. Chem. Phys. 54, 1523-1525

[15] Fede, P, Simonin, O., 2005, Application of a perturbated two-maxwellian approach for the modelling of kinetic stress transfer by collision in non-equilibrium binary mixture of inelastic particles, Proceedings of FEDSM2005, FEDSM2005-77127

[16] Patino, G. and Simonin, O., 2003, General derivation of eulerian-eulerian equations for multiphase flows, Internal technical report, Institute Mècanique des Fluides de Toulouse